Title	Theoretical Study of Electron Transport in Nanometer-scale Compound Semiconductor Devices
Author(s)	水田, 博
Citation	大阪大学, 1993, 博士論文
Version Type	VoR
URL	https://doi.org/10.11501/3070508
rights	
Note	

Theoretical Study of Electron Transport
in Nanometer - scale
Compound Semiconductor Devices

（ナノメータスケール化合物半導体素子における電子輸送の理論的研究）

Hiroshi Mizuta

Theoretical Study of Electron Transport in Nanometer-scale Compound Semiconductor Devices

(ナノメータスケール化合物半導体素子における電子輸送の理論的研究)

Hiroshi Mizuta

Theoretical Study of Electron Transport in Nanometer-scale Compound Semiconductor Devices

Hiroshi Mizuta

CONTENTS

Chapter 1 Introduction 1

- 1.1 Overview and background 1
- 1.2 Reference I 12

Chapter 2 Classical hydrodynamic electron transport in submicron heterojunction devices 18

- 2.1 Macroscopic drift-diffusion transport in semiconductor heterostructures with SRH carrier trap processes 18
  - 2.1.1 Drift-diffusion modelling of carrier transport in heterostructures 19
  - 2.1.2 Shockley-Reed-Hall (SRH) model for carrier emission-absorption processes via deep levels 22
- 2.2 Fermi-level pinning due to DX centres in submicron-gate AlGaAs/GaAs HEMTs 26
- 2.3 Effects of surface trap levels on characteristics of deep submicron devices 37
  - 2.3.1 Surface potential effects on nanometer-gate HEMTs 37
  - 2.3.2 Surface carrier recombination in an extrinsic base region of HBTs 44
- 2.4 Reference II 49

Chapter 3 Coherent quantum transport in resonant tunnelling diodes (RTDs) 52

- 3.1 Resonant tunnelling in double barrier heterostructures 52
- 3.2 Theory of global coherent resonant tunnelling 58

3.2.1 Transfer matrix theory of transmission probability 58
3.2.2 Self-consistent calculations - Introduction of space charge build-up - 63
3.3 Multiple-well resonant tunnelling structures and multi-valued logic applications 70
3.3.1 A triple-well RTD and its application to multiple-valued logic 72
3.3.2 An InGaAs/AlGaAs double-well resonant tunnelling diode 83
3.4 Effects of scattering process on coherent tunnelling 89
3.5 Reference III 96

Chapter 4 Dissipative quantum transport and electron dynamics in RTDs 100

4.1 Non-equilibrium electron distribution and 2D - 2D resonant tunnelling 102
4.2 Theory of dissipative quantum transport in RTDs 106
4.2.1 Time-dependent statistical density matrix equation 107
4.2.2 Femtosecond electron dynamics in RTDs 115
4.3 Space charge build-up and intrinsic bistability of RTDs 129
4.3.1 Numerical analysis of intrinsic bistability 129
4.3.2 Magnetotransport measurements on electron accumulation 134
4.4 Reference IV 141

Chapter 5 Quantum transport in three-dimensionally confined nanostructures 145

5.1 Low-dimensional resonant tunnelling structures 146
5.2 Theory of zero-dimensional resonant tunnelling 151
5.2.1 Three-dimensional S-matrix theory 151
5.2.2 Lateral mode conserving and non-conserving resonant tunnelling 156
5.3 Gated resonant tunnelling structures - squeezable quantum dots - 169
5.3.1 Variable area resonant tunnelling devices 172
5.3.2 Three-dimensional confinement effects on tunnelling characteristics 177
5.3.3 Tunnelling through a single impurity state 180
5.4 Reference V 188

Chapter 6 Summary 192
Acknowledgements 194
A list of publications and presentations 195

CHAPTER 1

INTRODUCTION

1.1 Overview and background

Since the metal-semiconductor field-effect transistor (MESFET) was first proposed by Mead in 1966 [1] there has been considerable interest in *compound semiconductor devices* because of their superior carrier transport properties in both low and high field regimes. For the last two decades, especially, crystal growth techniques for compound semiconductors such as molecular beam epitaxy (MBE) and metalorganic chemical vapor deposition (MOCVD) have rapidly progressed and have enabled us to utilize multi-layered *heterostructures*. The fact that heterojunctions between different materials with smooth heterointerfaces become available by using these techniques has greatly expanded a possibility of structural design. An idea of modulation doping was proposed by Dingle et al. [2] to separate conduction electrons and ionized donor impurities and achieve impurity-scattering-free electron transport. This new heterostructure has led to a novel high electron mobility transistors (HEMTs) [3],[4] in which two-dimensional electron gas (2DEG) formed at an heterointerface has extremely high mobility: Typical mobility as high as 10^6 cm^2/Vsec has been achieved at low temperatures [5]. A variety of HEMT structures has been examined for further improvement in transport properties of 2DEG: AlGaAs/InGaAs pseudomorphic HEMTs, double heterojunction HEMTs, and so on. Heterojunction bipolar transistors (HBTs) [6],[7] have been also proposed as a promising ultra-high speed device. A wide gap AlGaAs layer introduced in an emitter region suppresses hole injection from the base region into the emitter, and thus the use of heavy doping is allowed in the base. This fact results in reductions in base resistance and emitter-base charging time leading to great improvement in the high-speed performance. Recent sophisticated HBTs with advanced collector structures (ballistic collection transistors: BCTs) have exhibited the cut-off frequency over 100 GHz [8] by inducing ballistic transport in the collector regime. Even more functional devices have emerged by using the state-of-art growth and fabrication technologies as shown later in this thesis. Some of these compound semiconductor devices have already come onto a stage of a practical use and substituted conventional silicon-based devices in some applicational areas. For example, the pseudomorphic AlGaAs/InGaAs HEMTs have already been used for ultra low-noise amplifiers operating at high frequencies above 1GHz.

The trend of the compound semiconductor devices towards progressibly more complex structures has increased a demand for numerical simulation technologies of carrier transport and device characteristics (see Fig. 1.1). A classical *drift-diffusion* (DD) model of carrier transport in semiconductor devices has been intensively studied since one-dimensional numerical simulation of silicon bipolar transistor in a self-consistent iterative scheme has been reported by Gummel et al. in 1964 [9].

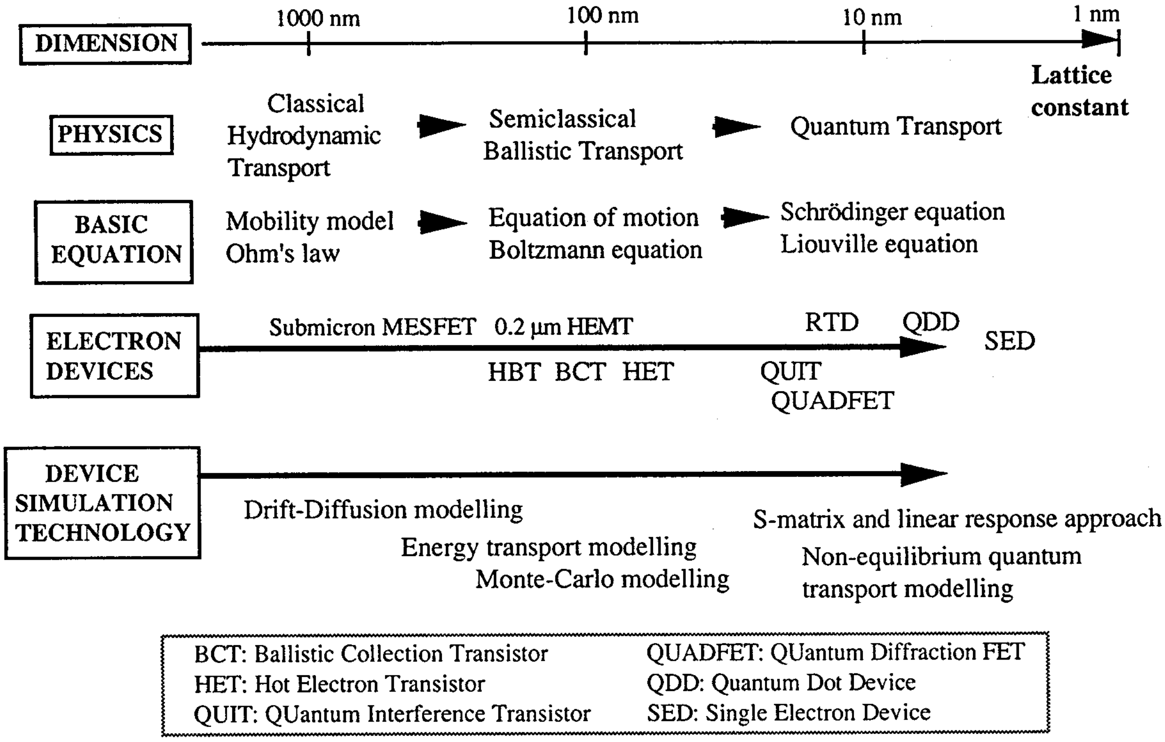

Figure 1.1 Trend of compound semiconductor devices and related device modelling.

Even though recent ultra-small devices with sizes as small as 100 nm or less (see Chapters 3 - 5) often show characteristics in which ballistic or even quantum mechanical features of carrier transport play significant roles beyond the DD feature, the numerical simulation based on the DD modelling is still in practice the most powerful tool to design the FETs and Bipolar transistors which are currently being developed. For silicon devices the two-dimensional and even three-dimensional device simulation technologies based on the DD model have already been established as a powerful and practical CAD tool. The DD modelling of the heterojunction compound semiconductor devices, on the other hand, have been still under investigation since some additional modellings of phenomena characteristic to compound semiconductors are necessary to have reasonable quantitative agreements between simulated and experimental results.

One of these difficulties arises purely from the use of heterojunctions: the DD modelling should be modified to describe an inhomogeneous nature of the structures [10]-[12] and the resultant current really depends on the modeling of transport across the heterointerfaces. Another difficulty, this may be more serious and often cumbersome, is caused by *carrier trap levels* which are located deeply in the energy band-gap. The deep levels are characteristic to compound semiconductors which could be formed both in bulk materials and at interfaces (including surfaces). The most well-known deep level is an EL2 donor state inevitably formed in semi-insulating GaAs substrate manufactured by using the conventional liquid encapsulated Czochralski method. It has been found that the semi-insulating property of the substrate stems from the EL2-donors compensating carbon shallow acceptors. The compensation phenomenon leads to Fermi-level pinning at the EL2-donor energy which is near the middle of the band gap. DX centres [13] in N-type AlGaAs layers grown by using MBE are also well-know deep levels which appear for mole fraction x more than about 0.25 [14] though their origin is still under a lively discussion. A common understanding of the DX centre is that a X-point induced defect state is somehow combined with donor levels and effectively gives rise to quite large x-dependent ionization energy of the donors. Additionally much more uncertain deep levels are reported for surfaces and interfaces of the devices: Fermi-level pinning due to surface states is known as a common phenomenon for compound semiconductor devices, and a phenomelogically unified defect model has been proposed by Spicer et al. in 1979 [15]. There are so many other deep levels which have not yet been made clear so far.

The modified DD-modelling has been also under study include energy and momentum relaxation effects. A simple velocity-field dependence used in the DD-modelling is replaced by numerical solutions of momentum and energy transport equations which enable to reproduce locally *ballistic (or hot electron)* transport in devices. This is often called semiclassical modelling as it allows to simulate non-equilibrium aspects of electron transport in smaller devices in a deep submicron regime [16]-[18]. Data on energy and momentum relaxation times required for the semiclassical modelling are usually taken from one-dimensional Monte Carlo simulations and incorporated as a data base. At present the semiclassical modelling may be the most practical and efficient way of simulating deep submicron devices currently being developed. For more detailed study of non-equilibrium transport large-scale self-consistent ensemble Monte Carlo simulation technology [19]-[21] is becoming popular with a steady improvement in computer resources available though it is still a bit tough for practical use.

Substantial improvement in MBE technique in 1980's has facilitated us to design exceedingly well-controlled multi-layered structures (superlattices) with an atomic-scale accuracy in layer thickness. It has definitely opened a door to a new research field of nanometer-scale semiconductor devices where the quantum mechanical wave-nature of electrons is expected to appear. Advances in the study of electron transport in this new regime are certainly going to make a novel trend for device development which is entirely different from the conventional trend based on a simple relation between device speed and dimension. Instead of conventional devices which utilize the drift-diffusion-type carrier transport, a variety of novel device concepts have been proposed based on the quantum-mechanical features of electrons such as tunnelling and interference. *Resonant Tunnelling Diodes (RTDs)* emerged as a pioneering device in this field in middle of 1970's which utilizes the electron-wave resonance in multi-barrier heterostructures. The idea of the resonant tunnelling in finite semiconductor superlattices was first proposed by Tsu and Esaki in 1973 [22] shortly after MBE technique appeared in the research field of compound semiconductor crystal growth. Experimental results [23] reported in those days showed only small shoulders in the current-voltage characteristics at low temperatures and were no more than to confirm a theoretical prediction on resonant tunnelling. This is because the MBE technique was still at an early stage and not good enough to grow the AlGaAs/GaAs double barrier structure in which tunnelling current through a resonant state dominates background current through crystal defects. A substantial development in the MBE technique, however, has made a remarkable improvement in negative differential conductance characteristics of the devices and has allowed us to utilize them to create a new functional device. An encouraging experimental result was reported in 1983 [24] about an observation of negative differential conductance at terahertz frequencies which has made this device really attractive from an application point of view. The large negative differential conductance obtained even at a room temperature directly leads to multi-stable device operation, and several new functional devices such as integrated RTDs [25], multiple-barrier RTDs [26]-[28], and three-terminal resonant tunnelling transistors [29]-[31] have been successfully developed which could take the place of conventional devices by making a totally new trend curve for device miniaturisation. In terms of both high operating temperatures and voltages, the resonant tunnelling device has become one of the most promising quantum mechanical devices which have already come into the field of circuit research.

At the same time, RTDs have attracted people's interests purely from the viewpoint of electron transport physics. RTDs provide enormous amount of information about non-equilibrium quantum transport despite the simple structure. The coherent electron-waves suffer from scattering processes which cause momentum and energy relaxations of electrons resulting in degradation of peak-to-valley current ratio of the device [32],[33]. Also many-body effects of electrons on transport such as self-consistent field due to electrons accumulated in a quantum well [34] or quantum correlations between electron-waves with different phases [35] have an influence on characteristics of the device. These complicated transport processes beyond the simple coherent tunnelling picture are now being lively discussed, and detailed analyses are needed to make them clear. Measurement techniques for the resonant tunnelling under magnetic field [36] or hydrostatic pressure [37] have been introduced to investigate the dissipation process and intervalley scattering in the device. A time-resolved photoluminescence technique with a picosecond laser has been also adopted [38] on purpose to study the dynamical aspect of the resonant tunnelling. One of the recent success may be to have revealed that the device has an intrinsic bistability in the negative differential conductance region [39] which stems from dynamical redistribution of electrons in the quantum well. To make clear this both intensive numerical studies based on the transient quantum transport calculations [40][35] and magnetotransport studies of electron accumulation in the quantum well [36] have been required. RTDs are thought to be a good laboratory to investigate quantum transport in semiconductor microstructures and has already played an important role in disclosing physics of electron transport more than being just a negative conductance device. In addition, a new idea of transport measurement like resonant tunnelling spectroscopy has been proposed [41] by utilizing the resonant tunnelling structure as an energy filter for electron-waves.

From theoretical standpoints the validity of the classical transport simulation technologies is obviously questionable in this regime and a new description of semiconductor transport is required based on *quantum transport theory.* It might be important to make clear that the term "quantum transport theory" here does not mean quantum mechanical corrections to the classical transport theory which have been repeatedly adopted to introduce the effects of multiple subbands of two-dimensional electron gas in HEMTs [42],[43]. The basis of quantum transport theory is addressed to completely different quantum statistical mechanics. There are basically two types of appropriate theories depending on how far the system is from equilibrium: *Linear response theory* and *non-equilibrium quantum transport theory.* Experimental results such as conductance fluctuations observed in quantum wires or conductance quantization in point contacts are phenomena in the linear response regime and can be well described by using the linear response theory (see Fig. 1.2). The linear response theory assumes that the change in the distribution function from the one in thermal equilibrium is very small and so only the spectrum function is required. This theory leads to *Landauer-Büttiker formula* of conducting current in which numerical calculations of *scattering matrix (S-matrix)* are required. The Landauer-Büttiker formula may be applied to the system not only under an infinitesimal bias but under a finite bias if there is no dissipative events in the system: The transport is called *global coherent transport* as *phase-coherence* of electron waves is conserved throughout the system. In the case of RTDs the Landauer-Büttiker formula reduce to widely used *Tsu-Esaki formula* of resonant tunnelling current based on a one-dimensional *transfer matrix.* Quantum-mechanical modeling based on the Tsu-Eaki formula has been preferably used, because of its simplicity, to analyze not only RTDs [32],[33], but also quantum wires and the quantum modulated transistor.

One major problem of the global coherent transport modelling is the fact that we have to assume the statistical distribution of carriers in advance. Systems are usually treated as perfect conductors with no dissipation process, so that this model can be applied only to completely ballistic systems. If the system is dissipative and far from equilibrium, i.e. the applied bias V is larger than E_F/q (see Fig. 1.2), a proper description of transport is then given in terms of a *non-equilibrium Green's function* [44] or alternatively a *statistical density matrix* [45]. In these descriptions the simultaneous specification of both position and momentum of electrons is prohibited according to Heisenberg's uncertainty principle in contrast with the classical distribution function expressed in the (r,p) phase space. Nevertheless it is sometimes useful to introduce a corresponding quantum distribution function, *Wigner distribution function* [53], which is defined as a Wigner-Weyl transform of the statistical density matrix. These non-equilibrium transport theories have not been widely used for device modelling because of the difficulty in implementation.

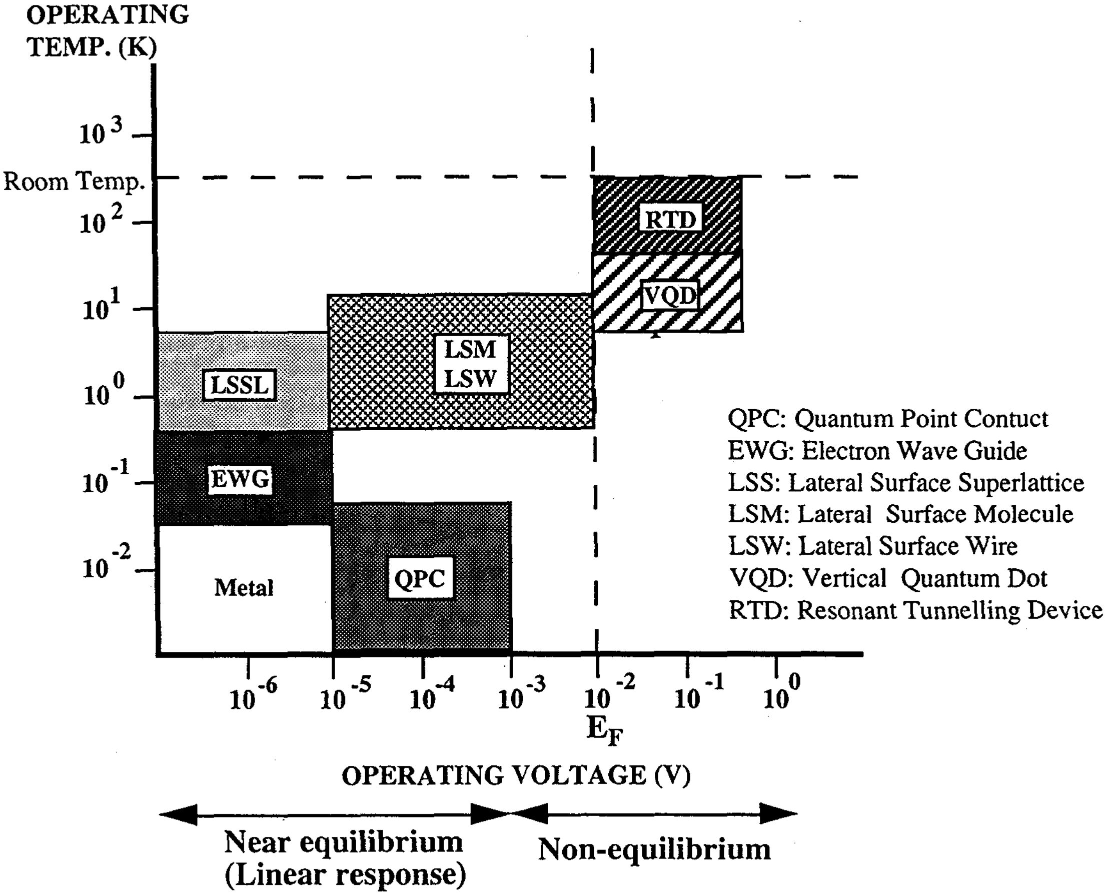

Figure 1.2 Classification of several quantum mechanical devices based on operating voltages and temperatures.

Among these descriptions non-equilibrium Green's function approach reported by Kadanoff, Baym [46], and Keldysh [47] may be the most fundamental ground for quantum transport simulation. The Kadanoff-Baym-Keldysh approach adopts four kinds of Green's function: Retarded, advanced, and two correlation functions which depend on both double times, t and t', and double positions, $\vec{r}$ and $\vec{r}'$. Starting with basic Dyson's equations for these four Green's functions they have successfully derived both transport and spectrum equations. These formula basically include all the necessary quantum mechanical processes due to many-body effects and non-local events and may eventually be basis of quantum device simulation. At the present stage, however, the KBK-formula are too much too far from a practical use as the non-equilibrium Green's functions have four variables, t, t', x, x', even four one-dimensional systems and numerical solutions for the transport and spectrum equations are hardly obtainable by using the present computer systems. Though some attempts have been very recently reported to solve these equations for a uniform one-dimensional system [48] or to simplify them to tractable forms to treat more complex systems [49]-[51], this approach requires more investigations for its practical use.

A bit more tractable description of quantum transport is given by using the density matrix or Wigner function. The density matrix is a double-space-single-time function which is obtained from the non-equilibrium Green's function by assuming translational invariance in time. The time evolution of the density matrix is then determined by the Liouville-von Neumann equation [52][53] which is basically an equation of motion of the density matrix with additional terms which represent collisional processes. Very recently, both the density matrix [35] and Wigner function [54],[40],[55] have been solved numerically to analyze electron transport in RTDs. The one-dimensional Liouville-von Neumann equation has been solved in the finite-difference scheme, and some calculated results have been reported on the steady-state I-V characteristics and transient behaviour of RTDs. Although some major problems such as boundary conditions and correct initial conditions for the density matrix and Wigner function are still under discussion, the successful application of these approaches to electron devices is certainly a significant advance in quantum device simulation technology.

Since later in 1980's the research on nanometer-scale semiconductor devices has proceeded to a new stage in parallel with a progress of lateral fabrication technology. Recent sophisticated manometer fabrication technologies such as electron beam (EB) lithography or focused ion beam (FIB) implantation have made it possible to confine electrons laterally in a small area with sizes below 100 nm. These nanometer-scale semiconductor structures are often called *mesoscopic systems*. Mesoscopic structures are basically classified into two groups depending on degrees of freedom of electrons in the system: One-dimensional (1D) and zero-dimensional

(0D) structures. The 1D-system is a structure in which electrons are laterally confined in one direction and thus still move freely in another lateral direction: Quantum wires, electron waveguides, and quantum point contacts are typical examples. One the other hand, if electrons are laterally confined in both dimensions electrons lose degree of freedoms completely, and thus the structures are called 0D-systems. When the confinement is complete in all dimensions a 0D-structure is not a conductive system but an isolated one. This is also called a *quantum dot* and the three-dimensional confinement effects on its optical properties have been studied. On the other hand, when a 0D-structure is weakly connected to reservoirs, it is virtually isolated but still conductive . It might be more appropriate to term this sort of system as a quasi-0D-structure, but following a common way, it is simply called a 0D-structure in the following chapters. Resonant tunnelling devices have also come into this regime and then called 0D-RTDs [56][57] because electrons are laterally confined as well as vertically. The 0D-RTD is an ideal system to investigate electron-wave transport properties through three-dimensionally quantized energy levels. By designing structural parameters such as barrier thickness, well width, and a size of lateral confinement, it is possible to realize a *"quantum box"* in which number of electrons is nearly quantized. Therefore the 0D-RTD recently attracts a great interest in regards to single charge assisted transport [58], so called Coulomb blockade. Also fine structure attributable to a single ionized impurity in a dot has been recently reported in this system. The 0D-RTDs now facilitate us to observe directly phenomena originated from a few-body problem which is one of the most cumbersome parts of quantum mechanical statistics.

Theoretical study of these transport phenomena has just begun, and only preliminary results have been reported. Ideally speaking the theoretical framework required to simulate the quantum transport in 0D-structures is the same as those explained above. However three-dimensional quantization and interactions among electrons at the quantized states make numerical simulations exceedingly difficult because of enormous amount of computational time and memory required as well as mathematical complexity. Very recently a fully three-dimensional numerical simulation of global coherent tunnelling has been reported for the 0D-RTDs based on 3D-S-matrix theory [59]. The simulated results have revealed that the quantum transport in the 0D-RTDs is a mixture of lateral mode conserving and non-conserving resonant tunnelling processes resulting in complicated fine structure in the I-V characteristics. Because number of electrons localized in a quantum dot can be less than ten, electron interactions and correlations are extremely interesting as well as dissipation processes in a dot. Quantum transport simulation of the 0D-systems beyond the coherent transport picture will be definitely important for thorough investigations of these phenomena.

The purpose of this work is to study electron transport in nanometer-scale compound semiconductor devices by using several new numerical modellings. The work presented in this thesis has been done at the Central Research Laboratory, Hitachi, Ltd. (HCRL), from 1985 to 1989, at Hitachi Cambridge Laboratory, Hitachi Europe Ltd., from 1989 to 1991, and again at HCRL after then. Though the whole work is presented by highlighting mainly numerical simulations a lot of relevant experimental results are also included which have been obtained in collaboration with Dr Masao Yamane* and Dr Tomonori Tanoue of Central Research Laboratory (*present address: Semiconductor Design & Development Centre), Hitachi, Ltd., and Dr Chris Goodings, Microelectronics Research Centre, Cavendish Laboratory, University of Cambridge. The present work is aimed not to cover the whole framework of proper transport theory but to investigate several interesting transport properties of nanometer-scale devices by using practical numerical modellings. The following chapters are organized in the manner that physics of transport is centred, and thus are not suited to have a general guide of transport theory.

In this first chapter a brief review of theoretical works on electron transport in compound semiconductor devices has been presented with a historical background of device miniaturization. The materials contained in the following chapters of this thesis progress from Chapter 2 on the drift-diffusion modelling of heterojunction devices in a submicron regime through Chapters 3 and 4 on coherent and dissipative quantum transport in multi-layered resonant tunnelling structures, concluding with Chapter 5 which deals with very recent quantum transport through 0D-nanostructures.

Chapter 2 deals with the classical drift-diffusion modelling of deep submicron heterojunction devices currently being developed. A conventional DD-modelling for homogeneous systems is extended by taking account of heterojunctions and deep trap levels characteristic to compound semiconductors. Carrier capture-emission processes via the deep trap levels are focused, and the Fermi-level pinning effects of DX centres and surface states in AlGaAs/GaAs HEMTs are analyzed as well as surface carrier recombination effects on the characteristics of AlGaAs/GaAs HBTs.

The following three chapters are dedicated to the study of quantum mechanical features of electron transport in semiconductor structures with sizes under 100 nm. Several theoretical studies are presented as well as experimental results on quantum transport in nanometer-scale heterostructures. Although these works are mainly on resonant tunnelling (RT) through finite superlattice structures, it should be first mentioned that the theoretical works described here are not really specific for RTDs but in general applicable to other quantum devices. The study of the quantum transport is divided into three parts.

Chapter 3 is intended to describe a coherent aspect of quantum transport of electrons in multi-layered nanostructures. Tsu-Esaki formula with the transfer matrix calculations are adopted to simulate an energy dependence of the transmission coefficients through the double barrier resonant tunnelling structures. The global coherent tunnelling model introduced here gives us an intuitive and clear picture of what is going on in the resonant tunnelling structures. The theory is then improved by taking account of Hartree's self-consistent field [34] to simulate the potential distribution not only inside the resonant tunnelling structures but also in the emitter and collector accurately. By using the present modelling multiple-well resonant tunnelling diodes are numerically studied, and possibility of their applications to multiple-valued logic is discussed by comparing the calculated results with experimental data. Finally in this chapter a problem of collisional broadening [32][33] related to P/V current ratios is raised and discussed by using a phenomelogical broadening model.

Chapter 4 investigates dissipative quantum transport in RTDs beyond the global coherent tunnelling model in Chapter 3. Non-equilibrium electron distribution and dynamical processes are theoretically studied by using the statistical density matrix [52] and the Wigner distribution function [53]. Time-dependent one-dimensional Liouville-von Neumann transport equation is numerically solved which is a quantum kinetic equation for the density matrix to analyze dissipative transport in double barrier RTDs. Femtosecond electron dynamics and quantum correlations in RTDs are discussed in regard to P/V ratio degradation due to dissipation process. Dynamical space-charge build-up is then demonstrated in the quantum well resulting in the intrinsic current bistability in the negative differential conductance regime of RTDs. Further investigations of the space-charge build up is experimentally done by using a magneto-transport measurement technique.

In chapter 5 quantum transport through three-dimensionally confined 0D-RTDs is studied theoretically and experimentally. Global coherent tunnelling calculations based on 3D-S-matrix theory are conducted to make clear the role of lateral mode non-conserving processes due to non-uniform confinement potential [59]. A new three-terminal 0D-resonant tunnelling device structure is then proposed to achieve quasi-uniform and controllable lateral confinement using focused ion beam implantation technique. Three-dimensional confinement effects on the I-V characteristics are studied by using both the 3D-S-matrix simulation and the experimental results obtained from fabricated gated 0D-RTDs. A new interesting transport phenomenon related to single electron tunnelling through a single ionized impurity state in a quantum dot is finally discussed.

Finally Chapter 6 is intended as a brief summary of the the whole chapters.

1.2 Reference I

[1] C. A. Mead, "Schottky barrier gate field-effect transistor", Proc IEEE, **54**, 307, 1966.

[2] R. Dingle, H. L. Störmer, A. C. Gossard, and W. Wiegmann, "Electron mobilities in modulation-doped semiconductor heterojunction superlattices", Appl. Phys. Lett., **33**, 665, 1978.

[3] T. Mimura, S. Hiyamizu, T. Fujii, and K. Nanbu, "A new field effect transistor with selectively doped GaAs/n-$Al_xGa_{1-x}As$ heterojunctions", Jpn. J. Appl. Phys., **19**, L225, 1980.

[4] S. Hiyamizu, T. Mimura, T. Fujii, and K. Nanbu, "High mobility of two-dimensional electrons at the GaAs/n-AlGaAs heterojunction interface", Appl. Phys. Lett. **37**, 805, 1980.

[5] S. Hiyamizu, J. Saito, K. Nanbu, and T. Ishikawa, "Improved electron mobility higher than 10^6 cm2/Vs in selectively doped GaAs/N-AlGaAs heterostructures grown by MBE", Jpn. J. Appl. Phys., **22**, L609, 1983.

[6] H. Kroemer, "Theory of a wide-gap emitter for transistors", Proc. IRE, **45**, 1535, 1957.

[7] P. M. Asbeck, D. L. Miller, W. C. Petersen, and C. G. Kirkpatrick, "GaAs/AlGaAs heterojunction bipolar transistors with cutoff frequencies above 10 GHz", IEEE Electron Device Lett., EDL-**13**, 366, 1982.

[8] T. Ishibashi and Y. Yamauchi, "A possible near-ballistic collection in an AlGaAs/GaAs HBT with a modified collector structure", IEEE Trans. Electron Devices, **ED-35**, 401, 1988.

[9] H. K. Gummel, "A self-consistent iterative scheme for one-dimensional steady state transistor calculations", IEEE Trans. Electron Devices, **ED-20**, 455,1964.

[10] D. Loret, "Two-dimensional numerical model for the high electron mobility transistor", Solid-State Electron., **30**, 1197, 1987.

[11] J. Yoshida and M. Kurata, "Analysis of high electron mobility transistors based on a two-dimensional numerical model", IEEE Electron Device Lett. **EDL-5**, 508, 1984.

[12] J. Y.-F. Tang, "Two-dimensional simulation of MODFET and GaAs gate heterojunction FET's", IEEE Trans. Electron Devices, **ED-32**, 1817,, 1985.

[13] D. V. Lang, R. A. Logan, and M. Jaros, "Trapping characteristics and a donor-complex (DX) model for persistent-photoconductivity trapping center in Te-doped AlxGa1-xAs", Phys. Rev. **B19**, 1019, 1979.

[14] T. Ishikawa, J. Saito, S. Sasa, and S. Hiyamizu, "Electrical properties of Si-doped $Al_xGa_{1-x}As$ layers grown by MBE", Jpn. J. Appl. Phys., **21**, L675, 1982.

[15] W. E. Spicer, P. W. Chye, P. R. Skeath, C. Y. Su, and I. Lindau, "New and unified model for Schottky barrier and III-V insulator interface states formation", J. Vac. Sci. Technol., **16**, 1422,1979.

[16] E. M. Azoff, "Energy transport numerical simulation of graded AlGaAs/GaAs heterojunction bipolar transistors", IEEE Trans. Electron Devices, ED-**36**, 609, 1989.

[17] T. Shawki, G. Salmer, and O. El-Sayed, "MODFET 2-D hydrodynamic energy modeling: Optimization of subquarter-micron-gate structures", IEEE Trans. Electron Devices, ED-37, 21, 1990.

[18] K. Tomizawa and D. Pavlidis, "Transport equation approach for heterojunction bipolar transistors", IEEE Trans. Electron Devices, ED-**37**, 519, 1990.

[19] Y. Awano, M. Kosugi, K. Kosemura, T. Mimura, and M. Abe, "Short-channel effects in subquarter-micrometer-gate HEMT's", IEEE Trans. Electron Devices, ED-**36**, 2260, 1989.

[20] I. C. Kizilyalli, M. Artaki, and A. Chandra, "Monte Carlo study of GaAs/$Al_xGa_{1-x}As$ MODFET's: Effects of $Al_xGa_{1-x}As$ composition", IEEE Trans. Electron Devices, ED-**38**, 197, 1991.

[21] G. U. Jensen, B. Lund, T. A. Fjeldly, and M. Shur, "Monte Carlo simulation of semiconductor devices", Computer Physics Communications, **67**, 1,1991.

[22] R. Tsu and L. Esaki, "Tunneling in a finite superlattice", Appl. Phys. Lett. **22**, 562, 1973.

[23] L. L. Chang, L. Esaki and R. Tsu, "Resonant Tunneling in Semiconductor Double Barriers", Appl. Phys. Lett. **24**, 593, 1974.

[24] T. C. L. G. Sollner, W. D. Goodhue, P. E. Tannenwald, C. D. Parker, and D. D. Peck, "Resonant Tunneling through Quantum Wells at Frequencies Up to 2.5 THz", Appl. Phys. Lett. **43**, 588, 1983.

[25] S. Sen, F. Capasso, A. Y. Cho, and D. Sivco, "Resonant Tunneling Device with Multiple Negative Differential Resistance: Digital and Signal Processing Applications with Reduced Circuit Complexity", IEEE Trans. Electron Dev. **ED-34**, 2185, 1987.

[26] T. Nakagawa, H. Inamoto, T. Kojima, and K. Ohta, "Observation of Resonant Tunneling in AlGaAs/GaAs Triple Barrier Diodes", Appl. Phys. Lett. **49**, 73, 1986.

[27] T. Tanoue, H. Mizuta, and S. Takahashi, "A Triple-Well Resonant Tunneling Diode for Multiple-Valued Logic Application", IEEE Electron Device Lett. **EDL-9**, 365, 1988.

[28] H. Mizuta, T. Tanoue, and S. Takahashi, "A New Triple-Well Resonant Tunneling Diode with Controllable Double-Negative Resistance", IEEE Trans. Electron Devices **ED-35**, 1951, 1988.

[29] F. Capasso and R. A. Kiehl, "Resonant Tunneling Transistor with Quantum Well Base and High-Energy Injection: A New Negative Differential Resistance Device", J. Appl. Phys. **58**, 1366, 1985.

[30] N. Yokoyama, K. Imamura, S. Muto, S. Hiyamizu, and H. Nishi, "A New Functional Resonant Tunneling Hot Electron Transistor (RHET)", Jpn. J. of Appl. Phys. **24**, L853, 1985.

[31] A. R. Bonnefoi, T. C. Mcgill, and R. D. Burnham, "Resonant Tunneling Transistors with Controllable Negative Differential Resistances", IEEE Electron Device Lett. **EDL-6**, 636, 1985.

[32] A. D. Stone and P. A. Lee, “Effect of Inelastic Processes of Resonant Tunneling in One Dimension”, Phys. Rev. Lett. **54**, 1198, 1985.

[33] H. Mizuta, T. Tanoue, and S. Takahashi, "Theoretical analysis of peak-to-valley ratio degradation caused by scattering processes in multi-barrier resonant tunneling diodes", Proceedings of IEEE/Cornell conference on advanced concepts in high speed semiconductor devices and circuits", 274, 1989.

[34] H. Ohnishi, T. Inata, S. Muto, N. Yokoyama, and A. Shibatomi, "Self-consistent analysis of resonant tunneling current", Appl. Phys. Lett. **49**, 1248, 1986.

[35] H. Mizuta and C. J. Goodings, "Transient Quantum Transport Simulation based on the Statistical Density Matrix", J. Phys.: Condens. Matter **3**, 3739, 1991.

[36] V. J. Goldman, D. C. Tsui, and J. E. Cunningham, "Resonant Tunneling in Magnetic Field: Evidence for Space-Charge Build-up", Phys. Rev. **B35**, 9387, 1987.

[37] E. E. Mendez, E. Calleja, and W. I. Wang, "Inelastic Tunneling in AlAs-GaAs-AlAs Heterostructures", Appl. Phys. Lett. **53**, 977, 1988.

[38] M. Tsuchiya, T. Matsusue, and H. Sakaki, "Tunneling Escape Rate of Electron From Quantum Well in Double-Barrier Heterostructures", Phys. Rev. Lett. **59**, 2356, 1987.

[39] V. J. Goldman, D. C. Tsui, and J. E. Cunningham, "Observation of Intrinsic Bistability in Resonant-tunneling Structures", Phys. Rev. Lett. **58**, 1257, 1987.

[40] N. C. Kluksdahl, A. M. Kriman, D. K. Ferry, and C. Ringhofer, "Self-consistent study of the resonant-tunneling diode", Phys. Rev. **B39**, 7720, 1989.

[41] F. Capasso, S. Sen, A. Y. Cho, and A. L. Hutchinson, "Resonant Tunneling Spectroscopy of Hot Minority Electrons Injected in Gallium Arsenide Quantum Wells", Appl. Phys. Lett. **50**, 930, 1987.

[42] T. Wang and C.-H. Hsieh, "Numerical analysis of nonequilibrium electron transport in AlGaAs/InGaAs/GaAs pseudomorphic MODFET's", IEEE Trans. Electron Devices, **ED-37**, 1930,1990.

[43] K. Yokoyama and K. Hess, "Monte Carlo study of electronic transport in $Al_{1-x}Ga_xAs$ /GaAs single-well heterostructures", Phys. Rev. **B33**, 5595,1986.

[44] D. Y. Xing, and C. S. Ting, "Green's-function approach to transient hot-electron transport in semiconductors under a uniform electric field', Phys. Rev. **B35**(8), 3971,1987.

[45] D. Ter Haar, "Theory and Applications of the density matrix", Reports on progress in Physics, **24**, 304, 1961.

[46] L. P. Kadanoff and G. Baym, *Quantum Statistical Mechanics*, W. A. Benjamin (1962), New York.

[47] L. V. Keldysh, "Diagram technique for nonequilibrium processes", Sov. Phys. JETP **20**, 1018, 1965.

[48] R. Bertoncini, A. M. Kriman, and D. K. Ferry, "Airy-coordinate technique for nonequilibrium Green's-function approach to high-field quantum transport", Phys. Rev. **B41**, 1390, 1990.

[49] M. J. McLennan, Y. Lee, and S. Datta, "Voltage drop in mesoscopic systems: A numerical study using a quantum kinetic equation", Phys. Rev. **B43**, 13846, 1991.

[50] G. Neofotistos, R. Lake, and S. Datta, "Inelastic-scattering effects on single-barrier tunneling", Phys. Rev. **B43**, 2442, 1991.

[51] S. Datta and R. K. Lake, "Voltage probes and inelastic scattering", Phys. Rev. **B44**, 6538, 1991.

[52] W. R. Frensley, "Simulation of resonant-tunneling heterostructure devices", J. Vac. Sci. Technol. **B3**, 1261, 1985.

[53] J. R. Barker and S. Murray, "A quasi-classical formulation of the Wigner function approach to quantum ballistic transport", Phys. Lett. **93A**, 271, 1983.

[54] W. R. Frensley, "Wigner-function model of a resonant-tunneling semiconductor device", Phys. Rev. **B36**, 1570, 1987.

[55] K. L. Jensen and F. A. Bout, "Numerical simulation of intrinsic bistability and high-frequency current oscillations in resonant tunnelling structures", Phys. Rev. Lett. **66**, 1078, 1991.

[56] M. A. Reed, J. N. Randall, R. J. Aggarwal, R. J. Matyi, T. M. Moore, and A. E. Westel, "Observation of Discrete Electronic States in a Zero-Dimensional Semiconductor Nanostructure", Phys. Rev. Lett. **60**, 535, 1988.

[57] S. Tarucha, Y. Hirayama, T. Saku, and T. Kimura, "Resonant Tunneling through One- and Zero-Dimensional States Constricted by $Al_xGa_{1-x}As/GaAs/Al_xGa_{1-x}As$ Heterojunctions and High-Resistance Regions Induced by Focused Ga Ion-Beam Implantation", Phys. Rev. **B41**, 5459, 1990.

[58] A. Groshev, "Single Electron Trapping in Ultrasmall Double Barrier Semiconductor Structures", 20th international conference on the physics of semiconductors, Thessaloniki, World Scientific, 1238, 1990.

[59] H. Mizuta, C. J. Goodings, M. Wagner, and S. Ho, "Three-dimensional numerical analysis of multi-mode quantum transport in zero-dimensional resonant tunnelling diodes", J. Phys.: Condens. Matter **4**, 8783, 1992.

CHAPTER 2

CLASSICAL HYDRODYNAMIC ELECTRON TRANSPORT IN SUBMICRON HETEROJUNCTION DEVICES

This first chapter is intended to provide the study of drift-diffusion (DD) classical transport in heterojunction devices in a deep submicrometer regime focusing on the effects of the deep levels on device characteristics which are characteristic to compound semiconductors. In Sec. 2.1 the modified drift-diffusion modelling is briefly described for heterojunction structures, and then the Shockley-Reed-Hall (SRH) statistics is introduced to model carrier emission-absorption processes due to the deep levels placed in energy gaps. Three types of deep levels are taken into account for the modelling by using multiple discrete deep donor and acceptor states: EL2-donor levels in semi-insulating substrates [1], DX-centres in N-AlGaAs layers grown by using MBE, and surface states which are less understood experimentally. The simple Spicer's two state model [2] is adopted to describe the surface levels though alternative advanced models have been also reported. Two-dimensional numerical simulation based upon these modellings is then applied mainly to AlGaAs/GaAs high electron mobility transistors (HEMTs) to investigate firstly the influences of the DX centres in an N-AlGaAs electron supply layer (Sec. 2.2) and secondly those of more vague surface states (Sec. 2.3.1) on the device performance. Deep level induced surface recombination and related Fermi-level depinning phenomenon are also demonstrated in Sec. 2.3.2 by focusing in the extrinsic base region of heterojunction bipolar transistors (HBTs).

2.1 Macroscopic drift-diffusion transport in heterostructures with SRH carrier trap processes

2.1.1 Drift-diffusion modelling of carrier transport in semiconductor heterostructures

To describe the motion of carriers in heterojuction devices we first have to introduce several new material parameters into the conventional drift-diffusion modelling of homogeneous semiconductor structures: An electron affinity χ and discontinuities of conduction and valence bands, ΔE_C and ΔE_V, (see Fig. 2.1). All the parameters for alloy materials including transport properties have dependences on mole fractions.

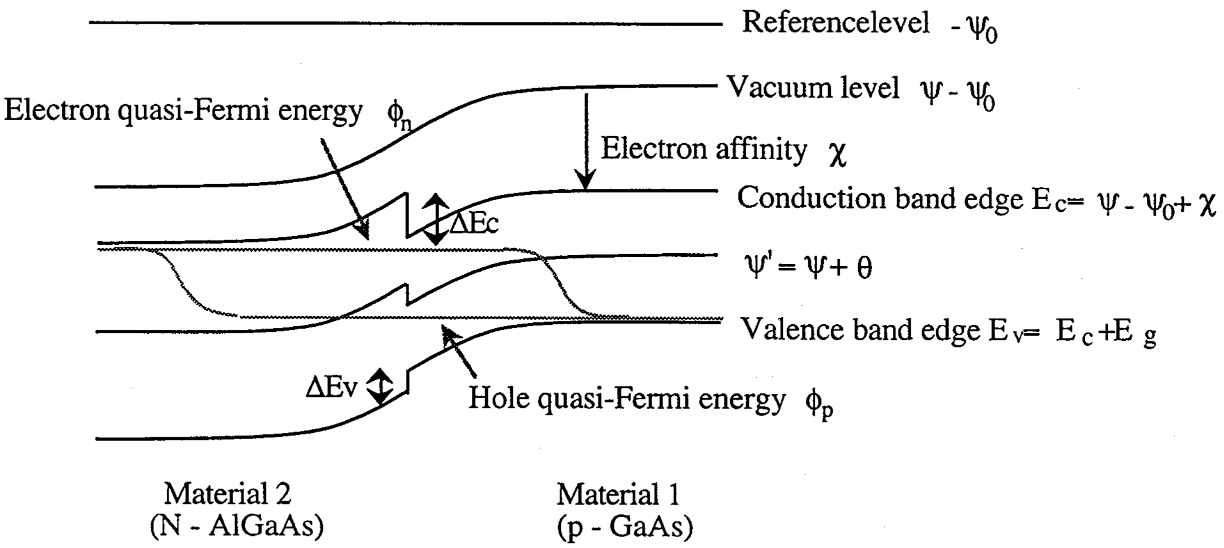

Figure 2.1 Schematic energy band-diagram of an N-AlGaAs/p-GaAs heterojunction with related parameters.

Quasi-Fermi energies for electrons and holes, ϕ_n and ϕ_p, are introduced in the conventional way to express electron and hole densities, n and p, as follows:

$$n = N_c F_{1/2}\left(\frac{E_c - \phi_h}{V_T}\right) \tag{2.1}$$

$$p = N_v F_{1/2}\left(\frac{\phi_p - E_v}{V_T}\right) \tag{2.2}$$

where N_c and N_v are effective densities of states in the conduction and valence bands, $F_{1/2}$ the Fermi-Dirac integral of order 1/2 [3], and V_T the thermal voltage ($= k_BT/q$). Equations (2.1) and (2.2) may be expressed in the following quasi-Boltzmann form:

$$n = n_i \exp\left[\frac{(\psi + \theta - \gamma_n) - \phi_n}{V_T}\right] \tag{2.3}$$

$$p = n_i \exp\left[\frac{\phi_p - (\psi + \theta - \gamma_p)}{V_T}\right] \tag{2.4}$$

by using the following degeneracy parameters, γ_n and γ_p,[4]:

$$\gamma_n = V_T \ln\left[\frac{\exp\{(E_c - \phi_n)/V_T\}}{F_{1/2}\{(E_c - \phi_n)/V_T\}}\right] \tag{2.5}$$

$$\gamma_p = V_T \ln\left[\frac{\exp\{(\phi_p - E_v)/V_T\}}{F_{1/2}\{(\phi_p - E_v)/V_T\}}\right] \tag{2.6}$$

In equations (2.3) and (2.4) θ is a band parameter [5] defined as follows:

$$\theta = -\psi_0 + \chi + \frac{E_g}{2} - \frac{V_T}{2} \ln \frac{N_v}{N_c} \tag{2.7}$$

where χ is electron affinity. The conduction and valence band discontinuities, ΔE_c and ΔE_v, at a heterojunction between material 1 and 2 (see Fig. 2.1) are given by the following expressions:

$$\Delta E_v = (1 - \beta)\left(E_{g2}^{\Gamma} - E_{g1}^{\Gamma}\right) \tag{2.8}$$

$$\Delta E_c = \min\left(E_{g2}^{\Gamma}, E_{g2}^{X}\right) - E_{g1}^{\Gamma} - \Delta E_v \tag{2.9}$$

where E_g^{Γ} and E_g^{X} are band-gaps at Γ and X points, and the discontinuity parameter β is chosen to be 0.6 for AlGaAs/GaAs heterojunctions [29] rather than the Dingle's value of 0.85 and 0.7 for other heterojunctions. The electron and hole current densities, $\vec{J_n}$ and $\vec{J_p}$, are then expressed by using quasi-Fermi potentials:

$$\vec{J_n} = -q\,\mu_n\,n\,\vec{\nabla}\,\phi_n \tag{2.10}$$

$$\vec{J_p} = -q\,\mu_p\,p\,\vec{\nabla}\,\phi_p \tag{2.11}$$

where μ_n, μ_p are low-field mobilities for electrons and holes. Substituting ϕ_n and ϕ_p for in Eqs. (2.3) and (2.4) Eqs. (2.10) and (2.11) lead to current densities which consist of conventional drift and diffusion components which is exactly the same as those for homogeneous systems, and additional terms which are non-zero only at heterointerfaces.

The low-field mobilities for carriers in AlGaAs layers are generally expressed as a function of both the mole fraction x and total impurity concentration N_I (= $N_D + N_A$):

$$\mu_n (N_I, x) = \mu_{n0} (N_I) \cdot f_n(x) \tag{2.12}$$

$$\mu_p (N_I, x) = \mu_{p0} (N_I) \cdot f_p(x) \tag{2.13}$$

$$\mu_{n0}(N_I) = \frac{A_n}{(1 + N_I/N_{n0})^{\alpha_n}} \tag{2.14}$$

$$\mu_{p0}(N_I) = \frac{A_p}{(1 + N_I/N_{p0})^{\alpha_p}} \tag{2.15}$$

where all the parameters and functions $f_n(x)$ and $f_p(x)$ are extracted from the experimental data reported by Neumann et al. [6] (see Fig. 2.2) and summarized in Table 2.1.

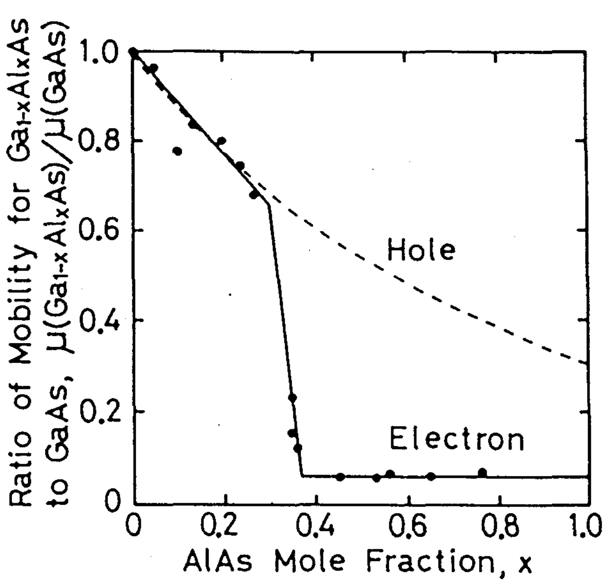

Figure 2.2 Electron and hole mobilities in Ga1-xAlxAs as a function of AlAs mole fraction, x. The mobilities are normalized by values in GaAs. Solid and broken lines represent model functions for electron hole mobilities, respectively. The experimental data for electron mobility are from Neumann et al. [6]. After Ohtoshi et al. [9].

Full transport properties of carriers are then simply modelled by using two types of velocity-field curves, velocity-overshoot and pieceiwse linear forms (see Fig. 2.3), in which the velocity in the low-field regime is given by the above mobility model. On the contrary the saturation velocity in the high-field regime is virtually independent of doping concentration and usually assumed to be 1.0×10^7 cm/sec which has been reported for bulk GaAs materials. For devices with very small dimensions, however, an appropriate figure of saturation velocity is controversial since velocity overshoot of carriers is seen locally in the conducting channel leading to an increase in current. In these circumstances more advanced transport calculations such as Monte Carlo simulations are usually adopted to estimate an effective saturation velocity which is sometimes more than twice as large as the bulk figure.

For electrons	*For holes*
$A_n = 7200$ [cm^2/Vs] $N_{n0} = 3.1 \times 10^{16}$ [1/cm^3] $\alpha_n = 0.28$ $f_n(x) = -1.133\,x + 1.000$ $(0.0 \leq x \leq 0.30)$ $-8.571\,x + 3.231$ $(0.30 < x \leq 0.37)$ 0.06 $(0.37 < x \leq 1.0)$	$A_n = 370$ [cm^2/Vs] $N_{n0} = 7.1 \times 10^{16}$ [1/cm^3] $\alpha_n = 0.30$ $f_p(x) = (m_{p0}/m_p)\cdot(1/\varepsilon_{h0} - 1/\varepsilon_{l0})/(1/\varepsilon_h - 1/\varepsilon_l)$ $m_{p0} = 0.48\ m_0$ $m_p = (0.48 + 0.31x)\ m_0$ $\varepsilon_{h0} = 10.90$ $\varepsilon_h = 10.90 - 2.74\,x$ $\varepsilon_{l0} = 13.1$ $\varepsilon_l = 13.1 - 3.0\,x$

***Table 2.1** Parameters used for the mobility model (2.12) and (2.13) for electrons and holes in $Al_xGa_{1-x}As$ layers.*

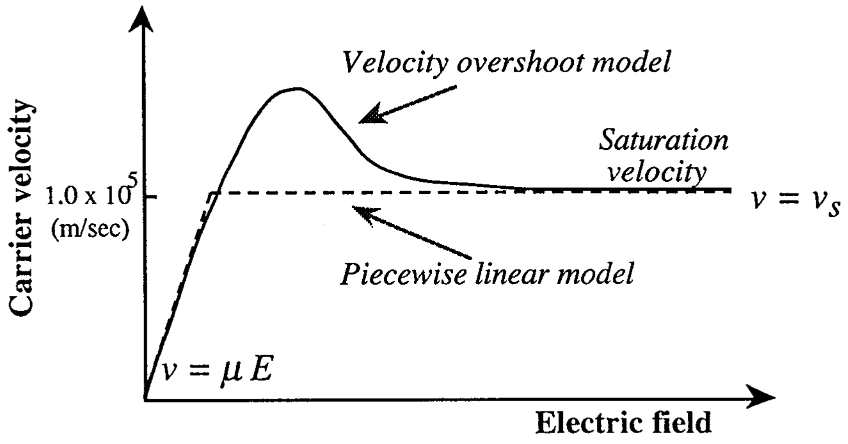

***Figure 2.3** Two types of velocity-field curves used for the present simulation: A velocity overshoot model (solid line) and a piecewise linear model (broken line).*

2.1.2 Shockley-Reed-Hall (SRH) model for carrier emission-absorption processes via deep levels

In this section carrier emission-absorption processes via deep levels in energy band-gaps are modelled based upon classical Schockley-Reed-Hall statistics. Baisc transport equations are then derived in which rate equations for these deep-level-induced processes are included. Let us start with derivation of rate equations for density at the deep trap states. The energies of deep donors and acceptors are first expressed in the following form:

$$\Delta E_{DD} = \Psi + \theta - \left(E_C - \delta E_{DD}\right) \tag{2.16}$$

$$\Delta E_{DA} = \Psi + \theta - \left(E_V + \delta E_{DA}\right) \tag{2.17}$$

where δE_{DD} is an energy interval between the deep donor state and the conduction band edge, and δE_{DA} that between the acceptor state and valence band edge (see Fig. 2.4).

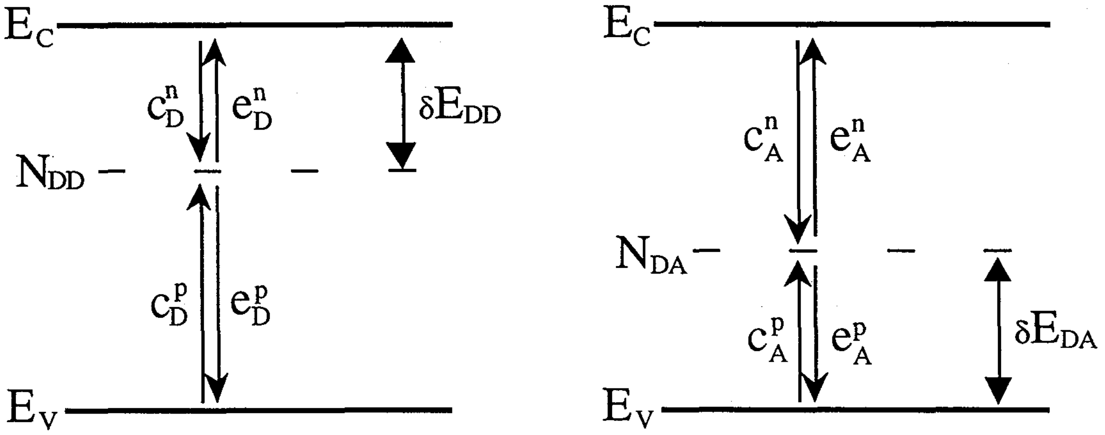

(a) Deep Donor *(b) Deep Acceptor*

Figure 2.4 *Carrier emission and capture processes through deep levels in semiconductors. Meaning of parameters is explained in the context.*

Major deep levels in compound semiconductors are summarised in Tab. 2.2. Parameters listed here are used in the following numerical calculations. The time evolution of the density of carriers at the deep levels is given by the following rate equations [7]:

$$\frac{\partial}{\partial t}\left(N_{DD} - N_{DD}^{+}\right) = \left\{C_D^n N_{DD}^{+} n - e_D^n \left(N_{DD} - N_{DD}^{+}\right)\right\} - \left\{C_D^p \left(N_{DD} - N_{DD}^{+}\right) p - e_D^p N_{DD}^{+}\right\} \tag{2.18}$$

$$\frac{\partial}{\partial t}\left(N_{DA} - N_{DA}^{-}\right) = \left\{C_A^p N_{DA}^{-} p - e_A^p \left(N_{DA} - N_{DA}^{-}\right)\right\} - \left\{C_A^n \left(N_{DA} - N_{DA}^{-}\right) n - e_A^n N_{DA}^{-}\right\} \tag{2.19}$$

Place	Semi-insurating substrate	N-AlGaAs	Surface (Spicer's model)	
Deep levels	EL2-donor	DX centre	Deep donor	Deep acceptor
δE_{DD}, δE_{DA} (eV)	0.82	*$E_{DX}(x)$	0.925	0.75
Electron capture rate (cm^3/sec)	1.7×10^{-13}	-	1.0×10^{-8}	1.0×10^{-8}
Hole capture rate (cm^3/sec)	2.0×10^{-18}	0	1.0×10^{-8}	1.0×10^{-8}
Density	$\sim 1.0 \times 10^{16}$ ($/cm^3$)	N_D-dependent	$\sim 1.0 \times 10^{13}$ ($/cm^2$)	$\sim 1.0 \times 10^{13}$ ($/cm^2$)

$$* E_{DX}(x) = \begin{cases} 4.00 & \text{(meV)} \quad (x \leq 0.25) \\ 1125\,x - 277.35 & \text{(meV)} \quad (0.25 < x \leq 0.37) \\ -261.54\,x + 235.77 & \text{(meV)} \quad (x > 0.37) \end{cases}$$

Table 2.2 *A list of major deep levels in compound semiconductor devices.*

where the emission rates e_D^n, e_D^p, e_A^n, e_A^p are connected to the capture rates C_D^n, C_D^p, C_A^n , C_A^p as follows:

$$e_D^n = C_D^n\, n_I^D \tag{2.20}$$

$$e_D^p = C_D^p\, p_I^D \tag{2.21}$$

$$e_A^n = C_A^n\, n_I^A \tag{2.22}$$

$$e_A^p = C_A^p\, p_I^A \tag{2.23}$$

where n_I^D, p_I^D, n_I^A, p_I^A are given by the following expressions:

$$n_I^D = n_i\, g_D \exp\left[\frac{(\Delta E_{DD} - \gamma_n)}{k_B T/q}\right] \tag{2.24}$$

$$p_I^D = n_i\, g_D \exp\left[\frac{(\gamma_p - \Delta E_{DD})}{k_B T/q}\right] \tag{2.25}$$

$$n_I^A = n_i\, g_A \exp\left[\frac{(\Delta E_{DA} - \gamma_n)}{k_B T/q}\right] \tag{2.26}$$

$$p_I^A = n_i\, g_A \exp\left[\frac{(\gamma_p - \Delta E_{DA})}{k_B T/q}\right] \tag{2.27}$$

In these equations g_D and g_A are the degeneracies of the deep donor and acceptor states. In steady states the concentrations of the ionized states are obtained from Eqs. (2.18) and (2.19) as follows:

$$N_{DD}^{+} = \frac{n_1^D / C_D^p + p / C_D^n}{\left(n + n_1^D\right) / C_D^p + \left(p + p_1^D\right) / C_D^n} N_{DD} \tag{2.28}$$

$$N_{DA}^{-} = \frac{n / C_A^p + p_1^A / C_A^n}{\left(n + n_1^A\right) / C_A^p + \left(p + p_1^A\right) / C_A^n} N_{DA} \tag{2.29}$$

These ionized deep donors and acceptors alter the electrostatic potential via the following *Poisson's equation* :

$$\nabla \cdot \left(\varepsilon \nabla \psi\right) = -q\left(N_D^{+} + N_{DD}^{+} - N_A^{-} - N_{DA}^{-} - n + p\right) \tag{2.28}$$

where q is the magnitude of an electronic charge, ε is the dielectric constant, N_D^{+} and N_A^{-} are the concentrations of ionized shallow donors and acceptors. It is normally assumed that shallow donors and acceptors in GaAs are fully ionized at room temperature ($N_D^{+} = N_D$, $N_A^{-} = N_A$) as these impurity states are located fairly close to the edge of the conduction or valence bands: In the case of Si donors in GaAs, these are about 4 meV below the conduction band edge and electrons are well thermally excited into the conduction band at high temperatures.

Additionally the deep levels induce the electron-hole recombination and so cause the change in the current distribution through the following continuity equations for carriers:

$$\begin{aligned} q\frac{\partial n}{\partial t} &= \nabla \cdot J_n + G - R - \left\{C_D^n N_{DD}^{+} n - e_D^n \left(N_{DD} - N_{DD}^{+}\right)\right\} \\ &\quad - \left\{C_A^n \left(N_{DA} - N_{DA}^{-}\right) n - e_A^n N_{DA}^{-}\right\} \end{aligned} \tag{2.29}$$

$$\begin{aligned} q\frac{\partial p}{\partial t} &= -\nabla \cdot J_p + G - R - \left\{C_D^p \left(N_{DD} - N_{DD}^{+}\right) p - e_D^p N_{DD}^{+}\right\} \\ &\quad - \left\{C_A^p N_{DA}^{-} p - e_A^p \left(N_{DA} - N_{DA}^{-}\right)\right\} \end{aligned} \tag{2.30}$$

where G and R represent the conventional electron-hole pair generation and recombination terms of bulk semiconductors. In steady states these equations reduce to the following *current continuity equations* :

$$\nabla \cdot J_n = -(G - R - R_{DD} - R_{DA}) \tag{2.31}$$

$$\nabla \cdot J_p = (G - R - R_{DD} - R_{DA}) \tag{2.32}$$

where R_{DD} and R_{DA} are the recombination rates through the deep donor and acceptor levels

$$R_{DD} = \frac{n\,p - n_1^D\,p_1^D}{(n + n_1^D)/C_D^p + (p + p_1^D)/C_D^n} N_{DD} \tag{2.33}$$

$$R_{DA} = \frac{n\,p - n_1^A\,p_1^A}{(n + n_1^A)/C_A^p + (p + p_1^A)/C_A^n} N_{DA} \tag{2.34}$$

Poisson's equation (2.28) and current continuity equations (2.31) and (2.32) are in general discretized on a two-dimensional finite difference mesh lattice and then numerically solved in an iterative way under the conventional Gummel's scheme: the ICCG (Incomplete Cholesky Conjugate Gradient) method [8],[9] has been adopted for solving the discretized linear equations as the resultant matrices are all symmetric. As the SRH terms introduced into the above equations have a non-linear dependence on variation in electrostatic potential, they should be expanded in a series of the change in electrostatic potential, and only linear terms are usually used in iterative calculations. This linearization avoids divergence in the numerical calculations due to a strong feedback from the SRH term which we often come across for the case that the density of the trap levels is relatively high.

2.2 Fermi-level pinning due to DX centres in submicron-gate AlGaAs/GaAs HEMTs

The existence of DX centres [10],[11] in Si-doped AlGaAs layers grown by using MBE has been one of the crucial problems in developing high-speed heterojunction devices. For example, persistent photoconductivity [10] in HEMTs, saturable pulsation of laser diodes [12], and persistent photocapacitance in p-N GaAs/AlGaAs heterojunction diodes [13] are attributed to DX centres. In AlGaAs/GaAs HEMTs, two-dimensional electron gas (2DEG) formed at the N-AlGaAs/undoped-GaAs heterointerface is used as a conducting channel. DX centres thus have an influence on the electron transfer between the N-AlGaAs and undoped-GaAs layers [14] - [16], resulting in the saturation in sheet electron density of 2DEG [17]. Therefore, it is vital to suppress the effects of DX centres to achieve further improvement in AlGaAs/GaAs HEMTs performance.

Up to now these effects of DX centres on performance of heterojunction devices have not yet been fully investigated. Several groups have reported one-dimensional numerical analysis of controllability of 2DEG via gate bias [18]-[20]. Park et al. [19] have shown by using a simple one-dimensional analysis that gate capacitance-voltage characteristics of AlGaAs/GaAs HEMTs are well modelled by taking account of Fermi-level pinning due to DX centres. In this section a fully two-dimensional numerical analysis of AlGaAs/GaAs HEMTs is presented based on a hydrodynamic device simulation introduced in the previous section. DX centres are modelled by using a single deep donor level which varies with aluminum mole fraction as shown in Tab. 2.2. Electron capture process caused by DX centres is then expressed by using the SRH rate equation. DX centres are shown to pin the quasi-Fermi level leading to a great decrease in transconductance of HEMTs. The superior performance of InGaAs/AlGaAs pseudomorphic HEMTs is discussed in terms of the disappearance of the Fermi-level pinning.

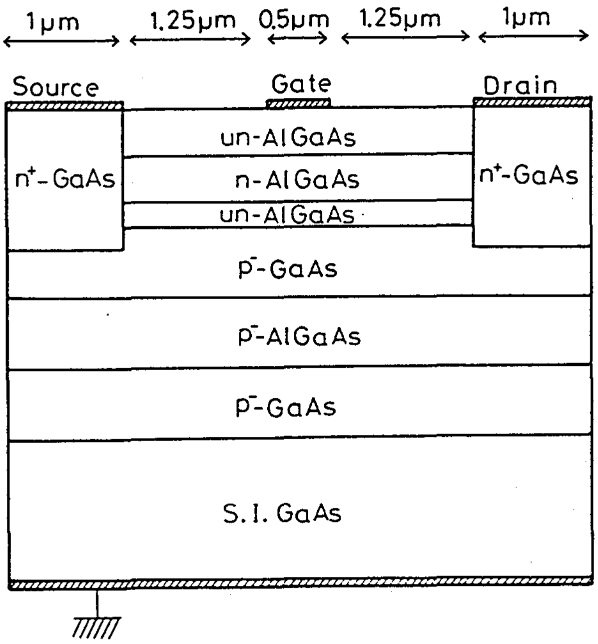

Figure 2.5 A cross sectional view of a 0.5 μm gate AlGaAs/GaAs HEMT.

Figure 2.5 shows a schematic cross section of a 0.5-mm-gate planar AlGaAs/GaAs HEMT which has a 15-nm-thick undoped $Al_{0.3}Ga_{0.7}As$ surface layer [21], a 25-nm-thick highly doped N-$Al_{0.3}Ga_{0.7}As$ layer, and a 0.2-nm-thick undoped $Al_{0.3}Ga_{0.7}As$ spacer layer above the 2DEG channel. A slightly doped p⁻-GaAs is adopted for the channel layer rather than undoped GaAs. The doping concentration of layers used is listed in Table 2.3. For simplicity the source and drain alloy regions are modelled by heavily doped n⁺-GaAs. The electron mobility in the undoped GaAs and N-AlGaAs layers are assumed to be 7200 and 1500 $cm^2/(V\cdot sec)$, respectively, according to the mobility model described in Sec. 2.1. The Schottky-barrier height of the gate electrode is assumed to be 0.8 V.

Layer	Doping concentration $(1/cm^3)$
undoped(p^{--})-$Al_{0.3}Ga_{0.7}As$	1.0×10^{13}
N -$Al_{0.3}Ga_{0.7}As$	2.0×10^{18}
undoped(p^{--})-$Al_{0.3}Ga_{0.7}As$	1.0×10^{13}
p^- -GaAs	1.0×10^{14}
p^- -$Al_{0.3}Ga_{0.7}As$	1.0×10^{14}
p^- -GaAs	1.0×10^{14}
Semi-insulating GaAs substrate	-

***Table 2.3** Doping concentration in each layer of the AlGaAs/GaAs HEMT*

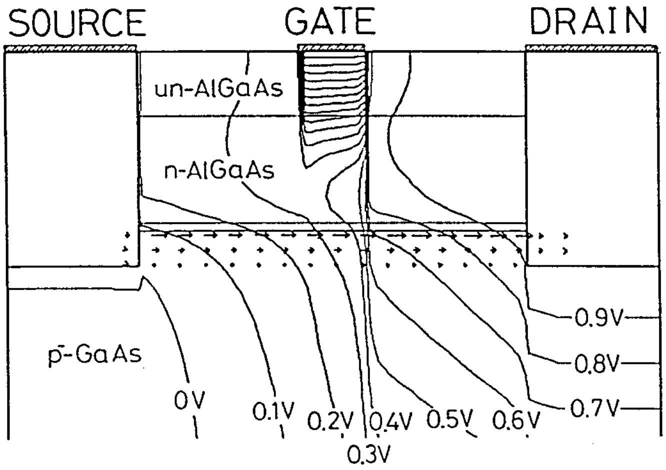

***Figure 2.6** Two-dimensional electrostatic potential distribution and electron current distribution around the AlGaAs/GaAs heterojuction for V_{ds} = 1.0 V and V_{gs} = 0V. Electrostatic potentials are shown by contour lines with an interval of 0.1 V.*

Figure 2.6 shows the two-dimensional electrostatic potential distribution and electron current distribution around the AlGaAs/GaAs heterojunction calculated at a source-drain bias, V_{ds}, of 1.0 V and a source-gate bias, V_{gs}, of 0 V. The length of arrows shown in Fig. 2.6 measures the magnitude of current densities at various points and so indicates that a major current flow is confined within a fairly thin region near the heterojunction as expected. No current flow is seen in the N-AlGaAs layer as the thickness and doping concentration have been chosen so that electrons are well depleted in this layer. Parallel conduction through the N-AlGaAs layer in general results in a decrease in transconductance as electron mobility in the N-AlGaAs is much lower than that of 2DEG and thus required to be negligibly small.

The full transistor characteristics of the HEMT with a gate width of 200 mm calculated at a room temperature is shown in Fig. 2.7(a). To make clear the effects of DX centres on the characteristics it is convenient to introduce another model in which all the donors in N-AlGaAs layers are assumed to be ideally ionized as well as n-GaAs layers: this model does not take account of DX centres at all and hence called *a perfect ionization model* in the following discussion. The characteristics calculated by using the perfect ionization model are shown in Fig. 2.7(b).

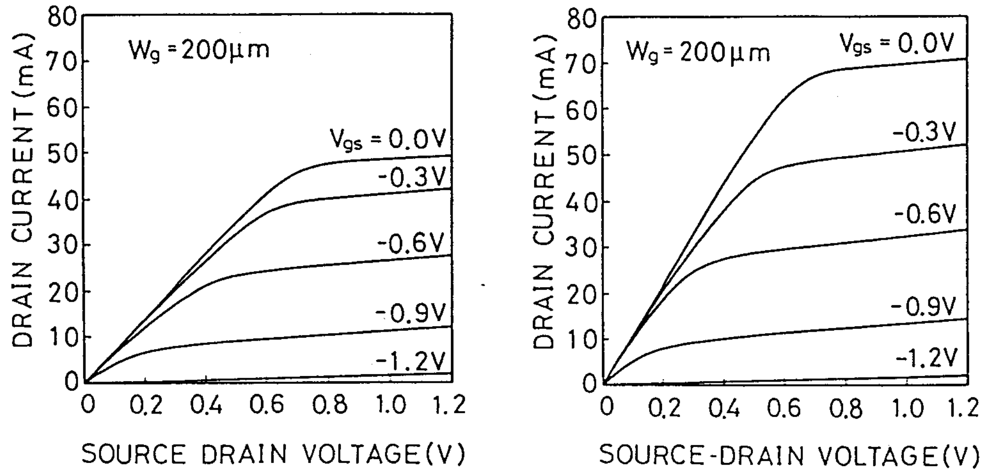

(a) (b)

Figure 2.7 The full transistor characteristics of the AlGaAs/GaAs HEMT with a gate width of 200 μm calculated at 300K. (a) Using the DX centre model. (b) Using the perfect ionization model.

The saturation current calculated by using the DX centre model is found about 30 percent of magnitude smaller than that obtained through the perfect ionization model. In addition an increase in drain current, I_{ds}, with increasing V_{gs} becomes smaller near zero gate bias (Fig. 2.7(a)) though a virtually equal increase is seen for the case of the perfect ionization model (Fig. 2.7(b)).

The situation becomes clearer by plotting the calculated gate bias dependences of drain current, I_{ds}, and transconductance, g_m,: Figures 2.8(a) and (b) shows I_{ds} versus V_{gs} and g_m versus V_{gs} at Vds = 1.2 V. Calculated results by using the DX centre model (solid lines) are compared with those by using the perfect ionization (broken lines).

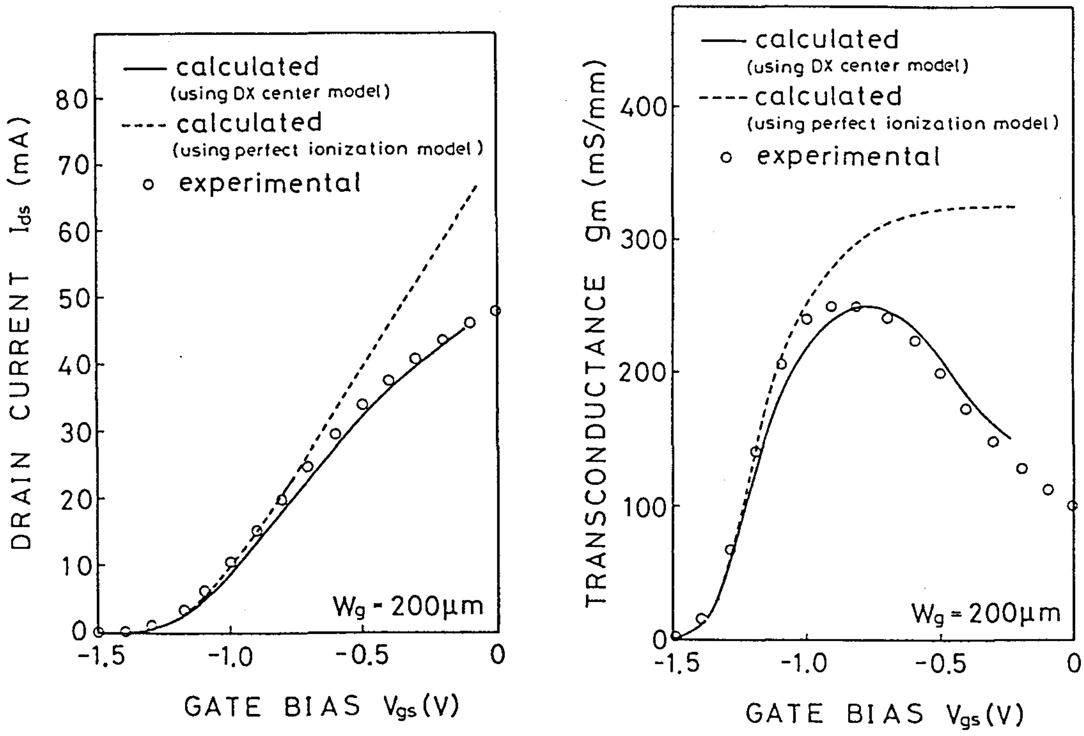

(a) (b)

Figure 2.8 Gate bias dependence of calculated and experimental (a) drain current I_{ds} *and (b) transconductance* g_m. *Solid lines represent the calculated results using the DX centre model, and broken lines using the perfect ionization model. The experimental data are shown by open circles.*

As shown in Fig. 2.8(a), the drain currents calculated by using these two models are nearly equal at the threshold voltage, but the difference between them increases when the gate bias approaches zero. The drain current calculated by using the DX centre model tends to saturate, and the transconductance falls off rapidly near $V_{gs} = 0$. Experimental results obtained from fabricated HEMTs with the same structural parameters as those in Table 2.3 are shown by using open circles in Figs. 2. 8(a) and (b) which are in a good agreement with the results calculated by using the DX centre model.

A brief discussion may be necessary on these results in terms of velocity overshoot in the 2DEG channel. As explained earlier the DD transport modelling obviously can not reproduce any local non-equilibrium effect of hot electrons on device characteristics which is expected to occur in the channel region between the gate and drain electrodes. Thus the velocity overshoot effect has been incorporated into the present calculations by adopting the enhanced saturation velocity, v_S, which has been determined by the following way. Figures 2. 9(a) and (b) show the calculated drain current and transconductance as functions of gate bias with various values of v_S.

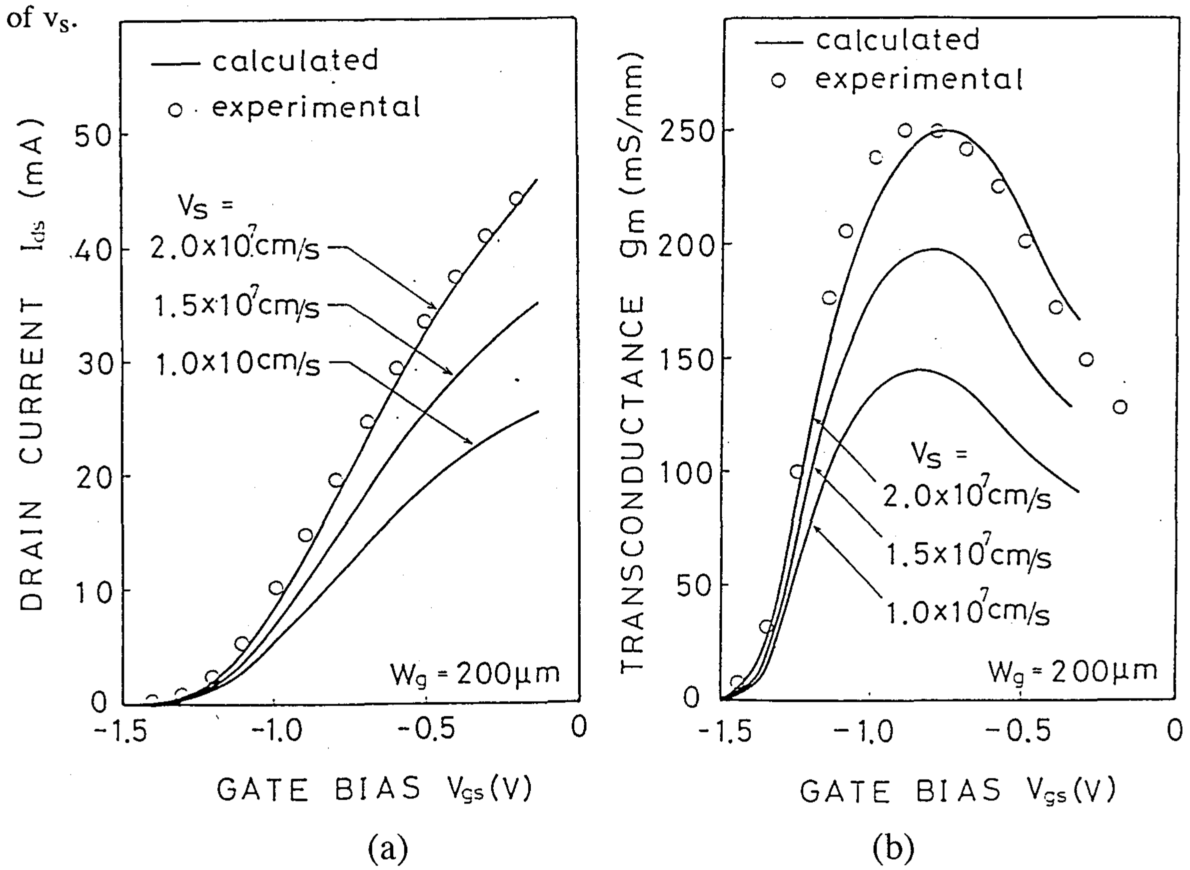

(a) (b)

Figure 2.9 Drain current (a) and transconductance (b) calculated as functions of gate bias with various values of v_S. Experimental results are plotted by open circles.

Excellent agreements with experimental data have been achieved for both quantities by using v_s of 2.0×10^7 cm/sec which is consistent with other reported values [20]-[23]. In the HEMT structures, the electrostatic potential steeply drops near the drain side edge of the gate electrode as is seen in Fig. 2.6. A high electric field appears over a very short length (about 0.05 μm) of the channel, and maximum electric field in this region is higher than 20 kV/cm. The electron velocity in this region is inferred to exceed the drift velocity of electron in a uniform 2DEG channel for which a figure as high as 1.5×10^7 cm/sec at 300K has been obtained by using Monte Carlo simulation [24]. Taking account of these, the field dependence of v_s estimated above is thought to be fairly reasonable.

Now we discuss the results obtained above in terms of the relation between DX centres and quasi-Fermi levels. Conduction band profiles as a function of depth from the surface which are calculated in equilibrium are shown in Figs. 2.10(a) and (b): (a) is the band diagram obtained by use of the DX centre model, and (b) the one by use of the perfect ionization model.

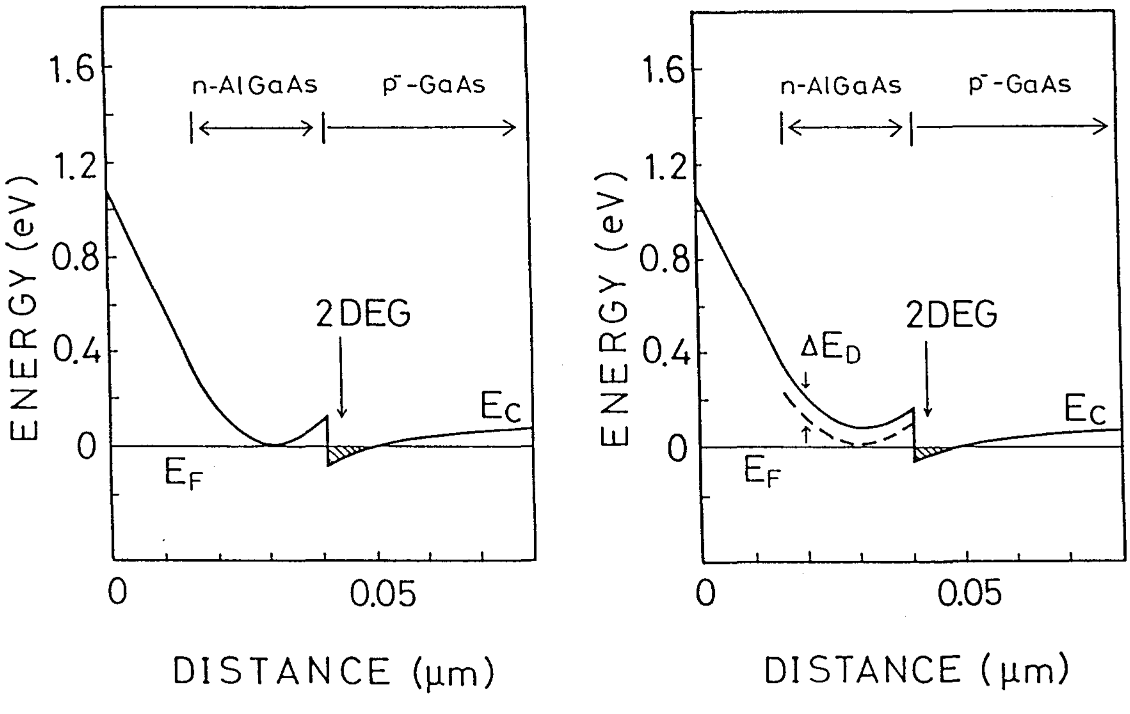

(a) (b)

Figure 2.10 Calculated energy-band diagram as a function of distance referred to the device surface in thermal equilibrium. (a) Using the DX centre model. (b) Using the perfect ionization model.

The DX centres in the N-AlGaAs layer are indicated by the thick broken line in Fig. 2.10(b). The Fermi level (thin solid line) shown in Fig. 2.10(a) is found to lie near the DX centres in the N-AlGaAs layer. In contrast, that in Fig. 2. 10(b) is located fairly close to the minimum of the conduction band edge. It should be noted that DX centres act as an effective conduction band edge.

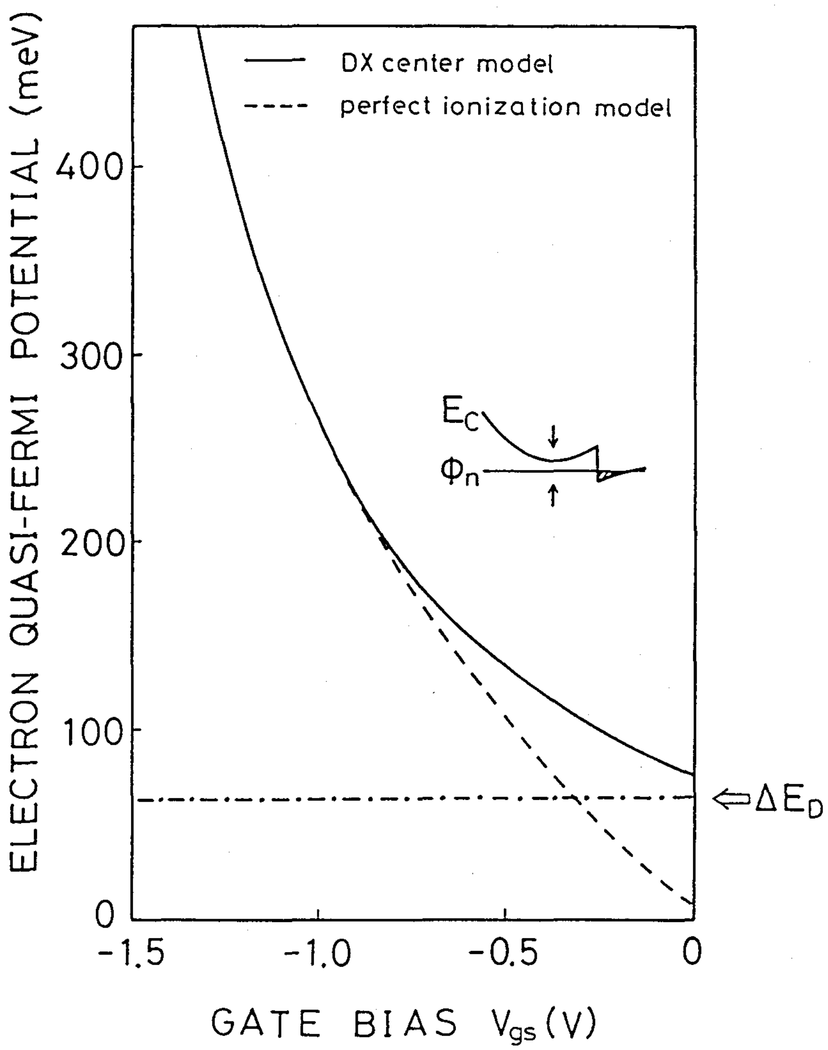

Figure 2.11 Calculated electron quasi-Fermi energy measured from the conduction band minimum as a function of gate bias. Solid lines represent the calculated results using the DX centre model, and broken lines using the perfect ionization model. The energy of DX centres at the conduction band minimum is indicated by a broken line with a dot.

Figure 2.11 shows the electron quasi-Fermi energy, ϕ_n, relative to the conduction band minimum (see inset of Fig. 2.11) as a function of gate bias: a solid line represents ϕ_n calculated by using the DX centre model and a broken line that by using the perfect ionization model. For gate bias $V_{gs} < -1.0V$, the result calculated by using the DX centre model is almost the same as that calculated by using the perfect ionization model. A splitting becomes noticeable between them around $V_{gs} = -0.8$ V and is as large as the energy of the DX centres (denoted as ΔE_0 in the figure) for $V_{gs} > -0.5$ V. With increasing gate bias towards zero, ϕ_n does not come close to the conduction band minimum as ϕ_n for the perfect ionization case but approaches to ΔE_D. Further increase in V_{gs} over zero actually results in saturation of ϕ_n at this energy: the electron quasi-Fermi level is *pinned* at the DX centre states in the N-AlGaAs layer.

The Fermi-level pinning in the N-AlGaAs layer influences on electron distribution in HEMTs in the following way. Figure 2. 12 shows the electron distributions under the gate electrode as a function of distance referred to the device surface calculated under the same conditions as Fig. 2. 12. It is seen that the peak value of the free electron concentration in the N-AlGaAs layer calculated by using the DX centre model is much smaller than that in the perfect ionization scheme. This is because fairly large numbers of electrons are still trapped by DX centres, which do no contribute to conduction. This indicates that parallel conduction in the N-AlGaAs layer is reduced by DX centres capturing conducting electrons which have lower mobility.

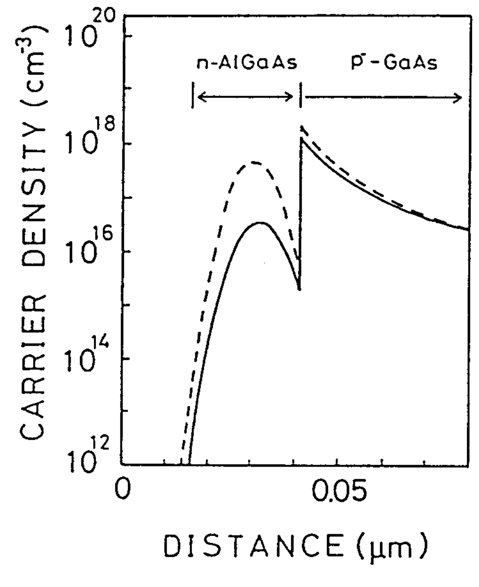

Figure 2. 12 Calculated electron distribution around the heterojunction in thermal equilibrium as a function of depth measured from the device surface.

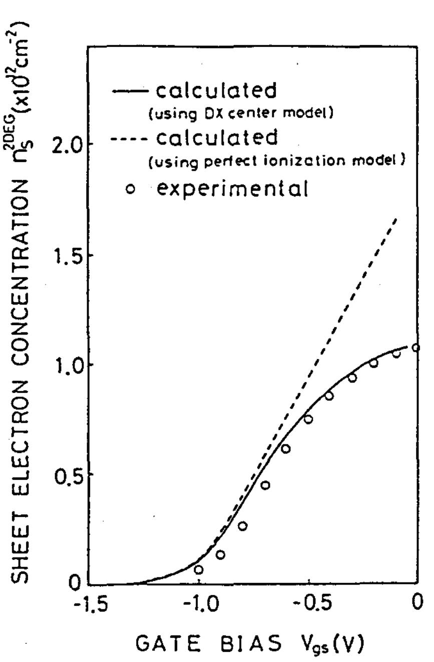

***Figure 2. 13** Calculated electron concentration accumulating at the heterointerface as a function of gate bias. A solid line represents the calculated results using the DX centre model, and a broken line using the perfect ionization model. Experimental results are plotted by open circles.*

At the same time, however, the Fermi level pinning due to DX centres affects the amount of high mobility 2DEG as well: a decrease in a peak concentration of 2DEG is seen in Fig. 2. 12. The gate bias dependences of the sheet electron concentration of 2DEG, n_s^{2DEG}, calculated by using the DX centre model (solid line) and the perfect ionization model (broken line) are shown in Fig. 2. 13 as well as the experimental data (open circles). The present DX centre model reproduces the observed non-linear dependence of n_s^{2DEG} on gate bias. These results manifest that the Fermi-level pinning due to DX centres makes it difficult to modulate n_s^{2DEG} through gate bias in the high gate bias regime. Degradation of transconductance seen in Fig. 2. 7 is attributable to lower controllability of n_s^{2DEG} in this regime.

Finally, in this section, the advanced performance of InGaAs/AlGaAs pseudomorphic HEMTs [25],[26] is discussed from standpoints of the Fermi-level pinning. Pseudomorphic HEMTs in which a strained InGaAs layer is adopted for a channel are going to substitute the conventional AlGaAs/GaAs HEMTs because of their excellent device characteristics. As the strained InGaAs has a narrower band gap a large conduction band discontinuity is easily achieved by using AlGaAs barrier layer with a small aluminum mole fraction ($x < 0.2$) in which DX centres are supposed not to be created (see Fig. 2.). The AlGaAs/InGaAs pseudomorphic HEMT structure, thus, enables us to obtain high values of n_s^{2DEG} without suffering from the

Fermi-level pinning due to DX centres. In addition, electron transport properties of InGaAs are better than those of GaAs both in low and high electric field regions: A lighter electron effective mass in InGaAs layers directly results in higher electron mobility, and a larger separation between the lowest Γ-valley and upper valleys leads to less intervalley scattering and thus high electron saturation velocity. In this discussion we focus on the DX-centre-free properties of the pseudomorphic system.

The AlGaAs/InGaAs pseudomorphic HEMT analyzed here has the same structure as the conventional HEMT investigated above except the following two points. All the $Al_{0.3}Ga_{0.7}As$ layers (including spacer and cap layers) are replaced with $Al_{0.15}Ga_{0.85}As$ layers without any change in thickness and doping concentration. A strained p^--$In_{0.25}Ga_{0.75}As$ layer then substitute the p^--GaAs channel layer; the indium mole fraction of 0.25 is chosen so that the resultant threshold voltage of the pseudomorphic HEMT is nearly equal to that of the above AlGaAs/GaAs HEMT. In the present simulation lattice mismatch induced change in the energy band gap is introduced only through a hydrostatic component of the elastic strain [27],[28]. The electron mobility in the strained InGaAs layer is controversial and, in this analysis, it is intentionally kept the same as that of GaAs to demonstrate only the DX centre related change in the device characteristics. For the same purpose the same saturation velocity is assumed for electrons in this layer as that in GaAs layers though higher values have been reported as mentioned above. We can then directly compare device performance with and without the DX centres' effect through these assumptions.

Figures 2. 14(a) and (b) show I_{ds} and g_m calculated for two HEMTs as functions of V_{gs}: the solid lines represent the calculated results for AlGaAs/InGaAs pseudomorphic HEMT, and the broken lines for the conventional AlGaAs/GaAs HEMT. It should be noted that improvements are seen for the pseudomorphic HEMT in the high gate bias regime. This is because the Fermi level is no longer pinned at such deep levels as DX centres and freely comes close to the conduction band edge leading to much larger electron accumulation in the 2DEG channel. The maximum transconductance is enhanced to 325 mS/mm which is about 30 percent larger than that of the conventional HEMT. It should be emphasized that the transconductance is increased even though the mobility and saturation velocity of electrons have been kept unchanged: The enhancement of g_m results entirely from the disappearance of the Fermi level pinning due to DX centres.

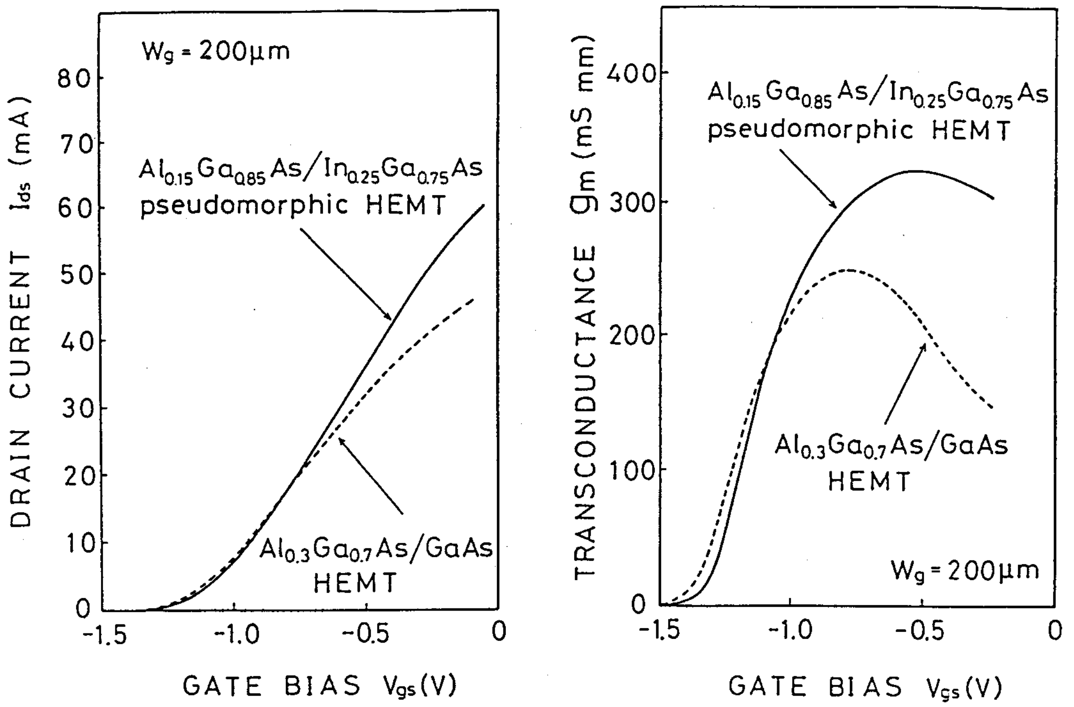

(a) (b)

Figure 2.14 Gate bias dependence of (a) drain current I_{ds} and (b) transconductance g_m. solid lines represent the calculated results for the AlGaAs/InGaAs HEMT, and broken lines for the AlGaAs/GaAs HEMT.

2.3 Effects of surface trap levels on characteristics of deep submicron devices

The shorter the gate length is the more the extrinsic regions of devices have influences on their performance. In this section two different phenomena caused by extrinsic surface of HEMTs and HBTs are investigated. Firstly, in Sec. 2.3.1, the Fermi-level pinning caused by deep levels on both sides of the gate electrode is investigated in deep submicron gate AlGaAs/GaAs HEMTs. Secondly, in Sec. 2.3.2, surface-level-induced carrier recombination is analyzed.

2.3.1 Surface potential effects on nanometer-gate HEMTs

A schematic cross sectional view of the deep submicron gate HEMT is shown in Fig. 2. 15. In these devices a deeply recessed gate structure is adopted both to reduce the parasitic source-to-gate resistance by introducing a thick highly doped GaAs cap layer and to achieve a high gate-to-drain breakdown voltage by putting the gate electrode away from the drain electrode. The deep submicron gate electrode is fabricated by using the EB lithography technique on the surface of the undoped AlGaAs layer after the highly doped GaAs cap layer is etched away around the electrode. The spacing between the edge of the gate electrode and that of the recessed GaAs region is designed to be 0.2 μm on both source and drain sides of the gate which is as long as (or even longer than) the gate length itself. Deep carrier states explained in Sec. 2.1 are then formed on whole the device surface indicated by using open circles in Fig. 2. 15. Among them the surface states those formed in the highly doped GaAs regions do not influence so much on carrier transport in the intrinsic region of the HEMT as they just capture some electrons near the surface of the highly doped regions which are relatively far from the 2DEG. On the other hand, however, those formed on the bottom of the recess are lying adjacent to the 2DEG and may cause serious change in the characteristics of the HEMT.

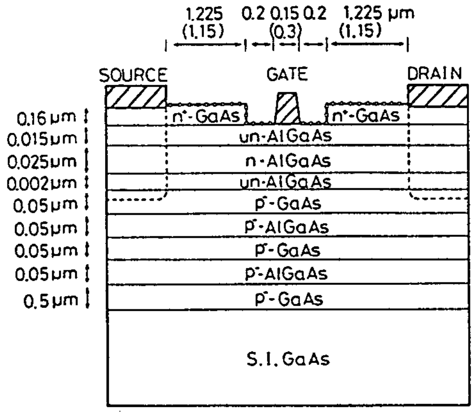

***Figure 2. 15** A schematic cross sectional view of the deep submicron recessed gate HEMT.*

In this section, therefore, let us focus on the effects of the surface states formed around the recessed gate structure. Spicer's two level model introduced in Sec. 2.1 is implemented in the following analysis, and the concentrations of the deep donors and acceptors are assumed to be 5 × 10^{12} /cm^2 which is generally supposed to be a typical figure for the free surface state density. Additionally the deep EL2-donors [1] and shallow carbon acceptors have been introduced for the semi-insulating substrate as well as the DX centres for the N-AlGaAs electron supply layer (see Sec. 2.2).

Figure 2. 16 shows the full transistor characteristics calculated for the gate length of (a) 0.3 μm and (b) 0.15 μm in which solid lines represent the results obtained by using the surface state model and broken lines those which do not take account of the surface states. The spacing between the gate and recess edges is kept 0.2 μm in common for the both cases. Experimental

data are shown in these figures by the use of open circles. It is found that the present surface state model reproduce both experimental results very well within an error of 5 percent overall. The results obtained by neglecting the surface states in general show larger drain conductance and thus the difference in the drain currents becomes larger with increasing drain voltage. Comparing Figs. 2. 16(a) and 2. 16(b) the difference between the solid and broken lines is seen to be larger for the 0.15 mm case than the 0.3 mm case.

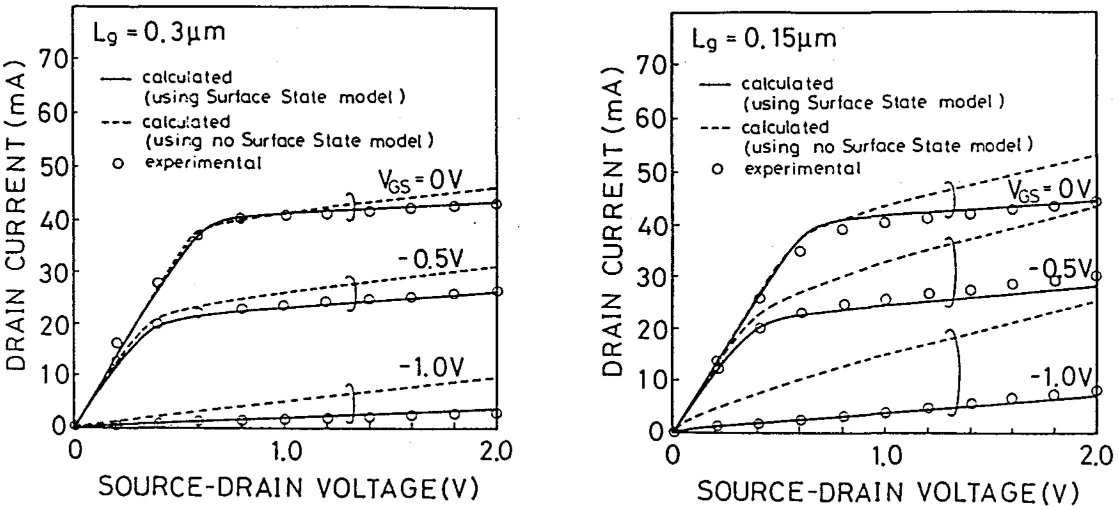

(a) (b)

Figure 2.16 The full transistor characteristics of the deep submicron gate AlGaAs/GaAs HEMTs with (a) Lg = 0.3 µm and (b) Lg = 0.15 µm. Solid and broken lines represent calculated results obtained by using Spicer's surface state model and the non-surface-state model, respectively. Experimental data are shown by using open circles.

The gate bias dependences of the drain current I_{ds} and transconductance g_m calculated for the gate length of 0.3 µm and 0.15 µm are also shown in Figs. 2.17 and 2.18, respectively: Figures 2.17(a) and 2.18(a) shows I_{ds} versus V_{gs} and Figs. 2.17(b) and 2.18(b) g_m versus V_{gs} at $V_{ds} = 2.0$ V. Solid and broken lines represent the calculated results in the same way as in Fig. 2.16. Generally speaking the non-surface-state model leads to a larger threshold voltage than the experimental one and consequently underestimates the maximum of the transconductance. In other words the non-surface-state model tends to enhance *the short channel effects* .

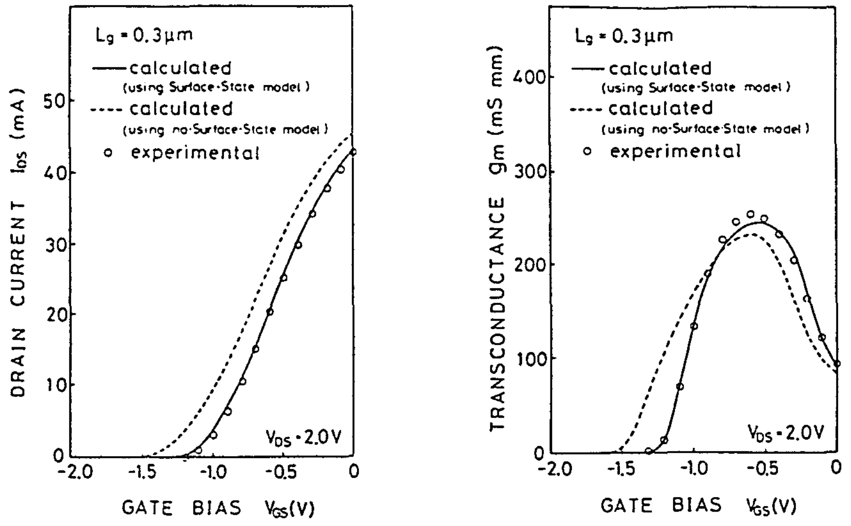

(a) (b)

Figure 2.17 The gate bias dependences of I_{ds} (a) and g_m (b) calculated for the gate length of 0.3 µm. The solid and broken lines represents the results by using two surface state models in the same manner as in Fig. 2.16. Open circles indicate experimental data.

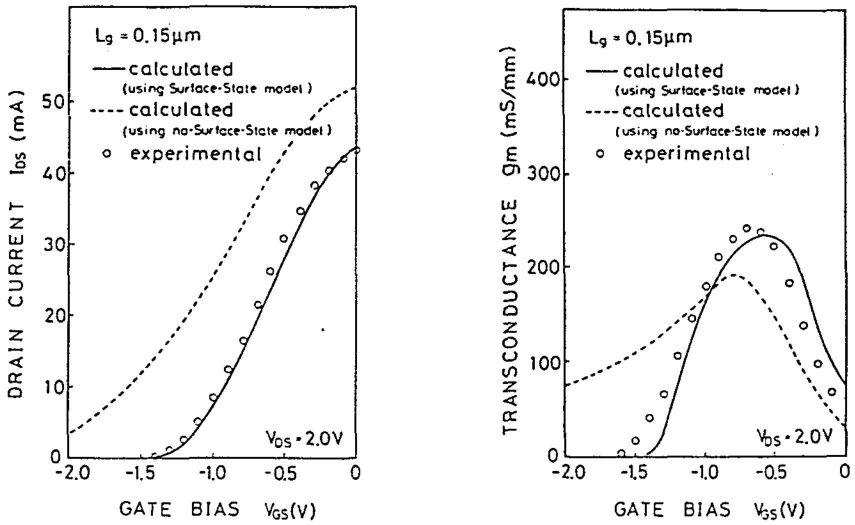

(a) (b)

Figure 2.18 The gate bias dependences of I_{ds} (a) and g_m (b) calculated for the gate length of 0.15 µm. The solid and broken lines represents the results by using two surface state models in the same manner as in Fig. 2.16. Open circles indicate experimental data.

This fact stands out for shorter gate lengths, and in the case of Lg = 0.15 µm the characteristics calculated for the non-surface-state model do not exhibit the current pinch-off. The results obtained by using the present surface state model exceedingly accord with the experimental data for both gate lengths. This fact implies that the surface states formed on the bottom of the recessed structure contribute to suppress the short channel effects.

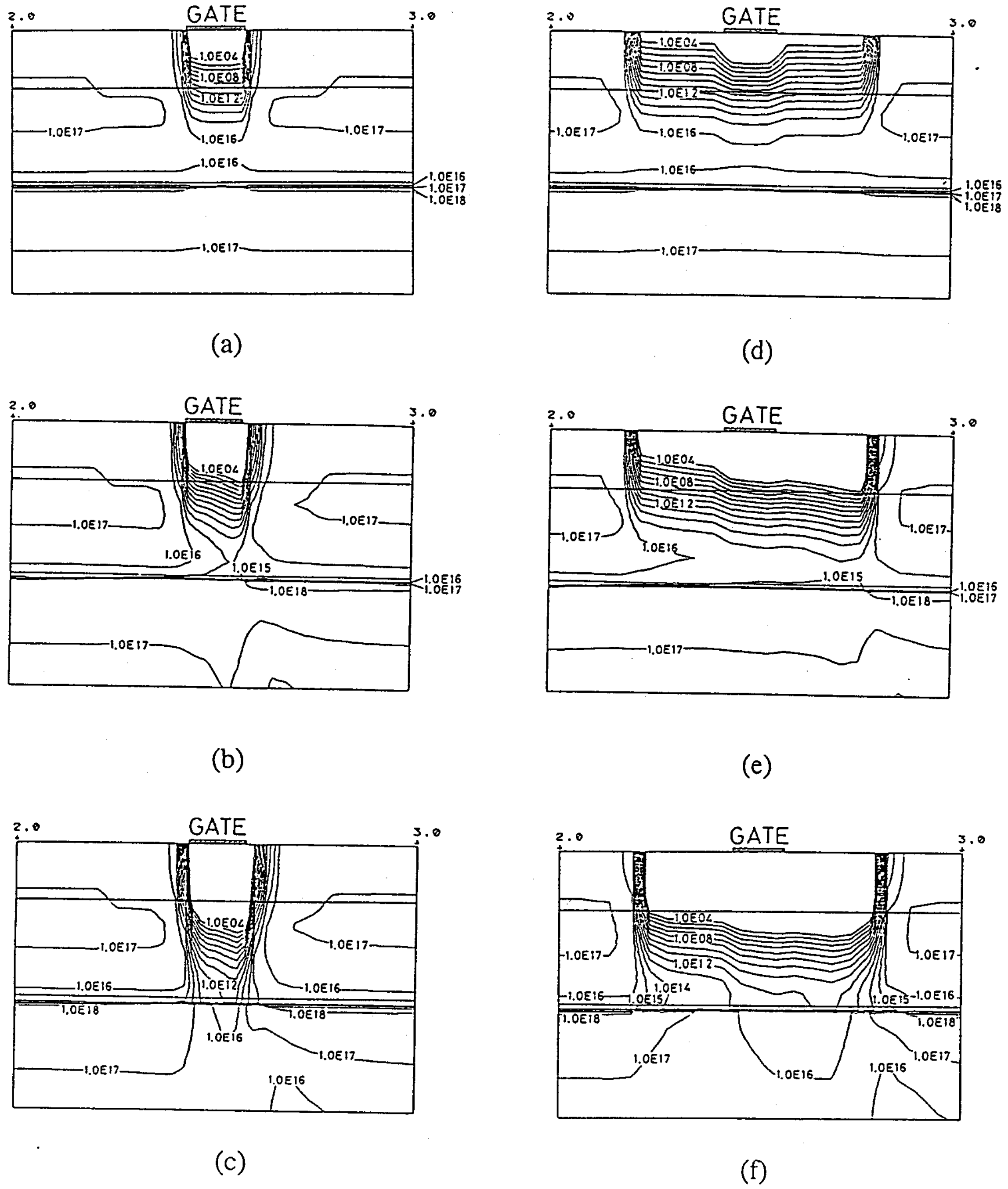

(a)

(d)

(b)

(e)

(c)

(f)

Figure 2.19 Two-dimensional electron distributions around the recessed gate calculated for three typical bias conditions by using the non-surface-state model ((a) - (c)) and the surface-state model ((d)-(f)): Figs. 2.19(a) & (d) are calculate in thermal equilibrium, (b) & (e) in a current saturation regime, and (c) & (f) near the threshold.

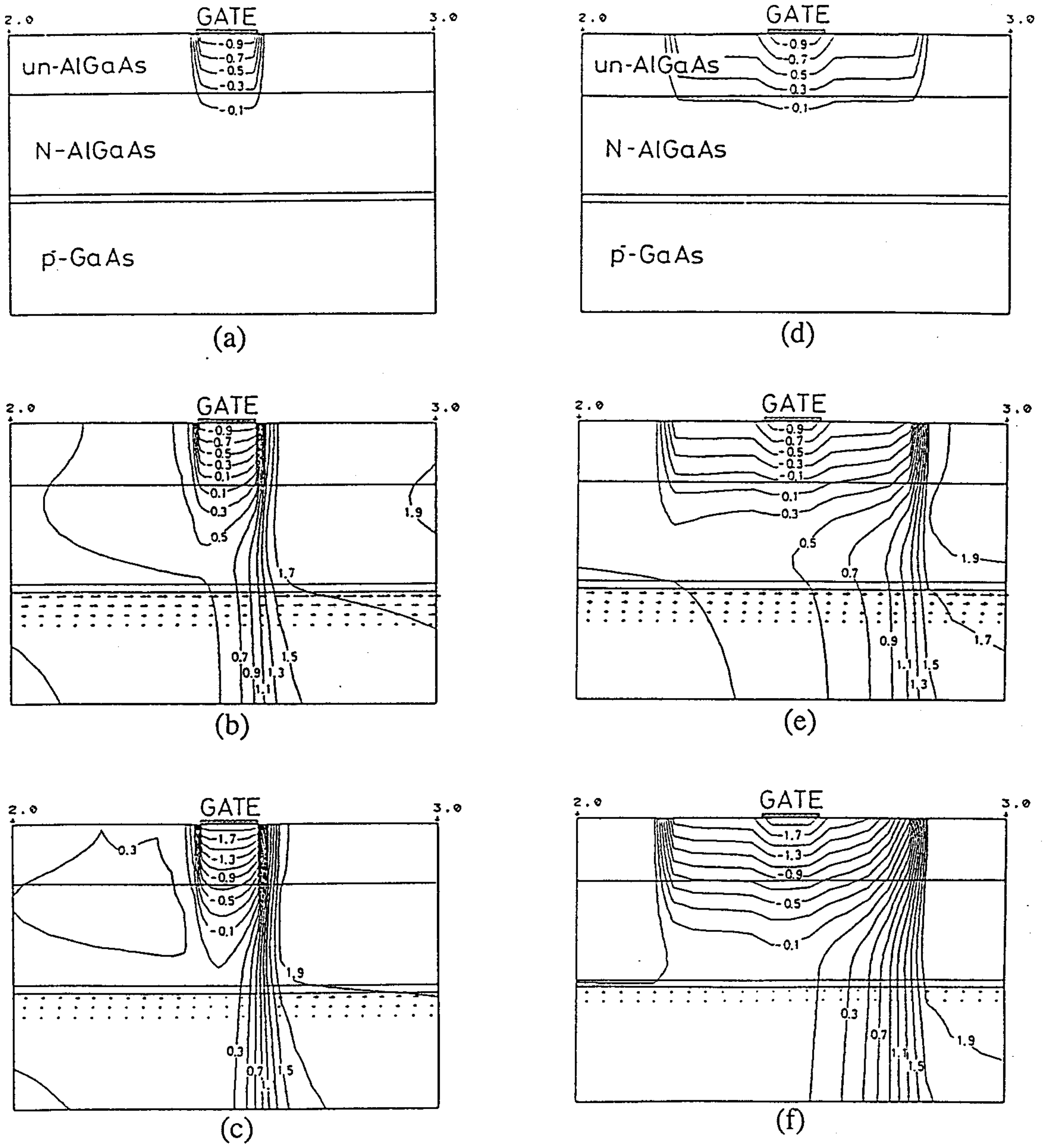

Figure 2.20 Two-dimensional electrostatic potential and current density distributions around the recessed gate calculated for three typical bias conditions by using the non-surface-state model ((a) - (c)) and the surface-state model ((d)-(f)): Figs. 2.20(a) & (d) are calculate in thermal equilibrium, (b) & (e) in a current saturation regime, and (c) & (f) near the threshold.

Now we consider these results in terms of changes in the potential and electron distributions around the gate electrode. Figures 2.19 shows the two-dimensional distribution of electron concentration around the recessed gate calculated in equilibrium (Figs. 2.19(a) and (d)), in a current-saturation regime, $V_{ds} = 2.0$ and $V_{gs} = 0.0$ V, (Figs. 2.19(b) and (e)), and near current threshold, $V_{ds} = 2.0$ and $V_{gs} = -1.0$ V, (Figs. 2.19(c) and (f)). Arrows in these figures indicate the edges of recessed n^+-GaAs regions. The three figures on the left side ((a) -

(c)) have been obtained by using the non-surface state model, and those on the right side ((d) - (f)) by using the surface state model. In the case of the non-surface state model, carrier modulation through gate bias is seen just under the gate electrode as usual. In the case of the surface state model, however, the electron depletion is seen over the whole region between the recess edges as if the whole surface would act as a gate electrode.

The corresponding electrostatic potential and current density distributions are also shown in Figs. 2.20(a) - (f). The intervals between equi-potential lines along the 2DEG channel turn out to be larger for the cases taking the surface states into consideration ((d) - (f)) than those for the surface-state-free cases ((a) - (c)). This indicates that the potential in the conducting channel varies in a more gradual way than that expected for these deep submicron HEMTs. Consequently the punch-through current flowing across the depletion region becomes much smaller, resulting in a reduction of the short channel effect on the characteristics.

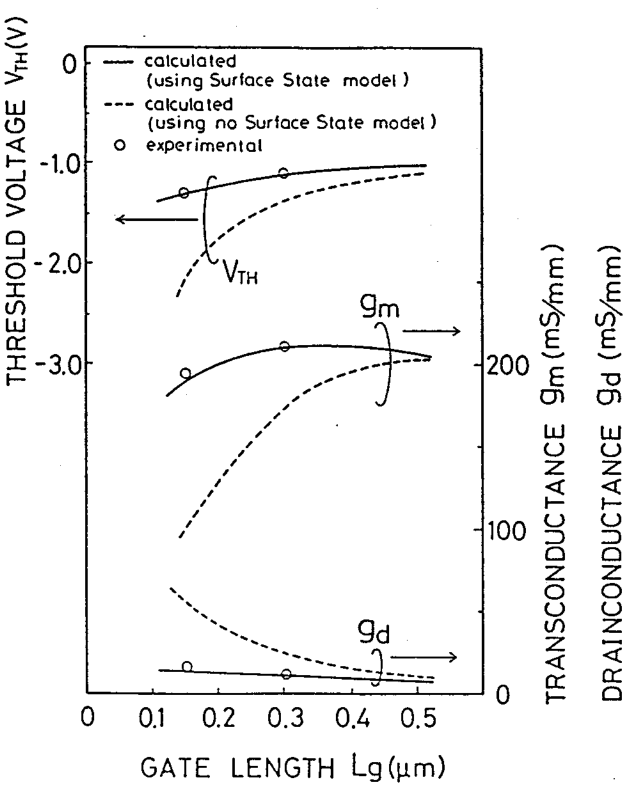

Figure 2.21 Threshold voltages, maximum transconductances, and drain conductances plotted as functions of the gate length. Solid and broken lines represent the results calculated by using the surface-state model and non-surface-state model. Experimental data are indicated by using open circles.

The resultant gate length dependences of threshold voltage, maximum transconductance, and drain conductance are summarized in Fig. 2.21: Calculated results by using the surface-state model and non-surface-state model are plotted by the solid and broken lines, respectively. It should be noted that the effects of the surface states become significant for the gate length less than 0.3 μm. It is apparent that these quantities shown in this figure are less dependent on the gate length than those obtained by assuming surface-state free recessed structure.

2.3.2 Surface carrier recombination in an extrinsic base region of HBTs

Another significant effect of the surface trap levels is electron-hole recombination which frequently occurs on the surface of the extrinsic base region of HBTs. The *surface carrier recombination* has been one of the serious problem for compound semiconductor bipolar transistors as it may result in a drastic increase in excess base current and so degrade current gain. This phenomenon is a combination of the Fermi-level pinning studied in the last section and the deep-level-induced recombination of majority carriers in the base region with injected minority carriers and so more complex than the conventional recombination seen in a bulk base regime. In this last section excess base current is simulated by using the same Spicer's model, and the relation between the surface trap density and current gain is investigated.

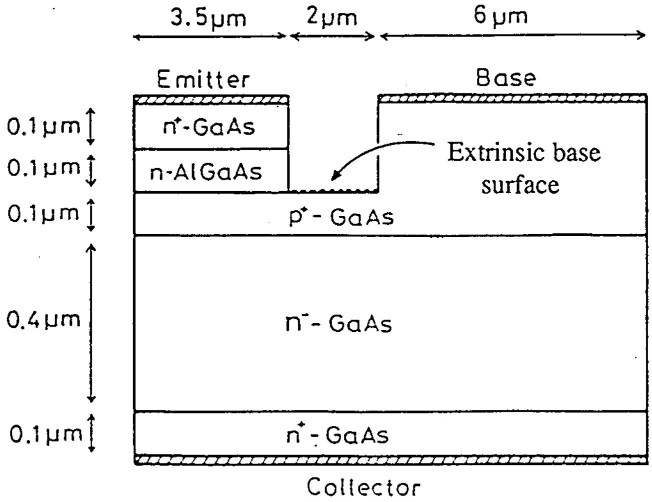

Figure 2.22 A schematic cross sectional view of an analized AlGaAs/GaAs HBT. Surface of an extrinsic base region is indicated by using a broken line.

Layer		Doping concentration (1/cm ^{3})
Emitter	n^+-GaAs	5.0×10^{18}
	N -$Al_{0.3}Ga_{0.7}As$	3.0×10^{17}
Base	p^+-GaAs	5.0×10^{18}
Collector	n^--GaAs	5.0×10^{16}
	n^+-GaAs	5.0×10^{18}

Table 2.4 Doping concentration in each layer of the AlGaAs/GaAs HBT.

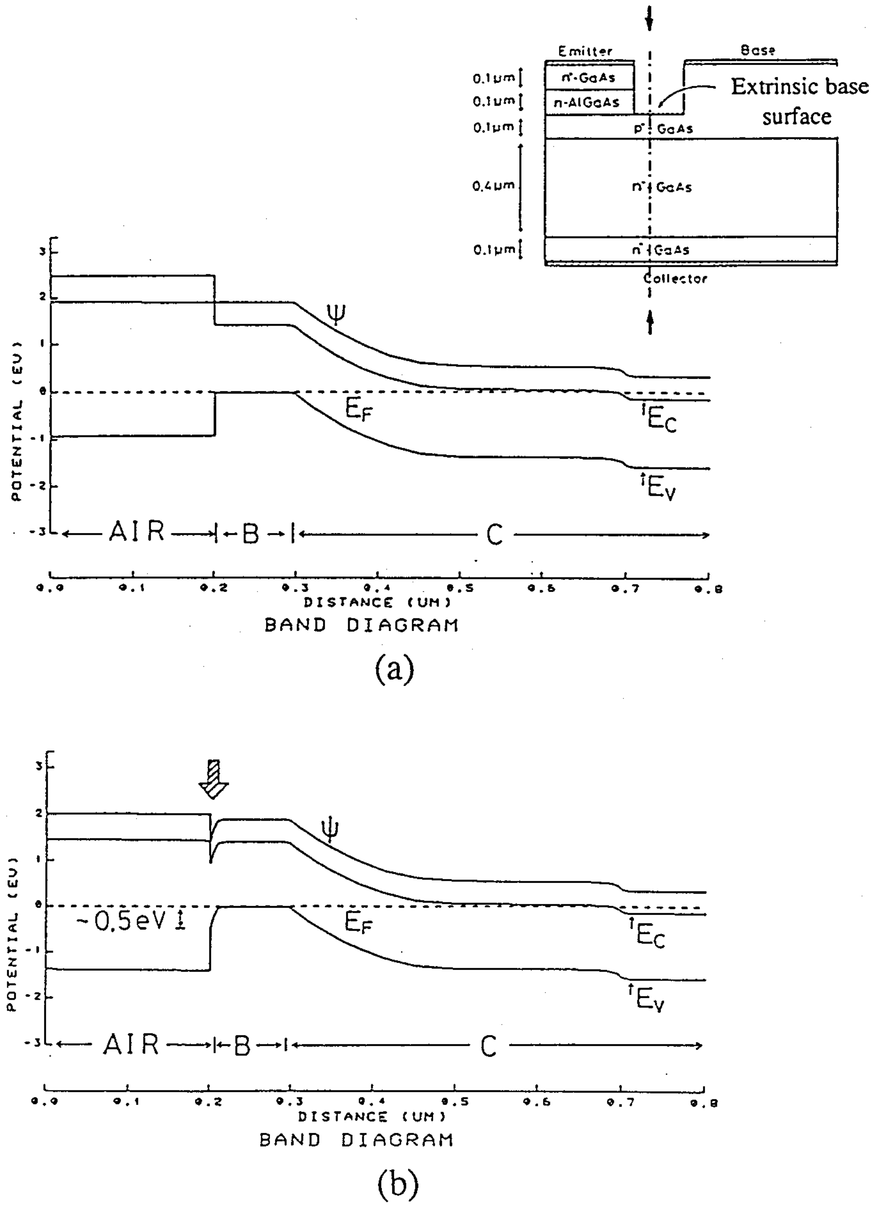

***Figure 2.23** Energy band-diagrams calculated along the vertical line across the extrinsic base surface (see inset): (a) Results calculated by using the deep-level-free surface model and (b) those by using Spicer's surface state model.*

Figure 2.22 shows cross sectional view of an AlGaAs/GaAs HBTs used for the present analysis: The interface between the extrinsic p$^+$-GaAs base region and air is indicated by a broken line for which the same surface-state model has been applied.

First we investigate the energy band-diagram in equilibrium along the vertical line across the extrinsic base surface (see inset of Fig. 2.23). Two equilibrium energy band-diagrams are shown in Fig. 2.23(a) and (b) which represent the results calculated by assuming ideal deel-level-free surface (a) and those by introducing deep levels with sheet concentration of 10^{13} /cm^2 (b).

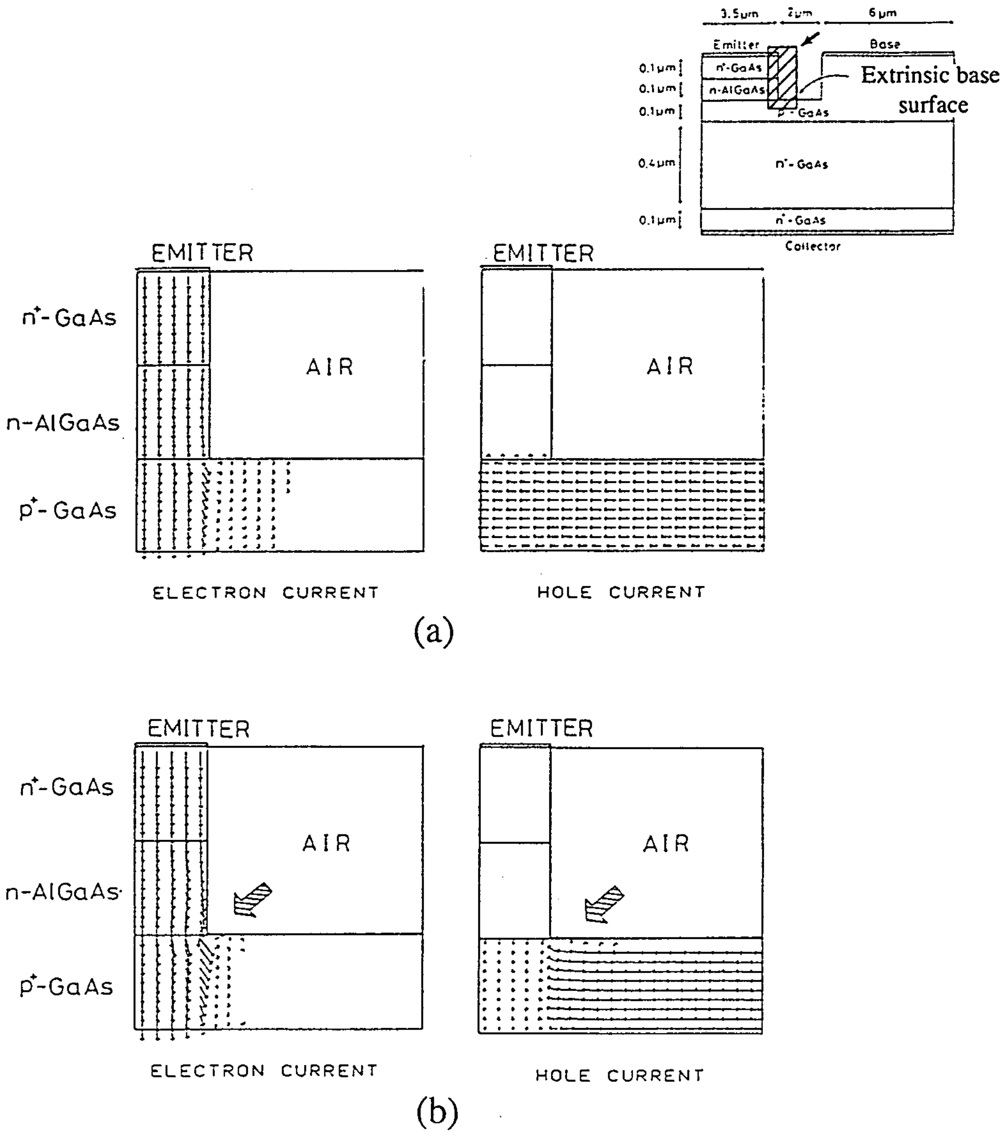

Figure 2.24 Electron and hole current flow around the edge of the extrinsic base surface (see inset): (a) Results calculated by using the deep-level-free surface model and (b) those by using Spicer's surface state model.

In Fig. 2.23(b) downward band bending is seen which is caused as electrons on high density deep donors compensate holes adjacent to surface. The Fermi-level is thus pinned at the surface donor energy (0.5 eV measured from the valence band edge). This acts as an attractive potential for electrons which come close to the surface.

Figure 2.24(a) shows visualized flow of electrons (right) and holes (left) around the edge of the extrinsic base surface calculated for the emitter-base bias V_{EB} of 1.2V and the base-collector bias of 0V. It is found that some electrons injected into the base region which are placed close to the extrinsic base surface change their directions towards the surface. These electrons reach the surface and then cause recombination with majority holes near the surface. This recombination leads to the excess base current which can be seen as a flow of holes towards the edge of the extrinsic base surface in Fig. 2.24(a). If there existed no surface state, no such flow could be found as is shown in Fig. 2.25.

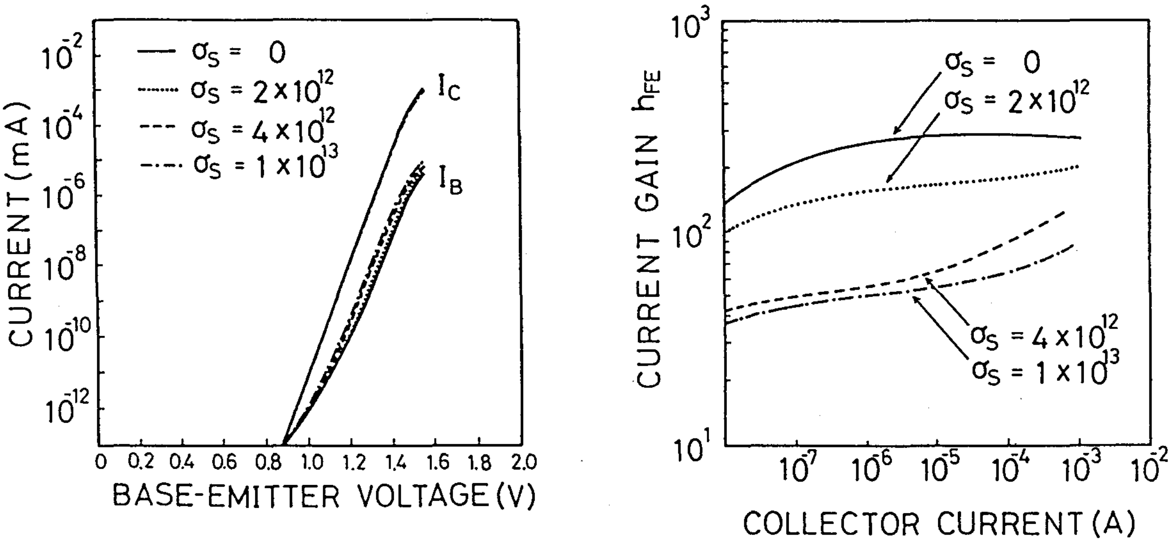

(a) (b)

Figure 2.25 *(a) Base-emitter bias V_{EB} dependences of collector and base currents and (b) collector current dependence of current gain h_{FE} calculated for various values of σ_S.*

Figure 2.25(a) shows the emitter-base bias dependences of collector and base currents, I_C and I_B, calculated with various values of surface state density σ_S. An increase in the base current induced by the surface carrier recombination is large enough to be seen in this figure while the decrease in the collector current is negligibly small. This becomes much clearer by plotting the collector current dependence of current gain, $h_{FE} = I_C/I_B$ in Fig. 2.25(b). It is found that h_{FE} is decreased down to about 60 for σ_S of 10^{13} /cm^2 from the value of about 300 obtained for the ideal surface-state-free case. These results are summarized in Fig. 2.26 as the dependences of the surface potential, Vs, and h_{FE} where Vs is the amount of the downward bending at the surface. It is seen that Vs increases steeply as σ_S is changed from 10^{12} to 10^{13} /cm^2. Correspondingly h_{FE} decreases drastically in this regime and turns out to be constant once the Fermi level pinning is completed around σ_S of 10^{13} /cm^2. In this regime the surface-recombination-induced base current proves to be crucial for h_{FE}.

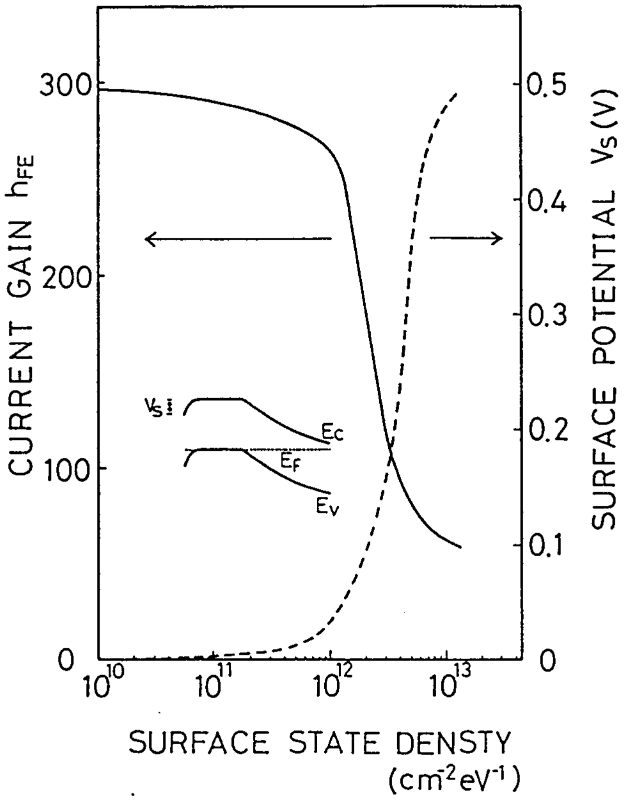

Figure 2.26 Current gain h_{FE}(solid line) and surface potential Vs (broken line: see inset) calculated as functions of surface state density σ_S.

Finally it should be noted in Fig. 2.25(b) that gradual increases can be seen in h_{FE} as I_C becomes relatively large. In this high current regime, the amount of electrons pulled by the surface field towards the extrinsic base becomes very large, and thus the surface recombination can not consume all the electrons which reach the surface leading to electron accumulation in the surface triangle potential well. The space charge build-up in the well then compensates the charge of ionised deep donors and gives rise to the *Fermi-level depinning* phenomenon. This self-induced field prohibits further electron-hole recombination on the surface and results in some amount of recovery of h_{FE}.

In summary of this chapter the SRH modelling of carrier emission-absorption processes has been successfully incorporated into DD-trasnport modelling of heterojunction devices. By using the present modeling it has been revealed that inevitable deep trap levels characteristic to compound semiconductor devices sometimes make great influences on device performances. One of the major effects is the Fermi-level pinning which, generally speaking, degrade controllability of conduction current via gate bias as has been seen for DX centres in the N-AlGaAs supply layer and the surface states in the conventional AlGaAs/GaAs. In addition, more complicated deep levels induced carrier recombination processes have also turned out to be crucial as demonstrated for the excess base current of AlGaAs/GaAs HBTs.

2.4 Reference II

[1] D. E. Holmes, R. T. Chen, K. R. Elliott and C. G. Kirkpatrick, "Stoichiometry-controlled compensation in liquid encapsulated Czochralski GaAs", Appl. Phys. Lett. **40**, 46, 1982.

[2] W. E. Spicer, P. W. Chye, P. R. Skeath, C. Y. Su and I. Lindau, "New and unified model for Schottky barrier and III-V insulator interface states formatios", J. Vac. Sci. Technol., **16**, 1442, 1979.

[3] D. Bedmarzyk and J. Bedmarzyk, "The approximation of the Fermi-Dirac integral $F_{1/2}(\eta)$", Phys. Lett., **64A**, 409, 1978.

[4] M. S. Lundstrom and R. J. Schuelke, "Numerical analysis of heterostructure semiconductor devices", IEEE Trans. Electron Devices, **ED-30**, 1151, 1983.

[5] M. Kurata and J. Yoshida, "Modeling and characterization for high-speed GaAlAs-GaAs n-p-n heterojunction bipolar transistors", IEEE Trans. Electron Devices, **ED-31**, 467, 1984.

[6] H. Neuman and U. Flohrer, "Electron mobility in $Al_xGa_{1-x}As$", Physica Status Solidi, **25a**, K145, 1974.

[7] W. Shockley and W. T. Read Jr, "Statistics of the recombination of holes and electrons", Phys. Rev. **87**, 835, 1952.

[8] J. A. Meijerink and H. A. van der Vorst, "An iterative solution method for linear systems of which the coefficient matrix is a symmetric M-matrix", Math. Comput., **31**, 148, 1977.

[9] T. Ohtoshi, K. Yamaguchi, T. Uda, M. Murayama, and Chinone, "A two-dimensional device simulator of semiconductor lasers", Solid-State Electron., **30**, 627, 1987.

[10] D. V. Lang, R. A. Logan, and M. Jaros, "Trapping characteristics and a donor-complex (DX) model for persistent-photoconductivity trapping center in Te-doped AlxGa1-xAs", Phys. Rev. **B19**, 1019, 1979.

[11] T. Ishikawa, J. Saito, S. Sasa, and S. Hiyamizu, "Electrical properties of Si-doped $Al_xGa_{1-x}As$ layers grown by MBE", Jpn. J. Appl. Phys. **21**, L675, 1982.

[12] J. L. Merz, J. P. van der Ziel, and R. A. Logan, "Saturable optical absorption of the deep Te-complex center in Al0.4Ga0.6As", Phys. Rev. **B20**, 654, 1979.

[13] M. I. Nathan, S. Tiwari, P. M. Mooney, and S. L. Wright, "DX centers in AlGaAs p-n heterojunctions and heterojunction bipolar transistors", J. Appl. Phys. **62**, 3234, 1987.

[14] P. Godts, E. Constant, J. Zimmermann, and D. Depreeuw, "Investigation of influence of DX centers on HEMT operation", Electron. Lett. **24**, 937, 1988.

[15] M. I. Nathan, P. M. Mooney, P. M. Solomonn, and S. L. Wright, “Room-temperature electron trapping in $Al_{0.35}Ga_{0.65}As$/GaAs modulation-doped field-effect transistors”, Appl. Phys. Lett. **47**, 628, 1985.

[16] A. Kastalsky and R. A. Kiehl, "On the low-temperature degadation of (AlGa)As/GaAs modulation-doped field-effect transistors", IEEE Trans. Electron Devices, **ED-33**, 414,, 1986.

[17] K. Hirakawa, H. Sakaki, and J. Yoshino, "Concentration of electrons in selectively doped GaAlAs/GaAs heterojunction and its dependence on spacer-layer thickness and gate electric field", Appl. Phys. Lett. **45**, 253, 1984.

[18] M. J. Moloney, F. Ponse, and H. Morkoc, "Gate capacitance-voltage characteristics of MODFET's: Its effect on transconductance", IEEE Trans. Electron Devices, **ED-32**, 1675, 1985.

[19] K. Park, H. B. Kim, and K. D. Kwack, "A model for the capacitance-voltage characteristics of MODFET's", IEEE Trans. Electron Devices, **ED-34**, 2422, 1987.

[20] Y. Ando and T. Itoh, "Analysis of charge control in pseudomorphic two-dimensional electron gas field-effect transistrs", IEEE Trans. Electron Devices, **ED-35**, 2295,, 1988.

[21] H. Hida, K. Ohata, Y. Suzuki, and T. Toyoshima, "A new low-noise AlGaAs/GaAs 2DEG FET with a surface undoped layer", IEEE Trans. Electron Devices, **ED-33**, 601, 1986.

[22] K. Yokoyama and K. Hess, "Calculation of warm electron trasport in AlGaAs/GaAs single heterostructures using a Monte Carlo method", J. Appl. Phys., **59**, 3798, 1986.

[23] Y. Takahashi and N. Kobayashi, "AlGaAs/GaAs 2-DEGFET's fabricated from MO-CVD wafers", IEEE Electron Device Lett., **EDL-6**, 154, 1985.

[24] W. P. Hong and P. K. Battacharya, "High-field transport in InGaAs/InAlAs modulation-doped heterostructures", IEEE Trans. Electron Devices, **ED-34**, 1491, 1987.

[25] A. Ketterson, M. Moloney, W. T. Masselink, C. K. Peng, J. Klem, R. Fischer, W. Kopp and H. Morkoc, "High transconductance InGaAs/AlGaAs pseudomorphic modulation-doped field-effect transistors", IEEE Electron Device Lett., **EDL-6**, 628, 1985.

[26] T. Henderson, M. I. Aksun, C. K. Peng, H. Morkoc, P. C. Chao, P. M. Smith, K.-H. G. Duh and L. F. Lester, "Microwave performance of a quarter-micrometer gate low-noise pseudomorphic InGaAs/AlGaAs modulation-doped field effect transistor", IEEE Electron Device Lett., **EDL-7**, 649, 1986.

[27] H. Asai and K. Oe, "Energy band-gap shift with elastic strain in $Ga_xIn_{1-x}P$ epitaxial layers on (001) GaAs substrates", J. Appl. Phys., **54**, 2052, 1983.

[28] K. Nishi, K. Hirose, and T. Mizutani, "Optical characterization of InGaAs-InAlAs strained-layer superlattices grown by molecular beam epitaxy", Appl. Phys. Lett. **49**, 794, 1986.

[29] T. W. Hickmott and P. M. Solomon, "Negative charge, barrier heights, and the conduction-band discontinuity in $Al_xGa_{1-x}As$ capacitors", J. Appl. Phys., **57**, 2844, 1985.

CHAPTER 3

COHERENT QUANTUM TRANSPORT IN RESONANT TUNNELLING DIODES (RTDs)

The following three chapters are intended to describe study of three different aspects of quantum transport in nanometer-scale semiconductor heterostructures. Firstly Chapter 3 deals with *coherent quantum transport* of electrons in multi-layered nanostructures in which electron waves propagate throughout device without experiencing any *phase-breaking scattering* events. Analysis mainly focuses on resonant tunnelling diodes (RTDs) which may be the most promising quantum mechanical device and have been intensively studied. The idea of *global coherent transport* is introduced to provide an intuitive and clear picture of the resonant tunnelling. Tsu-Esaki formula based on the linear response theory is adopted and combined with the transfer matrix method to calculate tunnelling current through the double barrier resonant tunnelling structures. The global coherent tunnelling model is then improved by taking account of Hartree's self-consistent field to simulate the potential distribution not only inside the resonant tunnelling structures but also in the emitter and collector accurately. By using the present modelling multiple-well resonant tunnelling diodes are numerically studied, and possibility of their applications to multiple-valued logic is discussed by comparing the calculated results with experimental data. Finally in this chapter the idea of incoherent resonant tunnelling induced by the phase-breaking scattering is introduced. The problem of collision-induced broadening is then discussed in terms of peak-to-valley (P/V) current ratio of the devices by using a phenomelogical Breit-Wigner broadening model.

3.1 Resonant tunnelling in double barrier heterostructures

Let's start with a simple discussion on the resonant tunnelling through a double barrier heterostructure depicted in Fig. 3.1(a). A resonant tunnelling diode in general consists of undoped quantum well layer sandwiched with undoped barrier layers with wider energy band gaps, and heavily doped emitter and collector contact regions on both sides.

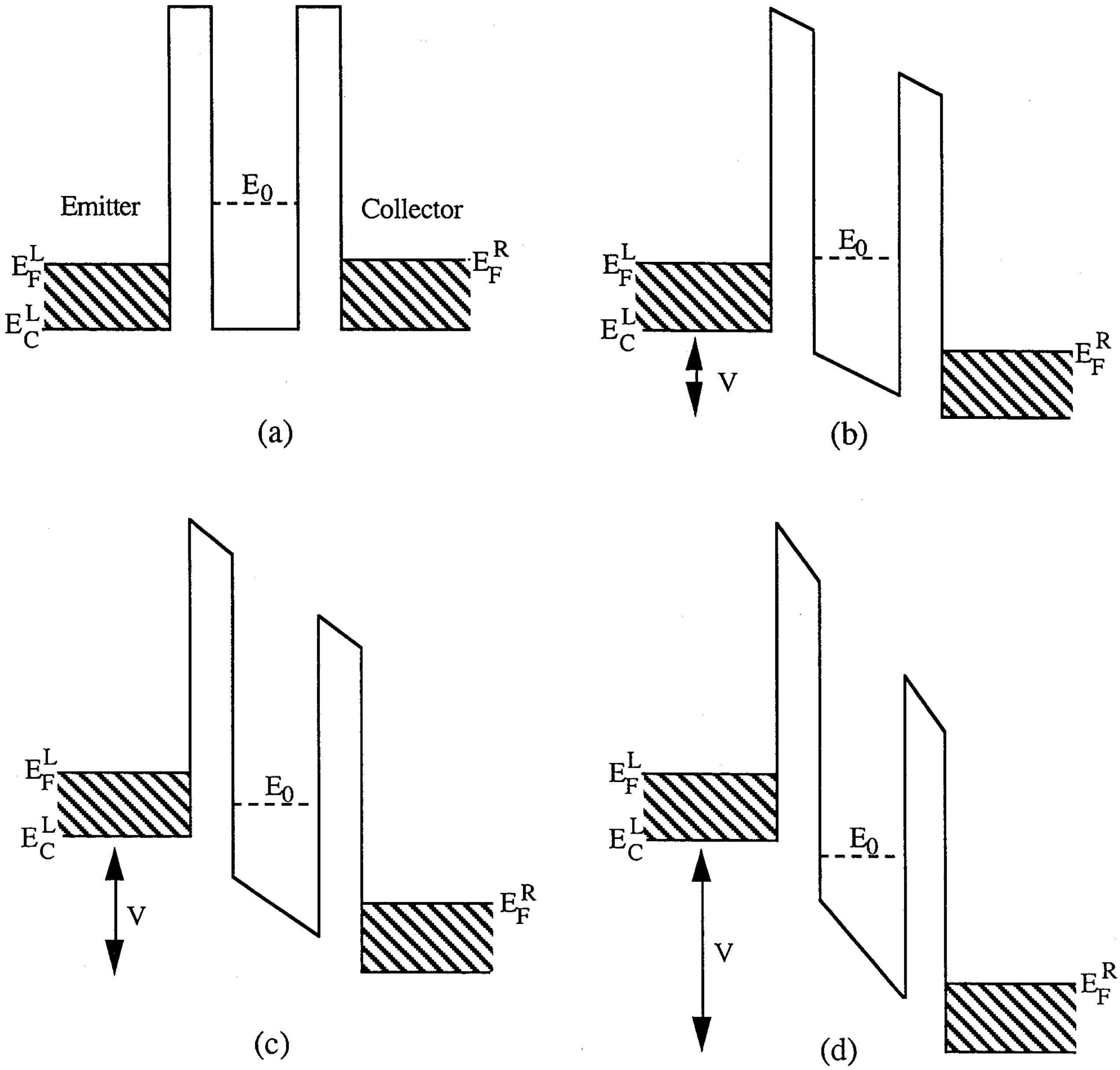

Figure 3.1 *Conduction band profiles of a double barrier resonant tunnelling diode at four different bias states: (a) zero bias, (b) threshold bias, (c) resonance, and (d) off-resonance. Hatched regions represent the Fermi sea in the emitter and collector layers.*

The RTD is thus an open system in which electronic states are all scattering states with continuous distribution in an energy space rather than bound states with discrete energy spectrum. Under these circumstances *quasi-bound states* are formed in the quantum well (the lowest state is denoted as E_0 in figures) which accommodate electrons for a certain time characteristic to the double barrier structure.

The energy-band structures of the double barrier RTD under four bias conditions are shown in Figs. 3.1(a) - (d): (a) at zero bias, (b) at threshold, (c) at the resonance, and (d) at the off-resonance.

Resonant tunnelling through the device occurs when the energy of the electrons coming from the emitter coincides with a quasi-bound state in the quantum well (denoted as E_0 in Fig. 3.1), and the effect of the external bias, V, is to sweep alignment of the emitter and quasi-bound states. Thus resonant tunnelling current starts to flow when E_0 reaches at the quasi-Fermi level, E_F^L, in the emitter (Fig. 3.1(b); this is hereafter called the threshold state), reaches its maximum while E_0 passes through the Fermi sea in the emitter (Fig. 3.1(c); the resonant state), and continues until E_0 falls below the conduction band edge in the emitter (Fig. 3.1 (d); the off-resonant state).

In this simple form of tunnelling both energy and momentum parallel to the barriers are conserved since the resonant tunnelling structure is totally translationally invariant. In other words total energy of electron, $E(\vec{k})$, can be separated into lateral (x- and y-directions) and vertical (z-direction) components as follows:

$$E(\vec{k}) = \frac{\hbar^2 (k_x^2 + k_y^2)}{2\,m^*} + E_z \tag{3.1}$$

as the lateral motion of electrons is simply expressed in a plane-wave form with a lateral wavevector, $\overrightarrow{k_{//}} = (k_x, k_y)$. Later we will show that this basic assumption is no longer correct when other effects which break the lateral symmetry in the system on the tunnelling characteristics are significant. In this chapter, however, this simple assumption will be adopted to give an intuitive understanding of resonant tunnelling.

Resonant tunnelling current through a double barrier structure basically depends on the detail of the transmission probability which is introduced later in this section. Nevertheless the expected shape of current-voltage characteristics can be obtained from the following simple consideration. In the three-dimensional emitter, at zero temperature, the electrons lie within a Fermi sphere of radius k_F where k_F is the Fermi wave number in the emitter (see Fig.3.2(a)).

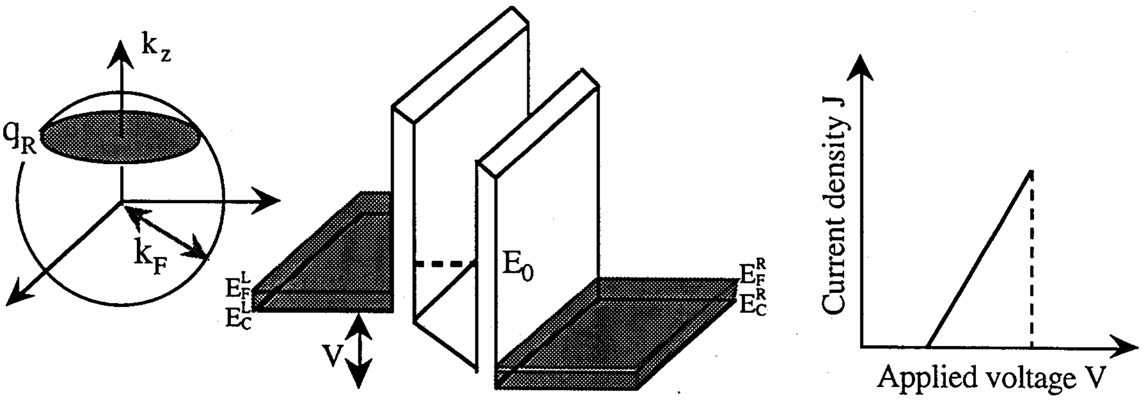

(a) (b)

Figure 3.2 (a) A Fermi sphere of electrons in the emitter and the corresponding schematic energy-band diagram. (b) Expected current-voltage characteristics.

So long as tunnelling into the quantum well conserves the lateral momentum, k_x and k_y, and the normal (z-direction) energy, the electronic states involved in such a process can be represented by the interaction of the plane $k_z = q_R$ with the Fermi sphere where q_R is the wave number associated with the energy of the resonant state referred to the conduction band edge:

$$q_R = \frac{\sqrt{2m^*\left(E_0 - E_C^L\right)}}{\hbar} \qquad (3.2)$$

where E_0 is the energy of the resonant state in the quantum well, and E_C^L is the energy of the conduction band edge in the emitter. The tunnelling current density will then be proportional the density of these states indicated by the gray intersecting circle in Fig. 3.2(a). Therefore, as long as transmission probability of the resonant state is nearly constant through the range of applied bias, the tunnelling current is expressed as follows:

$$J \propto \pi\left(k_F^2 - q_R^2\right) \propto \left(E_F^L - E_0\right) \qquad (3.3)$$

where E_F^L is the local Fermi energy in the emitter defined as $E_F^L = E_F + E_C^L$ (see Fig. 3.1). As $E_F^L - E_0$ is proportional to the applied bias, J increases linearly until E_0 goes below the conduction band edge in the emitter: the triangular shape of the I-V characteristics is then obtained as seen in Fig. 3.2(b).

The triangle shape obtained through the above simple discussion is indeed observed for the current-voltage characteristics of fabricated double barrier RTDs. Figure 3.3 shows a typical example of the I-V characteristics measured at 93K for the double barrier resonant tunnelling structure which consists of a GaAs quantum well layer sandwiched with two AlAs barrier layers [12]-[15].

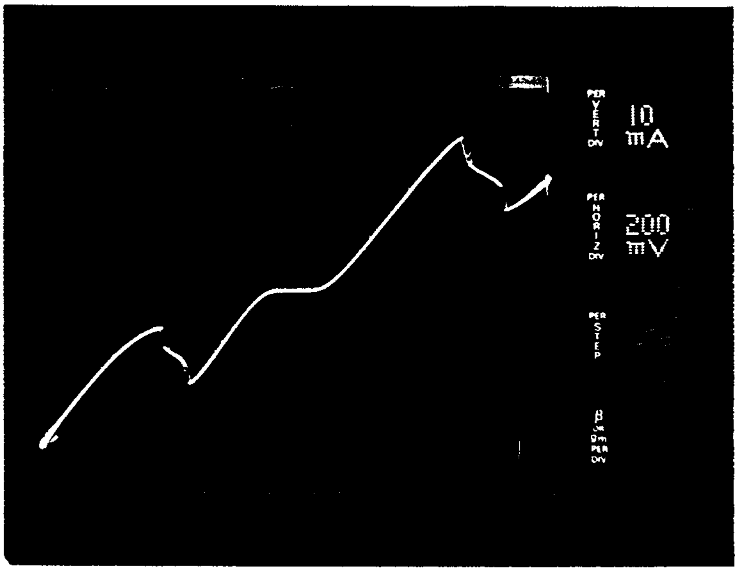

***Figure 3.3** Current-voltage characteristics for an AlAs/GaAs/AlAs double barrier RTD with a mesa area of 4 μm x 4 μm measured at 93K in both forward and reverse bias directions.*

Layer	Thickness (nm)
n - GaAs ($N_D = 1.0 \times 10^{18} cm^{-3}$)	20.0
undoped - GaAs	5.0
undoped - AlAs	1.5
undoped - GaAs	4.5
undoped - AlAs	1.5
undoped - GaAs	5.0
n - GaAs ($N_D = 1.0 \times 10^{18} cm^{-3}$)	20.0

***Table 3.1** Structural parameters of the double barrier RTD Sample 1.*

Detailed geometry of the layer structure of the fabricated RTD is listed in Table 3.1: the sample is called *Sample 1* in the following study. The characteristic is found to reflect the basic nature of the resonance although its details are quite different from those shown in Fig. 3.2(b).

An exact formulation of the tunnelling current at finite temperatures is derived from the following expressions:

$$J = J_{\rightarrow} - J_{\leftarrow} \tag{3.4.a}$$

$$\begin{aligned} J_{\rightarrow} &= 2 \sum_{k_x,\, k_y,\, k_z > 0} e\, v_z\, T(E_z)\, f_L(\vec{k}) \left\{1 - f_R(\vec{k})\right\} \\ &= \frac{1}{2\pi^2} \int_0^\infty k_{//}\, dk_{//} \int_0^\infty dk_z\, e\, v_z\, T(E_z)\, f_L(k_{//}, k_z) \left\{1 - f_R(k_{//}, k_z)\right\} \end{aligned} \tag{3.4.b}$$

$$\begin{aligned} J_{\leftarrow} &= 2 \sum_{k_x,\, k_y,\, k_z < 0} e\, v_z\, T(E_z)\, f_R(\vec{k}) \left\{1 - f_L(\vec{k})\right\} \\ &= \frac{1}{2\pi^2} \int_0^\infty k_{//}\, dk_{//} \int_{-\infty}^0 dk_z\, e\, v_z\, T(E_z)\, f_R(k_{//}, k_z) \left\{1 - f_L(k_{//}, k_z)\right\} \end{aligned} \tag{3.4.c}$$

where $T(E_z)$ is the *transmission probability* which will be explained in the next section, and $f_L(\vec{k})$ and $f_R(\vec{k})$ are the Fermi distribution functions in the emitter and collector regions:

$$f_{L,R}(\vec{k}) = \frac{1}{1 + \exp\left(\dfrac{E(\vec{k}) - E_F^{L,R}}{k_B\, T}\right)} \tag{3.5}$$

where $E_F^L = E_F^R + V$ when the external voltage of V is applied to the RTD. By using

$$v_z = \frac{1}{\hbar} \frac{dE_z}{dk_z} \tag{3.6}$$

and integrating over k_x and k_y,

$$J = \int_0^\infty dE_z\, T(E_z)\, S(E_z) \tag{3.7}$$

where $S(E_z)$ is the *electron supply function* defined as follows:

$$S(E_z) = \frac{m^*\, e\, k_B\, T}{2\, \pi^2\, \hbar^3} \ln \left[\frac{1 + \exp\left\{\dfrac{1}{k_B\, T}\left(E_F^L - E_z\right)\right\}}{1 + \exp\left\{\dfrac{1}{k_B\, T}\left(E_F^R - E_z\right)\right\}} \right] \tag{3.8}$$

It will be shown in the next section that the transmission function $T(E_z)$ in general varies far more quickly than the supply function $S(E_z)$. Replacing $T(E_z)$ with $\delta(E_z - E_0)$, it can be easily shown that Eqs. (3.6) and (3.7) reduce to the expression (3.3) at zero temperature under large applied bias ($eV > E_F$).

3.2 Theory of global coherent resonant tunnelling

In this section a simple theory of quantum transport is introduced which is based upon a *global coherent tunnelling* picture in which an electron goes throughout the device without having an experience of phase-coherence breaking events. Later in this chapter it is shown that this theory does not necessarily provide an appropriate description of the transport of the electron waves, especially in a system where the transport is very energy-dissipative. This theory, however, gives us an intuitive understanding of the quantum transport and always becomes a basis for more sophisticated transport theory. First the transfer matrix method for one-dimensional scattering problems is introduced to calculate the transmission probability function in Eq. (3.7). One-dimensional Schrödinger equation is numerically solved with scattering boundary conditions on the wavefunctions and the transfer matrices for an arbitrary heterostructures are calculated. The Schrödinger equation is solved without including any scattering potentials except the ideal multi-barrier potential resulting from the deferences in an electron affinity in heterojunction systems. In Sec. 3.2.1, the theory is expressed in a non-self-consistent scheme neglecting electron-electron interactions in the device. Then, in Sec. 3.2.2, the effects of space charge build-up in the quantum well on the global coherent tunnelling are taken into consideration by adopting Hartree's self-consistent field model.

3.2.1 Transfer matrix theory of transmission probability

Let's start from the one-dimensional time-independent effective mass Schrödinger equation:

$$H\,\Psi(z) = -\frac{\hbar^2}{2}\nabla\left(\frac{1}{m^*(z)}\nabla\right)\Psi(z) + V(z)\,\Psi(z) = E_z\,\Psi(z) \qquad (3.9)$$

where m*(z) is the z-dependent conduction band effective mass. The potential energy, V(z), consists of the electron affinity and the Hartree's self-consistent potential which will be introduced in Sec. 3.2.2. In the transfer matrix method the potential distribution of a resonant tunnelling structure is approximated by a series of small steps [16] as shown in Fig. 3.4. The wavefunction in the *i*-th section can be expressed in a plane wave form:

$$\Psi^{(i)}_{k_z^{(i)}}(z) = A^{(i)}_{k_z^{(i)}}\exp(i\,k_z^{(i)}\,z) + B^{(i)}_{k_z^{(i)}}\exp(-\,i\,k_z^{(i)}\,z) \qquad (3.10)$$

where $k_z^{(i)}$ is the complex wavenumber defined as follows:

$$k_z^{(i)} = \frac{\sqrt{2\, m^{*(i)} (E_z - V^{(i)})}}{\hbar} \qquad (3.11)$$

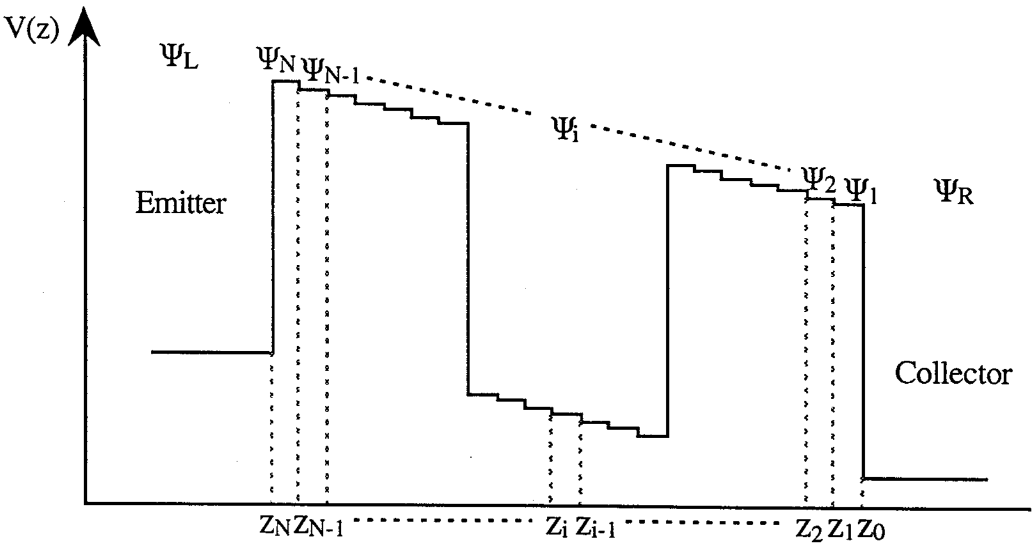

Figure 3.4 *A series of small potential steps used for the transfer matrix calculations of a double barrier resonant tunnelling structure.*

From the continuity of the probability flux of electrons, the following conditions on the wavefunctions hold at all boundaries:

$$\Psi^{(i)}_{k_z^{(i)}}(z_{i+1}) = \Psi^{(i+1)}_{k_z^{(i+1)}}(z_{i+1}) \qquad (3.12.a)$$

$$\frac{1}{m^{*(i)}} \left.\frac{\partial \Psi^{(i)}_{k_z^{(i)}}(z)}{\partial z}\right|_{z = z_{i+1}} = \frac{1}{m^{*(i+1)}} \left.\frac{\partial \Psi^{(i+1)}_{k_z^{(i+1)}}(z)}{\partial z}\right|_{z = z_{i+1}} \qquad (3.12.b)$$

The coefficients in the adjacent sections are then related each other as follows:

$$\begin{pmatrix} A^{(i+1)}_{k_z^{(i+1)}} \\ B^{(i+1)}_{k_z^{(i+1)}} \end{pmatrix} = T^{(i)} \begin{pmatrix} A^{(i)}_{k_z^{(i)}} \\ B^{(i)}_{k_z^{(i)}} \end{pmatrix} \qquad (3.13)$$

where the matrix $T^{(i)}$ is defined as

$$T^{(i)} = \begin{pmatrix} \alpha_+^{(i)} P & \alpha_-^{(i)} / Q \\ \alpha_-^{(i)} Q & \alpha_+^{(i)} / P \end{pmatrix} \qquad (3.14.a)$$

$$\alpha_\pm^{(i)} = \frac{1}{2}\left\{1 \pm \left(m^{*(i+1)} / m^{*(i)}\right)\left(k_z^{(i)} / k_z^{(i+1)}\right)\right\} \qquad (3.14.b)$$

$$P = \exp\left\{i\left(k_z^{(i)} - k_z^{(i+1)}\right) z_{i+1}\right\} \qquad (3.14.c)$$

$$Q = \exp\left\{i\left(k_z^{(i)} + k_z^{(i+1)}\right) z_{i+1}\right\} \qquad (3.14.d)$$

Thus the coefficients at the cathode and anode edges are connected by using the transfer matrix T as follows:

$$\begin{pmatrix} A^{L}_{E_z} \\ B^{L}_{E_z} \end{pmatrix} = T \begin{pmatrix} A^{R}_{E_z} \\ B^{R}_{E_z} \end{pmatrix} \tag{3.15.a}$$

$$T = T^{(N)}\, T^{(N-1)}\, T^{(N-2)} \ldots T^{(2)}\, T^{(1)} \tag{3.15.b}$$

A complete set of wavefunctions is obtained by using the following scattering boundary conditions:

$$\left(A^{L}_{E_z}, B^{R}_{E_z}\right) = (1, 0) \tag{3.16}$$

for an incident electron wave coming from the emitter edge, and

$$\left(A^{L}_{E_z}, B^{R}_{E_z}\right) = (0, 1) \tag{3.17}$$

when it comes from the collector edge of the device. The transmission probability $T(E_z)$ through the RTD is then given as follows:

$$T(E_z) = \frac{m^{*L}}{m^{*R}} \frac{k^{R}}{k^{L}} \frac{\left|A^{R}_{E_z}\right|^2}{\left|A^{L}_{E_z}\right|^2} \tag{3.18}$$

Numerical results for the energy dependence of the transmission probability at zero bias for Sample 1 is shown in Fig. 3.5.

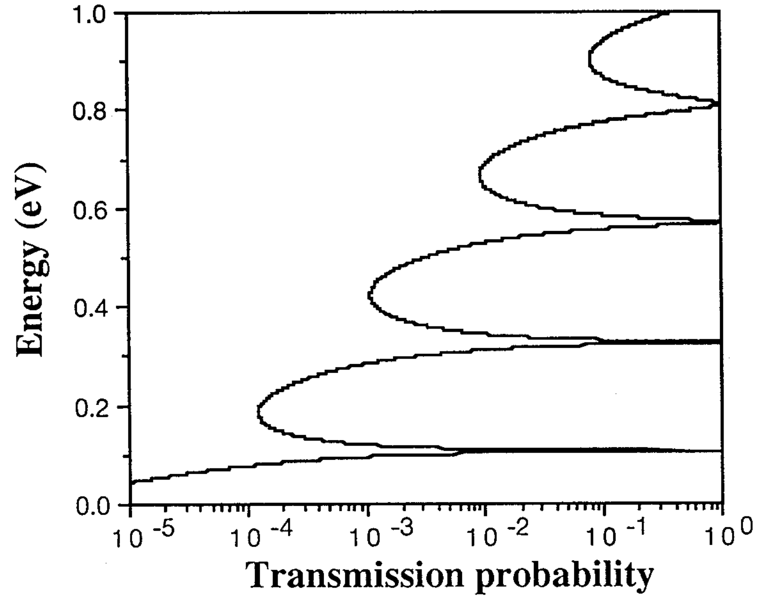

Figure 3.5 Transmission probability $T(E_Z)$ versus energy E_Z calculated for Sample 1 under zero external bias.

Material constants of AlGaAs/GaAs heterosystems used for the calculations are summarised in Table 3.2. With increasing Ez, the transmission probability through the double barrier structures increases as a whole and reaches unity at several values of energy. This is because a resonance occurs in the quantum well for certain wavelengths of incoming electrons giving a unity transmission probability - the situation is analogous to the Fabry-Perot interferometer in optics.

1. Electron effective mass m* $m^*(E) = 0.067(1 - 6\alpha(E - Ec)/Eg)$;GaAs $m^* = (0.067 + 0.083x)\, m_0$;$Al_xGa_{1-x}As$ Band gap Eg = 1.42 eV Non-parabolicity parameter a = -0.824
2. Couduction band discontinuity ΔEc $\Delta Ec(x) = \beta 1.247 x \quad (0 < x < 0.45)$ $\Delta Ec(x) = \beta (1.247x + 1.147 (x - 0.45)^2)$ $(0.45 < x)$ Band parameter $\beta = 0.6$ (Müller's rule)
3. Dielectric constant $\varepsilon(x)$ $\varepsilon(x) = 13.1 - 3.0\, x$

TABLE 3. 2 Material parameters of AlGaAs/GaAs heterostructures.

Although the transmission probability can be now calculated numerically for any kinds of multi-barrier structures it is worth deriving analytical expressions for some special tunnelling structures to study properties of $T(E_Z)$ in further detail. First we consider a single barrier structure under a zero bias condition shown in Fig. 3.6 (a). By using Eqs. (4.13) - (4.18) it is straightforward to show that $A^3_{E_z}/A^1_{E_z}$ is given by the following expression:

$$\frac{A^3_{E_z}}{A^1_{E_z}} = e^{-i k_z d}\left\{\cosh(\kappa_Z d) - i\,\frac{2E_Z - V}{2\sqrt{E_Z(V-E_Z)}}\,\sinh(\kappa_Z d)\right\}^{-1} \qquad (3.19)$$

and then the transmission probability through a single barrier, $T_{SB}(E_Z)$, as follows:

$$T_{SB}(E_z) = \left\{1 + \frac{V^2}{4E_z(V - E_z)} \sinh^2(\kappa_z d)\right\}^{-1} \quad (3.20)$$

where k_z and κ_z are defined as $\sqrt{2m^*E_z/\hbar^2}$ and $\sqrt{2m^*(V - E_z)/\hbar^2}$, respectively. If the energy Ez is much smaller than the energy barrier height V, Eq. (3.20) reduces to:

$$T_{SB}(E_z) \approx \frac{16E_z(V - E_z)}{V^2} e^{-2\kappa_z d} \quad (3.21)$$

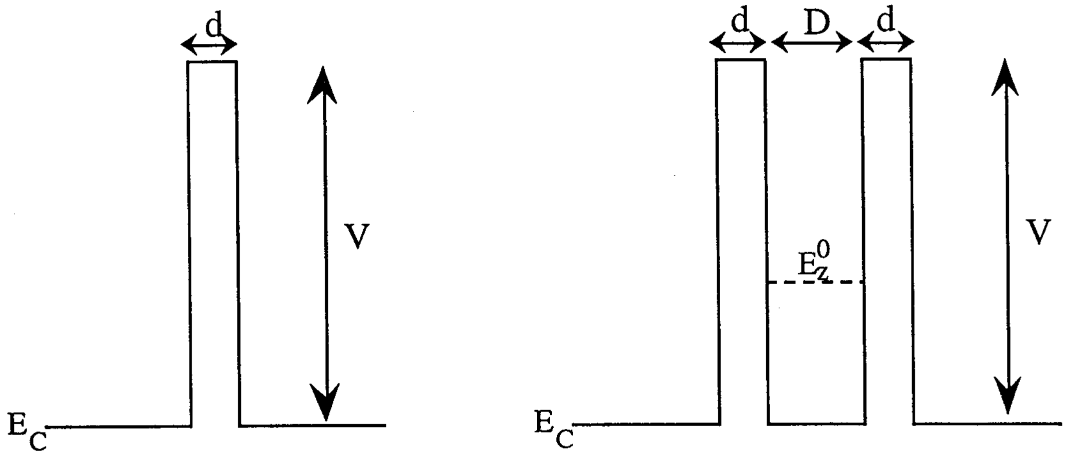

(a) (b)

Figure 3.6 Simplified conduction band profiles of (a) single barrier and (b) double barrier structures at zero bias.

The transmission coefficient for a double barrier structure [17] at zero bias (Fig. 3.6(b)) is also expressed in the following analytical form:

$$\frac{A^5_{E_z}}{A^1_{E_z}} = e^{-i k_z (2d + D)} \left[\left\{\cosh(\kappa_z d) - i \frac{2E_z - V}{2\sqrt{E_z(V-E_z)}} \sinh(\kappa_z d)\right\}^2 e^{-i k_z D} + \frac{4V^2}{E_z(V-E_z)} \sinh^2(\kappa_z d)\, e^{i k_z D}\right]^{-1}$$

(3.22)

It is shown that Eq. (3.22) is well reduced to the following simple form around a resonance [18]:

$$\frac{A^5_{E_z}}{A^1_{E_z}} \approx e^{-i k_z (2d + D)} \frac{\Gamma}{(E_z - E_z^0) + i\Gamma} \quad (3.23)$$

where the *resonant energy* E_z^0 and the *resonant width* Γ are approximately determined by the following equations:

$$2\cos\left(k_z^0 D\right) + \frac{V - 2E_z^0}{\sqrt{E_z^0\left(V - E_z^0\right)}} \sin\left(k_z^0 D\right) \cong 0 \tag{3.24}$$

$$\Gamma \cong 4E_z^0\, e^{-2\kappa_z^0 d}\left(k_z^0 D + 2k_z^0/\kappa_z^0\right)^{-1} \approx 2hT_{SB}\left(E_z^0\right) v_z^0/\left(D + 2/\kappa_z^0\right) \tag{3.25}$$

where v_z^0 is electron velocity ($= \hbar k_z^0/m^*$), and $T_{SB}\left(E_z^0\right)$ is the transmission probability through a single barrier (Eq. (3.21)) at $E_z = E_z^0$ given as follows:

$$T_{SB}\left(E_z^0\right) \approx e^{-2\kappa_z^0 d} \tag{3.26}$$

This simple expression (3.23) for the transmission coefficient is called a *Breit-Wigner form* [19] which is a general form to describe the resonant scattering spectrum and is widely used because of its simplicity.

Another important quantity, *tunnelling escape time* (or *dwell time*), τ_{esc}, [20][21] associated with the resonant width Γ is then defined through the following expression:

$$\tau_{esc} = \frac{\hbar}{2\Gamma} \approx \frac{1}{T_{SB}\left(E_z^0\right)} \frac{D + 2/\kappa_z^0}{v_z^0} \tag{3.27}$$

This proves to be equivalent to the classical *multiple reflection time* of an electron in a quantum well with a quantum mechanical correction term, $2/\kappa_z^0$, due to penetration of an electron wave into potential barriers.

3.2.2 Self-consistent calculations - Introduction of space-charge build-up -

The theory described in the previous section does not include any effects of electronic charge. Space charge distribution in RTDs basically reflects the existence probabilities of electrons like those shown in Fig. 3.5 and leads to non-uniform potential distribution. Determination of the charge distribution in RTDs under non-equilibrium conditions is one of crucial issues under a lively discussion as it is closely related to energy dissipation processes in the system which we study in Chapter 4. The energy dissipation process of tunnelling electrons such as LO-phonon emission varies the distribution function far from the one in equilibrium. Thus a simple Fermi-Dirac distribution function does not necessarily describe the accumulated electrons in the well and a complex non-equilibrium transport theory would be in general required. In this section, however, we stay within a frame of a global coherent tunnelling picture and then may express the electron distribution in RTDs as follows:

$$n(z) = 2\sum_{k_z > 0} \left|\Psi_{k_z}(z)\right|^2 f_L\left(\vec{k}\right) + 2\sum_{k_z < 0} \left|\Psi_{k_z}(z)\right|^2 f_R\left(\vec{k}\right)$$

$$= \frac{k_BT}{2\pi^2\hbar^2}\left(\int_0^{\infty}|\Psi_{k_z}(z)|^2\, m^*\ln\left\{1+\exp\left(\frac{E_F^L - E_z}{k_BT}\right)\right\}dk_z \right.$$

$$\left. + \int_{-\infty}^{0}|\Psi_{k_z}(z)|^2\, m^*\ln\left\{1+\exp\left(\frac{E_F^R - E_z}{k_BT}\right)\right\}dk_z\right) \qquad (3.28)$$

The space charge distribution determined by Equation (3.26) results in *a self-consistent potential* ,$V_{sc}(z)$, which is obtained through the following Poisson's equation:

$$\frac{d}{dz}\left(\varepsilon(z)\frac{dV_{sc}(z)}{dz}\right) = -e\left\{N_D^+(z) - n(z)\right\} \qquad (3.29)$$

The self-consistent potential is then added to V(z) in Schrödinger equation. The set of Equations (3.26) and (3.27) with Schrödinger equation is the well-known Hartree equation in which an exchange correlation between electrons is neglected. These equations are numerically solved in an iterative way until the self-consistent solutions for $\Psi_{k_z}(z)$ and $V_{sc}(z)$ are finally obtained [22]-[25].

Once we start a numerical calculation using the above self-consistent theory, the question would arise about the modelling of heavily doped emitter and collector regions (and, if used, undoped spacer regions as well): whether or not these regions can be treated in the same way as the resonant tunnelling barrier region. As mentioned earlier the present theory is based on an assumption that the electron waves propagate throughout the system without any phase-coherence breaking scattering. This could be a plausible assumption as long as the theory is applied only for a thin undoped double barrier structure though it will be shown soon later that the effect of scattering processes on the coherent tunnelling picture often becomes significant. In the thick heavily doped contact regions on both sides of the barrier structure, however, impurity scattering will occur frequently as well as LO-phonon scattering. Consequently these contact regions are frequently modelled by using a classical Thomas Fermi approximation in which electrons are assumed to occupy continuous energy states above the conduction band edge and so the electron density n(z) in Equation (3.27) is given only by the difference between the quasi-Fermi level and the conduction band edge. Fully quantum-mechanical treatment of the contact regions should be made by adopting a dissipative quantum transport theory such as the density matrix theory or non-equilibrium Green's function theory which we study in Chapter 4.

Examples of the self-consistent solutions based on these assumptions are shown in Fig. 3.7. These figures show the equilibrium energy-band diagrams and electron distributions calculated self-consistently at a room temperature for $Al_{0.26}Ga_{0.74}As/GaAs/Al_{0.26}Ga_{0.74}As$

double barrier structures with well thickness of (a) 5 nm, (b) 6 nm and (c) 7 nm (the barrier thickness is fixed to be 3 nm). Highly doped emitter and collector regions with donor concentration of 1.0×10^{18} cm^{-3} are set adjacent to the barriers without a spacer layer.

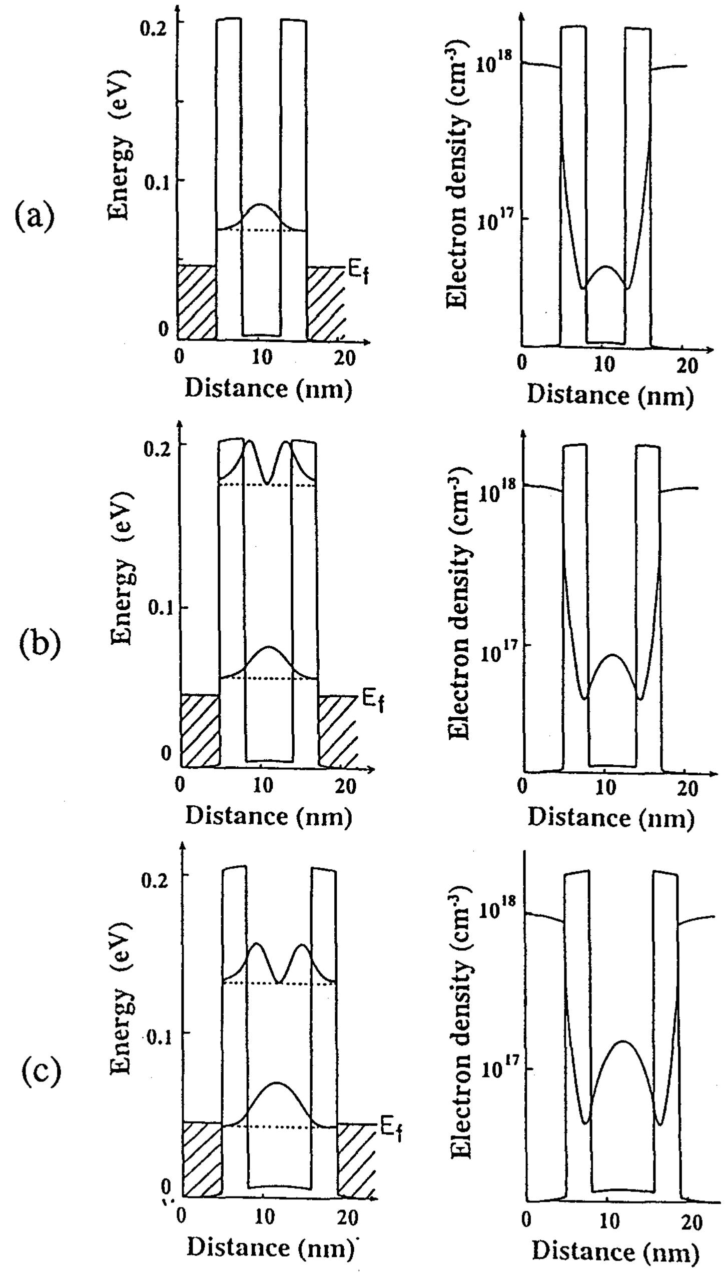

Figure 3.7 *Self-consistently calculated energy-band diagrams and electron distributions of double barrier RTDs with various well widths Lw: (a) 5 nm, (b) 6 nm, and (c) 8 nm. In the figures on the left the resonant energy levels and the existence probability of electrons are also shown by using dotted curves and solid curves, respectively.*

It can be seen that the conduction band edge at the centre of the quantum well is pushed towards higher energy with increasing the well width. This is because the energy of the lowest quasi-eigenstate comes down closer to the Fermi energy in the case of wider well and more electrons can populate this state. Larger electron accumulation in the quantum well gives rise to stronger self-consistent field resulting in a larger band bending.

The self-consistent modelling has been applied to Sample 1 (see Sec. 3.1): the I-V characteristics calculated at 77K (solid line) and 300K (broken line) are shown in Fig. 3.8.

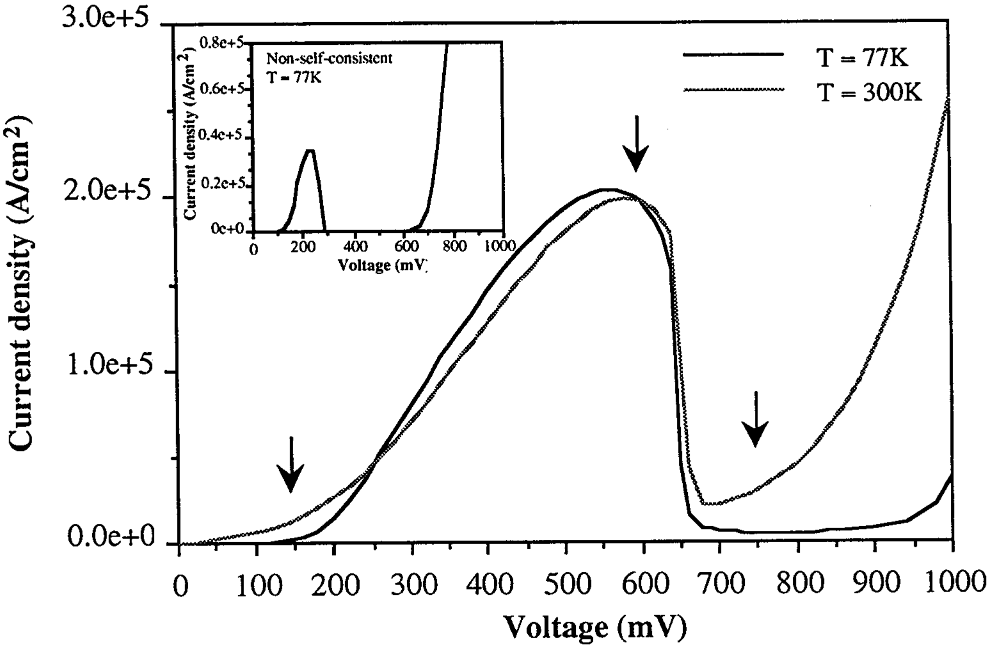

Figure 3.8 I-V characteristics calculated self-consistently for Sample 1 at 77K (solid line) and 300K (gray line). Arrows indicate three typical bias points: Threshold, peak, and valley voltages. The inset shows I-V curve calculated using piecewise linear model.

In Fig. 3.8 the I-V curve calculated by using the piecewise linear modelling of the band diagram (see, for example, Fig. 3.1(b) - (d)) is also shown in the inset to demonstrate the effect of the self-consistent calculations on the band diagram. It can be seen that the resonant peak voltage obtained from the self-consistent calculations is much larger than that from the non-self-consistent calculations since the applied voltage is assume to drop only in a double barrier region in the piecewise linear modelling of the band diagram. Calculated energy band diagrams are also shown for three typical bias points: At zero bias (Fig. 3.9(a)), at the peak state (Fig.

3.9(b)), and at the valley state (Fig. 3.9(c)). In the self-consistent modelling the voltage drop can be seen also in the emitter and collector regions leading to a relatively smaller voltage drop in the double barrier region. This results in a shift of the current peak towards a large voltage regime. The peak voltage obtained from the self-consistent calculations is 0.56 V which shows a good agreement with the value of 0.54 V observed experimentally (see Table. 3.3). This indicates that the self-consistent calculations reproduce the energy band diagrams in the device very well.

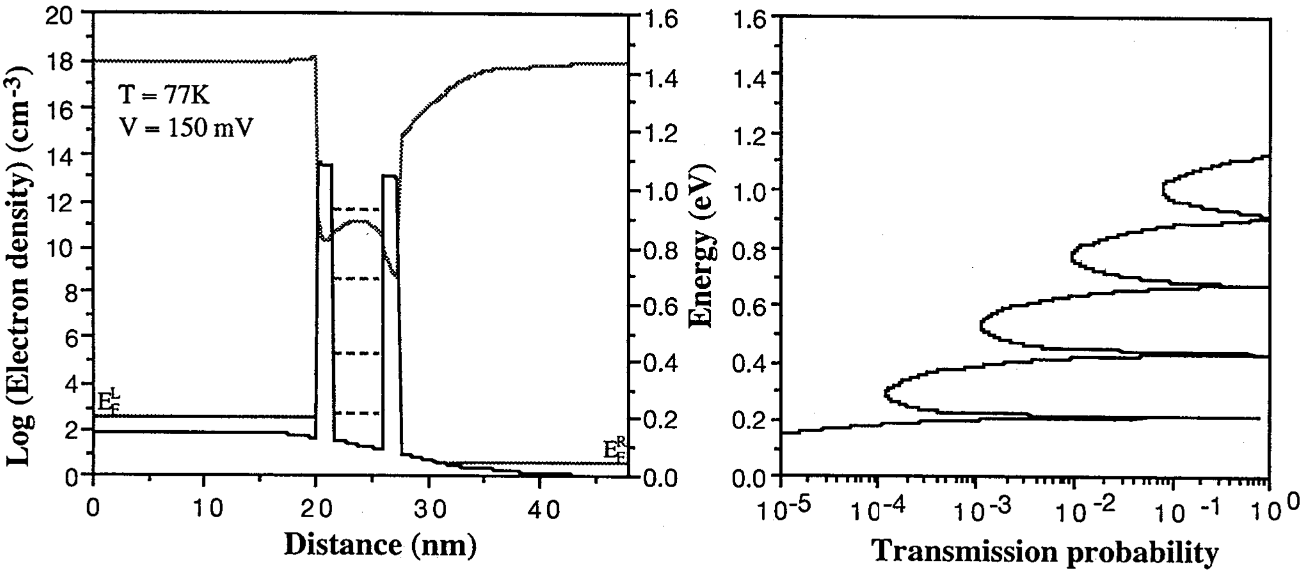

(a)

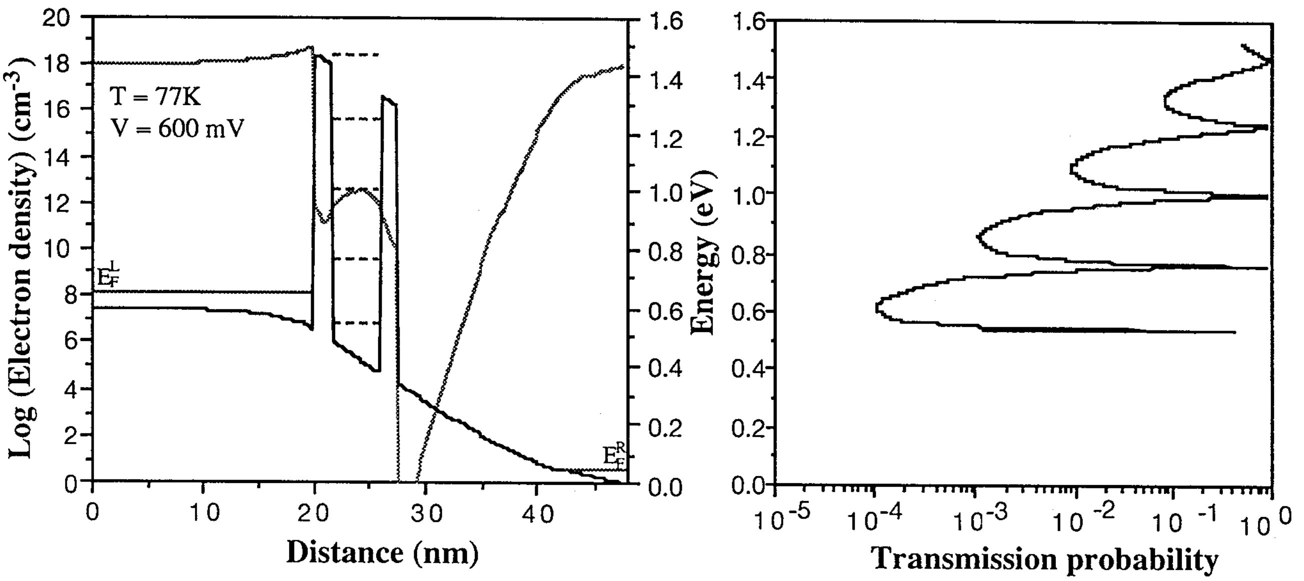

(b)

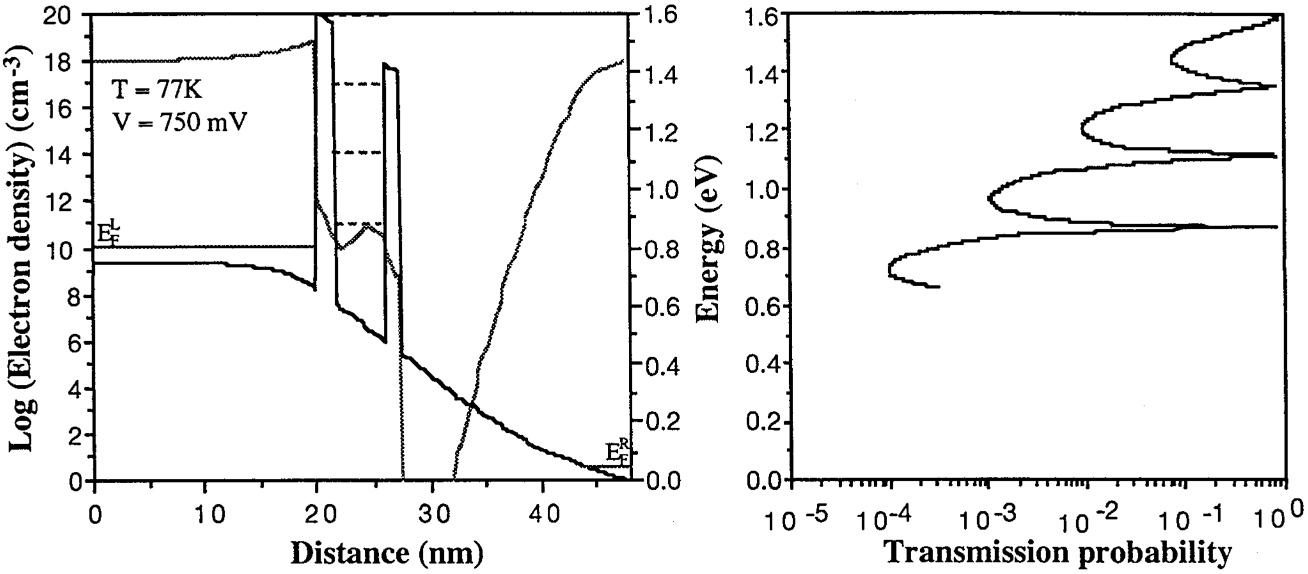

(c)

Figure 3.9 Self-consistently calculated energy-band diagrams and transmission properties at three different bias points indicated by using arrows in Fig. 3.8: (a) at current threshold, (b) at the peak current state, and (c) at the valley current state.

	Calculated (77K)	Observed (77K)
Peak voltage (mV)	560	540
Peak current density (A/cm^2)	2.04 x 10^5	1.6 x 10^5
Valley current density (A/cm ^{2})	5.01 x 10^3	6.2 x 10^4
P/V current ratio	41	2.6

Table 3.3 Comparison of the calculated peak voltage and current densities with experimental data.

The calculated peak and valley current densities are also given in Tab. 3.3 with experimental data. Taking consideration of an inevitable uncertainty in layer thickness (interface roughness) the calculated peak current density accords quite well with the experimental data. On the other hand, however, the calculated valley current density is far smaller than that observed in the experiment, and so the resulting P/V current ratio is more than one order of magnitude larger than experimental data. These differences between the calculated and observed valley currents are hardly attributable to the uncertainty of the material parameters used for the calculations and thought to result from a mechanism which has not been taken into account in this global coherent tunnelling theory. The mechanism we have to think of first is LO-phonon scattering which may play an important role even in the present structure because a typical momentum relaxation time of electrons due to the LO-phonon scattering is as short as the tunnelling escape time studied in Sec. 3.2.2. The inelastic LO-phonon scattering is in general expected to have influences both on the *spectrum* (i.e. transmission probability) and *distribution* of electrons. The change expected for the distribution results from frequent energy dissipation processes in the well (sequential tunnelling processes; see Fig. 3.10) and is investigated in Chapter 4 by using dissipative quantum transport theory. Another important effect of the electron-LO-phonon interactions is expected for the transmission probability. Firstly a *real* LO-phonon emission process may open additional resonant tunnelling channel which can be represented by a satellite transmission peak. Secondly a *virtual* LO-phonon emission-absorption process might cause a broadening of the transmission peak by breaking phase-coherence of electron waves under resonant tunnelling partly. These phenomena expected for transmission probability will be discussed in Sec. 3.4 by using a phenomelogical broadening model.

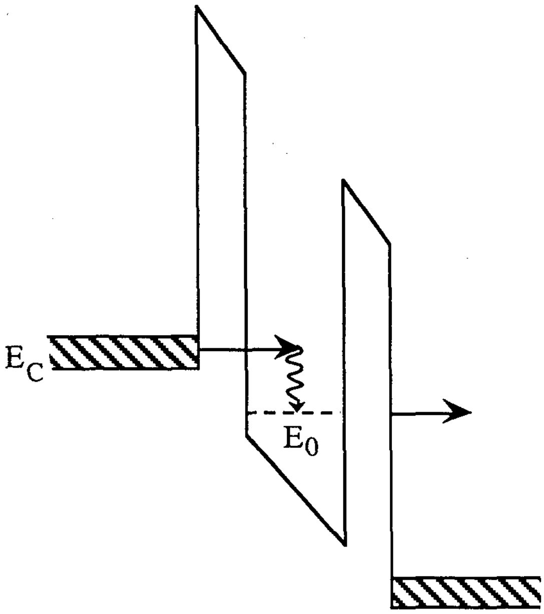

Figure 3.10 Schematic viewgraph of an energy relaxation process (sequential tunnelling) expected in a quantum well.

As shown above the simple global coherent tunnelling theory in general reproduces the characteristics of the double barrier RTDs quite well. The self-consistent calculations can provide the correct peak voltage of the RTDs by taking account of the electron accumulation and depletion regions in the emitter and collector. Also the calculated peak current density at resonance is in accordance with the experimental data. The calculated valley current and hence the P/V current ratio, however, are far from the experimental values. This implies that the completely coherent picture adopted here is not adequate to describe the off-resonance situation.

3.3 Multiple-well resonant tunnelling structures and multi-valued logic applications

In this section some more complicated resonant tunnelling structures than the conventional double barrier structures are studied by using the global coherent tunnelling theory described above. Device structures are here discussed from a viewpoint of their application to multiple valued logic. Several functional devices have been proposed based on the single NDC characteristics of the double barrier resonant tunnelling structures. Alternative way to use the resonant tunnelling diodes may lie in the field of multiple-valued logic which can reduce the number of devices needed for one logic function. For this purpose multiple negative differential conductance is necessary in which all the peak currents are nearly equal (see Fig. 3.11).

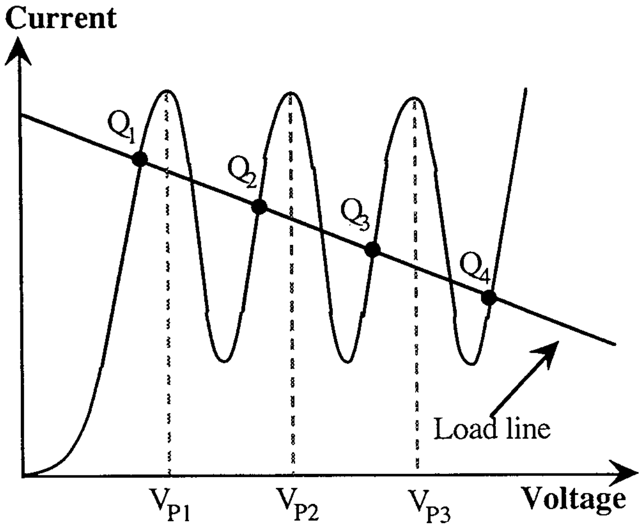

Figure 3.11 *Schematic current-voltage characteristics of a RTD suitable for multiple logic applications. Points Q1, Q2, Q3, Q4 represent stable points of a simple circuit which comprises of a RTD and a load resistance.*

In the case of simple double barrier structures shown in the previous section, the peak currents caused by higher order resonances are significantly larger than that at the first resonance (see Fig. 3.12). This results from the larger resonant widths at higher resonances as well as the increase in the non-resonant excess current under high applied bias conditions. It is, thus, fairly difficult to achieve the multiple NDC required for the multiple logic applications by the use of simple double barrier structures.

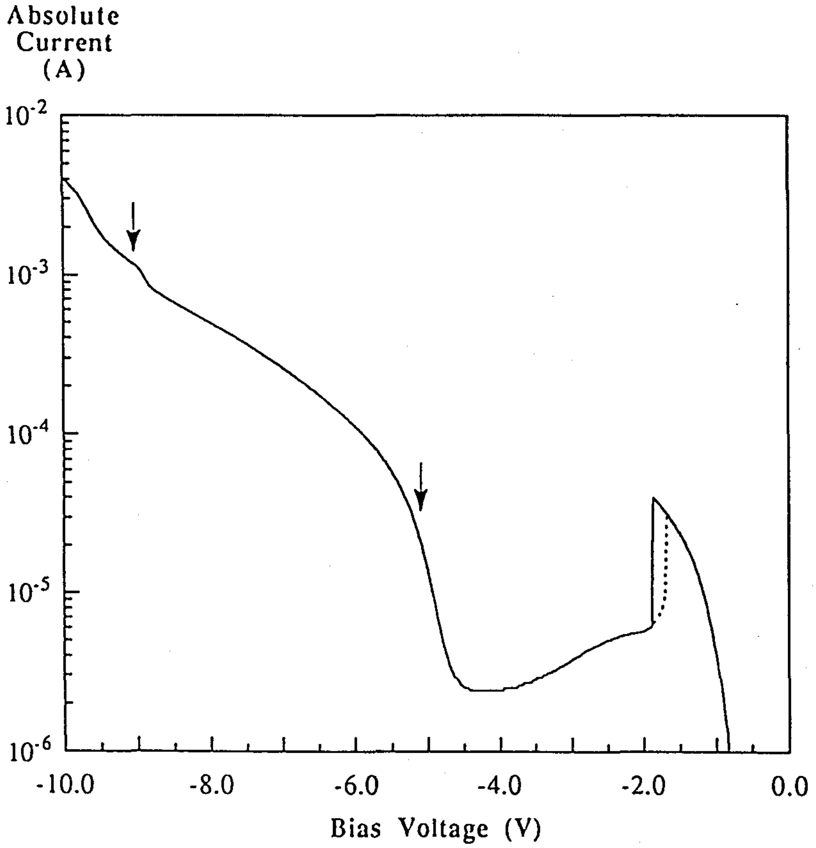

Figure 3.12 I-V characteristics for the AlAs/GaAs/AlAs double barrier RTD Sample 2 (see Chapter 4 for detail) for large applied voltages. Arrows show structures due to higher resonances. A broken line represents tunnelling current observed with decreasing bias which shows current hysteresis in the NDC region with a solid line for increasing bias.

One certain method to overcome the difficulty is to simply integrate several double barrier diodes in parallel or in sequential. These integrated double barrier RTDs provide the same number of equivalent current peaks as the number of integrated diodes. However this integrated RTD may lead to unexpected multi-stability in their current-voltage characteristics which results from heavily doped regions whose electrical potentials are not externally fixed. Unless all the double barrier structures are exactly the same, the system could be switched from one stable state to another with a different current density by a weak external perturbation.

The purpose of the work described in this section is to investigate possible resonant tunnelling structures in which multiple resonances can occur under the global coherent tunnelling picture resulting in the ideal multiple NDC characteristics. First a triple-well (quadruple-barrier) resonant tunnelling diode is examined and applied for triple-valued logic operation. The role of the first quantum well is discussed from viewpoints of its energy filtering effects on the incident electron waves compared with the conventional double barrier structures. Second alternative double-well (triple-barrier) resonant tunnelling structure is studied by using the InGaAs/InAlAs heterostructures which are all lattice-latched to InP substrate and known for their superior transport properties.

3.3.1 An AlGaAs/GaAs triple-well RTD for multiple-valued logic applications

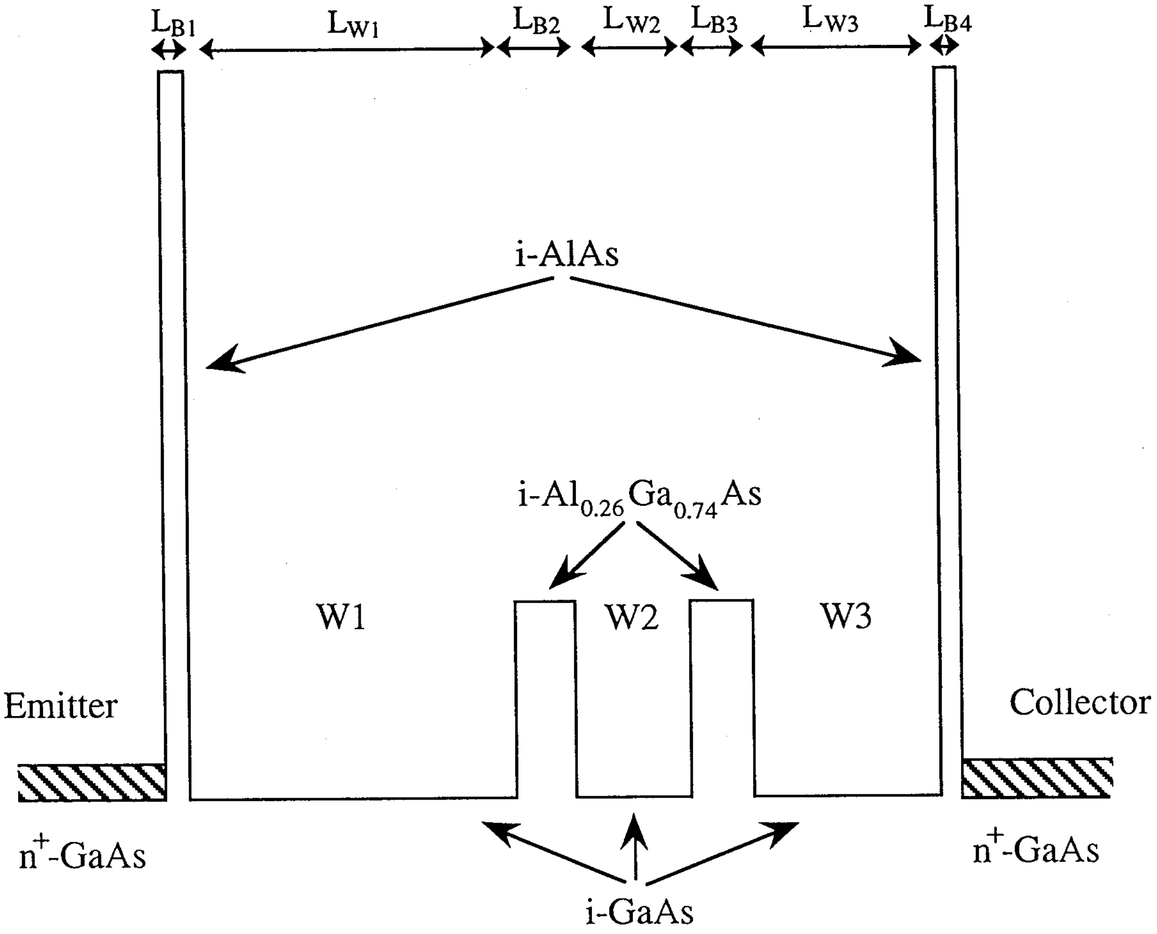

Figure 3.13 Schematic energy-band diagram of the triple-well resonant tunnelling structure

Figure 3.13 shows the band diagram of the newly proposed triple-well RTD [6],[7],[26] which consists of three quantum wells of undoped GaAs (denoted W1, W2, and W3), four barriers (two undoped AlAs and two undoped $Al_{0.26}Ga_{0.74}As$), and highly doped n-type GaAs ($N_D = 1.0 \times 10^{18}$ cm^{-3}) emitter and collector layers on both sides. Structural parameters are listed in Table 3.4.

Layer		Thickness (nm)
i-AlAs	L_{B1}	1.0
i-GaAs	L_{W1}	11.9
i-$Al_{0.26}Ga_{0.74}As$	L_{B2}	3.0
i-GaAs	L_{W2}	5.7
i-$Al_{0.26}Ga_{0.74}As$	L_{B3}	3.0
i-GaAs	L_{W3}	6.9
i-AlAs	L_{B4}	1.0

TABLE 3.4 Structural parameters of the triple-well RTD

The energy band diagram calculated self-consistently (see Sec. 3.2.3) near zero bias (V = 20 mV) is shown in Fig. 3.14(a) as well as the corresponding energy dependence of the transmission probability in Fig. 3.14(b). In Fig. 3.14(a) the existent probability of electrons at quasi-eigenstates is plotted over the energy band diagram. Calculation has been performed for the energy ranging from 0 to the top of the $Al_{0.26}Ga_{0.74}As$ barriers in which seven quasi-eigenstates are found. The electron density distribution, $|\Psi_R(z)|^2$, obtained self-consistently is also shown in Fig. 3.14(c). The three lowest quasi-eigenstates (denoted as Ψ_R^1, Ψ_R^2, and Ψ_R^3 hereafter) are now considered to derive double NDC in the I-V characteristics as described in the following.

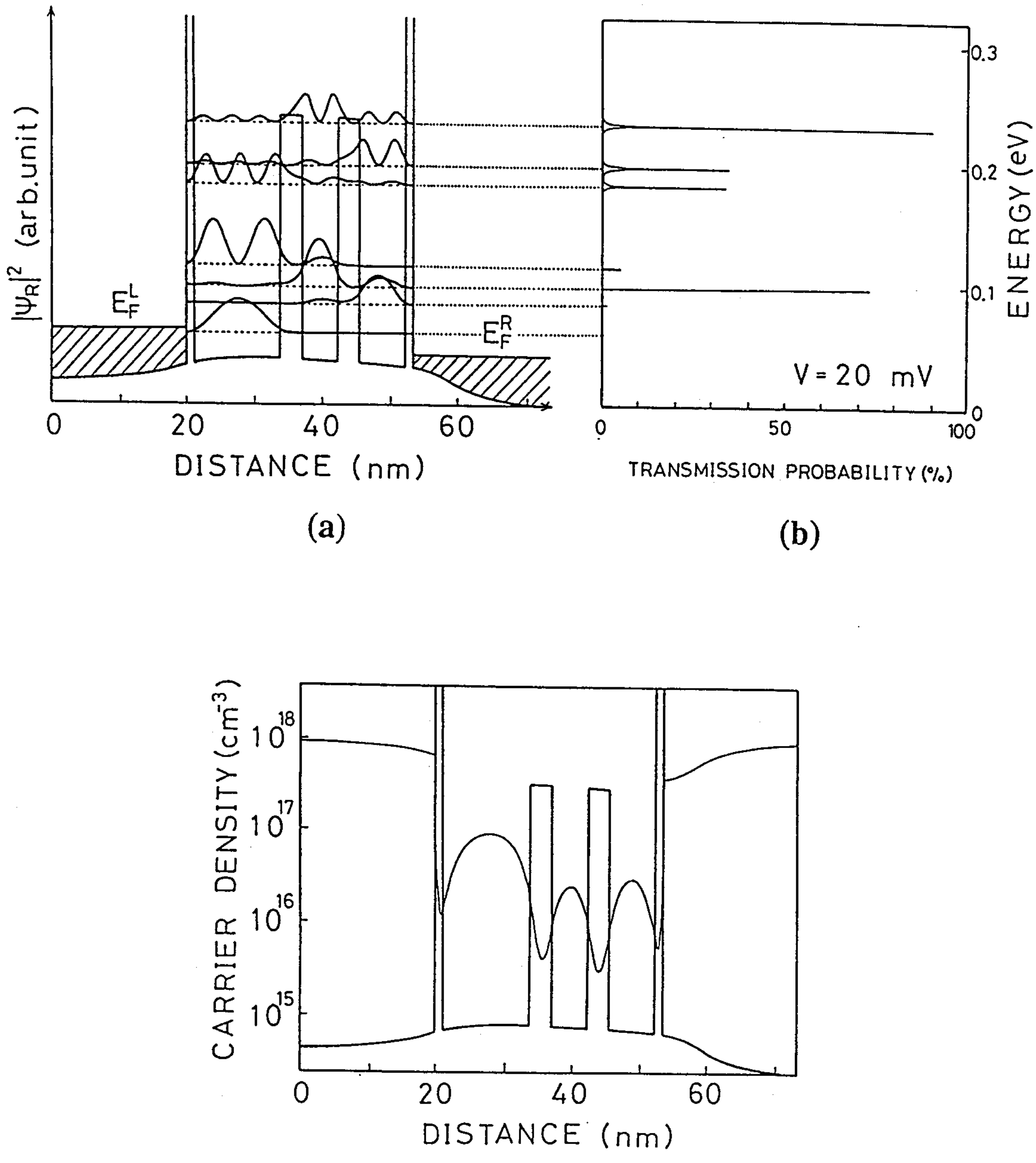

(a)

(b)

(c)

Figure 3.14 The energy-band diagram (a), transmission probability (b), and electron distribution (c) of the triple-well RTD self-consistently calculated at T = 220K near equilibrium.

As shown in Fig 3.14(a), $|\Psi_R^1(z)|^2$, $|\Psi_R^2(z)|^2$, and $|\Psi_R^3(z)|^2$ strongly reflect natures of ground states of the wells W1, W3, and W2, respectively. Consequently, the quasi-eigenenergies E_R^1, E_R^2, and E_R^3 are mostly determined by the well thickness L_{W1}, L_{W3}, and L_{W2}. In this structure the widest well W1 has been designed so that the lowest quasi-eigenstate is located below the quasi-Fermi energy in the emitter and plays as an injection level for incoming electrons. Only when incident electrons have energy close to E_R^1, this state would let them go into the well W1. The peak electron density in W1 is thus higher than those in W2 and W3 in Fig. 3.14(c). The electric field in W1 is largely screened by these accumulated electrons and the bottom of the well W1 is kept virtually flat until the resonances occur under large applied voltages. The width of narrower wells, L_{W2} and L_{W3}, are chosen so that the condition, $E_R^1<E_F^L<E_R^2<E_R^3$, can be satisfied. The transmission probability through this level is very small in equilibrium as is seen in Fig. 3.14(a), but approaches 100 percent when the states Ψ_R^2 or Ψ_R^3 just resonates with the injection level Ψ_R^1 under an larger applied bias. Therefore, current peak widths in the I-V characteristics would be very small, and valley currents are expected to be greatly decreased.

The current-voltage characteristics have been calculated by using the self-consistently obtained $T(E_Z)$ and Eq. (3.7). Figure 3.15 shows the I-V curve calculated at 220 K where nearly equal double current peaks are experimentally observed as shown later. The characteristics with double NDC could have three stable points with an appropriate load resistance as the valley current at the second off-resonance is smaller than the first peak current.

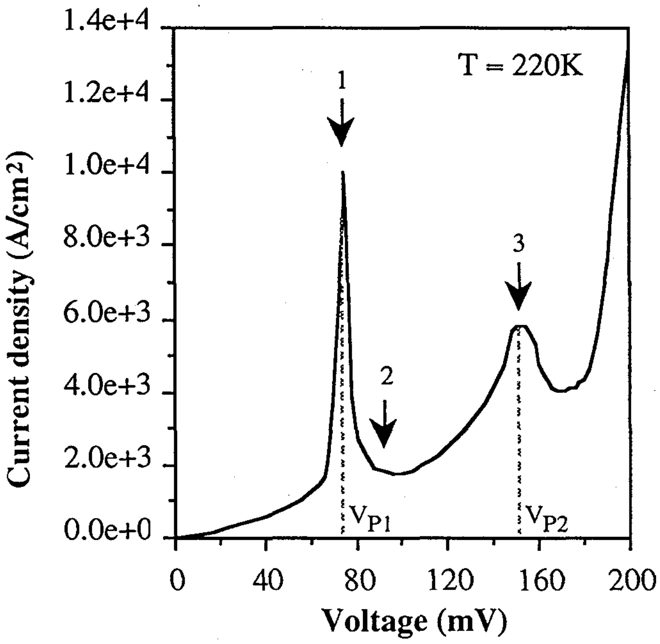

Figure 3.15 Calculated current-voltage characteristics of the triple-well RTD self-consistently calculated at 220K. Three typical states are pointed out by using arrows: an arrow 1 for the first current peak, 2 for the current valley, and 3 for the second current peak.

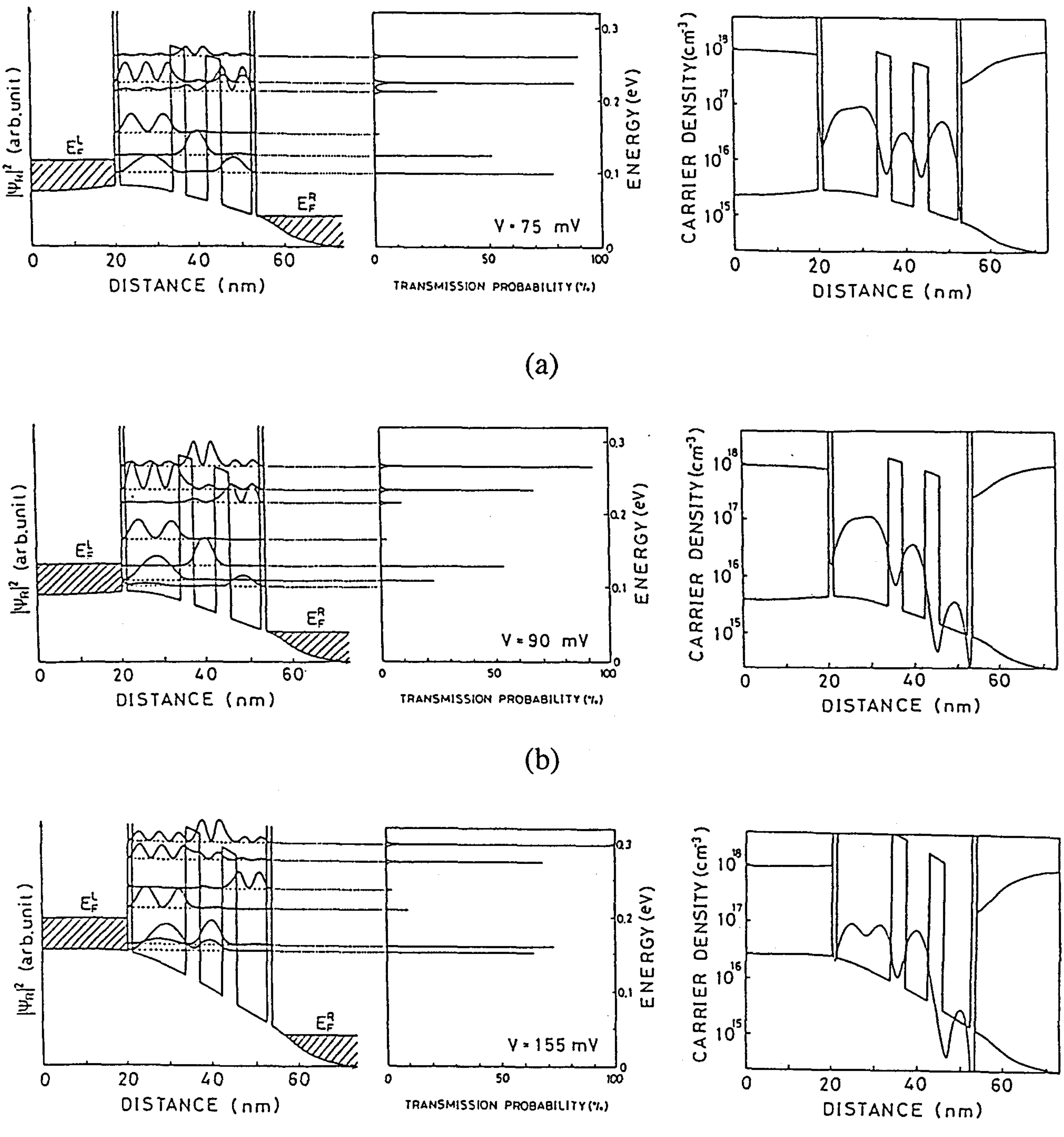

(a)

(b)

(c)

Figure 3.16 The energy-band diagram (left), transmission probability (centre), and electron distribution (rigft) of the triple-well RTD self-consistently calculated at the first resonance (a), the first valley (b), and the second resonance (c).

The first and second current peaks results from resonances of Ψ_R^2 and Ψ_R^3 with Ψ_R^1. Energy band diagrams, transmission probabilities, and electron density distributions are shown in Figs.

3.16(a) - (c) at three different states indicated by the arrows in Fig. 3.15: at the first resonance (Fig. 3.16(a)), at the off-resonance (Fig. 3.16(b)), and the second resonance (Fig. 3.16(c)). Therefore , two peak voltages V_{P1} and V_{P2} (see Fig. 3.15) are determined by the eigen-energy separations $E_R^2 - E_R^1$ and $E_R^3 - E_R^1$, respectively. Thus, two peak voltages can be independently altered with the well thickness L_{W3} and L_{W2} as shown in Figs. 3.17(a) and 3.17(b). These figures are the L_{W3} dependence of V_{P1} and V_{P2} (Fig. 3.17(a)) and the L_{W2} dependence of them (Fig. 3.17(b)). It is clearly seen that V_{P1} can be controlled through L_{W3} without changing V_{P2}, and similarly V_{P2} through L_{W2}. Such an independent controllability of V_{P1} and V_{P2} is a special feature of this triple-well RTD.

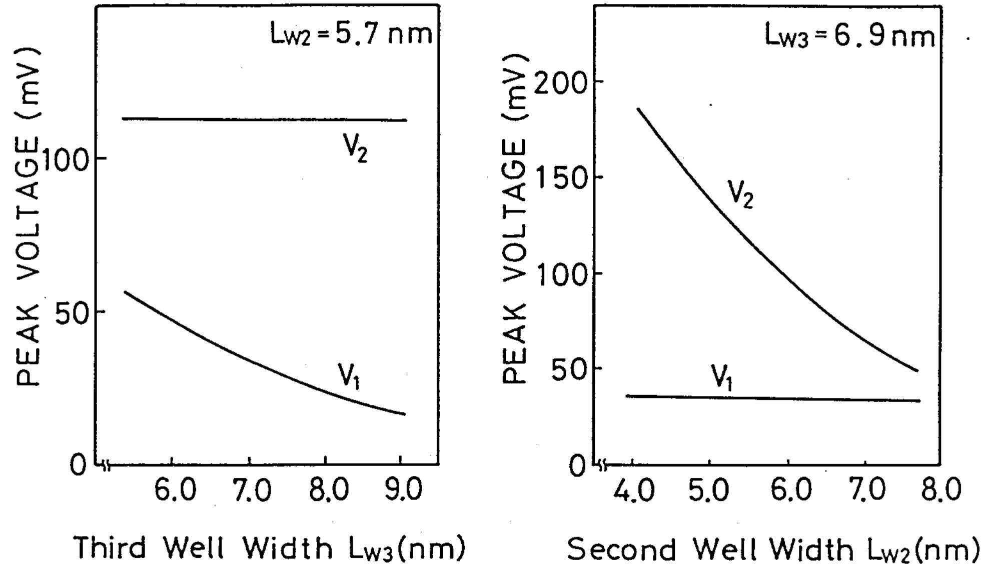

(a) (b)

Figure 3.17 Peak voltages versus quantum well widths: (a) L_{W3} dependence of the peak voltage V_{P1} and V_{P2} and (b) L_{W2} dependence of them.

Based on the numerical calculations, a triple-well RTD has been fabricated [6]. Figure 3.18 shows a cross sectional view of the device. On a Si-doped (100) GaAs substrate, a 500-nm Si-doped (1.0×10^{18} cm^{-3}) GaAs buffer layer, a 10-nm-thick undoped GaAs offset layer, a triple-well structure listed in Table 3.2, and finally, a 300-nm-thick Si-doped (1.0×10^{18} cm^{-3}) GaAs layer were successively grown. All the layers in a triple-well structure are unintentionally doped (typically p-type with a hole concentration of 1.0×10^{14} cm^{-3}). Growth was interrupted for 3 min at each interface between different materials. The offset layer introduced under the barriers is to avoid diffusion of ionized Si ions from n$^+$-GaAs collector region into the intrinsic region which would cause the impurity scattering in the quantum well. The wafer was processed by conventional photolithography and wet chemical etching to define device area, followed by a deposition of AuGe alloy, lifting off, and sintering at 400 C for 2 min in N2 gas ambient to form ohmic contacts. Devices with various sizes of top contact pad ranging from 4 × 4 μm^2 to 100 × 100 μm^2.

The current-voltage characteristics measured at 220 K and 300 K are shown in Figs. 3.19(a) and (b). The characteristics have quite a large temperature dependence as we discuss later, and at 220K two peak currents are nearly the same for this device. It can be seen that the device exhibits a significant double NDC and the characteristics at 220 K can be used for triple-value logic applications.

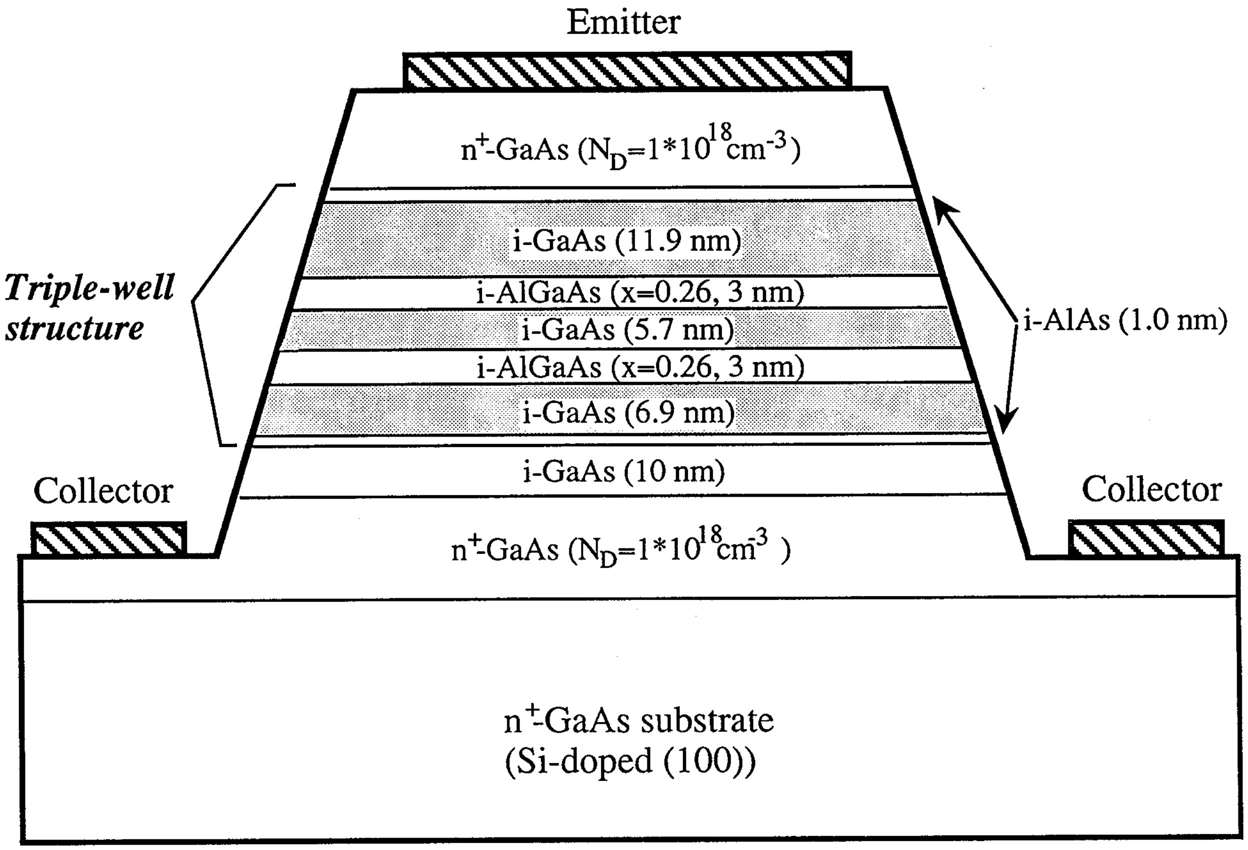

Figure 3.18 Schematic cross sectional view of a fabricated triple-well RTD. Shaded regions represent three quantum wells.

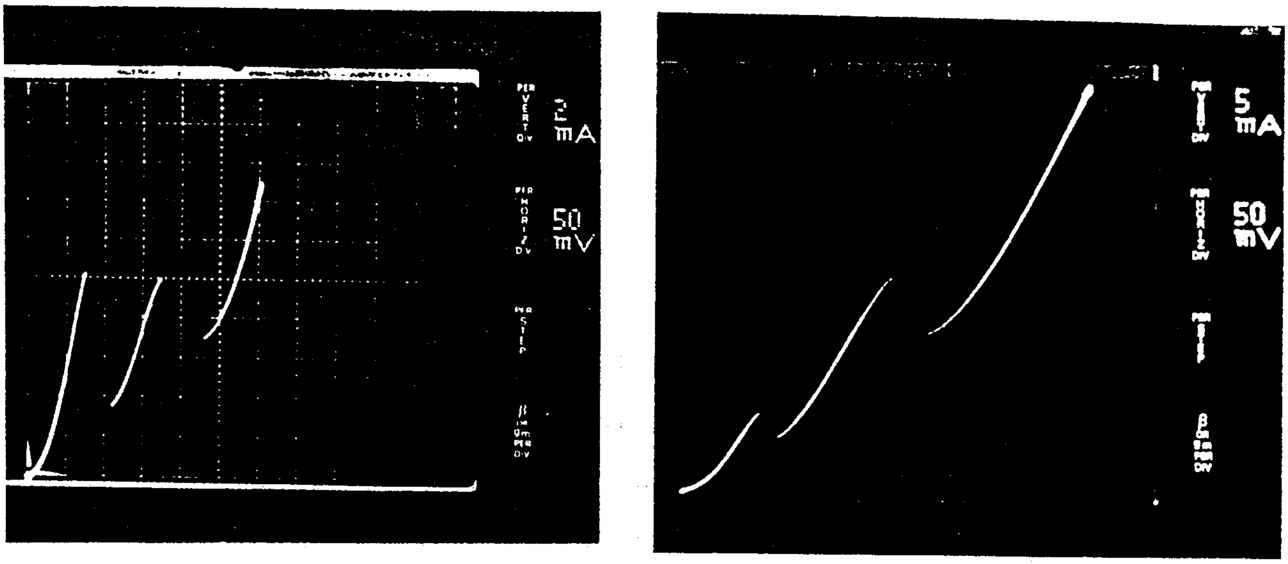

(a)

(b)

Figure 3.19 Current-voltage characteristics of a triple-well RTD exhibiting significant double NDC measured (a) at 220K and (b) at room temperature. Data (a) were taken from a sample with a mesa area of 100 μm x 100 μm and (b) from that of 75 μm x 100 μm.

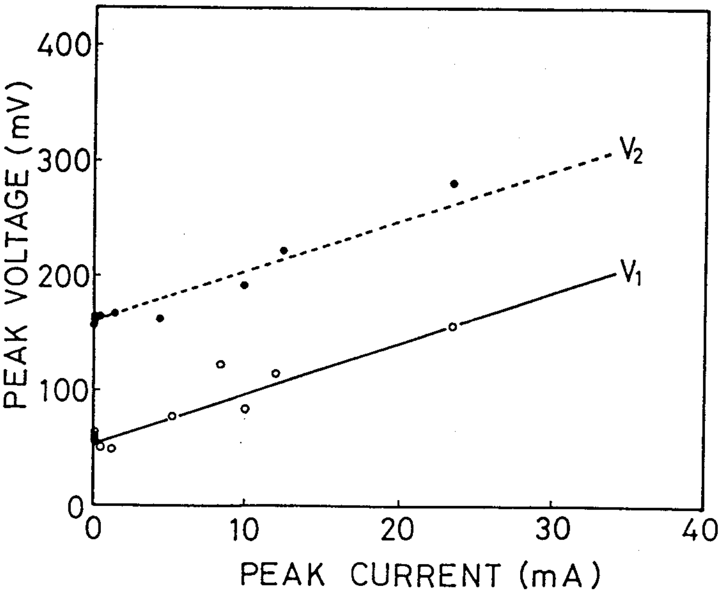

Figure 3.20 Dependence of two peak voltages on peak currents experimentally taken from devices with various sizes.

	Calculated	Observed
First peak voltage V_{P1}(mV)	74	60
Second peak voltage V_{P2}(mV)	152	160

***Table 3.5** Calculated and observed peak voltages V_{P1} and V_P*

The peak current dependences of two peak voltages extracted from devices with various areas are shown in Fig. 3.20: both are found to depend almost linearly on the current through a resistance of approximately 4 Ω which is supposed to be induced by the external measurement system and in series with the device. Intrinsic values of the peak voltages are extracted from the values at the intersections of V_{P1} and V_{P2} with the vertical axis ($I_P = 0$). These intrinsic peak voltages are listed in Table 3.5. The measured peak voltages are both in a good agreement with those obtained from the calculations despite a large voltage drop in the spacer region. This fact indicates that the present self-consistent modelling reproduces the overall band diagram quite well over a whole range of the applied bias.

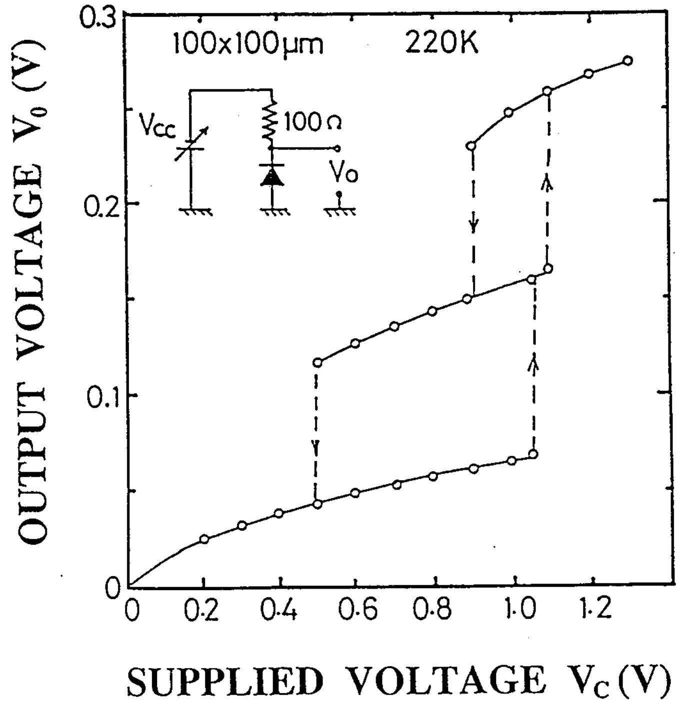

***Figure 3.21** Input-output characteristics of a simple circuit which consists of triple-well RTD and a load resistance of 100 W (see inset) measured at 220K. Three stable points are seen at 0.054, 0.155, and 0.25 V.*

By using the fabricated device with an area of 100 × 100 μm^2 a simple circuit has been designed with a load resistance of 100 Ω (see inset of Fig. 3.21). Input-output characteristics of this circuit is shown in Fig. 3. 21 in which three stable states are successfully observed at 0.065, 0.155, and 0.250 V when an input bias of 100 V is applied to the circuit. Since the second current decreases with a further decrease in temperature, the tri-stable operation can be observed only in the range from 230 K down to 180 K.

Before closing this section the temperature dependence of the second peak current is analyzed as this limits the temperature range of the device operation. As seen in Fig. 3.19 the second peak current has a strong temperature dependence: the I-V curves measured at various temperatures are shown in Fig. 3.22.

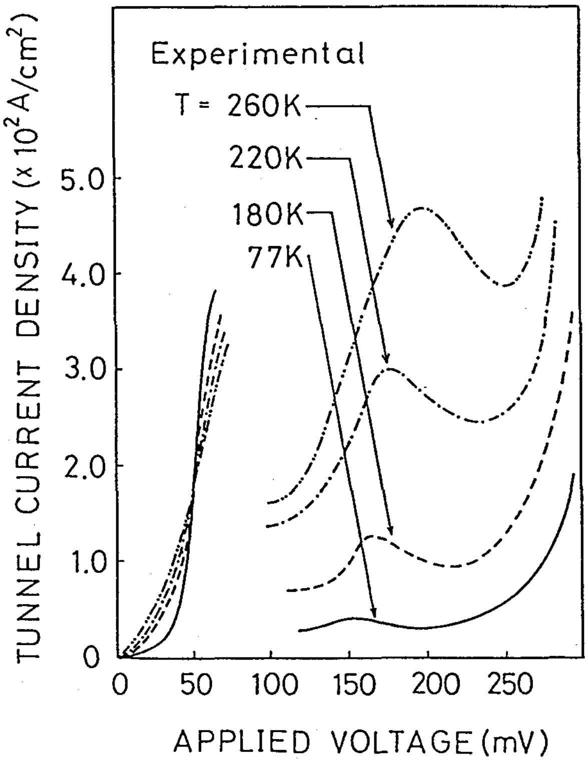

Figure 3.22 Current-voltage characteristics of the fabricated triple-well RTD measured at various temperatures.

To make clear the mechanism of this temperature dependence the second resonance state has been investigated in some detail. As we have seen, under relatively low bias conditions, the bottom of the injection well W1 is kept fairly flat and the lowest quasi-eigenstate can play as an injection level. This self-consistent field effect on the whole potential distribution continues until charge accumulation in other wells becomes comparable with that in W1. Approaching the second resonance (see Fig. 3.18), however, such locally enhanced screening is no longer effective since almost the same amount of electrons are accumulated in W2. The voltage drop, thus, occurs almost linearly over the whole structure resulting in a shift of the injection level Ψ_R^1 towards lower energy. It should be noted that the injection level Ψ_R^1 is located at an energy fairly close to the conduction band edge in the emitter region in Fig. 3.18(a). Let's take a look at the temperature dependence of this level. Figure 3.23(a) and (b) show the energy band diagrams and electron distributions calculated at 300 K (solid lines) and at 77 K (dashed lines). It can be seen that Ψ_R^1 at 77K is located below the conduction band edge in the emitter while that at 300K stays above it. Namely, Ψ_R^1 at 77K is not a scattering state but a half-bound state and no longer acts as an injection level for electrons from the emitter region.

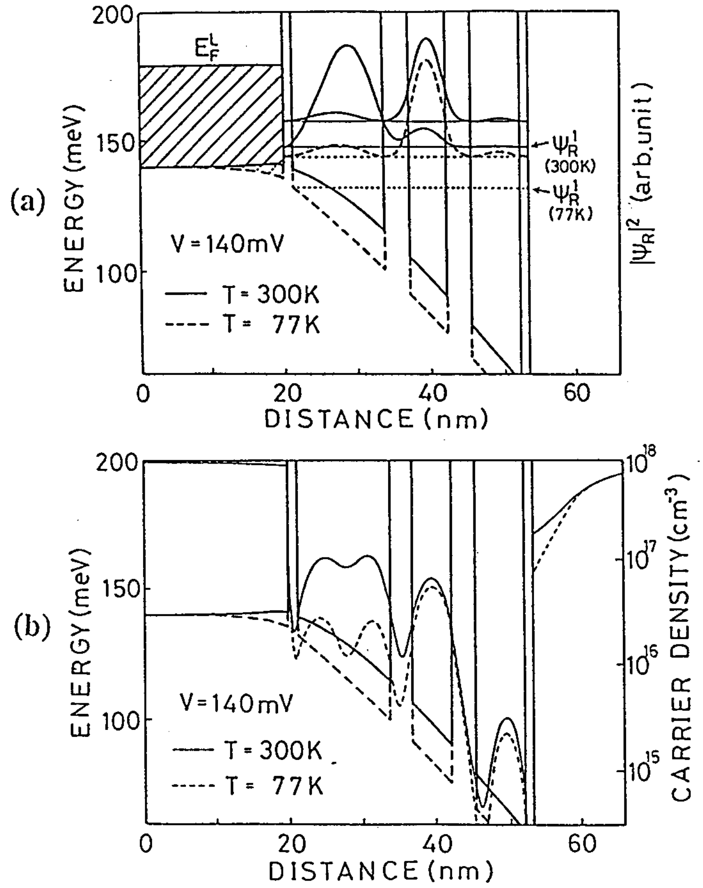

Figure 3.23 (a) The energy-band diagrams and (b) electron distributions calculated at 77K (dashed line) and 300K (solid line) calculated at the second resonance.

As a result of disappearance of the injection level the second peak current has the large temperature dependence as shown in Fig. 3.24 which agree qualitatively with the experimental results. These calculated results have been obtained under the global coherent tunnelling picture and may be affected by inclusion of dissipation process in the well which we discuss in the next chapter: a sequential tunnelling process could occur in the present structure in which electrons tunnel into the first excited state of W1, Ψ_R^4, then relaxed to Ψ_R^1, and finally tunnel out. As shown in Fig. 3. 16(c), however, Ψ_R^4 at the second resonance is still located above the quasi-Fermi level in the emitter region, and the tunnelling current due to this sequential process is supposed to be relatively small.

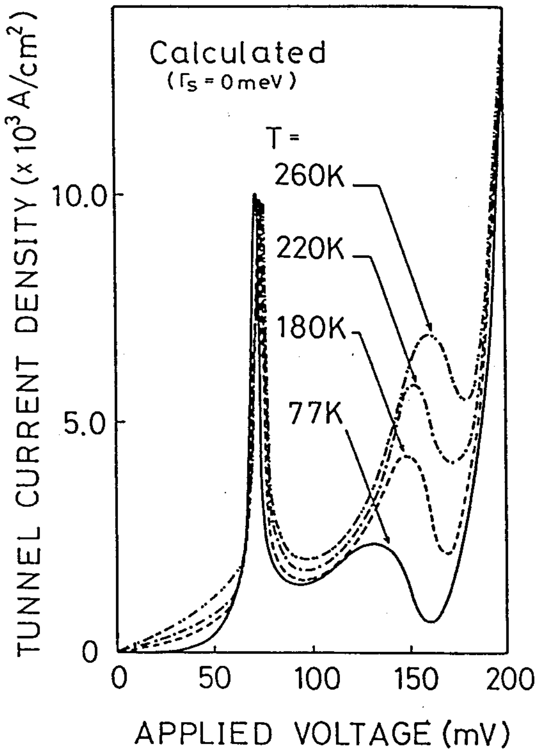

Figure 3.24 Current-voltage characteristics of the triple-well RTD calculated at various temperatures

3.3.2 An InGaAs/InAlAs double-well resonant tunnelling diode

As shown in the previous section a RTD with good P/V current ratios at all resonances is in general required for its multiple-valued logic applications. The P/V ratios obtained from the AlGaAs/GaAs triple-well RTD are much smaller than those calculated by using the global coherent tunnelling theory: the difference is attributable to the effects of phase-coherence breaking scattering which have been neglected so far. These results firstly indicate that other materials with better transport properties are favourable rather than conventional AlGaAs/GaAs systems. An InGaAs/InAlAs system grown on InP under a lattice-matching condition has been found to have an excellent transport characteristics: high electron mobility has been found in a HEMT based on this system as well as high saturation velocity. This superior transport properties are basically attributed to its different energy-band structure of L and X valleys which are located at much higher energies above the conduction band edge at the Γ point and so electron intervalley scattering is greatly reduced. It has been already demonstrated that an InAlAs/InGaAs/InAlAs double barrier RTD exhibits a superior P/V current ratio: these results are basically consistent with the good transport properties of the system.

The results in the previous sections secondly imply that a simpler (or we should say thinner) resonant tunnelling structures are much preferred for the purpose of preventing the phase-coherence breaking scattering. Thicker resonant tunnelling barriers generally result in a longer tunnelling escape time, and electrons bound in the structure are tend to suffer from the scattering more frequently. Therefore, a simpler double-well structure than the triple-well structure should be examined for the present purpose though two peak voltages can not be altered separately like the triple-well RTD.

A double-well resonant tunnelling structure has been already studied by Nakagawa et al [5] by using an AlGaAs/GaAs system. Their double-well structure is shown in Fig. 3.25: two equivalent quantum well are placed on the emitter side of a thick AlGaAs barrier.

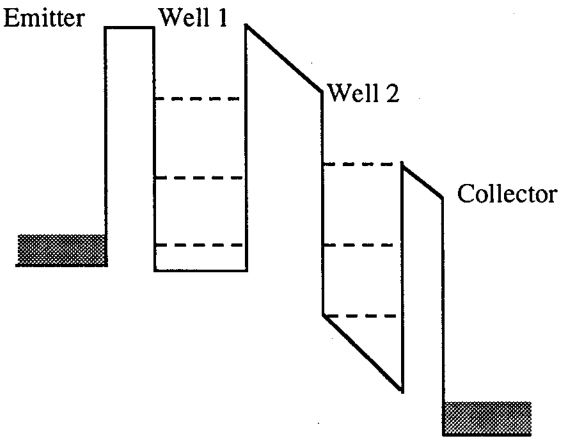

Figure 3.25 Energy-band diagram of a conventional double-well RTD proposed by Nakagawa et al. [5].

Observed multiple NDC characteristics were attributed to the resonances of quasi-eigenstates of the second narrower well with the lowest quasi-eigenstates of the first wider well (the injection level). Excellent P/V current ratios achieved in this device result from the energy filter function of the injection level for the incoming electron waves as explained in the previous section. Despite the good P/V ratios, however, peak currents due to higher resonances are more than one order of magnitude larger than that at the first resonance: the NDC characteristics are not suitable for the present purpose. It seems that nearly uniform peak current densities required for multiple valued logic applications are hardly achievable in this sort of simple structures.

To overcome this problem we have proposed the following new double well structure shown in Table 3.6.

Layer		Thickness (nm)
i-$In_{0.53}Ga_{0.47}As$	L_{SPACER}	10.0
i-$In_{0.52}Al_{0.48}As$	L_{B1}	2.5
i-$In_{0.53}Ga_{0.47}As$	L_{W1}	5.0
i-$In_{0.52}Al_{0.48}As$	L_{B2}	5.0
i-$In_{0.53}Ga_{0.47}As$	L_{W2}	15.0
i-$In_{0.52}Al_{0.48}As$	L_{B3}	2.5

***Table 3.6** A layer structure of the InGaAs/InAlAs double-well RTD*

1. Electron effective mass m* $m^*(In_{0.53}Ga_{0.47}As) = 0.044\ m_0$ $m^*(In_{0.52}Al_{0.48}As) = 0.084\ m_0$
2. Couduction band discontinuity ΔEc $\Delta Ec = \beta\ (E_g^{\Gamma}(In_{0.52}Al_{0.48}As) - E_g^{\Gamma}(In_{0.53}Ga_{0.47}As))$ $E_g^{\Gamma}(In_{0.53}Ga_{0.47}As) = 0.71\ eV$ $E_g^{\Gamma}(In_{0.52}Al_{0.48}As) = 1.51\ eV$ Band parameter $\beta = 0.667$
3. Dielectric constant ε $\varepsilon(In_{0.53}Ga_{0.47}As) = 13.9$ $\varepsilon(In_{0.52}Al_{0.48}As) = 12.45$

***Table 3.7** Material parameters of InP lattice-matched InGaAs/InAlAs heterostructures*

The structure is different from previously reported ones in the following points: first, the thickness ratio between two quantum wells is three which is much larger than the previous one, and second, the thinner quantum well (denoted as W1) is placed on the emitter side and used as an injection well (a wider well is denoted as W2 in the same way as in the previous section). The principle of operation and the advantages of this structure in realizing high peak current density and uniform NDC peaks are described in the following.

The large thickness ratio between two quantum wells leads to a large difference between the lowest quasi-eigenenergies of two quantum wells; consequently, resonances are expected to take place between the ground state of W1 and highly excited states of W2. The energy band diagram and associated quasi-eiegenstates are shown in Fig. 3.26.

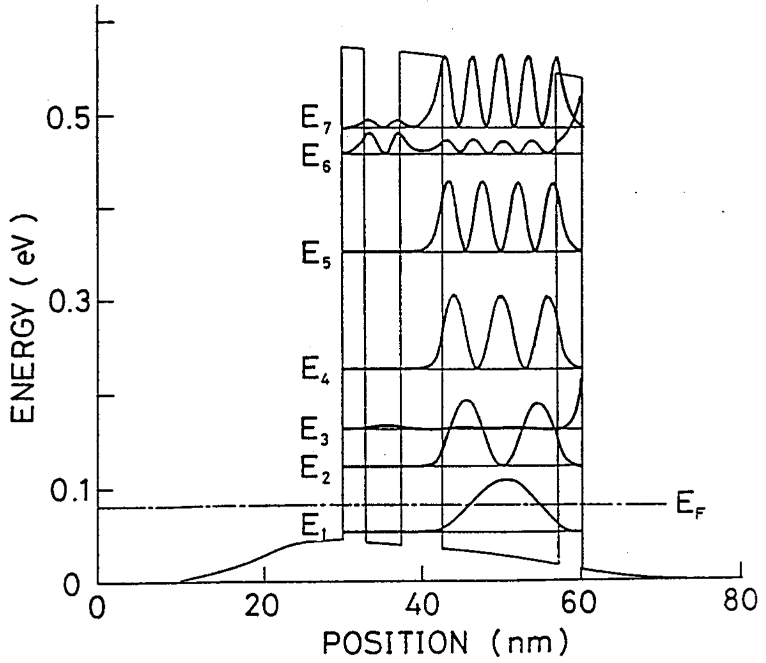

Figure 3.26 Energy band-diagram and asociated quasi-eigenstates of an InGaAs/ InAlAs double-well RTD calculated at zero bias.

As the quasi-eigenstates displayed in this figure is those calculated for an incident wave from the collector side, it may be a bit difficult to see the quasi-eigenstates of W1: the states indicated by E_3 and E_6 are the lowest and first excited quasi-bound states of W1. As seen in this figure, resonances of the second, third, and fourth excited states of W2 (E_4, E_5, and E_7) with the injection level E_3 would lead to multiple NDC in the I-V characteristics. The use of the excited states would provide high peak current densities as well as good P/V ratios which are attributed to less scattering events in the present InGaAs/InAlAs system than the conventional AlGaAs/GaAs systems.

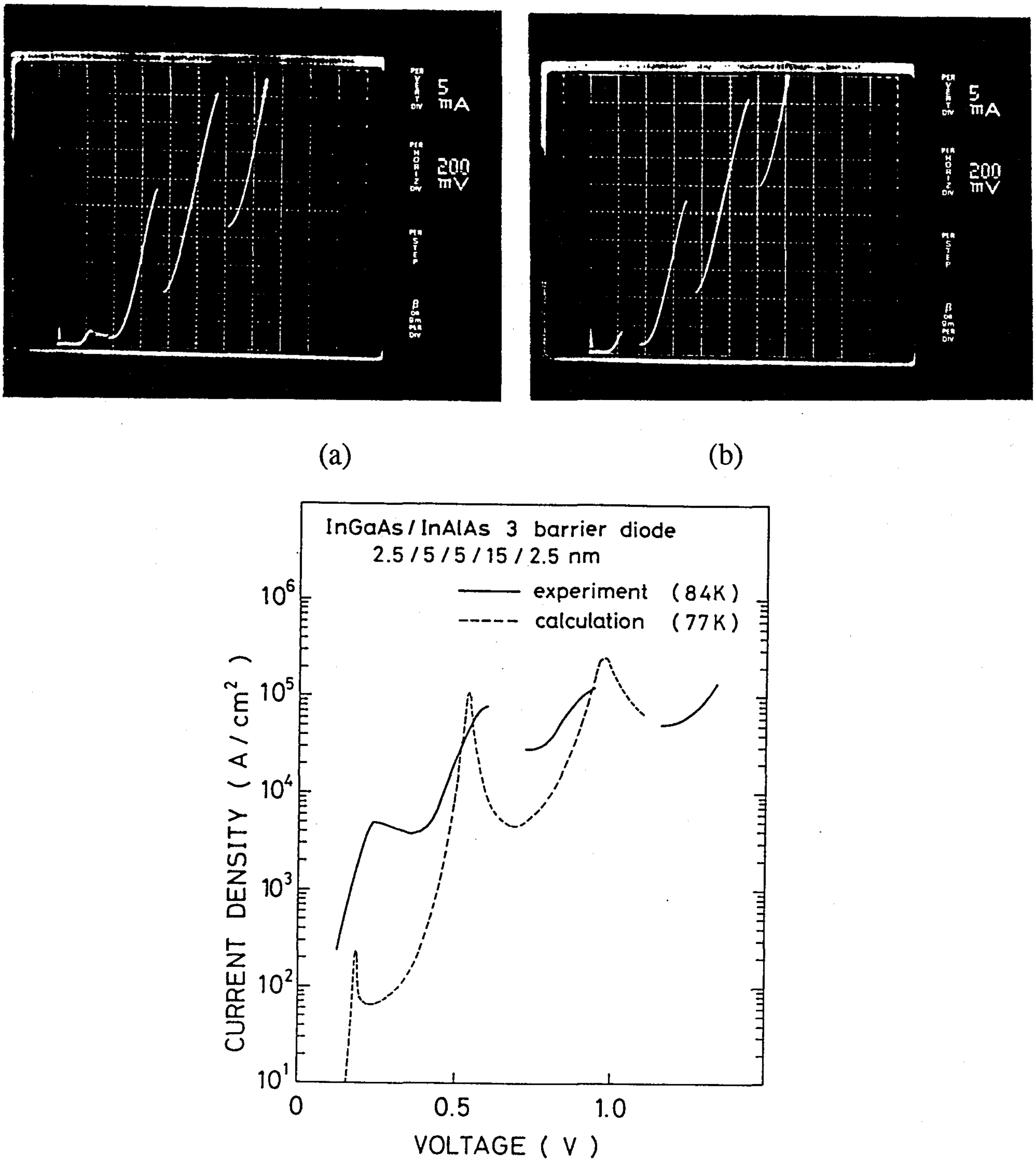

(a) (b)

(c)

Figure 3.27 Current-voltage characteristics of a InAlAs/InGaAs double-well RTD with a masa area of 6 mm x 6 mm measured at (a) 127K and (b) 179K. (c) shows the self-consistently calculated I-V curve with the experimental data.

An InGaAs/InAlAs double well structure described in Table 3.6 was grown on an semi-insulating InP substrate by MBE with a 2 min growth interrupt at each interfaces. The layers were all lattice matched to the substrate. The grown wafer was processesd into a mesa structure. Then Mo/Au non-alloyed ohmic electrode was formed on the top and the bottom layers. The I-V characteristics of the diode with 6 × 6 μm^2 in size measured at 84K is shown in Fig. 3.26. Three current peaks have been clearly observed with respective P/V ratios of 1.3, 2.9, and 2.1. The differences among the peak currents are much smaller than those of the AlGaAs/GaAs triple-well RTD as is expected. Furthermore, the second and third peak and valley currents satisfy the condition required for triple-value memory operation.

Self-consistently calculated I-V characteristics of the device is shown in Fig. 3.27 along with the experimental data. The overall agreement between them is again very good for peak voltages. It should be pointed out again that the excellect agreement between all the calculated and observed peak voltages confirmes that the self-consistent modelling can reproduce the potential distribution very well. Relatively good agreement has been seen also for peak currents, but the observed current peaks have turned out to be much broader than the calculated ones as we have seen in the previous section. Consequently, the observed valley currents are higher than those in the calculations. From temperature dependence of the valley currents, we would expect that LO-phonon scattering at least partly contributes to the broadening of the peaks as mentioned earlier.

Finally it is worth noting that, at the third resonance, the top of the third barrier adjacent to the collector goes down below the resonant level E_7 as shown in Fig. 3.28. The third resonance is not a resonance between two quasi-bound states as the first or second one. Instead, it is a resonance of an virtually bound (or interference) state E_7 with a quasi-bound state E_3. At this resonance, electrons tunnel through only first two barriers and, thus, tunnelling current could be much larger than those at the first or second resonances. Nevertheless, the peak current is just twice as large as the second one. This may be attributable to the use of an injection level; the injection level functions as an energy collimater as discussed before and limits the total number of electrons tunnelling through the structure. As it is desirable to have such multiple NDC characteristics, this limiting effect of the injection well on the tunnelling current is supposed to be crucial in designing RTDs for multiple-valued logic applications.

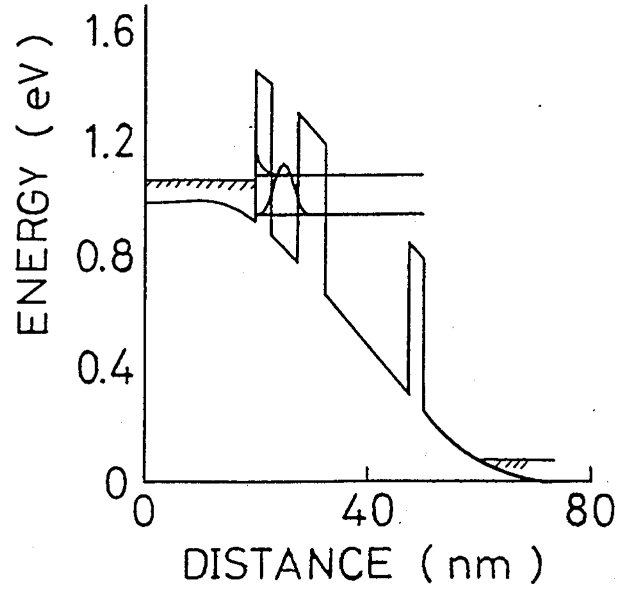

Figure 3.28 Energy band-diagram calculated at third resonance of the InGaAs/InAlAs double-well RTD.

3.4 Effects of scattering process on global coherent tunnelling

Up to now we have assumed that electrons do not experience any scattering process while they tunnel through double barriers and conserve energy and lateral momentum. This assumption has led to the picture of the global coherent tunnelling which is analogous to the resonant transmission of light through a Fabry-Perot etalon. It has been shown in the last section that the electrons are confined in the quantum well for a certain time, the intrinsic life time of the quasi-bound state τ_{esc} , which is determined by the strength of the electron transfer through the single barrier and then escape into the collector region. In a realistic situation, however, this is not necessarily a proper assumption because the tunnelling electrons in general interact with phonons, impurities, and even electrons each other. As explained in Sec. 3.2, complete transparency of the double barriers is achieved for an incident electron wave at resonance when backward electron waves with different phases which results from multiple reflections from the double barriers cancel out each other. The scattering process which is not only inelastic but also elastic apparently breaks the cancellation of the backwards waves and thus makes the resonant tunnelling partly *incoherent* [27]-[30].

We have already seen that the global coherent tunnelling theory always underestimates the valley current at off-resonance. The effects of the scattering events in RTDs on the valley currents have been discussed by many groups and some aspects of them have been made clear through experimental and theoretical investigations. In this section the effects of these scattering processes on the transmission probability, i.e. spectrum, are discussed. Another important effect on the electron distribution is investigated in the next chapter.

The most striking effect of the LO-phonon scattering process is the *LO-phonon assisted resonant tunnelling* [31],[33] (see Fig. 3.29(a)). Resonant tunnelling electrons emit a single LO-phonon during tunnelling. This tunnelling process leads to a replica peak in the valley current regime which is observable at low temperatures. A typical example of the characteristics is shown in Fig. 3.29(b). A low broad peak seen at about V is attributed to the LO-phonon assisted resonant tunnelling.

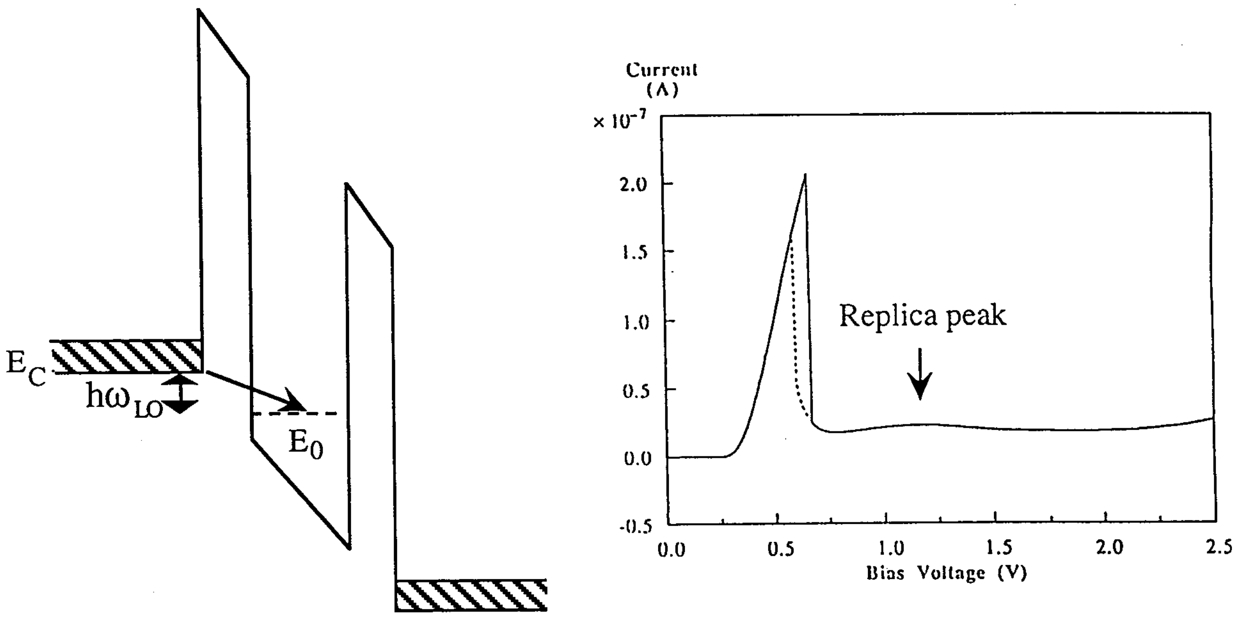

(a) (b)

Figure 3.29 *(a) The LO-phonon emission assisted resonant tunnelling process. (b) I-V characteristics of an AlAs/GaAs/AlAs double barrier RTD (Material 3; see Sec. 4.1 for detail) measured at 4.2K. A shallow broad peak after the main resonance is caused by the LO-phonon emission assisted tunnelling. Data taken by C Goodings, Microelectronics research centre, University of Cambridge, in collaboration with the author.*

Magnetotunnelling measurement (see Sec. 4.1) on this Material has revealed that the replica peak includes contributions of both GaAs-type phonon (37 meV) and an AlAs-type phonon (50 meV). This inelastic resonant tunnelling process can be still described within a framework of transmission probability though lateral momentum is no longer conserved in these processes: The transmission probability is then expressed as functions of both E_z and $k_{//}$ [35]. It has been shown that this process results in a satellite peak of the transmission probability found at a higher energy than the main resonant tunnelling peak .

Another important effect of the scattering is the *scattering induced broadening* of the transmission peaks: This is indeed more vital to achieve large P/V current ratios. The scattering broadening is a common phenomenon for various kinds of scattering processes which is attributed to the electron self-energy induced by multiple scattering events in the quantum well. Fertig et al [33],[34] performed numerical calculations of the total tunnelling current at zero temperature by using a microscopic perturbation theory and finally found that the results are in good agreement with those calculated by using the phenomelogical Breit-Wigner formula with an *impurity-scattering-induced broadening* parameter Γ_{im}. The *LO-phonon-scattering induced broadening* has been also theoretically reported by [35] as well as other scattering assisted processes explained above. These results indicate that the scattering broadening can be easily taken into consideration by using the extended Breit-Wigner type formulation of the transmission probability though the detailed mechanisms are quite different.

The phenomelogical broadening model may be incorporated with the transfer matrix theory described in Sec. 3.2 in the following way. As shown in Fig. 3.30 the multiple-well resonant tunnelling structures are divided into N-regions denoted as $T_1, T_2, T_3, \cdots\cdots, T_N$ in which well-localized quasi-eigenstates are defined. Introducing scattering broadening widths, Γ_{S1}, $\Gamma_{S2}, \Gamma_{S3}, \cdots\cdots, \Gamma_{SN}$, in these regions, the total transmission probability may be expressed as follows:

$$T(E_z) = \frac{m^{*L}}{m^{*R}}\frac{k^R}{k^L}\int_0^\infty \frac{\left|\Psi_T^1(E_z^1)\right|^2}{\left|\Psi_T^L(E_z^1)\right|^2}\frac{\Gamma_{S1}/\pi}{(E_z^1 - E_z)^2 + {\Gamma_{S1}}^2}\,dE_z^1 \cdot \int_0^\infty \frac{\left|\Psi_T^2(E_z^2)\right|^2}{\left|\Psi_T^1(E_z^2)\right|^2}\frac{\Gamma_{S2}/\pi}{(E_z^2 - E_z^1)^2 + {\Gamma_{S2}}^2}\,dE_z^2$$

$$\cdot \int_0^\infty \frac{\left|\Psi_T^3(E_z^3)\right|^2}{\left|\Psi_T^2(E_z^3)\right|^2}\frac{\Gamma_{S3}/\pi}{(E_z^3 - E_z^2)^2 + {\Gamma_{S3}}^2}\,dE_z^3 \quad \cdots\cdots\cdots\cdots\cdots\cdots\cdots\cdots\cdots\cdots$$

$$\cdot \int_0^\infty \frac{\left|\Psi_T^R(E_z^N)\right|^2}{\left|\Psi_T^{N-1}(E_z^N)\right|^2}\frac{\Gamma_{SN}/\pi}{(E_z^N - E_z^{N-1})^2 + {\Gamma_{SN}}^2}\,dE_z^N \qquad (3.30)$$

where $|\Psi_T^i|$ represents the amplitude of the going electron wave transmitted through the region T_i. It should be noted that Eq. (3.30) reduces to Eq. (3.18) when all the scattering broadening goes to zero as the Lorentzian functions are replaced by delta functions.

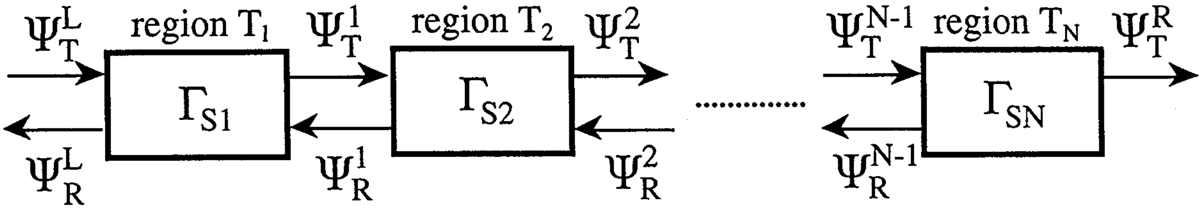

***Figure 3.30** A scattering broadening model for multi-barrier resonant tunnelling structures.*

Equation (3.30) has been applied to the triple-well RTD (see Sec. 3.3.2) by dividing the structure into three regions, obviously the quantum wells W1, W2, and W3. For simplicity, a common broadening width, Γ_S, is assumed for all the wells neglecting its energy dependence.

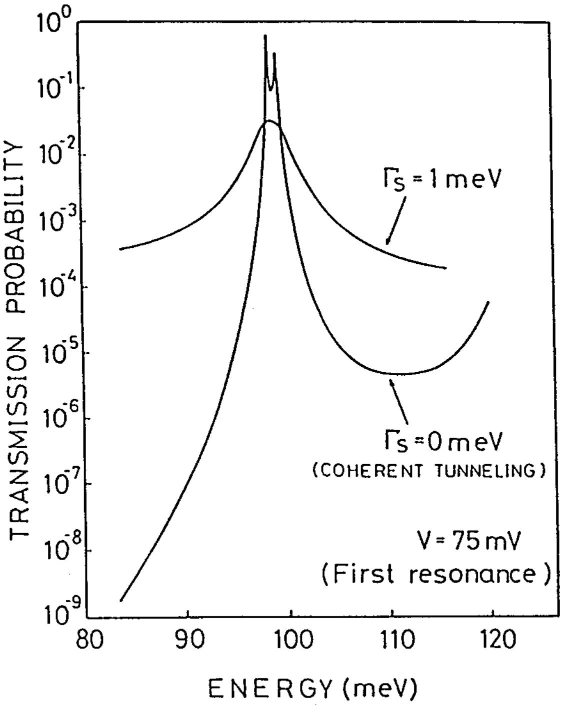

***Figure 3.31** Scattering broadening effects on the transmission probability at the first resonance. The energy dependence of the transmission probability calculated by using Γ_S = 1.0 meV is compared with that calculated by using global coherent tunnelling model (Γ_S = 0 meV).*

Figure 3.31 shows the energy dependence of the transmission probability at the first resonance of the device calculated by assuming Γ_S of 1 meV. For comparison the transmission probability under the global coherent tunnelling model ($\Gamma_S = 0$) has been also plotted. A small peak separation seen for the global coherent tunnelling model is attributed to a weak interference between the wells W1 and W2. This double peak structure has been smeared out by introducing the scattering broadening, and the whole transmission peak has become much broader. Also the peak transmission probability calculated by the scattering broadening model is found to decrease more than one order of magnitude from that by the global coherent tunnelling model.

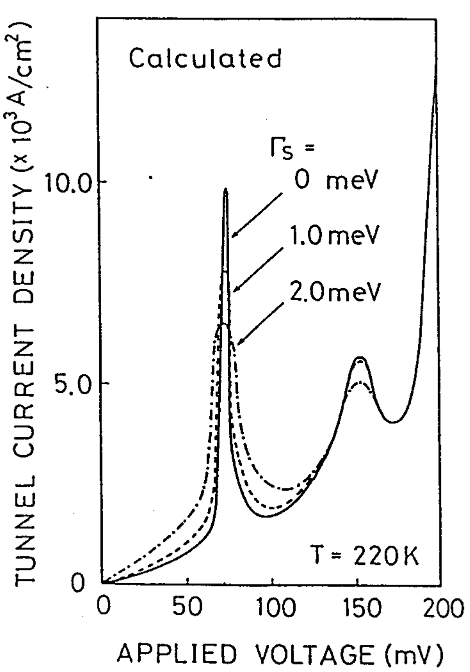

Figure 3.32 Current-voltage characteristics calculated by using various values of Γs.

The I-V curves calculated for Γ_S of 0, 1.0, and 2.0 meV are shown in Fig. 3.32. As a result of the decrease in the transmission probability at the resonance seen in Fig. 3.31, the first peak current decreases with increasing Γ_S. On the other hand, currents at the first off-resonant state increase with increasing Γ_S, resulting in a large degradation of the P/V current ratios. Similar changes are also found at the second resonance, but these are smaller than those at the first resonance as the intrinsic broadening of the quasi-bound state is larger and less sensitive for the increase in Γ_S in this range.

Figure 3.33 shows the Γ_S dependences of the first current peak width (solid line) and the first P/V current ratio. These quantities are plotted as functions both of Γ_S itself (bottom axis) and the ratio Γ_S/Γ_i (upper axis) where Γ_i represents the intrinsic broadening of the first quasi-eigenstate at resonance (corresponding to the resonant width Γ for double barrier structures defined by Eq. (3.25)) which is found to be about 0.3 meV from the global coherent tunnelling calculations (see Fig. 3.32).

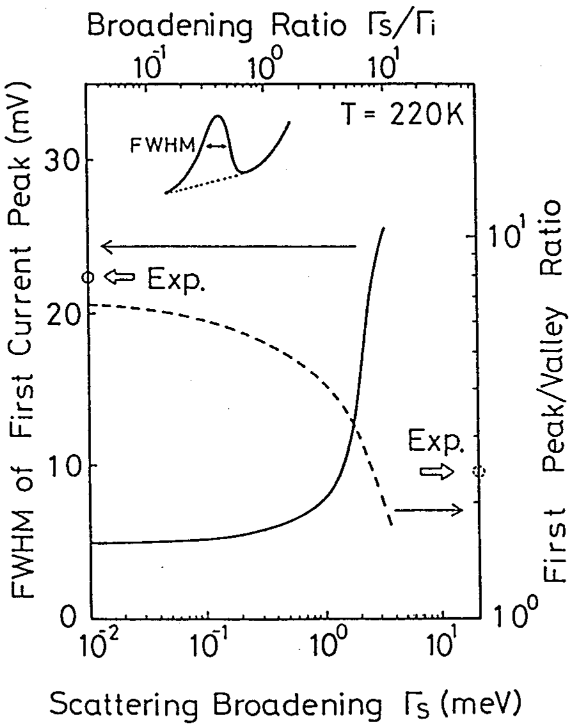

Figure 3.33 Γs-dependences of both the first current peaks width and P/V current ratios

It can be seen that the peak width increases and the P/V ratio decreases rapidly when the ratio Γ_S/Γ_i exceeds unity. This fact indicates that the ratio is a crucial quantity which measures to what extent the phase-coherence of the electron waves is maintained. If $\Gamma_S/\Gamma_i > 1$, the resonant tunnelling is far from the global coherent picture. The first resonant peak width and P/V ratio observed experimentally are indicated by open circles on both longitudinal axes in Fig. 3.33. By comparing the calculated results with these experimental data, it is found that Γ_S of approximately 2.5 meV gives a good agreement on both quantities.

Let's examine the value of Γ_S obtained by fitting the results above. Major causes of the scattering broadening would be polar-optical phonon scattering and acoustic deformation potential scattering. The momentum relaxation time, τ_m, due to these scattering may be given by the following expressions:

$$\frac{1}{\tau_m} = \left(\frac{1}{\tau_m}\right)_{LO} + \left(\frac{1}{\tau_m}\right)_{DP} \tag{3.31}$$

$$\left(\frac{1}{\tau_m}\right)_{LO} = \alpha\, \omega_{LO} \left(\frac{\hbar\omega_{LO}}{E}\right)^{1/2} N_q \left\{ \ln\left|\frac{a+1}{a-1}\right| + \exp\left(\frac{\Theta}{T}\right) \ln\left|\frac{1+b}{1-b}\right| \right\} \tag{3.32}$$

$$\left(\frac{1}{\tau_m}\right)_{DP} = \frac{(2\,E)^{1/2}\, m^{*3/2}\, D^2\, k_B T}{\pi\, \hbar^4\, C_L} \tag{3.33}$$

where N_q, a, and b are defined as follows:

$$N_q = \frac{1}{\exp\left(\frac{\Theta}{T}\right) - 1} \tag{3.34}$$

$$a = \left(1 + \frac{\hbar\omega_{LO}}{E}\right)^{1/2} \tag{3.35}$$

$$b = \mathrm{Re}\left(1 - \frac{\hbar\omega_{LO}}{E}\right)^{1/2} \tag{3.36}$$

Assuming the LO-phonon energy $\hbar\omega_{LO}$ of 36 meV, the Debye temperature Θ of 417K, the polar constant α of 0.067, the deformation potential constant D of 13.5 eV, the longitudinal elastic constant C_L of 1.44×10^{11} Nm^{-2}, and the electron energy E at the first resonance of about 48 meV, the values of $(1/\tau_m)_{LO}$ and $(1/\tau_m)_{DP}$ are estimated to be 5.21×10^{12} sec^{-1} and 4.34×10^{11} sec^{-1} at 220K, respectively. The scattering broadening may be obtained from the momentum relaxation time through the uncertainty principle:

$$\Gamma_S \approx \hbar/2\tau_m \tag{3.37}$$

Γ_S is then evaluated to be 1.9 meV (see Table 3.8) which is quite close to the value obtained in Figure 3.33.

	Momentum relaxation time τ_m (sec)	Scattering broadening Γ_s (meV)
Polar-optical phonon scattering	1.92×10^{-13}	1.72
Deformation potential scattering	2.30×10^{-12}	0.14
Total	1.77×10^{-13}	1.86

Table 3.8 Phonon induced scattering broadening derived from Eqs. (3.31) - (3.37).

In addition to the phonon induced scattering broadening, the ionized impurity scattering may contribute to the broadening as described earlier since Si ions are likely to diffuse from the heavily doped collector region into the quantum well as well as the inevitable residual impurities. In the present structure, however, the 10-nm-thick undoped GaAs spacer layer adopted in the present structure is supposed to prevent the diffusion of Si ions, and the effect of the ionized impurity scattering on Γ_s is much smaller than the above phonon-induced broadening. Also a different broadening also exists which arises from deviations of layer thickness from their averaged values [36]. All these factors may give a small influence on the P/V current ratios.

In summary of this section the effects of scattering events on the global coherent tunnelling has been discussed focusing on the change in the transmission spectrum of the resonant tunnelling barriers. By using the triple-well RTDs introduced in the previous section the LO-phonon scattering induced broadening has been studied. A phenomelogical broadening model explains the observed P/V current ratios by using a single broadening parameter obtained from the momentum relaxation times. These results indicate that the phase-coherence of electron waves is partly lost during the stay in the quantum well, and the change in the transmission probability is described by using a simple broadening model quite well. In the next chapter another vital effect of the scattering processes, the non-equilibrium aspect of the electron distribution, is studied in detail.

3.5 Reference III

[1] R. Tsu and L. Esaki, "Tunneling in a finite superlattice", Appl. Phys. Lett. **22**, 562, 1973.

[2] L. L. Chang, L. Esaki and R. Tsu, "Resonant Tunneling in Semiconductor Double Barriers", Appl. Phys. Lett. **24**, 593, 1974.

[3] T. C. L. G. Sollner, W. D. Goodhue, P. E. Tannenwald, C. D. Parker, and D. D. Peck, "Resonant Tunneling through Quantum Wells at Frequencies Up to 2.5 THz", Appl. Phys. Lett. **43**, 588, 1983.

[4] S. Sen, F. Capasso, A. Y. Cho, and D. Sivco, "Resonant Tunneling Device with Multiple Negative Differential Resistance: Digital and Signal Processing Applications with Reduced Circuit Complexity", IEEE Trans. Electron Dev. **ED-34**, 2185, 1987.

[5] T. Nakagawa, H. Inamoto, T. Kojima, and K. Ohta, "Observation of Resonant Tunneling in AlGaAs/GaAs Triple Barrier Diodes", Appl. Phys. Lett. **49**, 73, 1986.

[6] T. Tanoue, H. Mizuta, and S. Takahashi, "A Triple-Well Resonant Tunneling Diode for Multiple-Valued Logic Application", IEEE Electron Device Lett. **EDL-9**, 365, 1988.

[7] H. Mizuta, T. Tanoue, and S. Takahashi, "A New Triple-Well Resonant Tunneling Diode with Controllable Double-Negative Resistance", IEEE Trans. Electron Devices **ED-35**, 1951, 1988.

[8] F. Capasso and R. A. Kiehl, "Resonant Tunneling Transistor with Quantum Well Base and High-Energy Injection: A New Negative Differential Resistance Device", J. Appl. Phys. **58**, 1366, 1985.

[9] N. Yokoyama, K. Imamura, S. Muto, S. Hiyamizu, and H. Nishi, "A New Functional Resonant Tunneling Hot Electron Transistor (RHET)", Jpn. J. of Appl. Phys. **24**, L853, 1985.

[10] A. R. Bonnefoi, T. C. Mcgill, and R. D. Burnham, "Resonant Tunneling Transistors with Controllable Negative Differential Resistances", IEEE Electron Device Lett. **EDL-6**, 636, 1985.

[11] A. C. Seabaugh, W. R. Frensley, J. N. Randall, M. A. Reed, D. L. Farrington, and R. J. Matyi, "Pseudomorphic bipolar quantum resonant-tunneling transistor", IEEE Trans. Electron Devices **ED-36**, 2328, 1989.

[12] M. Tsuchiya, H. Sakaki, and J. Yoshino, "Room tenperature observation of differential negative resistance in an AlAs/GaAs/AlAs resonant tunneling diodes", Jpn. J. Appl. Phys. **24**, L466, 1985.

[13] M. Tsuchiya and H. Sakaki, "Precise control of resonant tunneling current in AlAs/GaAs/AlAs double barrier diodes with atomically-controlled barrier widths", Jpn. J. Appl. Phys. **25**, L185, 1986.

[14] M. Tsuchiya and H. sakaki, "Dependence of resonant tunneling current on well widths in AlAs/GaAs/AlAs double barrier diode structures", Appl. Phys. Lett. **49**, 88, 1986.

[15] D. Landheer, G. C. Aers, and Z. R. Wasilewski, "Effective mass in the barriers of GaAs/AlAs resonant tunneling double barrier diodes", Superlattices and Microstructures **11**, 55, 1992.

[16] A. Harwit, J. S. Harris, Jr., and A. Kapitulnik, "Calculated quasi-eigenstates and quasi-eigenenergies of quantum well superlattices in an applied electric field", J. Appl. Phys. **60**, 3211, 1986.

[17] B. Ricco and M. Y. Azbel, "Physics of resonant tunneling. The one-dimensional double-barrier case", Phys. Rev. B**29**, 1970, 1984.

[18] H. C. Liu, "Tunneling time through heterojunction double barrier diodes", Superlattices and Microstructures **3**, 379, 1987.

[19] D. D. Coon and H. C. Liu, "Frequency limit of double barrier resonant tunneling oscillators", Appl. Phys. Lett. **49**, 94, 1986.

[20] N. Harada and S. Kuroda, "Lifetime of resonant state in a resonant tunneling system", Jpn. J. Appl. Phys. **25**, L871, 1986.

[21] M. Tsuchiya, T. Matsusue, and H. Sakaki, "Tunneling escape rate of electrons from quantum well in double-barrier heterostructures", Phys. Rev. Lett. **59**, 2356, 1987.

[22] H. Ohnishi, T. Inata, S. Muto, N. Yokoyama, and A. Shibatomi, "Self-consistent analysis of resonant tunneling current", Appl. Phys. Lett. **49**, 1248, 1986.

[23] K. F. Brennan, "Self-consistent analysis of resonant tunneling in a two-barrier-one-well microstructure", J. Appl. Phys. **62**, 2392, 1987.

[24] M. A. Reed, W. R. Frensley, W. M. Duncan, R. J. Matyi, A. C. Seabaugh, and H. L. Tsai, "Quantitative resonant tunneling spectroscopy: Current-voltage characteristics of precisely characterized resonant tunneling diodes", Appl. Phys. Lett. **54**, 1256, 1989.

[25] B. Jogai, C. I. Huang, and C. A. Bozada, "Electron density in quantum well diodes", J. Appl. Phys. **66**, 3126, 1989.

[26] H. Mizuta, T. Tanoue, and S. Takahashi, "Theoretical analysis of peak-to-valley ratio degradation caused by scattering processes in multi-barrier resonant tunneling diodes", Proceedings of IEEE/Cornell conference on advanced concepts in high speed semiconductor devices and circuits", 274, 1989.

[27] S. Luryi, "Physics of resonant tunneling devices", Proceedings of International Workshop on Future Electron Devices - Superlattice Devices -, Tokyo, 21, 1987.

[28] A. D. stone and P. A. Lee, "Effect of inelastic processes on resonant tunneing in one dimension", Phys. Rev. Lett. **54**, 1196, 1985.

[29] M. Jonson and A. Grincwaig, "Effect of inelastic scattering on resonant and sequential tunneling in double barrier heterostructures", Appl. Phys. Lett. **51**, 1729, 1987.

[30] B. Movaghar, J. Leo, and A. Mackinnon, "Elastic and inelastic tunneling in multiple quantum well structures", Surface Science **196**, 381, 1988.

[31] V. J. Goldman, D. C. Tsui, and J. E. Cunningham, "Evidence for LO-phonon-emission-assisted tunneling in double-barrier heterostructures", Phys. Rev. B**36**, 7635, 1987.

[32] M. L. Leadbeater, E. S. Alves, L. Eaves, M. Henini, O. H. Hughes, A. Celeste, J. S. Portal, G. Hill, and M. A. Pate, "Magnetic field studies of elastic scattering and optic-phonon emission in resonant-tunneling devices", Phys. Rev. B**39**, 3438, 1989.

[33] H. A. Fertig and S. Das. Sarma, "Elastic scattering in resonant tunneling systems", Phys. Rev. B**40**, 7410, 1989.

[34] H. A. Fertig, Song He, and S. Das. Sarma, "Elastic-scattering effects on resonant tunneling in double-barrier quantum-well structures", Phys. Rev. B**41**, 3596, 1990.

[35] N. Zou and K. A. Chao, "Inelastic electron resonant tunnelling through a double-barrier nanostructure", Phys. Rev. Lett., **69**, 3224, 1992.

[36] Y. Fu and M. Willander, "Lateral-nonuniformity effect on the I-V spectrum in a double-barrier resonant-tunneling structure", Phys. Rev. B**44**, 13631, 1991.

CHAPTER 4

DISSIPATIVE QUANTUM TRANSPORT AND ELECTRON DYNAMICS IN RESONANT TUNNELLING DIODES

Following the study of the coherent quantum transport in the previous chapter this chapter deals with investigation of more complicated incoherent aspect of quantum transport. The simple global resonant tunnelling model based on a quantity of the transmission probability throughout the structures has been shown to facilitate an intuitively understandable picture of resonant tunnelling. It has been also shown that the idea of the transmission probability could have been extended into a partly incoherent transport regime in which the phase-coherence breaking scattering events affect the tunnelling. Namely we have concentrated on the spectrum of the resonant tunnelling structures. In this chapter we go beyond the simple global coherent tunnelling picture and investigate two other important aspects of electron transport in RTDs: *non-equilibrium distribution* and *femtosecond dynamics* of tunnelling electrons. As discussed in Sec. 3.4 the coherent electron-waves may suffer from scattering processes which cause momentum and energy relaxations of electrons resulting in a more complicated transmission spectrum than that obtained from the global coherent tunnelling model. These relaxation processes, at the same time, might cause a change in the electron distribution in the quantum well. In Sec. 3.2.2 we have calculated the self-consistent energy-band diagram and electron distribution, and studied the effect of electrons accumulated in the well. This self-consistent theory has been completely based on an assumption of the global coherent tunnelling and is no longer correct if the relaxation processes occur so frequently that they alter the electron distribution in an energy space. It has been shown that this indeed happens in some cases and transport is then described by an incoherent *sequential tunnelling* picture [1] rather than the global coherent tunnelling.

The sequential tunnelling model has been proposed by Luryi [1], [2] as an alternative explanation of resonant tunnelling about ten years after the global coherent resonant tunnelling was reported by Tsu and Esaki. This model describes the resonant tunnelling as two continuous tunnelling processes, that is tunnelling from the emitter into the quantum well followed by that to the collector. Between these two processes the electrons suffer from the phase breaking scattering processes in a quantum well and are relaxed into a locally quasi-equilibrium states. This sequential tunnelling picture is thus a mixture of both coherent and incoherent tunnelling processes. In the limit of no scattering the sequential tunnelling model has been shown [3] to naturally reduce to the coherent global tunnelling as is expected from the definition of the model.

Proper theoretical description of this situation obviously should rely on non-equilibrium quantum transport theory such as the density matrix [4], the Wigner function [5], Green functions [6], and path-integrals [7]. The non-equilibrium transport theory has not yet been well established itself, and numerical calculations based on these modelling are still far from practical use. Very recently, however, the quantum-mechanical Wigner function has been solved numerically [8]-[11] to analyze electron transport in RTDs. The equation of motion based on the Wigner function, which is derived from the Liouville-von Neumann equation for the statistical density matrix by applying the Wigner-Weyl transformation, has been solved in the finite-difference scheme, and some calculated results have been reported on the steady-state I-V characteristics and transient behaviour of RTDs.

New experimental techniques have been also introduced to investigate the dissipation process, non-equilibrium electron distribution and electron dynamic process in RTDs. Magnetotransport and magnetocapacitance measurement techniques have turned out to be an excellent method to directly measure space-charge build-up and non-equilibrium distribution of electrons in resonant tunnelling structures. One of the recent success is to have revealed that the device has an intrinsic bistability in the negative differential conductance region which stems from dynamical redistribution of electrons in the quantum well. A time-resolved photoluminescence technique with a picosecond laser has been also adopted on purpose to study the dynamical aspect of the resonant tunnelling.

In this chapter, resonant tunnelling through a double barrier structure is studied in some detail by focusing on non-equilibrium distribution and femtosecond dynamics of electrons. First, in Sec. 4.1, electron accumulation in a triangle potential well in the emitter and related 2D

- 2D resonant tunnelling are discussed to introduce the idea of energy dissipation into the coherent tunnelling picture in the previous chapter. Second numerical calculations based on the density matrix theory are carried out in Sec. 4.2 to analyze femtosecond dynamics of electrons in RTDs as well as dynamical space charge build-up in the double barrier structure. In Sec. 4.3, magnetotransport measurement is then introduced to estimate the space charge build-up experimentally.

4.1 Non-equilibrium electron distribution and 2D - 2D resonant tunnelling

In the previous chapter we have seen that the energy-band diagram in the emitter region sometimes exhibits a shallow triangle potential well with an emitter barrier under large applied bias (for example, see Fig. 3.9). We have assumed that the electronic states in the emitter and collector regions are described by using both classical continuous energy spectrum with Fermi-Dirac equilibrium distribution function. This convenient assumption is, however, no longer valid if a relatively thick undoped (or even low-doped) spacer layer is introduced on the emitter side. In these cases an external voltage largely drops in these undoped regions as well as the double barrier structure resulting in a pseudo-triangle quantum well as shown in Fig. 4.1.

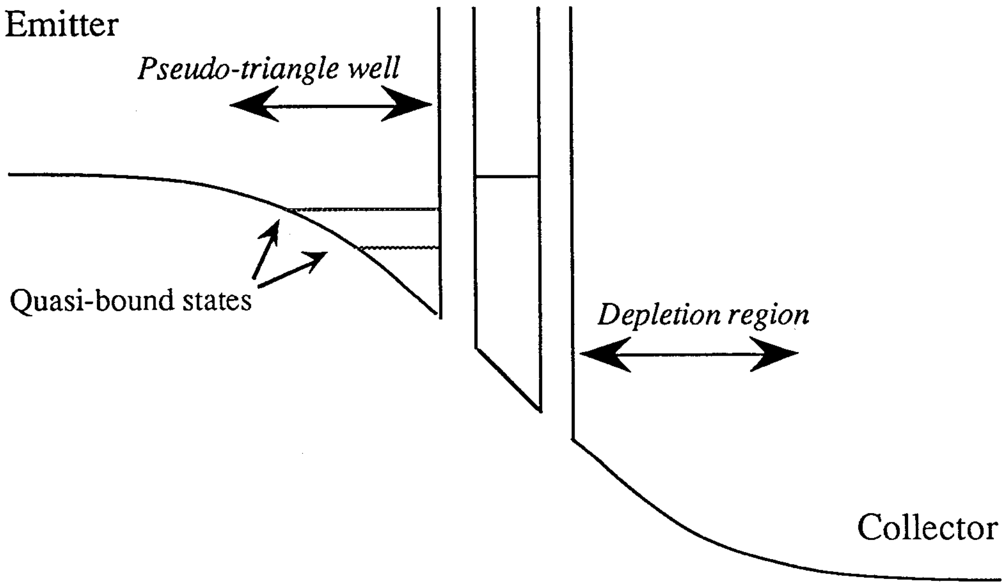

Figure 4.1 Schematic energy-band diagram of a double barrier RTD with thick low-doped regions on both side of the barriers.

In general low doping concentration near resonant tunnelling barriers results in large P/V current ratios and hence is widely used though current densities are relatively low. An example of advanced contact structures are shown in Figs. 4.2: in these structures a graded doping profile has been adopted in which doping concentration is varied from 5×10^{18} cm^{-3} at the edge of emitter to 1×10^{16} cm^{-3} near the barriers. In the following sections two AlAs/GaAs/AlAs double barrier RTDs which have this graded contact structure are newly introduced. These are hereafter called as Sample 2 (4.2nm/5.9nm/4.2nm) and Sample 3 (5.0nm/7.0nm/5.0nm).

Emitter

n-GaAs	(Si: 5×10^{18}/cm^3)	150 nm
n-GaAs	(Si: 2×10^{17}/cm^3)	150 nm
n-GaAs	(Si: 8×10^{16}/cm^3)	200 nm
n-GaAs	(Si: 3×10^{16}/cm^3)	250 nm
n-GaAs	(Si: 1×10^{16}/cm^3)	450 nm
undoped-GaAs		5 nm
Double barrier structure		
undoped-GaAs		5 nm
n-GaAs	(Si: 1×10^{16}/cm^3)	450 nm
n-GaAs	(Si: 3×10^{16}/cm^3)	250 nm
n-GaAs	(Si: 8×10^{16}/cm^3)	200 nm
n-GaAs	(Si: 2×10^{17}/cm^3)	150 nm
n-GaAs	(Si: 5×10^{18}/cm^3)	500 nm

Collector

Figure 4.2 *Emitter and collector structures with a graded doping profile used for Samples 2 & 3.*

Under a large external bias the low-doping region in the emitter forms a pseudo-triangular quantum well next to the emitter barrier. Electronic states in this triangle well are both quasi-bound states in the low energy region (see Fig. 4.1) and scattering states in the high energy region. Electrons which occupy the quasi-bound states of the triangle well form a two-dimensional electron gas (2DEG). Resonant tunnelling then occurs between these two dimensional states in the triangle well and the resonant state in the double barrier structure: this is hence called *2D - 2D resonant tunnelling* [12] and distinguished from the conventional resonant tunnelling which should be now denoted as 3D - 2D resonant tunnelling in a corresponding manner.

A question then arises about the distribution of electrons in the triangle well: how are the incoming electrons redistributed between the quasi-bound states and scattering states? As long as we use the global coherent tunnelling model introduced in the previous section, the incoming electrons run through this triangle well in a completely ballistic way without any change in the occupation of these quasi-bound states because they are located below the conduction band edge of the emitter (see Fig. 4.3(a)). This is, however, not a realistic assumption as the incoming electrons may suffer from dissipative scattering processes and redistribute through these quasi-bound states (see Fig. 4.3(b)). In this case, the electron distribution is not expressed simply by the Fermi-Dirac distribution function which is basically for equilibrium system but a complicated *non-equilibrium* distribution function. Thus the electrons tunnelling into the resonant state in the double barrier structure may come from both these 2D quasi-bound states (2D - 2D RT) and the 3D scattering states (3D -2D RT) depending on temperature. If both electrons equally contribute to the resonant tunnelling, some distinguishable structures might be seen in the current-voltage characteristics.

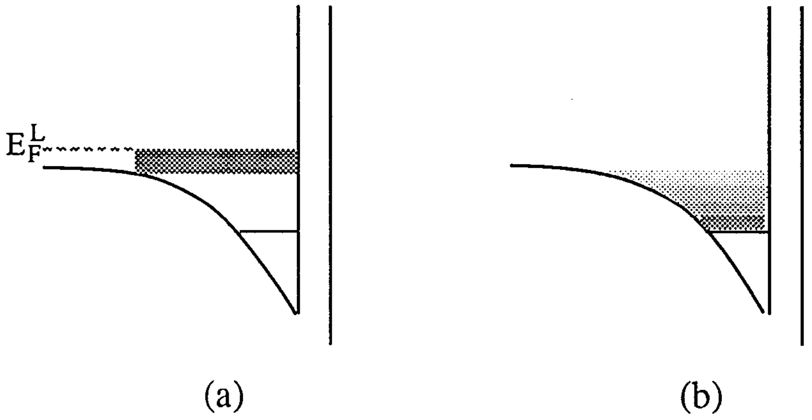

Figure 4.3 Two extreme cases for electron accumulation in a pseudo-triangle potential well: (a) no charge build-up due to ballistic electron transport, and (b) significant build-up caused by electrons which suffer from energy dissipation processes.

The current-voltage and conductance-voltage characteristics are given for both Samples 2 and 3 at various temperatures in Figs. 4.4 and 4.5. A single sharp current peak is seen at low temperatures which is thought to reflect the nature of 2D - 2D resonant tunnelling discussed above. For both samples, however, a broad current shoulder becomes noticeable at higher temperatures before the main resonance occurs. Such a feature has been observed by Gobato et al. [13] and Zheng et al. [14] who both saw similar characteristics and ascribed them to the electrons which go through the 3D scattering states ballistically. Contributions of these 3D ballistic electrons have been successfully modelled by Chevoir & Vinter [15]. Also Goldman et al. [16] has discussed a more complex case in which only the lowest quasi-eigenstate in the triangle well is resolved and others are merged with the 3D continuous scattering states.

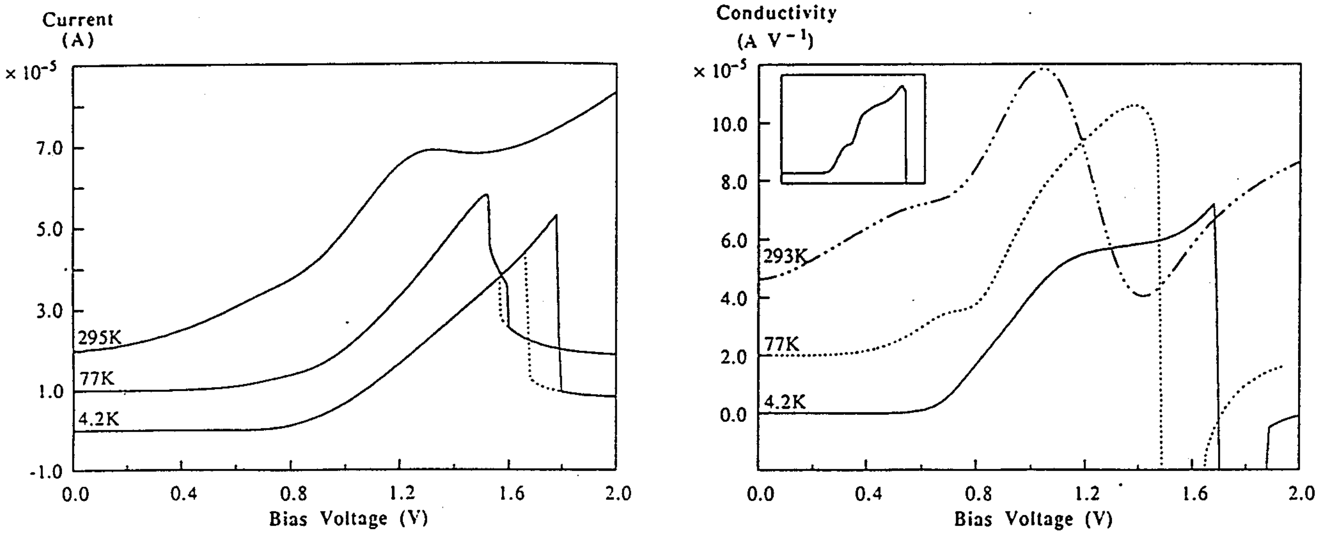

(a) (b)

Figure 4.4 Current (a) and conductance (b) versus voltage measured for Sample 2 at various temperatires. For clarity curves have been offset in both graphs. Dotted lines in (a) show hysteresis in NDC regime.

The fact that the current shoulders are observed more clearly at higher temperatures is consistent with these theoretical explanations because the number of electrons which occupies the 3D continuous states will increase. In addition it is easily expected from these theoretical explanations that application of an magnetic field perpendicular to the barriers separates the 3D components from the 2D ones [14]. This has been observed in Sample 2 as shown in the inset to Fig. 4.4(b): two distinct peaks can be seen in the conductance-voltage characteristics even at 4.2K.

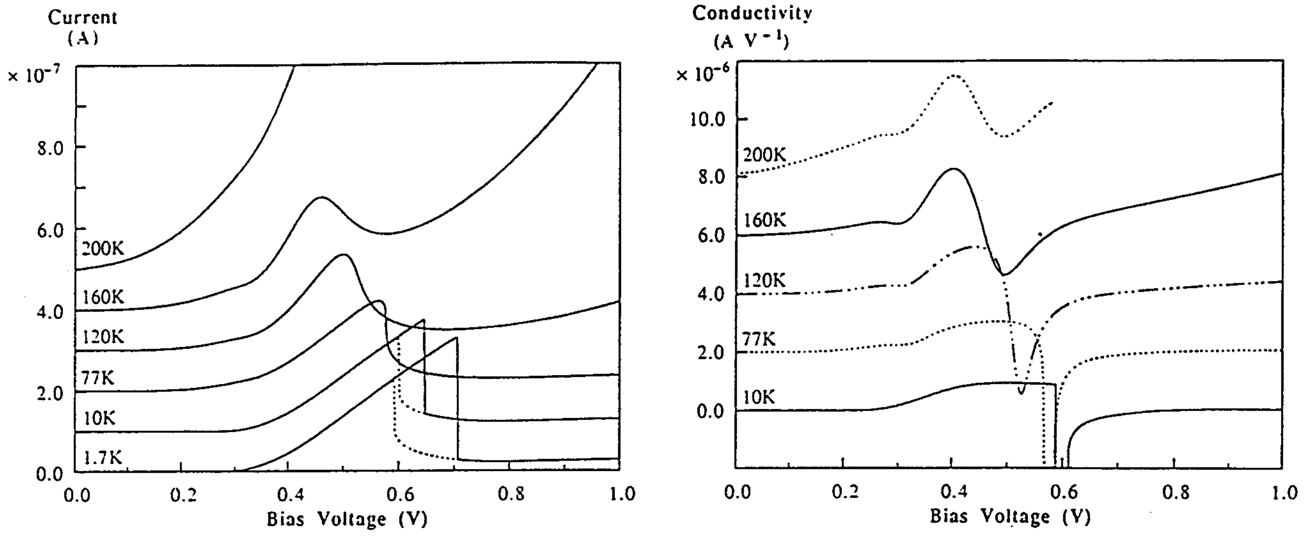

(a)

(b)

Figure 4.5 Current (a) and conductance (b) versus voltage measured for Sample 3 at various temperatires. For clarity curves have been offset in both graphs. Dotted lines in (a) show hysteresis in NDC regime.

The results shown in this section manifest that the electron distribution in the pseudo-triangle well of the emitter is not expressed by a simple equilibrium distribution function. The reality lies in an intermediate situation between these two extreme cases shown in Fig. 4.1(a) and (b). Electrons in those non-equilibrium distributions tunnel into the double barrier structure and therefore make the distribution between double barriers more complex. In the following sections dynamic electron accumulation in double barrier structures is focused and investigated theoretically and experimentally.

4.2 Theory of dissipative quantum transport in RTDs

In this section a numerical study of non-equilibrium transport in RTDs is presented based upon the density matrix equation [4] which is the most fundamental equation in statistical quantum-mechanical physics. The statistical density matrix is a wavefunction-wavefunction correlation function, and its off-diagonal elements directly measure the phase-coherence of wavefunctions: one of the most significant parameters in electron-wave device design. The first numerical calculation of the density matrix equation was reported by Frensley [17], who observed for the first time the time evolution of the density matrix for the resonant tunnelling diode. At the same time, however, a lot of problems were pointed out in this formalism, such as Ohmic contact boundary conditions, a correct initial density matrix, a self-consistent Hartree potential, and numerical instability in transient calculations. Very recently, the Monte Carlo calculation was also reported to simulate the effect of electron-phonon interaction on the density matrix [18]-[20]. In this section, we report a numerical quantum device modelling based on the direct calculation of the density matrix equation, which includes new boundary- and initial-conditions for the density matrix and an implicit scheme for time-integration. The correct density matrix in thermal equilibrium is calculated by solving the Schrödinger equation and Poisson's equation self-consistently. Using the thermal equilibrium density matrix as an initial state, the time-dependent density matrix equation is then solved directly. The Hartree self-consistent field model and the relaxation-time approximation are introduced for electron-electron interactions and scattering processes, respectively. The present simulation technology is applied to the simple AlGaAs/GaAs resonant tunnelling diodes, and transient behaviours of electron build-up in the quantum-well and development of long-range phase-correlations between quasi-bound electron-waves and free electron-waves are demonstrated. In addition, the switching behaviour from the peak (valley) to the valley (peak) of the I-V characteristics and the effects of scattering on the peak-to-valley current ratio are discussed.

4.2.1 Time-dependent statistical density matrix and Wigner distribution function

The first step of the quantum device simulation is to find the correct *statistical density matrix* for a system in thermal equilibrium, which is used as an initial condition for the time-dependent density matrix equation. Provided that an unperturbed quantum-mechanical open system is in thermal equilibrium with its surroundings, the statistical density matrix based on the independent-particle approximation is expressed by the following equation:

$$\rho_0(\mathbf{x},\mathbf{x}';0) = \left\langle \Psi(\mathbf{x})\Psi^*(\mathbf{x}') \right\rangle = \sum_{\mathbf{k},\sigma} \Psi_{\mathbf{k}}(\mathbf{x})\Psi^*_{\mathbf{k}}(\mathbf{x}')\ f(\mathbf{k}) \qquad (4.1)$$

where $\Psi_{\mathbf{k}}(\mathbf{x})$ is the eigen-function of the unperturbed Hamiltonian, and $f(\mathbf{k})$ is the Fermi-Dirac distribution function. Equation (4.1) shows that the statistical density matrix is a function of the two positions **x** and **x'**: The diagonal elements represent the real electron density in the system and the off-diagonal elements measure the phase correlations of the wavefunctions. Also it is sometimes convenient to introduce the following *Wigner distribution function*, $f_w(\chi, k, t)$, which is the Weyl transform of the density matrix:

$$f_W(\chi, k, t) = \int \frac{d\zeta}{2\pi} e^{ik\zeta} \rho(\chi, \zeta, t) \qquad (4.2)$$

where χ and ζ are absolute and relative coordinates, (x+x')/2 and x-x', respectively. This is in analogy to the classical distribution function defined in the (**k**, **x**) phase space. A complete set of wave functions required to calculate the density matrix (4.1) is obtained by solving the time-independent effective-mass Schrödinger equation:

$$H\,\Psi_k(x) = -\frac{\hbar^2}{2}\nabla\left(\frac{1}{m^*(x)}\nabla\right)\Psi_k(r) + V(x)\Psi_k(x) = E_k\Psi_k(x) \qquad (4.3)$$

where $m^*(x)$ is the electron effective mass and $V(x)$ is the potential energy distribution which consists of the electron affinity, $V_0(x)$, and the Hartree potential, $V_{SC}(x)$, due to the charge density of electrons and ionized donors. The Hartree potential is determined self-consistently by solving Poisson's equation:

$$-\nabla^2 V_{SC}(x) = \frac{1}{\varepsilon(x)}\left(N_D^+(x) - \sum_{k,\sigma} |\Psi_k(x)|^2 f(k)\right) \qquad (4.4)$$

The Schrödinger equation (4.2) is solved by using the finite-difference method rather than the transfer matrix method. From the point of view of numerical calculations, the transfer matrix method is more accurate than the finite difference method because wavefunctions between mesh points are stored as plane-wave states. However, the use of the solutions obtained by the transfer matrix method sometimes brings about an unrealistic current density at hetero-interfaces when the resultant density matrix is used as an initial solution for the time-dependent density matrix equation. This is because of the difference in the ways in which the Schrödinger equation and the density matrix equation are discretized. In the present work, we adopt exactly the same finite difference discretization for both equations.

A set of incoming scattering states (emitter- and collector-incident plane waves) [21] is used as boundary conditions to solve the Schrödinger equation. When the finite-difference method is used for solving the Schrödinger equation solutions are no longer expressed as coefficients of plane waves. It is therefore necessary to decompose the wavefunctions obtained at the edge of devices into incident and reflected plane waves to find a normalization factor. From the unnormalized solutions on the first two mesh points, we evaluate the coefficients for the incident and reflected waves and normalize the wavefunctions. Accuracy of this normalization method depends on the first mesh-spacing and, to some extent, can be judged from the resultant electron density calculated at the emitter and collector edge.

In the present work, we adopt the simple structure of an AlGaAs/GaAs double barrier resonant tunnelling diode to examine the new simulation technology. The assumed structure consists of a undoped GaAs quantum well of 5 nm in thickness, two undoped $Al_{0.33}Ga_{0.67}As$ barriers of 4 nm in thickness, and highly doped n-type GaAs($N_D = 1\times10^{18}$ cm^{-3}) emitter and collector layers of 20 nm in thickness with undoped GaAs spacer layers of 6 nm in thickness. The conduction band discontinuity in the GaAs/AlGaAs heterostructure is assumed to be 60 percent of the Γ -band energy gap difference. Positional dependence of electron effective mass, $m^*(x)$, is taken into account by assuming the simple Al-mole fraction dependence of electron mass in AlGaAs: $m^*(GaAs) = 0.067\ m_0$ and $m^*(Al_{0.33}Ga_{0.67}As) = 0.094\ m_0$. Figure 4.6 (a) shows the real parts of the equilibrium density matrix (the imaginary parts are exactly zero), and Fig. 4.6 (b) the energy band-diagram calculated self-consistently at a temperature of 300 K. An energy mesh with a spacing of 0.5 meV was used to calculate and store all the wavefunctions of the system with eigenenergies up to 200 meV. The normalization method for wavefunctions described above appears to be successful since charge neutral regions assured by the flat energy-band are obtained near the emitter and collector edges. The small peak in the centre of Fig. 4.6 (a) represents accumulated electrons in the quantum well. These electrons are thermally distributed around the first quasi-bound state (the resonant state) at the energy of about 60 meV measured from the bottom of the quantum well. The steep decrease in electron density near the double barriers stems from a quantum repulsion of electron-waves [10]. In Fig. 4.6 (b), the upward shift of the potential diagram near the heterointerfaces in the emitter and collector layers is caused by the self-consistent field from electrons injected into the spacer layers. A typical mesh grid adopted for the density matrix of the resonant tunnelling diode is shown in Fig. 4.7: Mesh spacing was chosen to be smaller in the region of the double barrier structure. This sort of non-uniform mesh is useful to save the computational time and memory when solving the density matrix equation although it complicates the coefficient matrix of the discretized equation.

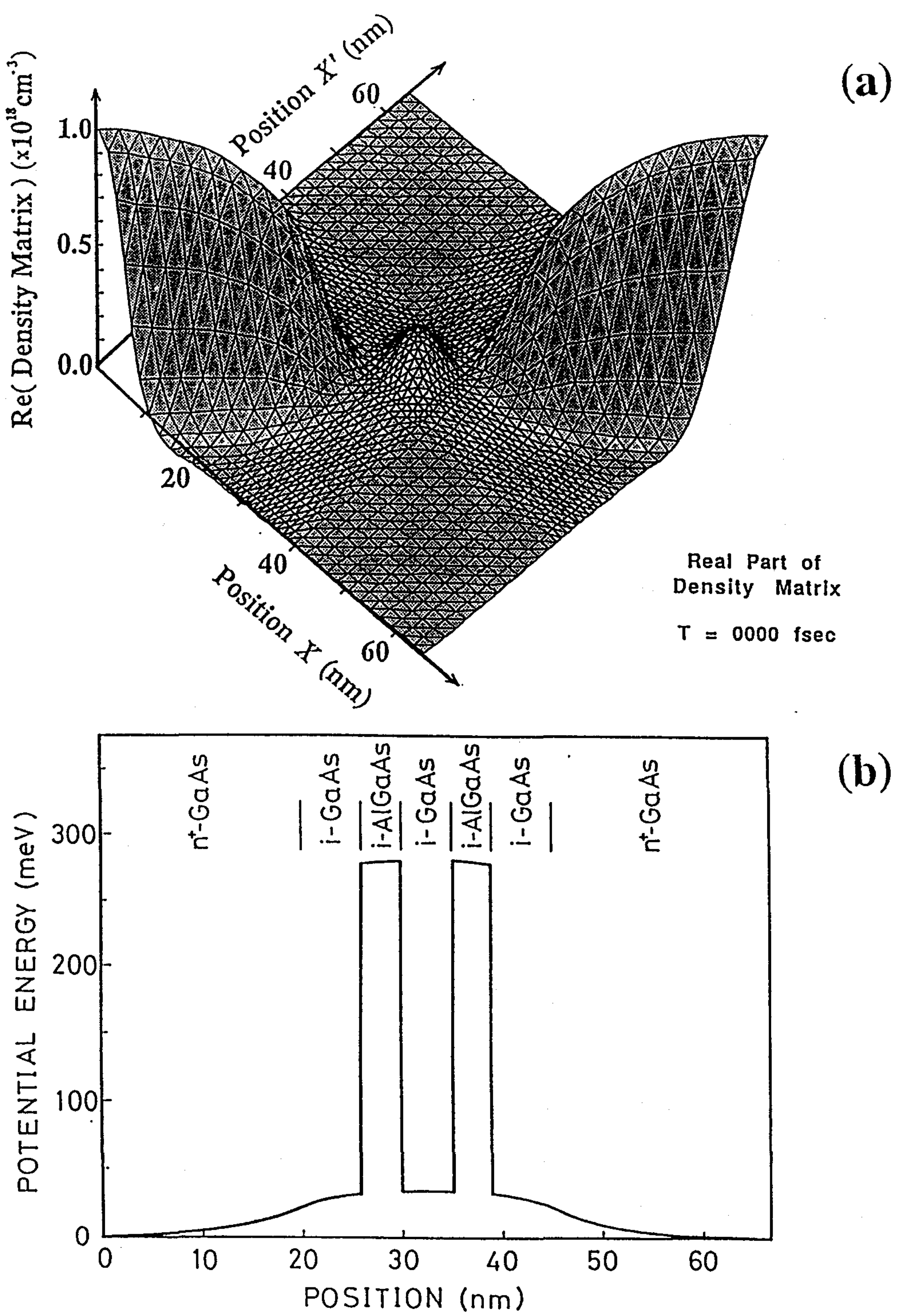

Figure 4.6 (a) Equilibrium density matrix and (b) energy-band diagram, self-consistently calculated for the AlGaAs/GaAs double barrier RTD at a temperature of 300K. The transverse axis in (b) has been adjusted so that the diagonal of the density matrix, that is electron distribution, is displayed with the same position as the band-diagram.

As mentioned earlier, off-diagonal structures of the density matrix measure the phase-correlations between the electron wavefunctions at different positions. In Fig. 4.6(a), the density matrix in the emitter and collector regions varies steeply along the cross-diagonal direction, and its dependence on a relative distance x-x' is approximately expressed by the following Gaussian-like analytical form for the free electron density matrix:

$$\rho_{FE}(x,x') \cong \frac{1}{\sqrt{2\pi^3}\,\lambda_T^3} \exp\left\{-\,(x-x')^2/2\lambda_T^2 + E_F/k_BT\right\} \tag{4.5}$$

where a thermal coherence length of the electron wave, λ_T, is defined as follows:

$$\lambda_T^2 = \hbar^2/(m^*k_BT) \tag{4.6}$$

The thermal coherence length, which is about 7 nm for GaAs at room temperature, is a critical length in multi-mode (multi-phased) electron wave devices, and the correlation between thermally distributed free electrons decreases steeply beyond λ_T because of the superposition of electron waves with various phases. In Sec. IV, the development of dynamical interference between these free electron-waves and quasi-bound electron-waves at the resonant state is demonstrated.

The second step of the quantum device simulation is to solve the fundamental equation of motion for the density matrix. The equilibrium density matrix, ρ_0, obtained in the previous section is used as an initial state for the density matrix equation. The time evolution of the density matrix under an applied electric field is given by the following Liouville-von Neumann equation:

$$\frac{\partial\rho}{\partial t} = \frac{1}{i\hbar}\,[H(t),\rho] + C_{col}\rho \tag{4.7}$$

where H(t) is the Hamiltonian under an applied bias, and C_{col} is a collision operator, discussed later. Using the position-space representation, the density matrix equation is given by the following expression:

$$\frac{\partial\rho(x,x';t)}{\partial t} = \frac{i\hbar}{2}\left[\frac{\partial}{\partial x}\left(\frac{1}{m^*(x)}\frac{\partial}{\partial x}\right) - \frac{\partial}{\partial x'}\left(\frac{1}{m^*(x')}\frac{\partial}{\partial x'}\right)\right]\rho(x,x';t)$$
$$+ \frac{1}{i\hbar}\,\{V(x;t) - V(x';t)\}\,\rho(x,x';t) + C_{col}\,\rho(x,x';t) \tag{4.8}$$

$$V(x;t) = V_0(x) + V_{SC}(x;t) \tag{4.9}$$

where the time-dependent Hartree potential $V_{SC}(x;t)$ is determined by the diagonal elements of the density matrix as follows:

$$\frac{d}{dx}\left\{\varepsilon(x)\,\frac{dV_{SC}(x;t)}{dx}\right\} = -\,q\left\{N_D^+(x) - \mathrm{Re}(\rho(x,x;t))\right\} \tag{4.10}$$

The time-dependent conduction current density, j(x;t), is then calculated by the following formula:

$$j(x;t) = \frac{q\hbar}{2m^*(x)\, i}\left(\frac{\partial}{\partial x} - \frac{\partial}{\partial x'}\right)\rho(x,x';t)\Bigg|_{x'=x} \tag{4.11}$$

Equation (4.7) is discretized in x and x' by using exactly the same spatial grid as the equilibrium density matrix and then deformed to algebraic equations. For the time integral of Eq. (4.8), an implicit scheme is used to obtain stable convergence in the numerical calculations because explicit schemes usually require extremely small time steps [17]. Since the Hartree potential depends on the density matrix(Eq. (4.10)), full implicit treatment for Eq. (4.8) gives rise to a complicated system of coupled non-linear equations. Here, we employ the implicit scheme only for the density matrix and treat the Hartree potential explicitly. The resultant finite-difference equation is as follows:

$$\begin{aligned}
\frac{\rho_{i,j}(t+\Delta t) - \rho_{i,j}(t)}{\Delta t} = c\Bigg[\frac{i\hbar}{2}\Bigg\{&\frac{1}{\Delta\tilde{x}_i}\left(\frac{1}{m^*_{i+\frac{1}{2}}}\frac{\rho_{i+1,j}(t+\Delta t) - \rho_{i,j}(t+\Delta t)}{\Delta x_i} + \frac{1}{m^*_{i-\frac{1}{2}}}\frac{\rho_{i-1,j}(t+\Delta t) - \rho_{i,j}(t+\Delta t)}{\Delta x_{i-1}}\right)\\
&- \frac{1}{\Delta\tilde{x}_j}\left(\frac{1}{m^*_{j+\frac{1}{2}}}\frac{\rho_{i,j+1}(t+\Delta t) - \rho_{i,j}(t+\Delta t)}{\Delta x_j} + \frac{1}{m^*_{j-\frac{1}{2}}}\frac{\rho_{i,j-1}(t+\Delta t) - \rho_{i,j}(t+\Delta t)}{\Delta x_{j-1}}\right)\Bigg\}\\
&+ \frac{1}{i\hbar}(V_i(t) - V_j(t))\,\rho_{i,j}(t+\Delta t) + [C_{col}\rho]_{i,j}(t+\Delta t)\Bigg]\\
+ (1-c)\Bigg[\frac{i\hbar}{2}\Bigg\{&\frac{1}{\Delta\tilde{x}_i}\left(\frac{1}{m^*_{i+\frac{1}{2}}}\frac{\rho_{i+1,j}(t) - \rho_{i,j}(t)}{\Delta x_i} + \frac{1}{m^*_{i-\frac{1}{2}}}\frac{\rho_{i-1,j}(t) - \rho_{i,j}(t)}{\Delta x_{i-1}}\right)\\
&- \frac{1}{\Delta\tilde{x}_j}\left(\frac{1}{m^*_{j+\frac{1}{2}}}\frac{\rho_{i,j+1}(t) - \rho_{i,j}(t)}{\Delta x_j} + \frac{1}{m^*_{j-\frac{1}{2}}}\frac{\rho_{i,j-1}(t) - \rho_{i,j}(t)}{\Delta x_{j-1}}\right)\Bigg\}\\
&+ \frac{1}{i\hbar}(V_i(t) - V_j(t))\,\rho_{i,j}(t) + [C_{col}\rho]_{i,j}(t)\Bigg] \qquad (i,j = 1,2,\cdots,N)
\end{aligned} \tag{4.12}$$

where indices i and i+1/2 represent original- and half- meshpoints, Δx_i and $\Delta\tilde{x}_i$ the distances between the original- and half-meshpoints, respectively. A numerical constant, c, varies from zero to unity depending on the implicit scheme used: the scheme c=1/2 is a usual Crank-Nicolson-type implicit scheme, and c=1 is a backward Euler. The coefficient matrix of these simultaneous equations (4.11) is basically sparse (except for the unknown collision term) although it is not symmetric and contains complex elements. This contrasts with the fact that the coefficient matrix in the Wigner-function formalism is generally dense. The discretized Wigner function requires storage proportional to $N_xN_k^2$ [9] where N_x and N_k represent numbers of meshpoints in the position and momentum spaces, while the density matrix equation only necessitates storage proportional to N^2 where N represents the number of meshpoints in x and x' dimensions. Thus, from the viewpoint of numerical calculation, the density matrix formalism has the great advantage of saving computational memory. By converting these N complex equations into 2N equations with real coefficients, equation (4.11) can be solved by several methods for sparse linear systems. We adopt here the conjugate gradient method for non-symmetric sparse matrices.

The collision term, $C_{col}\rho$, which introduces dissipation processes and causes time-irreversibility of the system, is a nontrivial part of the quantum transport theory. Several discussions have been reported on the collision term in the density matrix formalism. First, an accurate quantum-mechanical expression for electron-phonon interaction was reported by Levinson [23]. He derived the closed equation for the density matrix of electrons which are weakly interacting with equilibrium phonons. In his formula, however, the interaction term involves time integrations (i.e. the past history of the system), for which numerical calculations are non-trivial. Second, a semi-classical model was proposed by Caldeira and Legget [24] relating to the theory of quantum Brownian motion:

$$C_{col}\rho(x,x';t) = -\gamma(x-x')\left(\frac{\partial\rho(x,x';t)}{\partial x} - \frac{\partial\rho(x,x';t)}{\partial x}\right) - \frac{2m^*\gamma k_BT}{\hbar^2}(x-x')^2\rho(x,x';t) \quad (4.13)$$

where γ is the coupling constant of electrons to a reservoir system. Although the expression is simple enough to be applied to numerical simulations, it is verified that this model is only correct when thermal energy, k_BT, is much larger than the coupling energy between the electrons and the reservoir. Third, the simplest model for the collision term is a well-known relaxation-time approximation:

$$C_{col}\rho(x,x';t) = \frac{\rho(x,x';t) - \rho_{QE}(x,x')}{\tau_s} \quad (4.14)$$

where ρ_{QE} is the quasi-equilibrium density matrix under an external bias, and τ_s is a macroscopic relaxation-time parameter which represents all of the scattering processes. In the present work, we choose the relaxation-time approximation because of its simplicity in numerical calculations. One difficulty with the use of this approximation for a real device is the fact that the distribution of electrons varies with position and external bias. Equation (4.13) has an effect on the position-space distribution of electrons and, if the thermal equilibrium density matrix ρ_0 is used directly as ρ_{QE}, this results in a breaking of the current continuity. Obviously, an adequate model for ρ_{QE} is necessary which has the same electron distribution as $\rho(x,x';t)$. The following approximation for ρ_{QE} has been proposed by Frensley [17] assuming Boltzmann statistics for electrons:

$$\rho_{QE}(x,x';t) = \sqrt{\rho(x,x;t)\,\rho(x',x';t)}\;\exp\left\{-\,(x - x')^2/\lambda_T^2\right\} \tag{4.15}$$

This expression is easily found to be correct for the thermally distributed free-electrons, but its general justification might rely on the fact that Eq. (4.15) reproduces the correct thermal equilibrium density matrix given by Eq. (4.1) [17]. In the present work, we adopt Eq. (4.15) for ρ_{QE} by adding a numerical correction for the difference between Boltzmann and Fermi-Dirac distributions. The resultant expression gives us a quantitatively proper reproduction of off-diagonal elements of ρ_0 in thermal equilibrium.

The ohmic contact boundary condition for the density matrix is also an active field of study in the quantum transport theory in connection with the time-irreversibility of quantum devices. The density matrix elements on boundaries represent correlations between wavefunctions at an electrode and at all other points in the device. Obviously, Dirichlet-type boundary conditions cannot be used on the density matrix because it means that quantum current density at the ohmic contact is fixed from the beginning (see Eq. (4.11)). This fact is one of the big problems of the density matrix method in contrast to the Wigner function formalism where the so-called time-irreversible boundary condition [9],[25] has been proposed. One possible solution is to use Neumann-type boundary conditions. Frensley [17],[25] proposed the following special boundary condition:

$$\left(\frac{\partial}{\partial x} + \frac{\partial}{\partial x'}\right)\rho(x,x';t)\bigg|_{\text{boundary}} = 0 \tag{4.16}$$

for the density matrix taking account of the symmetry of the density matrix for thermally distributed free electrons (see Eq. (4.5)). From the physical point of view, this boundary condition models a black-body contact which absorbs incoming electron-waves. The boundary condition (4.16) conserves electron density at the device edge when external bias is applied to the device. Thus, it is suitable to describe the boundary of the so-called ohmic region near electrodes where free electrons are thermally distributed. This boundary condition, however, cannot be used for the whole boundary because it is correct only when the system has at least approximately translational invariance. For example, it is successfully applied to simple structures such as n^+ - n^- - n^+ diodes where the electron-wavefunctions are spatially widespread over the system, and the wavenumber **k** is a good quantum number. Typical quantum device structures, however, such as finite superlattices and quantum wells make (quasi-)bound electron states and are no longer translationally invariant except in the ohmic regions near the emitter and collector electrodes. The correlations between those localised electrons and free electrons in the emitter and collector layers are long-range, and the density matrix varies along x and x' directions rather than the cross-diagonal direction. In these cases, therefore, the following Neumann boundary conditions

$$\left.\frac{\partial \rho(x,x';t)}{\partial x}\right|_{x=0,\,L} = 0$$
$$\left.\frac{\partial \rho(x,x';t)}{\partial x'}\right|_{x'=0,\,L} = 0 \qquad (4.17)$$

are plausible rather than the boundary condition (4.16). These boundary conditions physically mean that there is no source at the electrodes to have an influence on the correlation function within the device. In the present work, we divide the system into two parts: the ohmic region which is now defined as the n^+-GaAs region of 20 nm in thickness, and the essential double-barrier region (with spacer layers) causing quantum mechanical effects. The boundary condition (4.16) is used only for the boundaries of the ohmic regions, and those of the active region are treated by using Eq. (4.17).

4.2.2 Femtosecond electron dynamics in RTDs

In this section the transient behaviour of the resonant tunnelling diode under an applied bias is simulated numerically by solving the discretized density matrix equation (4.12). The equilibrium density matrix obtained in Sec. 4.2.1 is used as an initial condition, and the spatial mesh grid shown in Fig. 4.7 is adopted. The new Neumann-type boundary condition described in the previous section is implemented to solve the density matrix equation.

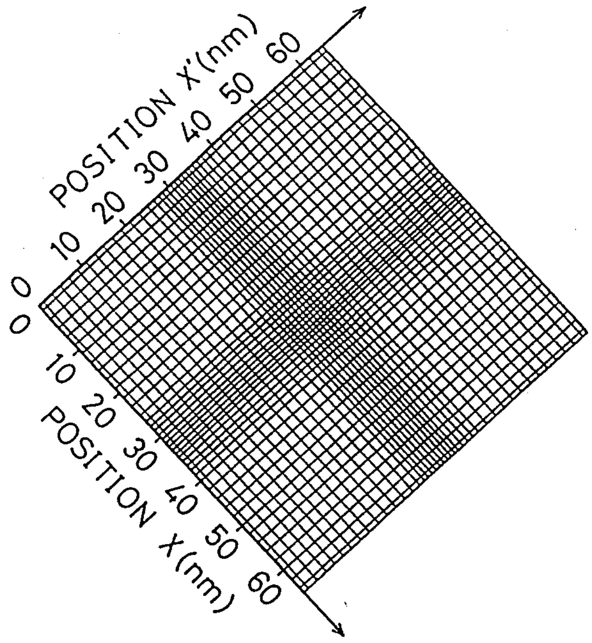

***Figure 4.7** Position mesh grid used for the density matrix of the double barrier RTD. Mesh spacing has been chosen to be small for AlGaAs barriers and the GaAs quantum well.*

In the present calculations values of 1.0 to 2.0 femtoseconds are used for the time step, Δt, which are small enough to represent the transient response of the resonant tunnelling diode. The relaxation-time parameter, τ_s, due to scattering is typically set to be 100 femtoseconds, which corresponds to a mobility of 2600 $cm^2V^{-1}sec^{-1}$ for n-GaAs with donor concentration of 1×10^{18} cm^{-3} at room temperature. The density matrix, potential profile, and current density calculated by using Eq. (4.11) are monitored to see the convergence of the system to a steady state. The correctness of the thermal equilibrium density matrix as an initial condition is continually checked by solving the density matrix equation under zero applied voltage. The maximum errors in the potential profile and current density under zero bias are less than 1.0 meV and 1.0 A/cm^2 at a time of 1500 femtoseconds, respectively. These are small enough to assure the propriety of evaluated values under an applied voltage. The transient calculation has been done on a DECsystem 5810 (18.7 MIPS machine) and usually required approximately 180 minutes of CPU time to reach a steady state.

The calculated transient response of the density matrix for the resonant tunnelling diode is shown in Figs. 4.8 and 4.9. These figures show the evolution of the real (Fig. 4.8) and imaginary (Fig. 4.9) parts of the density matrix at time t after an external voltage of 120 mV, corresponding to the peak voltage of the device, is suddenly applied at t=0: (a) at t=50 fsec;

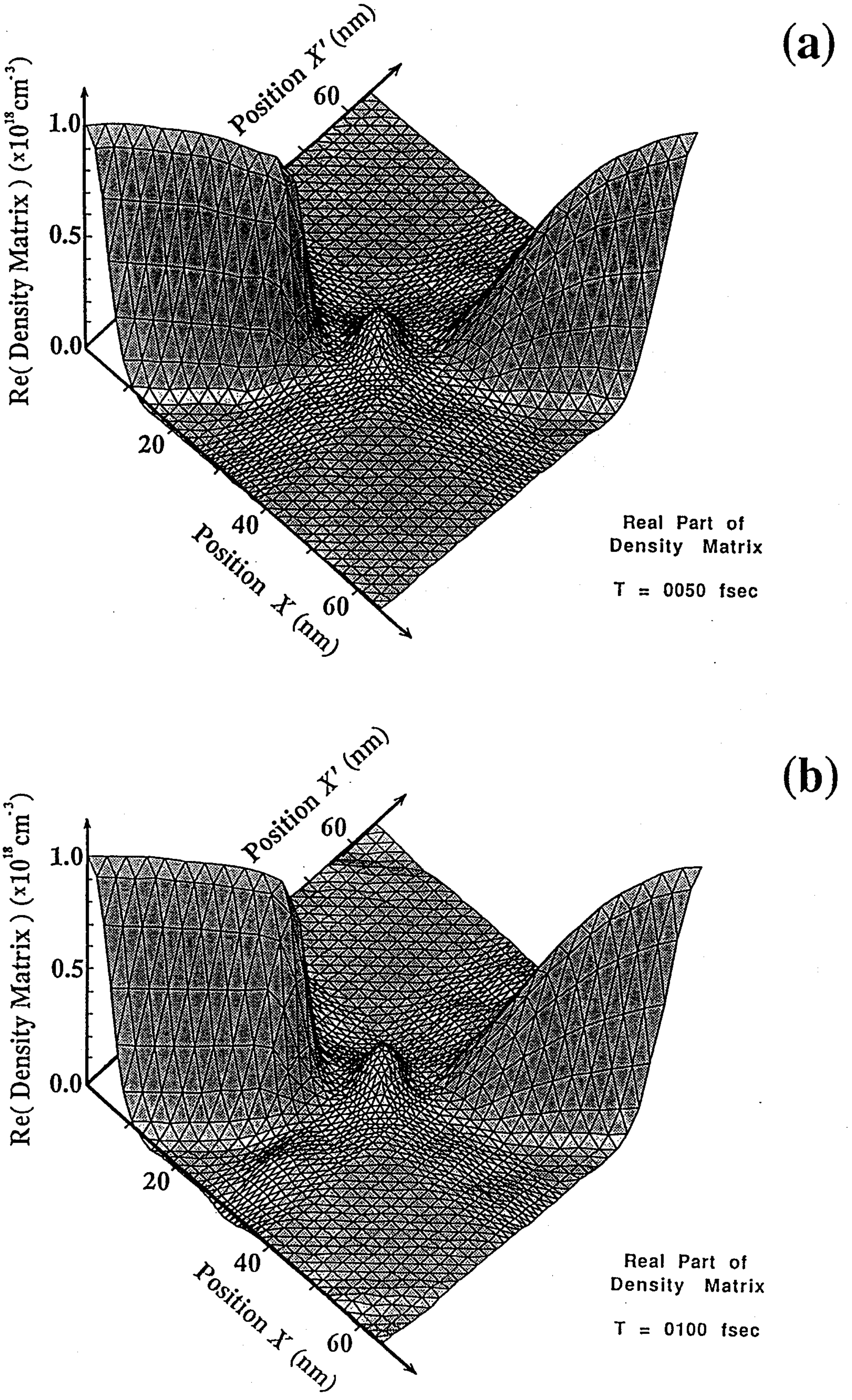

Figure 4.8 Real parts of the density matrix at various times under an applied bias of 120mV: (a) at 50 fsec; (b) at 100 fsec; (c) at 200 fsec; (d) at 600 fsec; and (e) at 1000 fsec. It can be seen that density of electrons accumulated in the quantum well increases with time. Electron depletion in the collector layer and accumulation in the emitter layer can be seen.

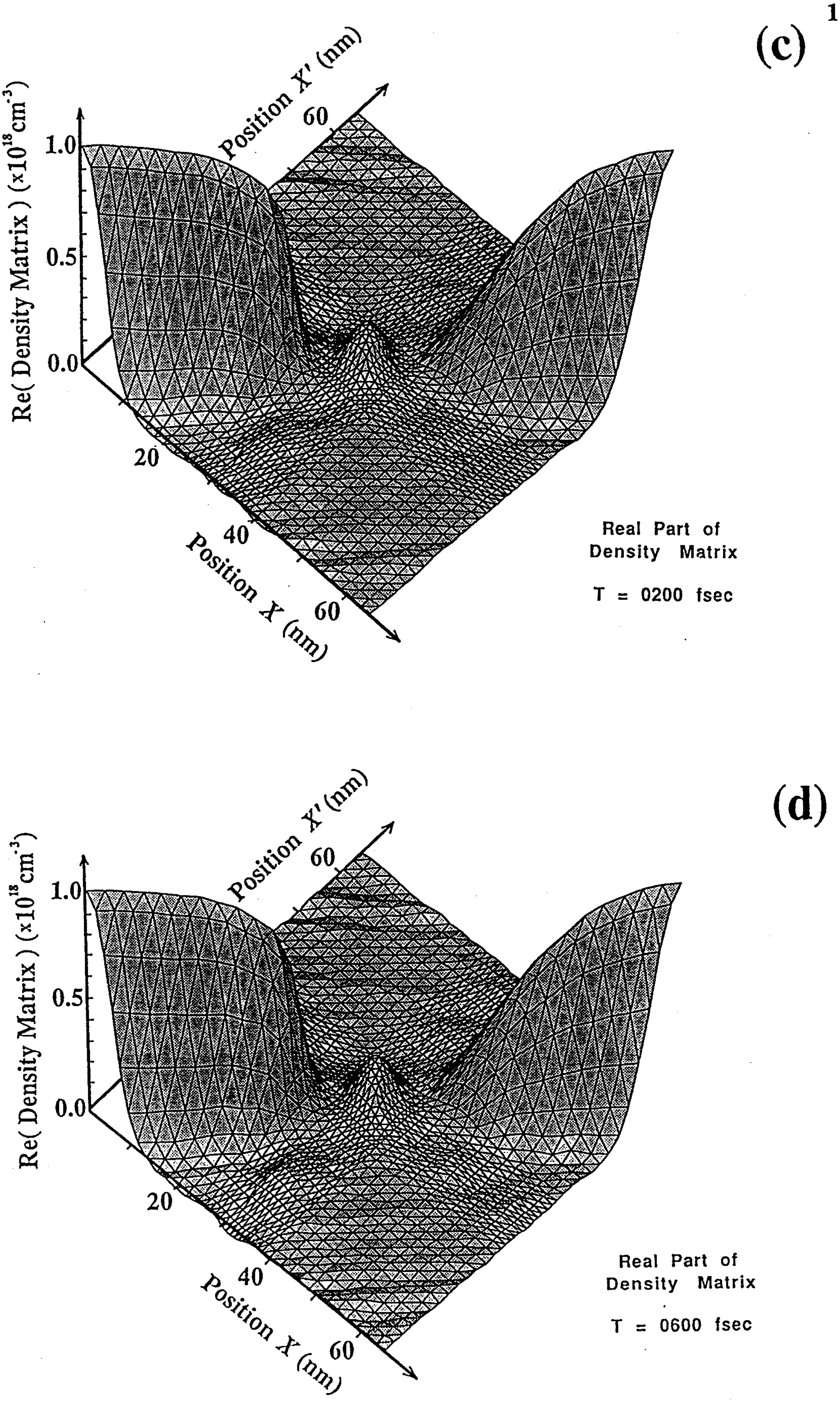

Figure 4.8 Continued.

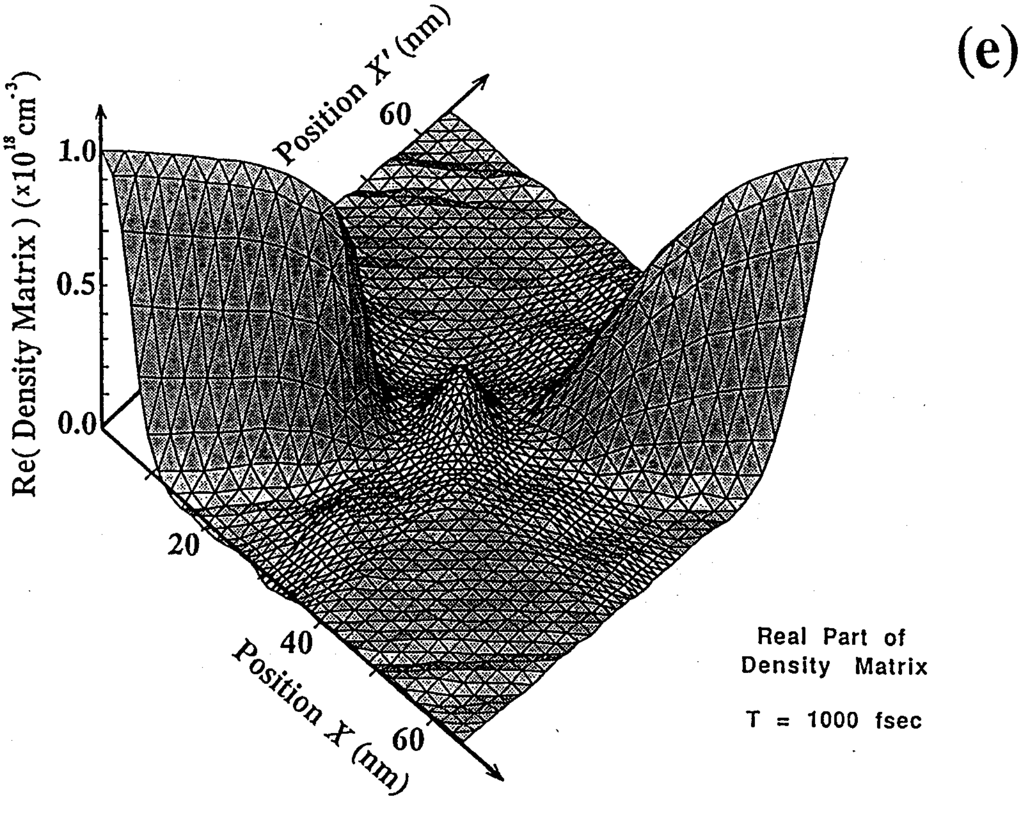

Figure 4.8 continued

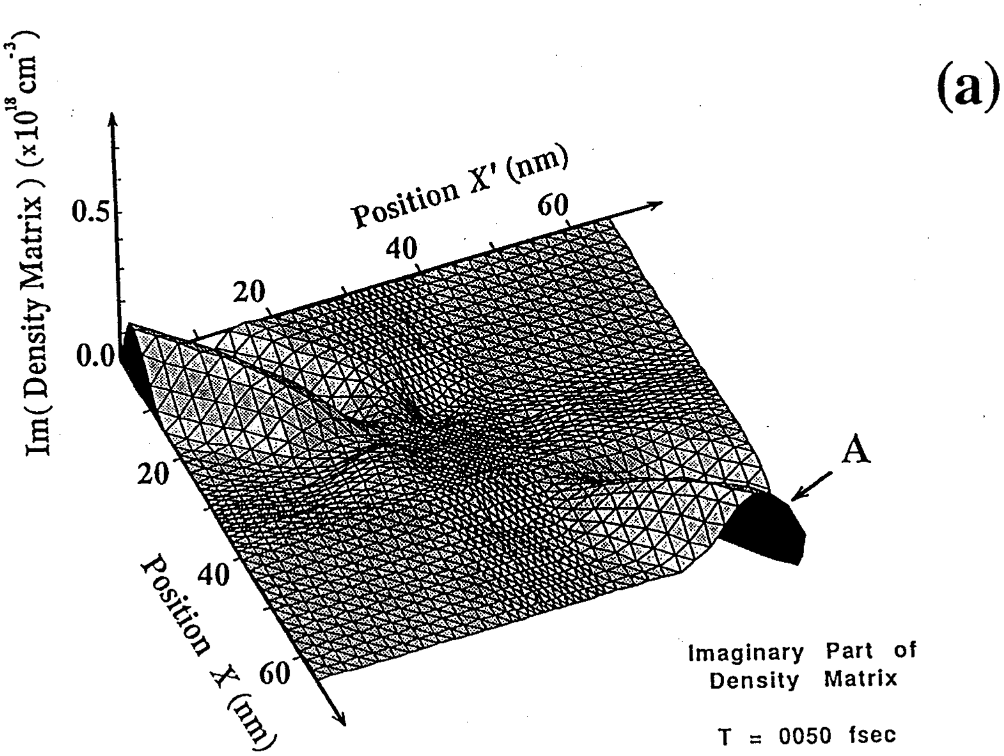

Figure 4.9 Imaginary parts of the density matrix at the same times as in Fig. 4.8. Large cross-diagonal variation (indicated by A) represents plasma oscillation. The remarkable oscillatory feature (indicated by B in (e)) measures quantum interference between the resonant-tunnelling electron and free electrons in the emitter and collector.

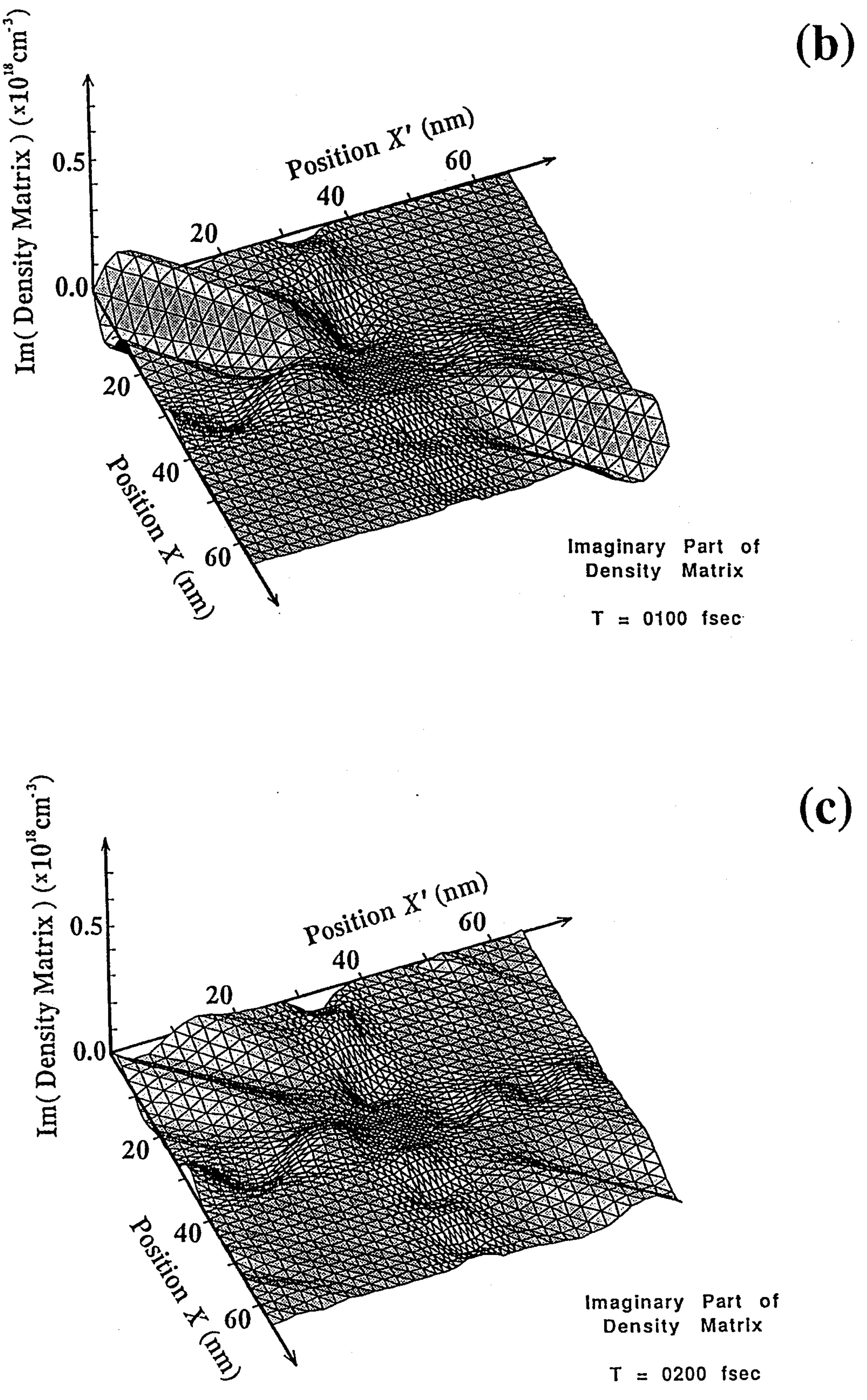

Figure 4.9 continued.

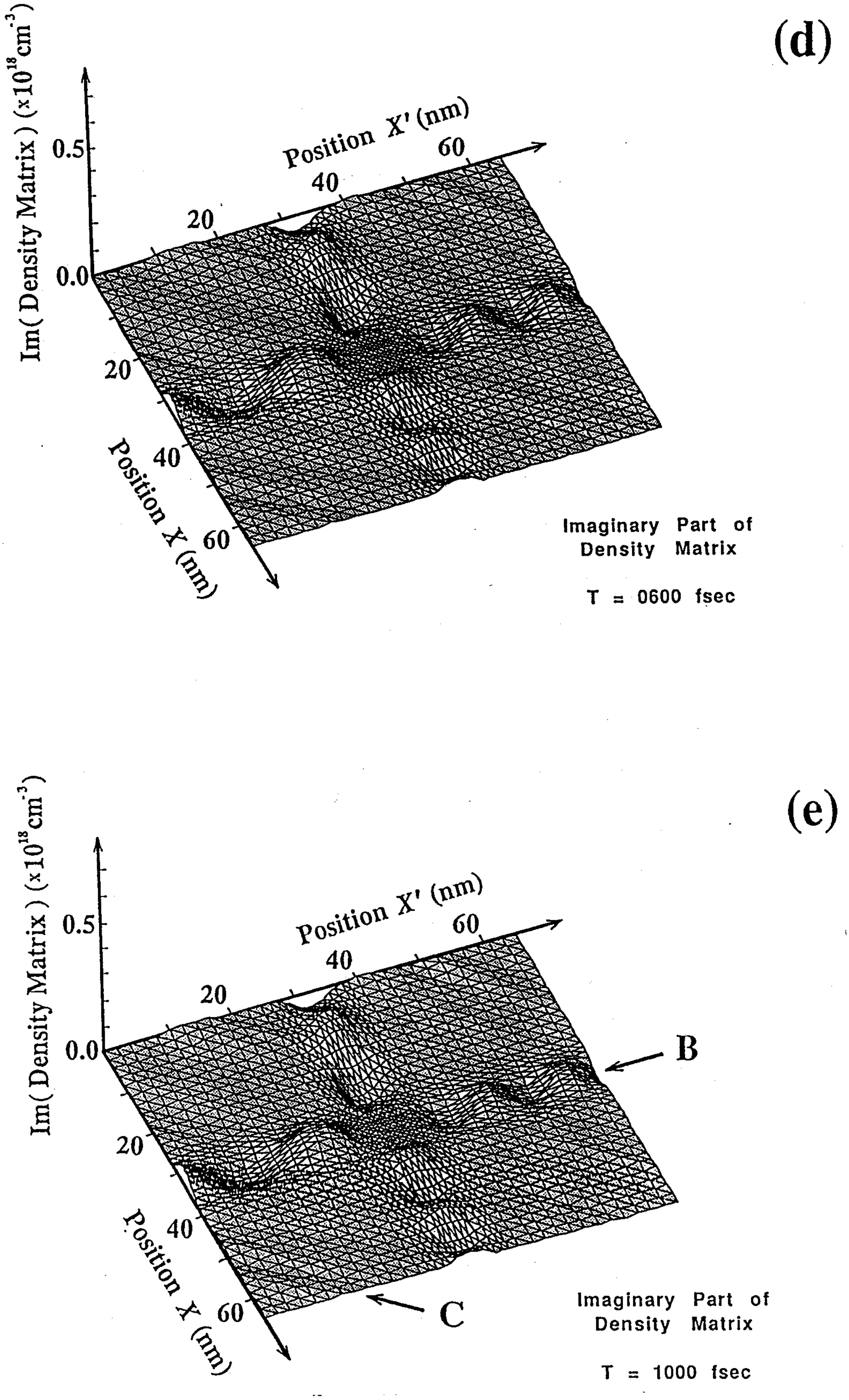

Figure 4.9 continued.

(b) at t=100 fsec; (c) at t=200 fsec; (d) at t=600 fsec; and (e) at t=1000 fsec. The system reaches the steady state at a time of about 1000 fsec, and no numerical instability [17] was observed. This is presumably because of improvements in the present model such as the self-consistent Hartree field, a correct initial condition, the new boundary condition, and the implicit scheme for time integration. The calculated density matrix enables us to observe not only the time-dependent variation of the electron distribution but also that of the electron correlations in the system. The diagonal of the real parts shows time-dependence of electron-build-up in the quantum well as well as that of electron accumulation in the emitter region and depletion in the collector region. In the steady state, peak concentration of electrons in the quantum well amounts to 2.5×10^{17} cm^{-3} . In Figs. 4.8 and 4.9, three major features should be noticed on the off-diagonal elements of the density matrix. The large cross-diagonal structure (indicated by point A in Fig. 4.9 (a)) in the imaginary parts represents short-range phase-correlations, which cause plasma current oscillations. If the momentum-space representation is used instead of the position-space representation, it is equivalent to the centre of the distribution function oscillating along the momentum axis. In other words, electrons are in collective motion in the emitter and collector regions . This phenomenon can be also observed as an oscillation of real electron density (the diagonal of Fig. 4.8).

The most remarkable feature is an oscillatory behaviour of the imaginary parts (indicated by point B in Fig. 4.9 (e)). It should be noted that this extends from the centre to the edges of the domain. It is caused by a quantum interference between the quasi-bound electron-waves at the resonant state and free electron-waves in the emitter and collector layers. We believe this to be the first direct observation of the dynamical correlations of the electron-waves in the resonant tunnelling diode under an applied voltage. The calculated results reveal that the electron-waves at the resonant state correlate with free electron-waves over the whole device. In other words, the phase-coherence of the resonant electron-waves is still maintained although they are suffering from degradation of coherence due to scattering. The relation between amplitude of the oscillation and the scattering relaxation time is discussed in the next section. Another oscillatory behaviour along the diagonal direction (indicated by point C in Fig. 4.9 (e)) represents correlations between free electrons in the emitter and collector regions by normal tunnelling through the double barriers, which can be observed even in a single barrier structure.

The corresponding transient current calculated by using equation (4.11) is shown in Fig. 4.10, and its interpretation is given below. Strictly speaking, the current density defined by equation (4.11) is correct only in the steady state since we do not include the time-dependent displacement current . Because of this simplification, the transient current density has a positional dependence in Fig. 4.10: the current density at the emitter edge, the collector edge, and in the quantum well are shown by a solid line, a broken line, and a broken line with a dot, respectively. Although it is possible to calculate the displacement current from the time-derivative of the self-consistent Hartree potential, we intentionally show only the time-dependence of the current caused by the change in electron density. The current density at the emitter edge (or the collector edge) can be regarded as the total current because the displacement current at the device edge is nearly zero.

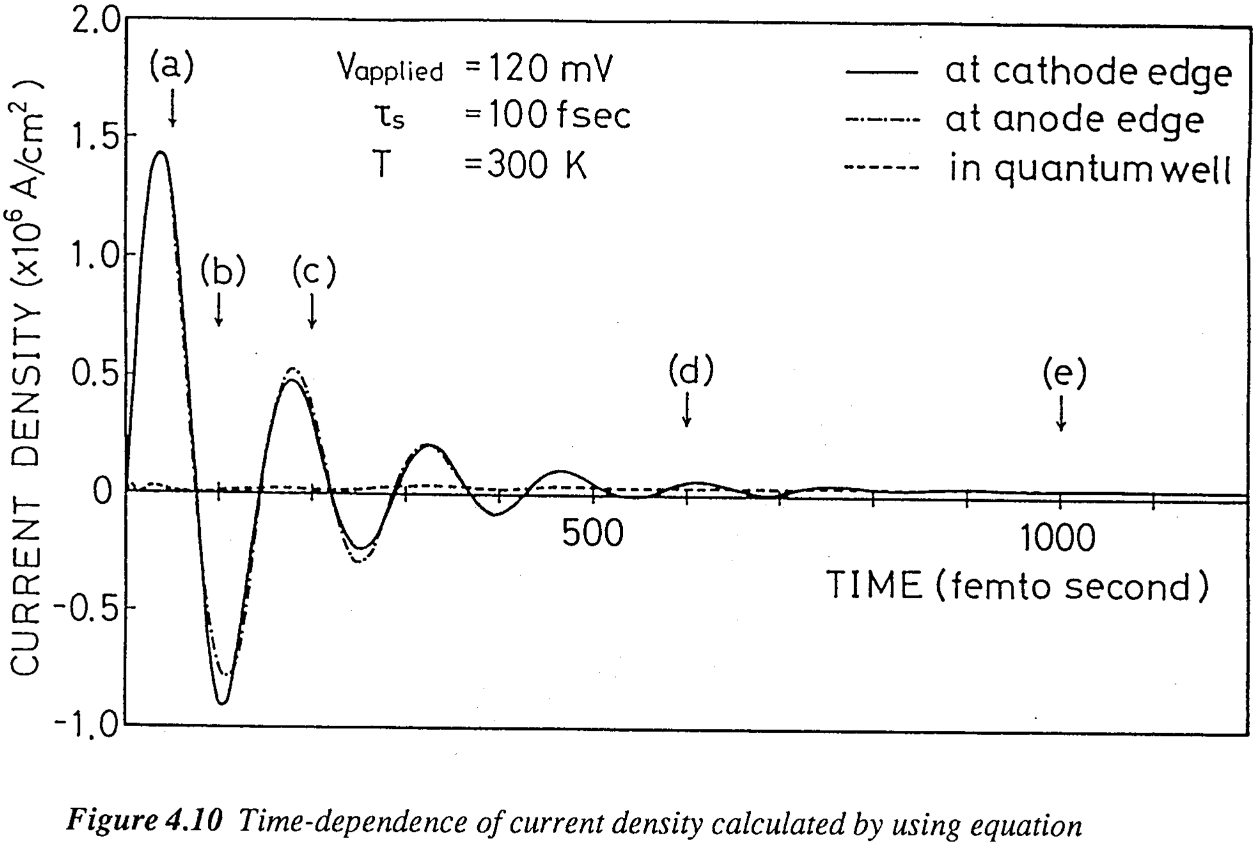

Figure 4.10 Time-dependence of current density calculated by using equation (4.11). Current densities at different positions in the device are monitored versus time: at the emitter edge (solid line); at the collector edge (broken line); and in the quantum well (broken line with a dot). The first arrows in the figure ((a) - (e)) indicate the times when the real and imaginary parts of the density matrix were drawn in Fig. 4.8 and 4.9.

As described above, large current oscillation is observed in Fig. 4.10 as a result of a plasma-type motion of electrons in the emitter and collector regions, which was seen in the imaginary parts of the density matrix(Figs. 4.9(a) ~ (e)). The period of the current oscillation of about 150 fsec is mainly determined by the density and effective mass of electrons in the emitter and collector layer. The system reaches the steady state at a time of about 1000 fsec, resulting in the steady current of 3.1×10^4 A/cm^2. It should be noted that the first peak-current of the plasma oscillation is more than one order of magnitude larger than the steady current.

The corresponding transient Wigner distribution functions defined by Eq. (4.2) are also shown in Fig. 4.11 in a position-wavenumber plane as the classical distribution functions. Space-charge build up in the quantum well as well as in the emitter region explained above can be seen in these figures. In addition current plasma oscillation observed above is seen as a variation in the Wigner distribution functions in the emitter and collector regions.

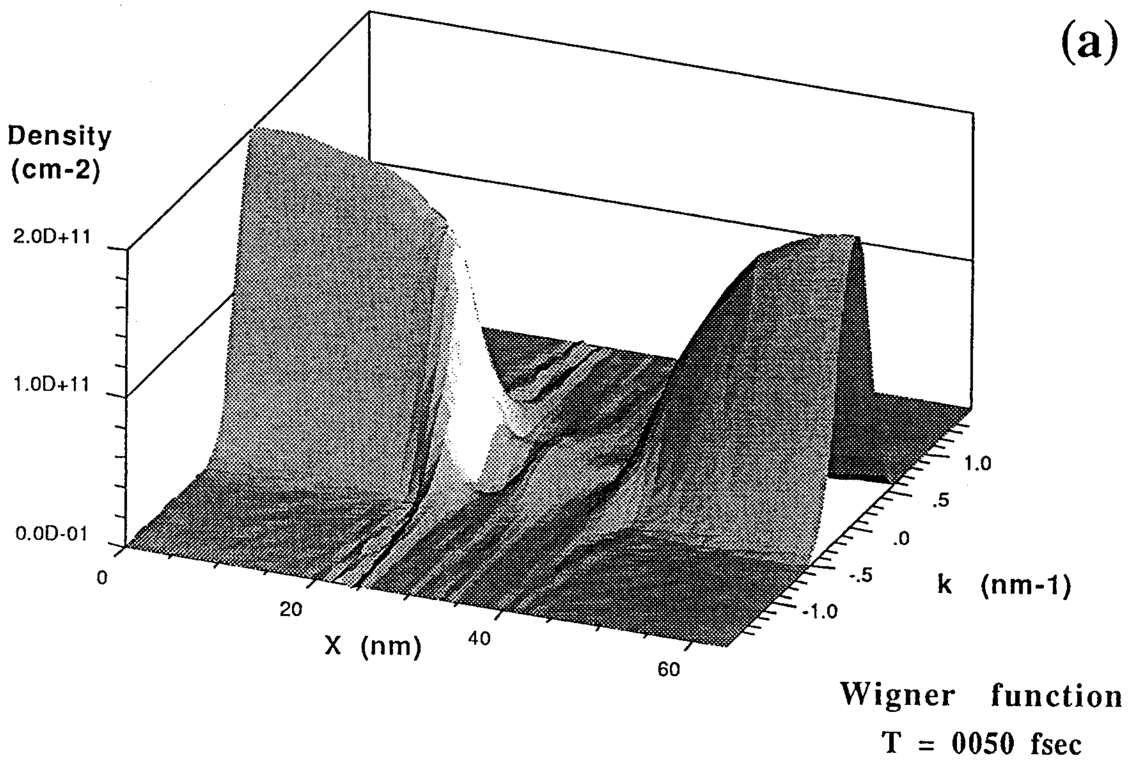

Figure 4.11 Transient Wigner distribution functions calculated at the same times as in Fig. 4.8 and 4.9 by using Eq. (4.2): (a) at 50 fsec; (b) at 100 fsec; (c) at 200 fsec; (d) at 600 fsec; and (e) at 1000 fsec.

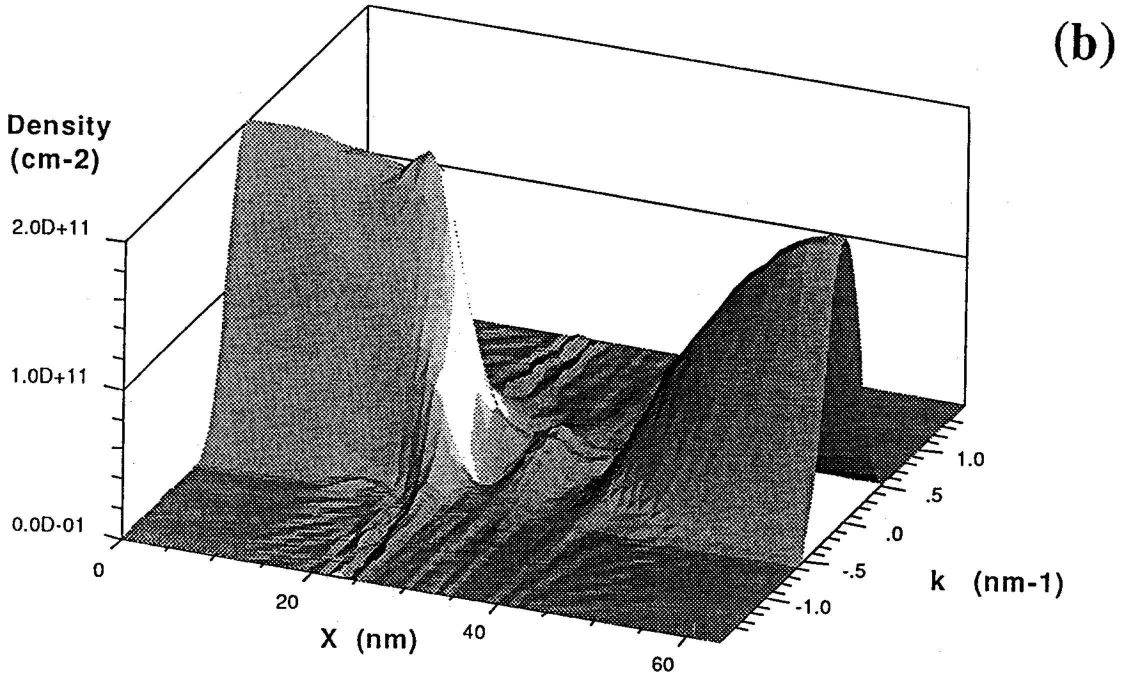

Wigner function
T = 0100 fsec

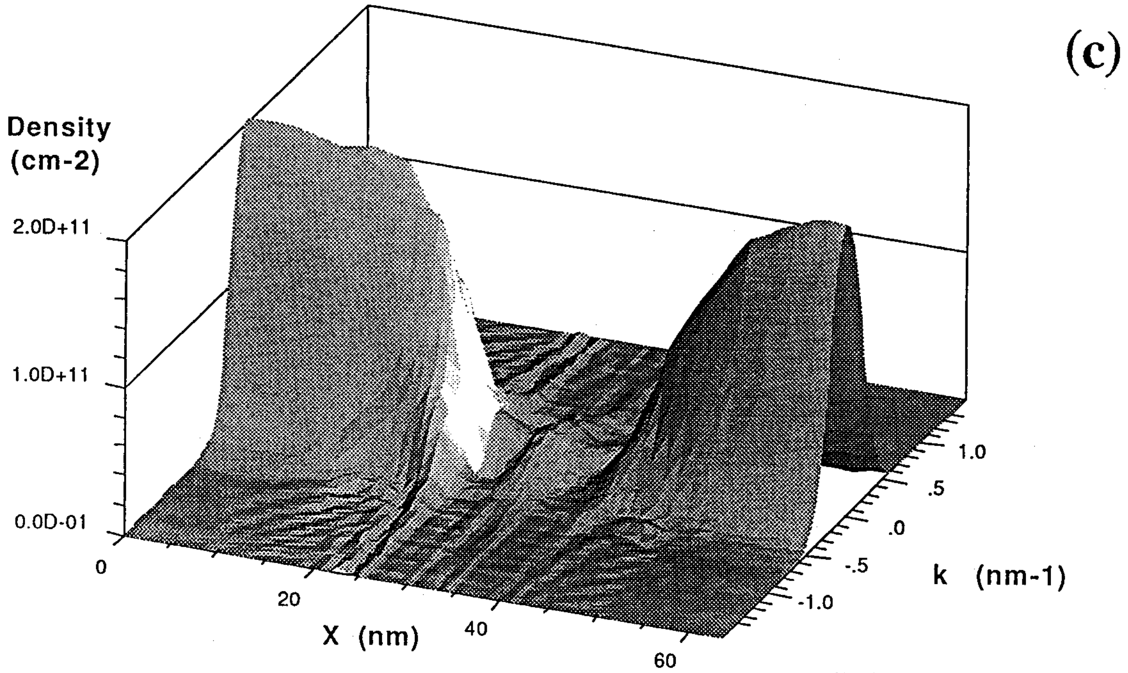

Wigner function
T = 0200 fsec

Figure 4.11 continued.

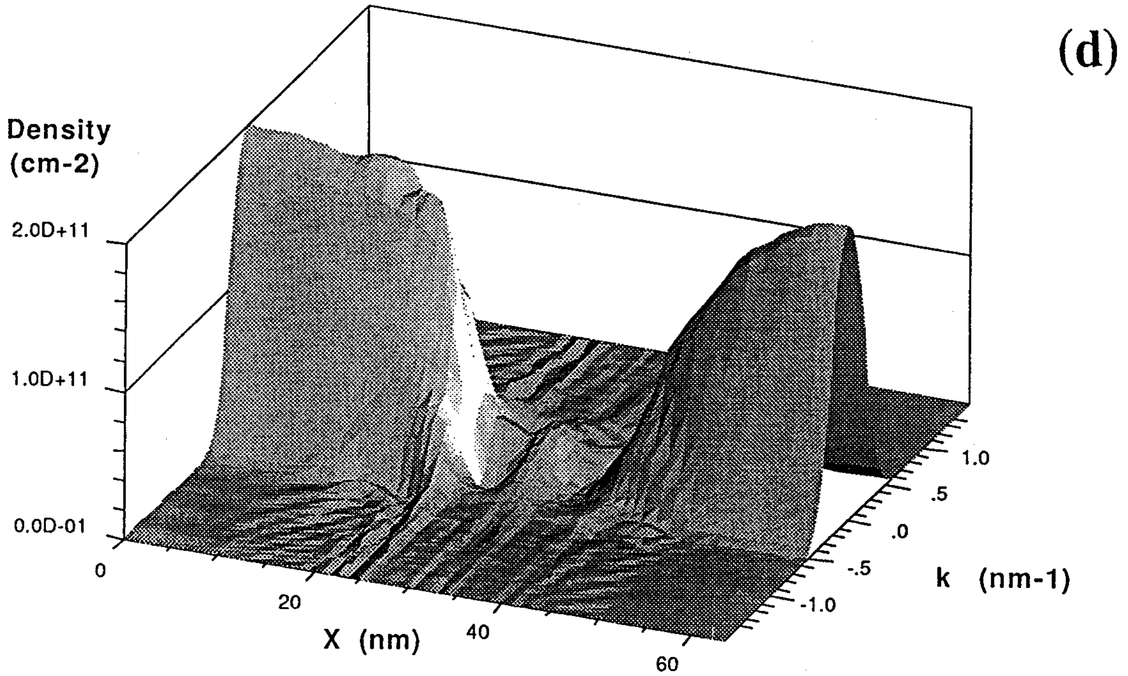

Wigner function
T = 0600 fsec

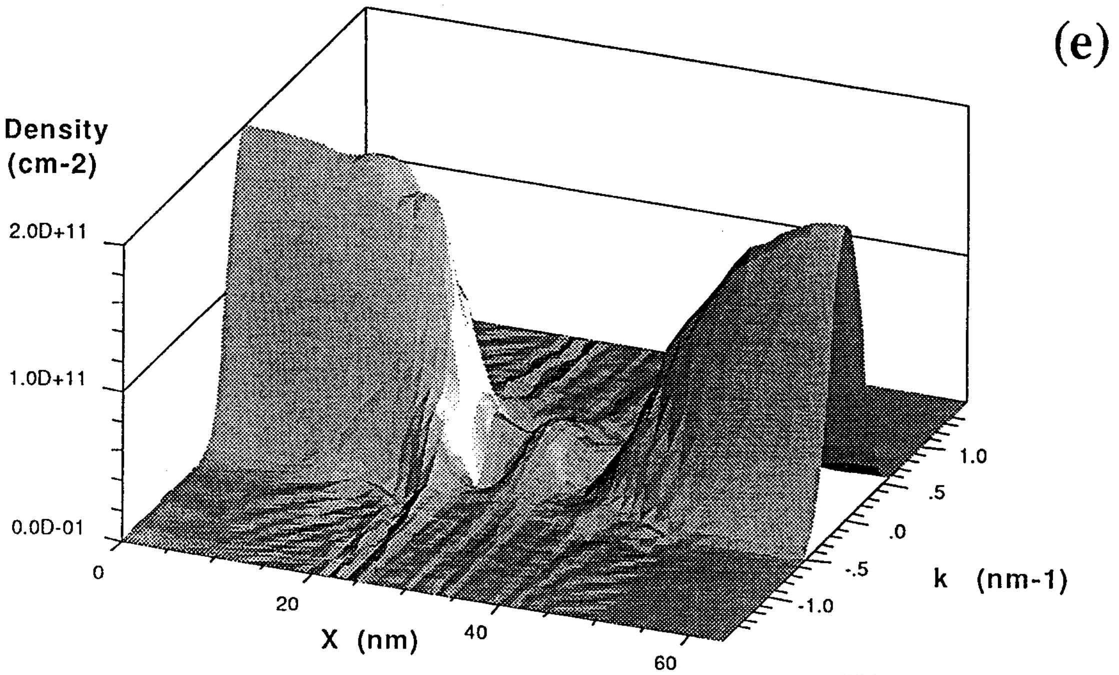

Wigner function
T = 1000 fsec

Figure 4.11 continued.

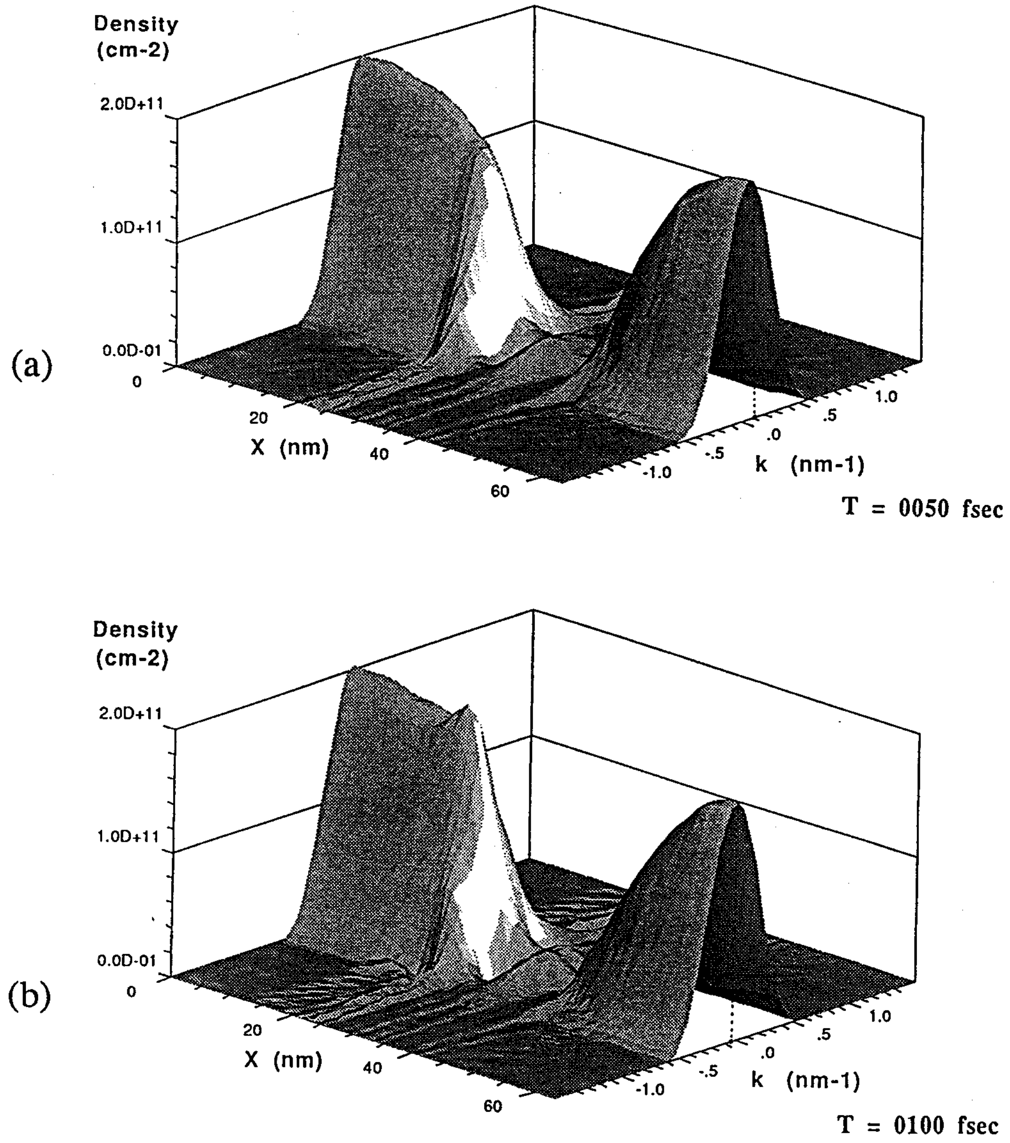

Figure 4.12 *Wigner distribution functions at 50 fsec (a) and 100 fsec (b) seen from a different angle from those in Fig. 4.11.*

The Wigner functions at T = 50 fsec and 100 fsec seen from a different angle are shown in Fig. 4.12(a) and (b). It can be seen that the centre of the distribution function at the edge of the device is displaced from the origin of the k-axis representing the current flow. Comparing Figs. 4.12(a) and (b) it is found that the overall distribution function shifts along the k-axis depending on a time. This actually demonstrates that electrons in the highly doped emitter and collector regions are in a collective mode, plasma oscillation, resulting in the current oscillation in Fig. 4.10.

Calculated switching behaviours of the device with spacer layers are also shown in Fig. 4.13. Figure 4.13 (a) shows the current transient when the initial bias of 115 mV, corresponding to the peak voltage, is suddenly switched to 170 mV, corresponding to the valley voltage. The initial state at t=0 is a steady state under an applied bias of 115 mV, which was obtained as a result of continuous transient calculations with an small applied bias as described above (see inset in Fig. 4.13 (a)).

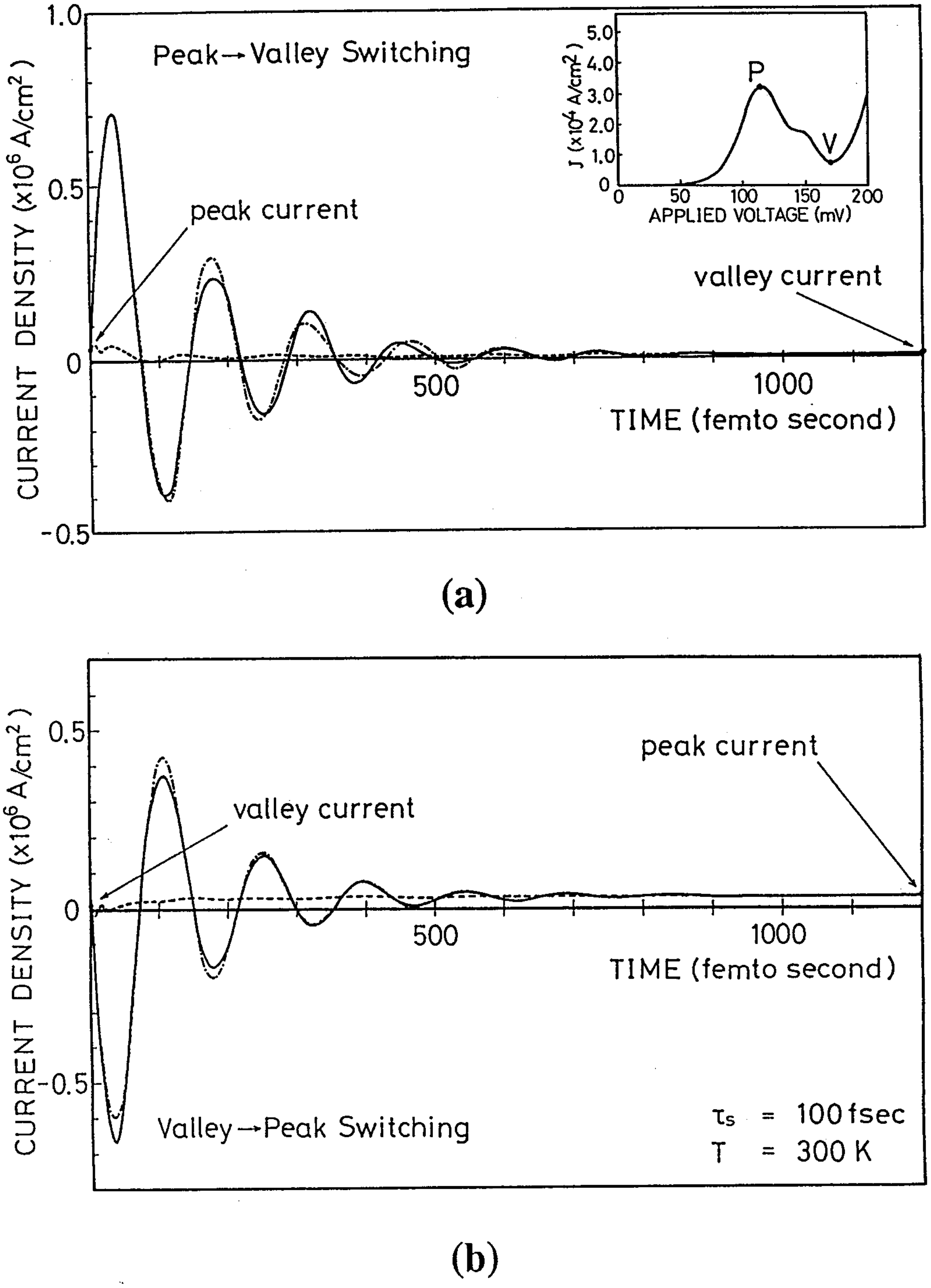

Figure 4.13 Time-dependence of current density for (a) peak-to-valley and (b) valley-to-peak switching of the device with spacer layers (see inset in (a)).

The meanings of three lines in these figures are the same as in Fig. 4.10. Plasma current oscillation with the same period as Fig. 4.10 is observed in the emitter and collector layers. The time-dependence of current density in the quantum well shows small oscillatory behaviour within some tens of femtoseconds. Because a similar rapid current transient has been observed in Wigner function calculations which neglect the self-consistent Hartree potential [9], this can be considered to arise from the rapid change in density of electrons accumulated in the quantum well after a sudden increase in applied voltage. The current transient for the reverse switching is shown in Fig. 4.13(b). The applied bias is suddenly switched from 170 mV to 115 mV. The current density initially drops, and then oscillates with almost the same period as in (a). For both peak-to-valley and valley-to-peak switching, the device reaches the steady-state at about one thousand femtoseconds, and the switching time is mainly determined by the plasma current oscillation which is a result of introducing the Hartree self-consistent field.

4.3 Space-charge build-up in a quantum well and intrinsic current bistability

4.3.1 Numerical analysis of intrinsic bistability

As mentioned in Chapter 3 double barrier RTDs frequently exhibit current hysteresis in their NDC regime which have given rise to heated controversies about its origin over a few years. One simple origin of the hysteresis is, as easily understood, current oscillation seen in the whole system which consists of this sort of NDC devices and series resistance in the extrinsic parts. This circuit-induced current bistability is exceedingly common among NDC devices and not characteristic to RTDs at all: This is thus called *extrinsic bistability* [26],[27] to distinguish it from another bistability which is significant from a physical point of view. A simple way to get rid of the extrinsic bistability and observe intrinsic characteristics is to connect a capacitor in parallel to the RTDs. In 1987 Goldman et al. [16] have first reported a different kind of current bistability which can be seen even after suppressing the oscillations. They termed it *intrinsic bistability* and ascribed it to dynamical charge build-up in the quantum well. Figures 4.14 (a) and 4.14 (b) show I-V characteristics near the first resonance for Samples 2 and 3, respectively. Both samples show a clear hysteresis. The fact that the hysteresis is similar in both cases, even though the currents are a factor of 100 different, suggests that it cannot be attributed to the extrinsic effects of series resistance.

Let's start with the following simple discussion based on continuity of tunnelling current. The sheet concentration of the electrons accumulated in the well, σ_w, can be expressed by using density of the resonant tunnelling current, J, and the tunnelling escape time, τ_{esc}, of electrons in the well introduced in Sec. 3.2.1:

$$\sigma_w = \frac{J\cdot\tau_{esc}}{e} \tag{4.18}$$

This means that σ_w has a feedback dependence on the tunnelling current. The electrostatic interactions between the electrons accumulated in the well give rise to the energy shift of the quasi-bound state in the well leading to the change in the tunnelling current. Thus there is a possibility, at least qualitatively, of having two stable states of the device, high current with large accumulation and low current with small accumulation, in some voltage regime though numerical calculations are obviously necessary for further discussions on this issue.

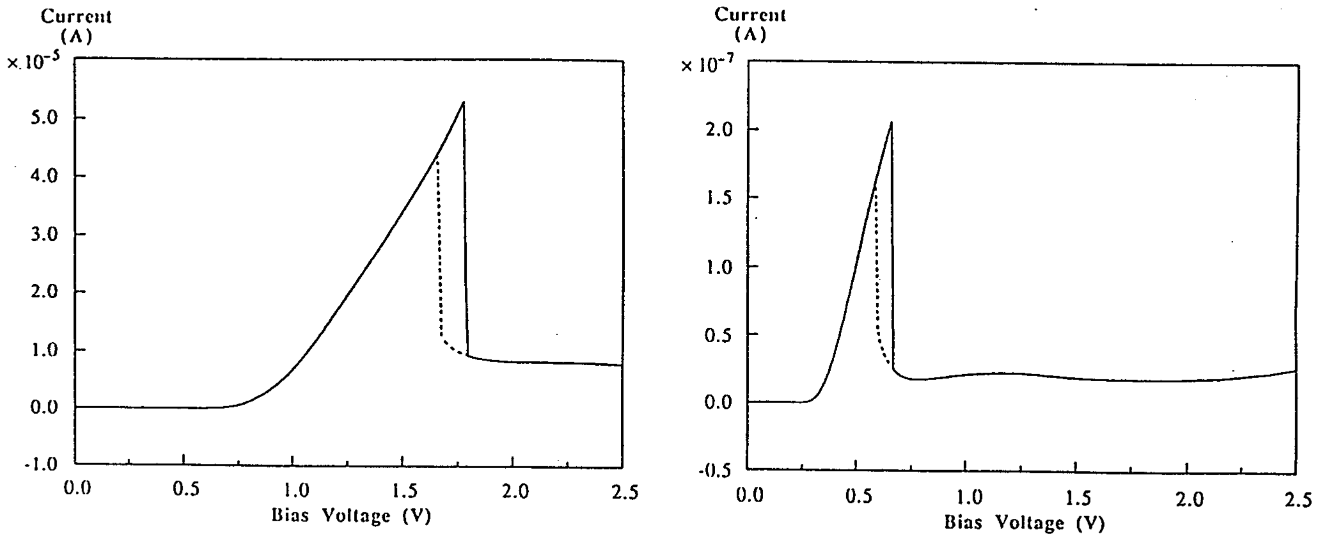

(a) (b)

Figure 4.14 I-V characteristics for Samples 2 (a) and 3 (b)at 4.2K. The bias voltage was swept in both directions to show the hysteresis - the solid lines are for increasing voltage and the dashed line for decreasing voltage. where the lines overlay, only the solid curve is shown.

In parallel to the experimental work by Goldman et al. several theoretical studies has been also reported to demonstrate the possibility of the space charge build-up: analysis based on the self-consistent calculations of tunnelling current (see Sec. 3.2.2) by Berkowtz et al [28], Mains et al [29] and more analytical calculations based on the rate equation for the electron occupancies in the well conducted by Sheard et al [30] are pioneering works to demonstrate the space charge build-up phenomenon inherent to RTDs. In these works the electrons stored in the well have been evaluated in two extreme situations, i.e. the global coherent tunnelling and incoherent sequential tunnelling limits. Recent numerical simulations [10],[22],[31] based on the quantum transport theory shown in the previous section facilitates us to investigate the dynamics of tunnelling electrons in the more realistic intermediate non-equilibrium regime. Figure 4.15 shows the I-V characteristics of the device calculated at room temperature by using the density matrix theory described in Sec. 4.2.1. The steady-state I-V characteristics have been obtained by repeating the transient calculations shown in Sec. 4.2.2. First, a small external voltage, which is typically 5 to 10 mV, is applied to the device in thermal equilibrium. The current value after a time of 1500 fsec is stored as a steady-state current, and then the same step voltage is applied to this steady-state value. This process is repeated until the external bias reaches its maximum value. The I-V characteristics of the device without a spacer layer (thicknesses of highly doped n-type GaAs emitter and collector layers set to 24 nm) is also shown in this figure. Then the potential is decreased by applying a small negative bias to observe any hysteresis in the I-V characteristics. The peak voltage of the device with the spacer layers becomes larger than that without spacer layers because of the large voltage drop across them. The calculations in the negative differential resistance (NDR) regions are found to be slightly unstable compared with the positive differential resistance regions, and longer calculations were generally required to reach the steady-state. Small intrinsic bistabilities in NDR regions are observed in both devices. In the case of the device with spacer layers it seems that, when bias is decreased, the I-V curve in the NDR region shifts towards a lower voltage. Figure 4.16 shows energy-band diagrams corresponding to the two stable states of the device for an external bias of 0.15 V. When the bias is increasing, electrons with sheet concentration of 2.1×10^{11} cm^{-2} are accumulated in the quantum well at this bias. However, in the case of decreasing bias, the electron concentration goes down to 1.5×10^{11} cm^{-2}. The difference in the space charge build-up leads to a different Hartree self-consistent field, and the bottom of the quantum well in the case of increasing bias is almost 10 meV higher than that in the case of decreasing bias.

Let's quickly take a look at the current shoulder in the NDR regions in Fig. 4.15. Similar structure has been sometimes observed experimentally in samples with large P/V current ratios, and several studies have been reported [32],[33] on *extrinsic instability* due to the bias circuit.

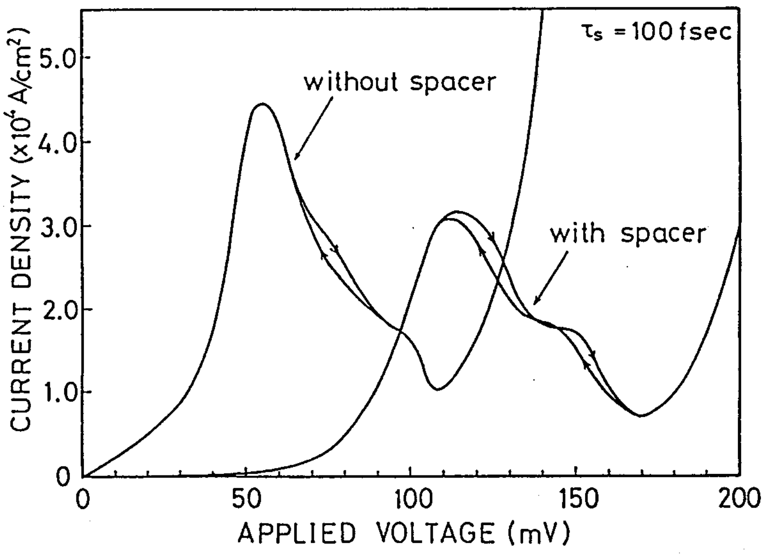

Figure 4.15 I-V characteristics calculated for RTDs with and without spacer layers. Applied bias is decreased after it reaches a maximum to see hysteresis. Bistability observed in the negative differential conductance region arises from dynamical electron redistribution in the quantum well.

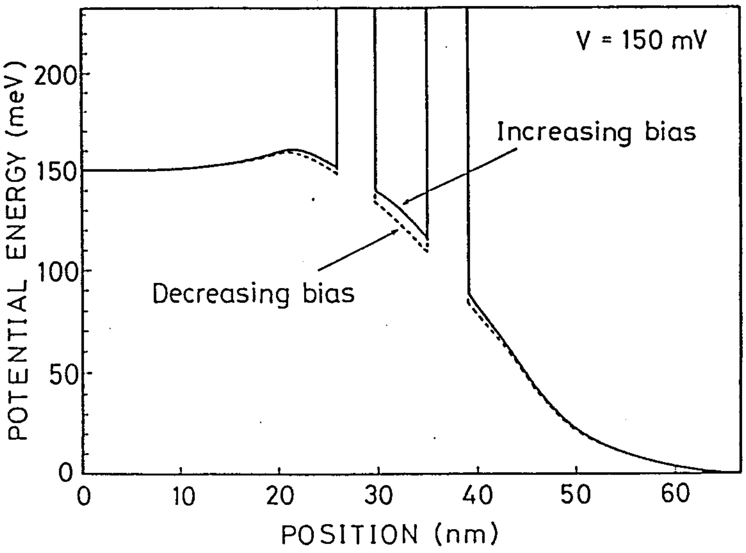

Figure 4.16 Self-consistent energy-band diagrams calculated at two stable states under an applied bias of 0.15 V. Upper curve corresponds to the larger current state, and the lower curve the smaller current state.

From macroscopic circuit theory, it has been revealed that the I-V characteristics of the RTD with a bias circuit have a current shoulder whose shape depends on LCR parameters of the external circuit [33]. Because dynamics of electrons not only in the quantum well but also in the emitter and collector regions are now simulated exactly, the present results might show the existence of *intrinsic instability* of the system. We found that this current shoulder in the NDR region depends on the scattering-relaxation time and generally vanishes with decreasing relaxation time. This fact implies that the structure is produced by the electrons undergoing coherent tunnelling and becomes small as the phase-coherence of the electron-waves degrades with increasing scattering. However the microscopic physical mechanism causing this structure is not clear at present, and further investigation is necessary.

Although the intrinsic bistability of symmetric double barrier RTDs have been well founded theoretically as shown here, its experimental observations have been a bit disputable because of the extrinsic bistability. A concrete experimental foundation of its existence was made by Alves et al. [34] and Leadbeater et al. [35] by the use of an *asymmetric* double barrier RTD (see Fig. 4.17). They have investigated the I-V characteristics of an $Al_{0.4}Ga_{0.6}As$(8.3 nm)/ GaAs(5.8 nm)/ $Al_{0.4}Ga_{0.6}As$(11.1 nm) double barrier RTD in both bias directions and found that the current bistability is observed only when the bias is applied so that the thicker barrier is on the collector side (this bias direction is defined reverse). The schematic energy band-diagram is shown in Fig. 4.17 at the first resonance in the reverse bias direction.

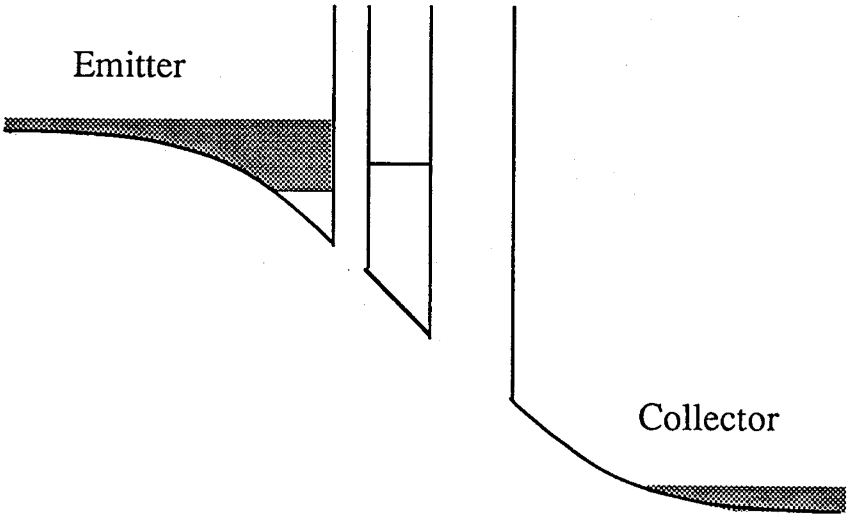

Figure 4.17 Schematic energy band-diagram of an asymmetric double barrier RTD proposed by E. S. Alves et al.

In these circumstances the electrons which tunnel through the thinner barrier are stored in the quantum well for a long time because of the next thicker barrier leading to the large space charge build-up. On the contrary, in the forward bias direction, the electrons are much less accumulated in the quantum well since the electrons tunnel through the thinner barrier quickly from the quantum well. By using this device it was found that the I-V characteristics exhibit current bistability only in the reverse bias direction. This observation have reconfirmed the existence of the intrinsic bistability caused by the space charge build-up in the quantum well.

4.3.2 Magnetotransport measurements on space charge build-up

A more direct evidence of the space charge build-up in RTDs has been obtained by using magnetotransport measurement technique: It has been demonstrated that the amount of electron accumulation can be determined by analyzing oscillations of current and capacitance seen in a magnetic field perpendicular to the barriers [36]-[40]. In this section this powerful technique is adopted for further investigation of the space-charge build up and intrinsic bistability.

First let's see the simple discussion on resonant tunnelling in a magnetic field perpendicular to the barriers. It is well known that the lateral electronic states in both the accumulation region and the quantum well are given by replacing the lateral kinetic energy $\hbar^2 k_{//}^2/2m^*$ with Landau subband energy, and thus the total electron energy E is expressed in both regions as follows:

$$E = E_0 + (N + 1/2)\hbar\omega_c \qquad (4.19)$$

where E_0 is the lowest 2D-state energy in the emitter or quantum well, N the Landau-level quantum number, and ω_c the cyclotron frequency (= $e\hbar B/m^*$). Then a condition on resonant tunnelling under a magnetic field is simply expressed as follows:

$$E_0(\text{emitter}) + (N + 1/2)\hbar\omega_c = E_0(\text{quantum well}) + (N' + 1/2)\hbar\omega_c \qquad (4.20)$$

Difference between N and N' represents the change in Landau level during the tunnelling. From Eq. (4.19) the N-th Landau level aligns to the local Fermi energy E_F^{local} when the following condition is satisfied:

$$(1/B) = \left(N + \frac{1}{2}\right)\frac{e\hbar}{m^* E_F^{local}} \qquad (4.21)$$

This means that the tunnel current I and conductance G versus B curves exhibit peaks whenever the Landau Levels pass through the local Fermi level leading to oscillations with a definite period in 1/B. The interval between these peaks $\Delta(1/B)$ is thus related to the local Fermi energy E_F^{local} by the following equation:

$$\left(\Delta(1/B)\right)^{-1} = \frac{m^* E_F^{local}}{e\hbar} \qquad (4.22)$$

Therefore, the local Fermi energy can be extracted from the gradient of a graph of (1/B) versus the Landau index number N which for this purpose is arbitrary. Furthermore, if we assume that all of the Landau levels beneath the local Fermi level are full, that is electrons are completely thermalized, then the sheet concentration of the locally accumulated electrons σ_{local} is deduced from E_F^{local} obtained above as follows:

$$E_F^{\text{local}} = \frac{\hbar^2 \pi \sigma_{\text{local}}}{m^*} \tag{4.23}$$

An example of magneto-current characteristics for Sample 2 taken by C. Goodings, Microelectronics Research Centre, University of Cambridge, in collaboration with the author is shown in Fig. 4.18(a), where we see periodic structure. The positions of the peaks (or troughs) were extracted and plotted as (1/B) versus an arbitrary index N (see the inset). The data measured for Sample 3 (see Fig. 4.18(b)) are clearer than those for Sample 2, allowing the characteristics to be taken for a greater range of bias voltage.

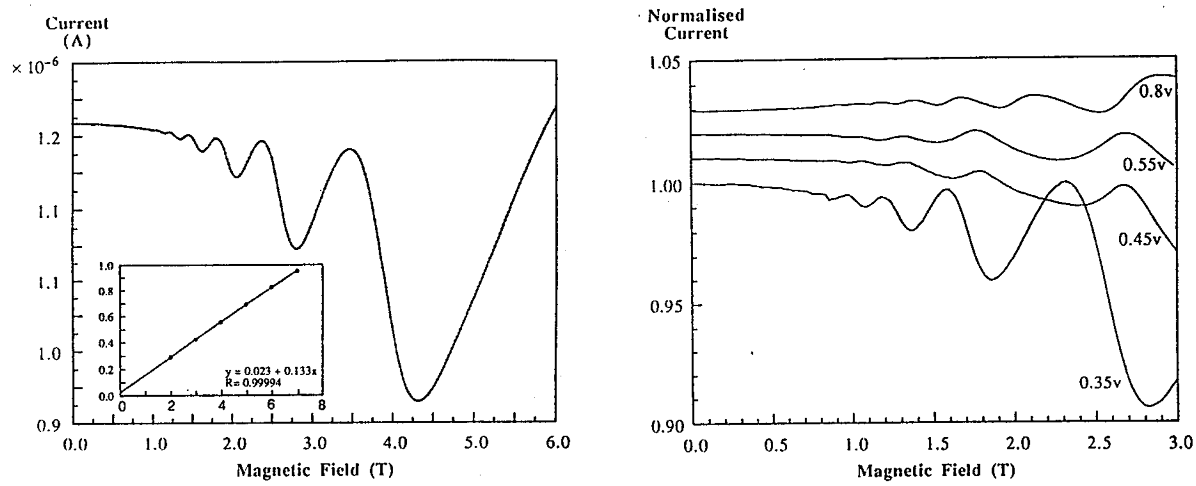

(a) (b)

Figure 4.18 Magneto-current curves at 4.2K (a) for Sample 2, and (b) for Sample 3. The inset of (a) shows a plot of 1/B versus the Landau index used to extract the Fermi energy and carrier density. (b) gives a set of normalised and offset curves for various bias voltages showing the asymmetry found at some biases. Data taken by C. Goodings, Microelectronics Research Centre, University of Cambridge, in collaboration with the author.

Thus for Sample 3 results could be obtained for the charge build-up in the post-resonance regime, while for Sample 2 this was not the case. The symmetry of the peaks was seen to vary with the applied bias - an observation also made by Thomas et al. [40]. Fig. 4.18(b) shows a series of magneto-current curves that show this effect for Sample 3, normalised to their zero-field values and offset. The characteristics with greatest asymmetry appear in the range of bias between the threshold and peak resonance voltage (0.3-0.6 V).

Bias dependence of charge accumulation in the emitter has been successfully measured for Sample 3 above the threshold voltage. The values obtained for E_F^e and σ_e in the emitter are shown in Fig. 4.19. Although the charge build-up in the quantum well σ_w has not been measured directly in this experiment, it can be determined in the following way. The main process that occurs between the threshold voltage and the peak resonance voltage is the build-up of charge in the quantum well. This gives a large amount of electrostatic feedback, screening the emitter barrier and accumulation region from the increasing fields. Thus we would expect, and see, the Fermi energy E_F^e and the charge build-up in the emitter σ_e to remain roughly constant in this range. As the bias is increased beyond the resonance peak, the resonant level in the quantum-well falls below that in the emitter and so the well suddenly becomes depopulated, giving a step change in the bias across the emitter barrier and accumulation region. This gives a sudden change in E_F^e and σ_e as seen in Fig. 4.19.

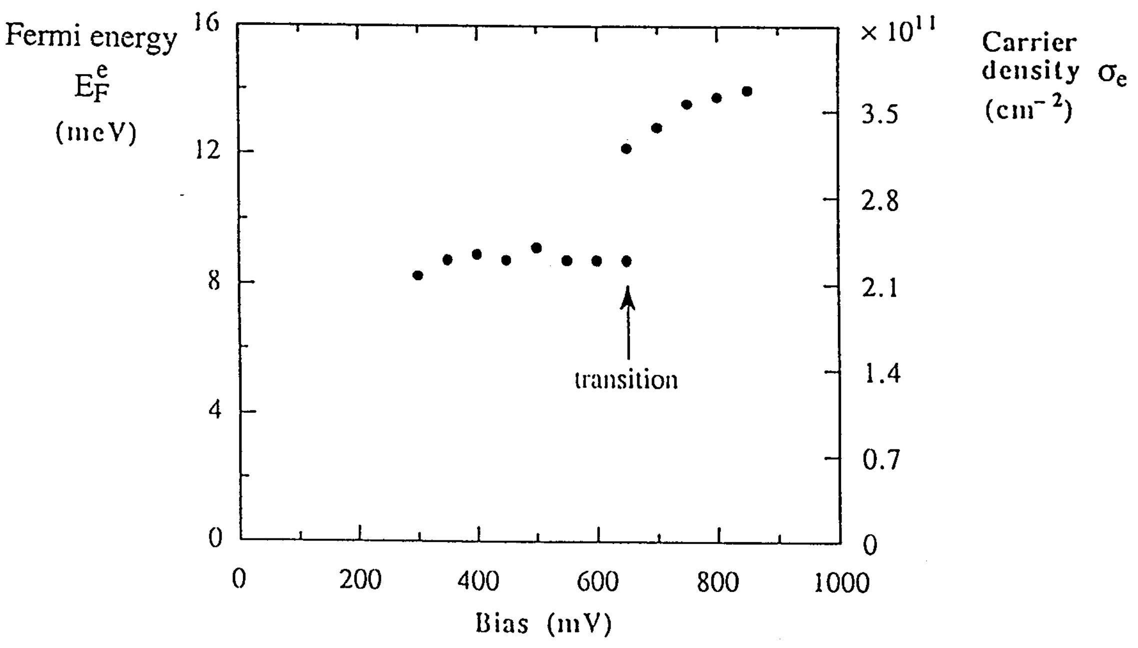

Figure 4.19 Energy spacing between the local Fermi level and the lowest 2D-state in the accumulation layer and carrier density in the emitter region for Sample 3. The results show a marked step in charge accumulation at the resonance peak (marked by the arrows). Data taken by C. Goodings, Microelectronics research centre, University of Cambridge, in collaboration with the author.

Electrostatic feedback provided by the voltage drop across the depletion region ensures that the charge lost from the quantum well is roughly balanced by the charge gained in the accumulation region, i.e. $\sigma_w \approx \Delta(\sigma_e)$. In Fig. 4.19, we see that the charge in the accumulation region increase from 2.3×10^{11} cm^{-2} to 3.3×10^{11} cm^{-2} as the device switches, and thus charge accumulation in the quantum well σ_w is estimated to be about 1×10^{11} cm^{-2}. At resonance σ_e of 3.7×10^{11} cm^{-2} and 2.3×10^{11} cm^{-2} were measured for Samples 2 and 3. Goldman et al. [41] suggest a very simple model for the estimation of the charge accumulation in a sample with no depletion region by treating the structure as a parallel-plate capacitor. Adapting this model, the following expression is derived for the charge accumulation in the emitter:

$$\sigma_e \approx \frac{\varepsilon}{q}\frac{E_0}{d + w/2} \tag{4.24}$$

Using values of E_0 obtained from the transmission probability calculations, the charge accumulations of 6.2×10^{11} cm^{-2} and 3.5×10^{11} cm^{-2} are found for Samples 2 and 3, in reasonable agreement with, but about 50% higher than, the measured values.

An alternative technique was used by Leadbeater et al. [39]. The capacitance of a RTD will depend upon the charge contained since this affects the size of the depletion region, so that a periodic structure will be observed in the magneto-capacitance data as well. This technique has the advantage that the the charge can be measured even when there is no current flow, for example below threshold. However, the values of the capacitance are small, and for the relatively small-area devices would have been less than 1 pF and completely swamped by stray capacitances. Hence this method could be used only for large area devices. By using this magneto-capacitance method, Leadbeater et al. were able to separate the charge build-up in the quantum well and the accumulation region by taking the Fourier transform of the oscillatory structure. They measured the voltage dependence of the differential capacitance C of the asymmetric $Al_{0.4}Ga_{0.6}As$(8.3 nm) /GaAs(5.8 nm) /$Al_{0.4}Ga_{0.6}As$(11.1 nm) double barrier RTD in the low frequency regime from 10 kHz to 2 MHz. From the detailed Fourier analysis of the data they have found two series of oscillations which arise from the space charge build-up in the quantum well σ_w and in the accumulation region in the emitter σ_e. A similar bias dependence of σ_e was found with a step increase at the current peak voltage. In addition it was clearly seen that the value of σ_w begins to increase over threshold while σ_e is kept constant to be 1.9×10^{11} cm^{-}

^{2} and reaches 1.6×10^{11} cm^{-2} near the peak voltage. They have also found the difference in the magneto-oscillations corresponding to the current bistability in the NDC regime.

Finally in this section we will consider again about the assumption adopted to derive Eq. (4.22): the local Fermi energy E_F^{local} requires an attention for its meaning. In the non-equilibrium situation there is no justification of using the idea of Fermi energy for electrons in the quantum well: the distribution function is in general different from the Fermi distribution function. In the case that electrons frequently suffer phase-coherence breaking scattering in the quantum well, however, we may define the local quasi-Fermi energy for the equilibriated electrons in an approximate way. The theoretical analysis of the space charge build-up has been done by using the density matrix calculations shown in the last section.

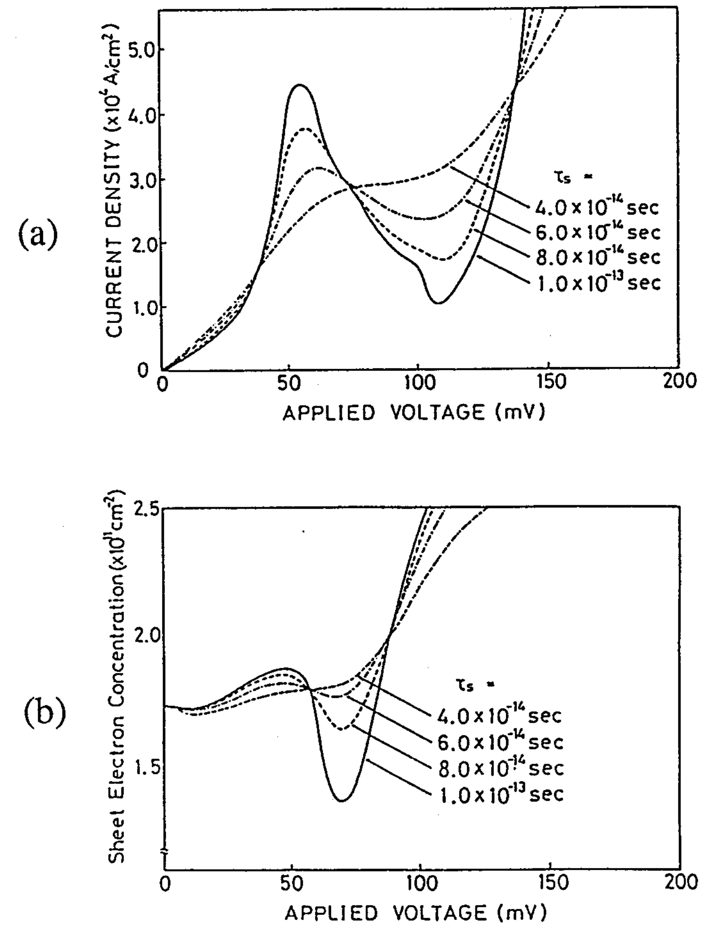

Figure 4.20 Applied voltage dependence of (a) current density and (b) sheet electron concentration in the quantum well calculated for the device without spacer layers with various values of τ_s.

Fig. 4.20(a) shows the I-V characteristics of the device without spacer layers calculated with various values of relaxation time due to scattering: τ_s = 100 fsec (solid line); 80 fsec (broken line); 60 fsec (one-point broken line); and 40 fsec (dotted line). As shown in this figure, the peak current decreases, and the valley current rapidly increases as the relaxation time decreases, resulting in a large degradation in the peak-to-valley current ratio. It should be noted that the I-V curve for a scattering time of 40 fsec no longer has a NDR region. This strong τ_s-dependence of the P/V current ratio is understood as follows: Fig. 4.20(b) shows the voltage dependence of the sheet concentration, n_S, of electrons accumulated in the quantum well calculated with various values of the relaxation time. It can be seen that the n_S -V curves have similar peak-to-valley structures corresponding to the NDR of the I-V characteristics, and the peak-to-valley ratios also decreases with decreasing τ_s. A shorter relaxation time corresponds to more frequent momentum relaxation of electrons in the quantum well. In other words, the phase-coherence of the electron-waves at resonance degrades, and the tunnelling mechanism changes from coherent tunnelling to sequential tunnelling. The increase in n_S for the valley-state indicates that a number of electrons are still present on the quasi-bound level even at off-resonance, resulting in a large valley current.

Figure 4.21 shows the imaginary parts of the density matrix at the peak-current state: calculated with τ_s of (a) 100 fsec and (b) 40 fsec. As explained earlier, the phase-coherence of the electron-waves at resonance can be observed as the oscillatory behaviour of the off-diagonal elements. Comparing these two figures, it can be clearly seen that amplitude of the oscillation in Fig. 4.21(b) is much smaller than that in Fig. 4.21(a). These figures show us directly the degradation of the electron-wave-coherence due to scattering.

In summary of this chapter dissipative transport and non-equilibrium electron distribution in RTDs have been investigated. The statistical density matrix theory has been used to develop a tractable numerical modelling of dissipative aspect of resonant tunnelling in double barrier RTDs. By introducing the Hartree self-consistent field model for electron-electron interactions and the relaxation-time approximation for scattering processes, the one-dimensional time-dependent Liouville-von Neumann equation for the electron density matrix has been solved. The modelling has been applied to the simple AlGaAs/GaAs double barrier RTDs and the femtosecond time-evolution of the density matrix under an applied field has been demonstrated.

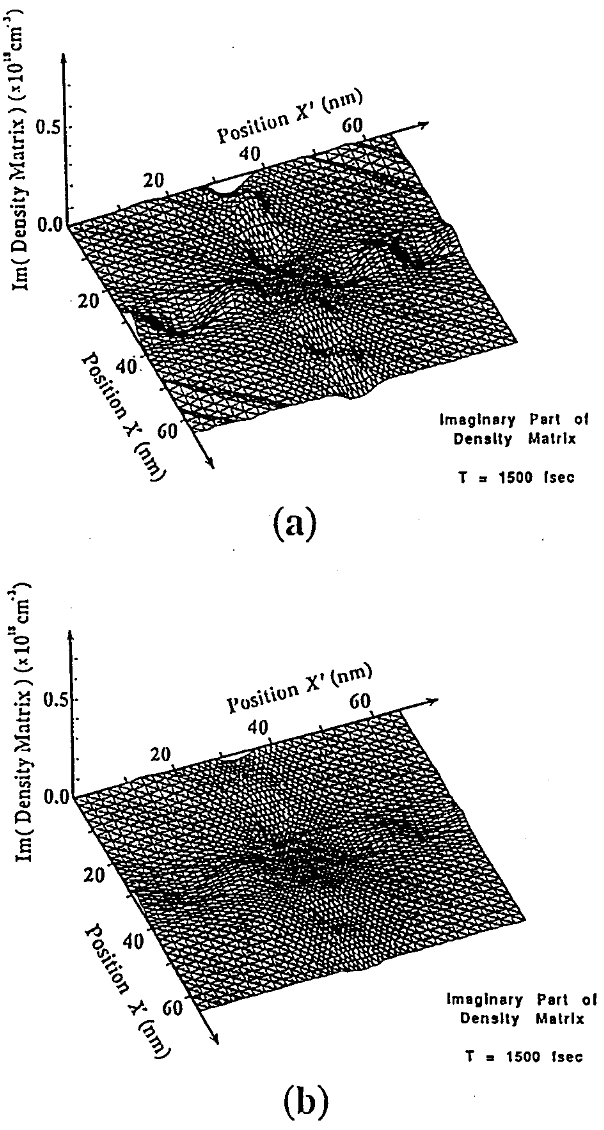

Figure 4.21 *Imaginary part of the steady-state density matrix (at a time of 1500 fsec) calculated with τ_S of (a) 100 fsec and 9b) 40 fsec. The reduced oscillatory behaviour of the off-diagonal elements in (b) signifies degradation of the phase-coherence in the device due to a shorter scattering relaxation time.*

Remarkable oscillatory behaviour found in the off-diagonal elements reveals the existence of long-range phase-correlations of the electron-wave in the resonance state. Intrinsic bistability and switching characteristics of the device have been investigated from the viewpoint of charge accumulation in the quantum well, and the peak-to valley current ratio is discussed in terms of phase-coherence degradation of electron-waves due to scattering.

In addition,magnetotransport measurement technique has been used to observe the space charge build up and resultant intrinsic current bistability of RTDs. Reasonable values of the concentration of electrons accumulated in the pseudo-triangle well and quantum well have been obtained. These results manifest that electrons tunnelling into the quantum well are partly thermalized by phase-breaking scattering processes leading to the P/V current ratios of RTDs.

4.4 Reference IV

[1] S. Luryi, "Frequency limit of double-barrier resonant-tunneling oscillators", Appl. Phys. Lett. **47**, 490, 1985.

[2] S. Luryi, "Coherent versus incoherent resonant tunneling and implications for fast devices", Superlattices and Microstructures, **5**, 375, 1989.

[3] T. Weil and B. Vinter, "Equivalence between resonant tunnelling and sequential tunnelling in double-barrier diodes", Appl. Phys. Lett. **50**, 1281, 1987.

[4] D. Ter Haar, "Theory and Applications of the density matrix", Reports on progress in Physics, **24**, 304, 1961.

[5] J. R. Barker and S. Murray, "A quasi-classical formulation of the Wigner function approach to quantum ballistic transport", Phys. Lett. **93A**, 271, 1983.

[6] D. Y. Xing, and C. S. Ting, "Green's-function approach to transient hot-electron transport in semiconductors under a uniform electric field', Phys. Rev. **B35**, 3971,1987.

[7] B. A. Mason, and K. Hess, "Quantum Monte Carlo calculations of electron dynamics in dissipative solid-state systems using real-time path integrals', Phys. Rev. **B39**, 5051, 1989.

[8] U. Ravaioli, A. M. Osman, W. Poetz, N. C. Kluksdahl, and D. K. Ferry, "Investigation of ballistic transport through resonant-tunneling quantum wells using Wigner function approach", Physica **134B**, 36, 1985.

[9] W. R. Frensley, "Wigner-function model of a resonant-tunneling semiconductor device", Phys. Rev. **B36**, 1570, 1987.

[10] N. C. Kluksdahl, A. M. Kriman, D. K. Ferry, and C. Ringhofer, "Self-consistent study of the resonant-tunneling diode", Phys. Rev. **B39**, 7720, 1989.

[11] W. R. Frensley, "Quantum kinetic theory of nanoelectronic devices", NANOSTRUCTURE PHYSICS AND FABRICATION, Proceedings of the International Symposium, Academic Press, Inc., 231, 1989.

[12] J. S. Wu, C. Y. Chang, C. P. Lee, K. H. Chang, D. G. Liu, and D. C. Liou, "Resonant tunneling of electrons from quantized levels in the accumulation layer of double-barrier heterostructures", Appl. Phys. Lett. **57**, 2311, 1990.

[13] Y. G. Gobato, F. Chevoir, J. M. Berroir, P. Bois, Y. Guldner, J. Nagle, J. P. Vieren and B. Vinter, "Magnetotunnelling analysis of the scattering processes in a double-barrier structure with a two-dimensional emitter", Phys. Rev. B**43**, 4843, 1991.

[14] H. Zheng and F. Yang, in *Resonant Tunneling in Semiconductors: Physics and Applications*, edited by L. L. Chang (pllenum, New York, 1990).

[15] F. Chevoir and B. Vinter, in *Resonant Tunneling in Semiconductors: Physics and Applications*, edited by L. L. Chang (pllenum, New York, 1990).

[16] V. J. Goldman, D. C. Tsui, and J. E. Cunningham, "Observation of inelastic bistability in resonant tunneling structures", Phys. Rev. Lett. **58**, 1256, 1987.

[17] W. R. Frensley, "Simulation of resonant-tunneling heterostructure devices", J. Vac. Sci. Technol. **B3**, 1261, 1985.

[18] R. Brunetti, C. Jacoboni, and F. Rossi, "Quantum theory of transient transport in semiconductors: a Monte Carlo approach", Phys. Rev. **B39**, 10781, 1989.

[19] P. Menziani, F. Rossi, and C. Jacoboni, "Impurity scattering in quantum transport simulation", Sol. State Electr. **32**, 1807, 1989.

[20] F. Rossi and C. Jacoboni, "A quantum description of drift velocity overshoot at high electric fields in semiconductors", Sol. State Electr. **32**, 1411, 1989.

[21] A. M. Kriman, N. C. Kluksdahl, and D. K. Ferry, "Scattering states and distribution functions for microstructures", Phys. Rev. **B36**, 5953, 1987.

[22] H. Mizuta and C. J. Goodings, "Transient quantum transport simulation based on the statistical density matrix", J. Phys.: Condens. Matter **3**, 3739, 1991.

[23] I. B. Levinson, "Translational invariance in uniform fields and the equation for the density matrix in the Wigner representation", Sov. Phys. **JETP 30**, 362,1970.

[24] A. O. Caldeira and A. J. Leggett, "Path integral approach to quantum brownian motion", Physica **121A**, pp. 587-616, 1983.

[25] W. R. Frensley, "Boundary conditions for open quantum systems driven far from equilibrium", Rev. of Mod. Phys. **62**, 745, 1990

[26] T. C. L. G. Sollner, "Comments on "Observation of intrinsic bistability in resonant-tunneling structures", Phys. Rev. Lett. **59**, 1622, 1987.

[27] T. J. Foster, M. L. Leadbeater, L. Eaves, M. Henini, O. H. Hughes, C. A. Payling, F. W. Sheard, P. E. Simmonds, and G. A. Toombs, "Current bistability in double-barrier resonant tunneling devices", Phys. Rev. **B39**, 6205, 1989.

[28] H. L. Berkowitz and R. A. Lux, "Hysterisis predicted in I-V curve of heterojunction resonant tunneling diodes simulated by a self-consistent quantum method", J. Vac. Sci. Technol. **B5**, 967, 1987.

[28] R. K. Mains, J. P. Sun, and G. I. Haddad, "Observation of intrinsic bistability in resonant tunneling diode modeling", Appl. Phys. Lett. **55**, 371, 1988.

[30] F. W. Sheard and G. A. Toombs, "Space-charge buildup and bistability in resonant-tunneling double-barrier heterostructures", Appl. Phys. Lett. **52**, 1228, 1988.

[31] K. L. Jensen and F. A. Bout, "Numerical simulation of intrinsic bistability and high-frequency current oscillations in resonant tunnelling structures", Phys. Rev. Lett. **66**, 1078, 1991.

[32] Jeff. F. Young, B. M. Wood, H. C. Liu, M. Buchanan, D. Landheer, A. J. SpringThorpe, and P. Mandeville,"Effect of circuit oscillations of the dc current-voltage characteristics of double barrier resonant tunneling structures", Appl. Phys. Lett.**52**, 1398, 1988

[33] C. Y. Belhadj, K. P. Martin, S. Ben Amor, J. J. L. Rascol, R. C. Potter, H. Hier, and E. Hempfling,"Bias circuit effects on the current-voltage characteristic of double-barrier tunneling structures: Experimental and theoretical results", Appl. Phys. Lett. **57**, 58, 1990

[34] E. S. Alves, L. Eaves, M. Henini, O. H. Hughes, M. L. Leadbeater, F. W. Sheard, G. A. Toombs, G. Hill, and M. A. Pate, "Observation of intrinsic bistability in resonant tunnelling devices", Electron. Lett. **24**, 1190, 1988.

[35] M. L. Leadbeater, E. S. Alves, L. Eaves, M. Henini, O. H. Hughes, F. W. Sheard, and G. A. Toombs, " ", Semicond. Sci. Technol. 3, 1060, 1988.

[36] V. J. Goldman, D. C. Tsui, and J. E. Cunningham, "Resonant tunneling in magnetic fields: Evidence for space-charge buidup", Phys. Rev. **B35**, 9387, 1987.

[37] L. Eaves, G. A. Toombs, F. W. Sheard, C. A. Payling, M. L. Leadbeater, E. S. Alves, T. J. Foster, P. E. Simmonds, M. Henini, O. G. Hughes, J. C. Portal, G. Hill, and M. A. Pate, "Sequential tunneling due to intersubband scattering in double-barrier resonant tunneling devices", Appl. Phys. Lett. **52**, 212, 1988.

[38] C. A. Payling, E. S. Alves, L. Eaves, T. J. Foster, M. Henini, O. H. Hughes, P. E. Simmonds, F. W. Sheard, G. A. Toombs, and J. C. Portal, "Evidence for sequential tunnelling and charge build-up in double barrier resonant tunnelling devices", Surface Science **196**, 404, 1988.

[39] M. L. Leadbeater, E. S. Alves, F. W. Sheard, L. Eaves, M. Henini, O. G. Hughes, and G. A. Toombs, "Observation of space-charge build-up and thermalization in an asymmetric double-barrier resonant tunnelling structure", J. Phys: Condense. Matter **1**, 10605, 1989.

[40] D. Thomas, "Magneto-tunneling studies of charge build-up in double barrier diodes", Superlattices and Microstructures **5**, 219, 1989.

[41] V. J. Goldman, Bo Su, and J. E. Cunningham, in Resonant Tunneling in Semiconductors: Physics and Applications, edited by L. L. Chang (Plenum, New York, 1990).

CHAPTER 5

QUANTUM TRANSPORT IN THREE-DIMENSIONALLY CONFINED HETEROSTRUCTURES

The last chapter is devoted to the study of quantum transport through ultimate nanometer-scale heterostructures, *quantum dots*. Recent rapid advance in nanofabrication technique has naturally led to an idea of resonant tunnelling through a three-dimensional confined quantum dot. Ultrasmall resonant tunnelling structures [1]-[8] in which electrons are confined laterally as well as vertically have become of great interest from the standpoints of both physics of quantum transport through three-dimensionally confined electronic states and device miniaturization towards highly integrated functional resonant tunnelling devices. The zero-dimensional resonant tunnelling diode (0D-RTD) is a virtually isolated quantum dot only weakly coupled to reservoirs and so is well suited to investigate electron-wave transport properties through three-dimensionally quantized energy levels. By designing structural parameters such as barrier thickness, quantum well width, and dimensions of lateral confinement, it is possible to realize a ”quantum box” in which the number of electrons is nearly quantized so the effect of single charge assisted transport, or called Coulomb blockade [9]-[11], becomes significant. After Reed et al. reported in 1988 their pioneering work on resonant tunnelling through a quantum pillar which was fabricated by using electron beam lithography and dry etching, several theoretical and experimental works have been reported to investigate the mechanism of the observed fine structures. Transport in the 0D-RTD is generally much more complicated than that in a conventional large area resonant tunnelling diode (this is hereafter called a 2D-RTD): problems such as lateral mode mixing due to non-uniform confinement potential, charge quantization in a quantum well, and an interplay between resonant tunnelling and Coulomb blockade single electron tunnelling are recently invoked for the 0D-RTDs and still far from their conclusions.

This chapter is not intended to discuss the proper description of quantum transport in these systems but, by using preliminary but numerically tractable modellings, to make clear some novel transport properties. Theoretical framework adopted in this chapter is a natural expansion of the S-matrix theory used to describe the global coherent tunnelling in Chapter 3 into the present three-dimensional nanostructures. The classical hydrodynamic device simulation technique is utilized to have confinement potential profiles in the easiest way which are not completely exact but reasonably plausible. This method gives us numerical results which can be used to discuss the experimental results quantitatively by using currently usable computer resources. Taking consideration of these numerical results a novel gated 0D-RTD is proposed and fabricated by using focused ion beam technique. Three-dimensional confinement effects and novel single impurity effects on the transport properties are investigated as quantitatively as possible.

5.1 Low-dimensional resonant tunnelling diodes

A pioneering work on resonant tunnelling through a three-dimensionally confined quantum well ("quantum dot") has been done by Reed et al. [1],[2]. The conventional resonant tunnelling wafer was etched vertically down to the n^+-GaAs bottom contact layer and quantum pillars (see Fig. 5.1) were defined in the wafer. Reed et al. fabricated a collection of the quantum pillars with a diameter in the range 100-250 nm. An initial epitaxial structure is a 5 nm undoped $In_{0.08}Ga_{0.92}As$ strained well sandwiched between 4 nm undoped $Al_{0.25}Ga_{0.75}As$ barriers with 10 nm undoped GaAs spacer and 20 nm graded n-GaAs layers grown on an n^+-GaAs contact layer. Electron beam lithography and highly anisotropic reactive ion etching were used to fabricate these structures with ohmic contact metal on top. Similar structure has also been formed by Su et al. [4] by using wet chemical etching. In these etched structures there exist defect states on the lateral surface of the pillar capture electrons and the density of the surface states is high enough to pin Fermi-level on the surface. Thus electrons in the nanostructure are laterally confined in a gutter shaped potential well shown in Fig. 5.2 which consists of parabolic ($r_c < r < r_s$) and flat ($0 < r < r_c$) parts. This nanostructure is hereafter called a *zero-dimensional resonant tunnelling diode* (0D-RTD) compared to the conventional large area RTDs in which motion of electrons are not quantized in a two-dimensional plane parallel to a heterointerface and so should be referred as 2D-RTDs in this chapter. Reed et al. measured the

I-V characteristics of the *single 0D-RTD* at various temperatures [1],[2]. At high temperatures the 0D-RTD shows a negative differential conductance in the I-V characteristics which is basically the same as that of the 2D-RTDs. Lowering the temperature, however, a series of small current peaks appears which is superimposed on the negative differential conductance. These fine structures were attributed to resonant tunnelling through three-dimensionally quantized states in the quantum dot.

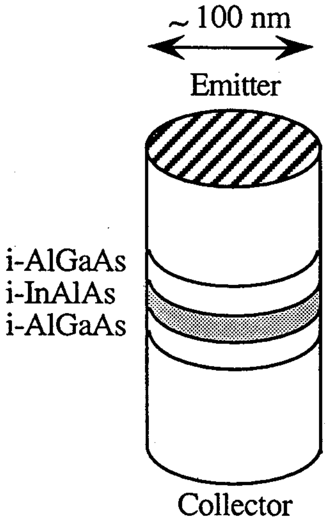

Figure 5.1 *A schematic viewgraph of a simply etched quantum piller fabricated by Reed et al.*

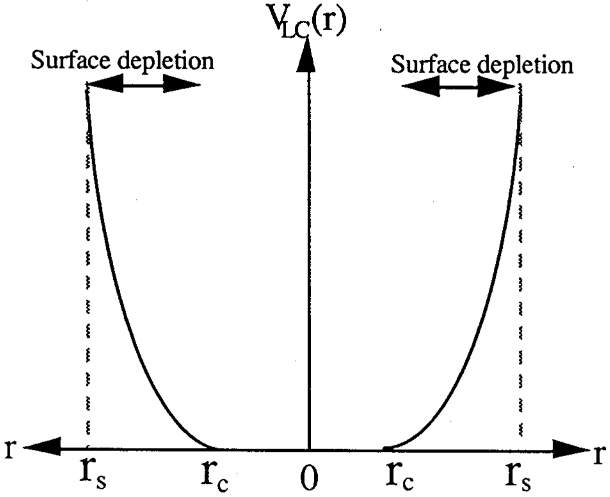

Figure 5.2 *A gutter shaped lateral confinement potential formed in the simply etched structure.*

A different type of the low-dimensional-RTD has been reported by Tarucha et al [3],[5]. They used focused Ga-ion beam implantation to define a zero-dimensional structure instead of etching shown above. A 100-nm-diameter Ga-FIB with a dose of 5×10^{12} cm^{-2} was scanned on the surface of the resonant tunnelling wafer leaving a small rectangular area as illustrated in Fig. 5.3. After a rapid thermal annealing the implanted Ga ions convert n-type GaAs regions in the wafer into p-type and then form the PN-jucntion based lateral confinement potential similar to that of the etched nanostructure (Fig. 5.2).

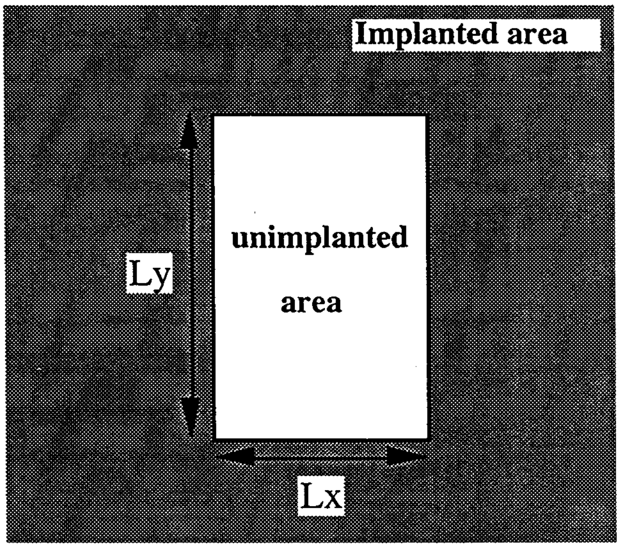

***Figure 5.3** Schematic top view of a zero-dimensional structure fabricated by Tarucha et al. by using Ga ion-beam implantation.*

They have focused on the structures with rectangular lateral confinement (Lx < Ly) in which electronic states are quantized only in x-dimension as Ly is not small enough to achieve quantization: these structures are thus called 1D-RTDs. This structure enables us to see the effects of lateral quantization in a clearer way since electrons are confined in the one-dimensional gutter potential well resulting in nearly equal splitting between quantized energy E_x in the x-dimension. They measured the I-V characteristics of the 1D-RTDs with various areas (Lx×Ly) at 4 K [3]. The largest sample with Lx of 310 nm shows only single NDC associated with the first quasi-bound state of the double barrier structure. A series of small current peaks is observed for the smaller samples in the NDC regime which is attributable to the quantization in the x-dimension and is more pronounced in the case of Lx of 155 nm with a bigger interval between them. Tarucha et al. analyzed the observed peak voltages by comparing with subband energies calculated for the one-dimensional gutter potential and assigned these peaks up to the 7th quantized level in relatively good agreement with the calculations [3].

Theoretical description of the 0D-resonant tunnelling is much more complicated than that for the conventional 2D-resonant tunnelling because of the lateral confinement. The difficulty stems from the *non-uniform* lateral confinement potential which is formed by differences in surface depletion even though the device is fabricated to be geometrically straight in a vertical direction. Figure 5.4 shows an example of the lateral confinement potential distribution which looks like an hourglass along the channel: the detail of this figure is explained in the next section. This non-uniform confinement mainly results in the following two effects. First the lateral quantized energies varies gradually in the z-dimension. The energy separation between the lateral energies in the quantum well is larger than that in the cathode and anode regions. Second the non-uniform confinement causes lateral wavefunction mismatch and mixes the lateral electronic states (*lateral mode mixing*): theoretical work reported by Bryant [13]-[15] has demonstrated the importance of the lateral mode mixing in this system. It is therefore difficult to serve an intuitive picture of the 0D-resonant tunnelling and proper theoretical modelling requires three-dimensional transport theory as shown in the next section. A rather simple modelling, however, was proposed by Reed et al. [5] based on the transfer Hamiltonian type picture which is worth introducing before preceding the three-dimensional theory.

Following the early theoretical work by Bryant [14] Reed et al. introduced two quantum numbers n and n' to describe lateral motions of electrons in the cathode region and in the quantum well, respectively. Thus energy of electrons in these two regions are approximately expressed as $\varepsilon_\gamma + E_{k_z}$ and $\varepsilon_{\gamma'} + E_{k_{z0}}$ where ε_γ is the energy of the γ-th lateral mode, E_{k_z} the z-component of electrons ($= h^2k_z^2/2m^*$), and $E_{k_{z0}}$ the energy of the lowest quasi-bound state in the quantum well. An interval of the lateral energy $\varepsilon_{\gamma+1} - \varepsilon_{\gamma'}$ in the quantum well is thus larger than $\varepsilon_{\gamma+1} - \varepsilon_\gamma$ in the cathode region. A series of quantized levels in these regions is schematically shown in Fig. 5.5 (a). Reed et al. reported that the observed fine structure can be modelled as resonances of the levels in the well with those in the cathode under an applied bias (see Fig. 5.5 (b)). Each time when a level in the well crosses one of the levels in the cathode electrons tunnel through to the anode region leading to a resonant current peak.

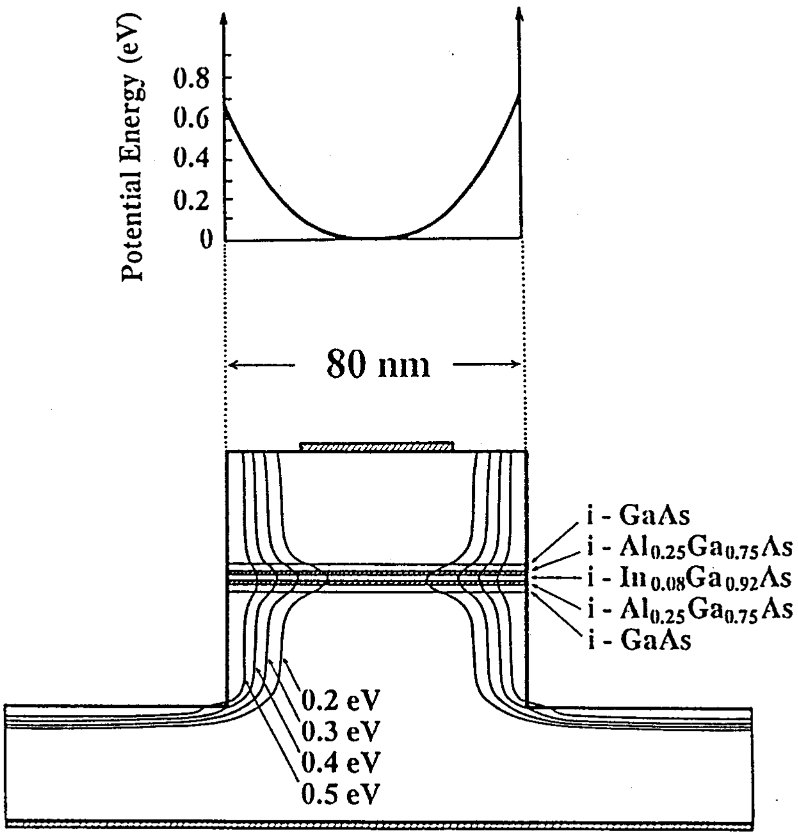

Figure 5.4 Lateral confinement potential distribution in a simply etched zero-dimensional resonant tunnelling structure numerically calculated by using a classical hydrodynamic device simulation HIHEART taking account of surface carrier trap states.

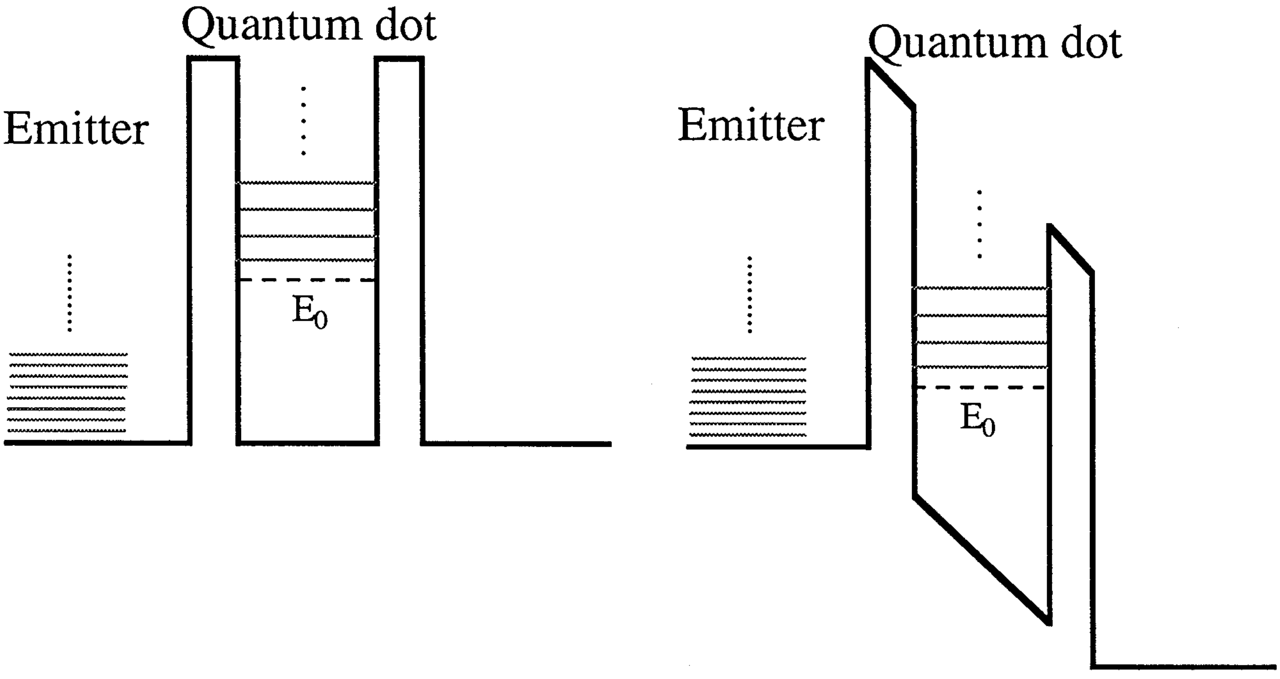

(a)

(b)

Figure 5.5 Schematic energy-band diagram with lateral eigenstates in the emitter and quantum dot (a) at zero bias and (b) under an applied bias.

If $\gamma = \gamma'$ the tunnelling conserves lateral mode (momentum) and if not it is lateral mode non-conserving tunnelling. To evaluate transition rates and selection rules for these tunnelling, three-dimensional numerical calculations by using the profile of the confinement potential are apparently necessary. Reed et al. picked up all the crossings of the quantum well levels with the cathode levels as a function of applied bias and compared with the observed peak voltages [2]. The calculated results agree well with the experimental results as shown in [2] and indicate that the lateral mode non-conserving tunnelling actually contributes to the current. Tarucha et al. also adopted this model to analyze the experimental results of the 1D-RTDs [5] and found that extra structures newly observed at lower temperatures are attributable to the lateral mode non-conserving tunnelling.

As shown above this simple model gave us an intuitive understanding of the low-dimensional resonant tunnelling. In the next section further quantitative analysis of multi-mode resonant tunnelling is presented by introducing the three-dimensional S-matrix theory which fully includes lateral mode mixing.

5.2 Theory of zero-dimensional resonant tunnelling

5.2.1 Three-dimensional S-matrix theory

In this section a multi-mode S-matrix theory based on the three-dimensional Schrödinger equation for open systems is presented to look into the detail of electron transport through the 0D-RTDs. Several theoretical studies of the two-dimensional scattering equation have been reported for laterally patterned two-dimensional electron gas systems [17]-[24]. Because direct numerical calculations usually have large computational time and memory requirements, several useful alternative methods have also been proposed. Also the three-dimensional Schrödinger equation has been solved by Kumar for a completely isolated quantum dot under a magnetic field [25] and a structure periodic in one direction [26]. Since the electronic states become completely bound states or subbands rather than continuous scattering states in these circumstances, this method is not adequate for the present purpose. Very recently, Nakazato et al. [27] have analyzed transport properties of lateral quantum wires with geometrical confinement by solving the two-dimensional scattering equation numerically and have shown anti-resonance dips of conductance resulting from lateral mode mixing. In this paper we present the three-dimensional scattering formulation and calculate the scattering matrix (S-matrix) numerically to investigate the effect of two-dimensional lateral mode mixing on transport properties of 0D-RTDs. In the present calculation the self-consistent Hartree potential, which would be crucial to analyze Coulomb blockade, is neglected for simplicity.

We start from the three-dimensional time-independent Schrödinger equation:

$$-\frac{\hbar^2}{2m^*}\left(\frac{\partial^2}{\partial x^2}+\frac{\partial^2}{\partial y^2}+\frac{\partial^2}{\partial z^2}\right)\Psi(x,y,z) + V(x,y,z)\Psi(x,y,z) = E\Psi(x,y,z) \qquad (5.1)$$

where m* is the conduction-band effective mass and V(x,y,z) is the three-dimensional potential distribution which consists of lateral confinement potential $V_{LC}(x,y,z)$, the electron affinity $V_0(z)$ and the potential along a channel due to an external bias $V_{EX}(z)$ which are both assumed to be dependent only on z-coordinate, and any other scattering potentials such as a single ionised donor potential $V_{IM}(x,y,z)$ discussed in sec. 5.3.3:

$$V(x,y,z) = V_{LC}(x,y,z) + V_0(z) + V_{EX}(z) + V_{IM}(x,y,z) \qquad (5.2)$$

The three-dimensional wavefunction $\Psi(x,y,z)$ is decomposed by using a complete set of two-dimensional lateral wavefunctions at each z point, $\varphi_\gamma(x,y \mid z)$, as follows:

$$\Psi(x,y,z) = \sum_{\gamma} \varphi_\gamma(x,y \mid z)\chi_\gamma(z) \qquad (5.3)$$

The lateral wavefunction $\varphi_\gamma(x,y \mid z)$ is obtained by solving numerically the following two-dimensional Schrödinger equation:

$$-\frac{\hbar^2}{2m^*}\left(\frac{\partial^2}{\partial x^2}+\frac{\partial^2}{\partial y^2}\right)\varphi_\gamma(x,y \mid z) + V_{LC}(x,y,z)\varphi_\gamma(x,y \mid z) = \varepsilon_\gamma(z)\varphi_\gamma(x,y \mid z) \qquad (5.4)$$

with the Dirichlet boundary conditions, $\varphi_\gamma(x,y \mid z) = 0$, on the boundaries of the device. The index γ represents a two-dimensional lateral mode number and $\varepsilon_\gamma(z)$ a corresponding γ-th lateral eigenenergy.

Substituting Eq. (5.3) into Eq. (5.1), the three-dimensional Schrödinger equation reduces to the following one-dimensional scattering equation for the z-component of the wavefunction $\chi_\gamma(z)$:

$$\frac{d^2}{dz^2}\chi_\gamma(z) + k_\gamma^2(z)\chi_\gamma(z) + \sum_{\gamma'}\left(2C_{\gamma,\gamma'}^{(0,1)}(z)\frac{d}{dz}\chi_{\gamma'}(z) + C_{\gamma,\gamma'}^{(0,2)}(z)\chi_{\gamma'}(z)\right) = 0 \qquad (5.5)$$

where $k_\gamma(z)$ denotes a complex wavenumber given by

$$k_\gamma^2(z) = \frac{2m^*}{\hbar^2}\left(E - \varepsilon_\gamma(z) - V_0(z) - V_{EX}(z)\right) \qquad (5.6)$$

Mode mixing coefficients $C^{(0,1)}_{\gamma,\gamma'}$ and $C^{(0,2)}_{\gamma,\gamma'}$ are written as

$$C^{(0,1)}_{\gamma,\gamma'}(z) = \int dx \int dy\ \varphi_{\gamma}(x,y\,|z)\frac{\partial}{\partial z}\varphi_{\gamma'}(x,y\,|z) \tag{5.7}$$

$$C^{(0,2)}_{\gamma,\gamma'}(z) = \int dx \int dy\ \varphi_{\gamma}(x,y\,|z)\frac{\partial^2}{\partial z^2}\varphi_{\gamma'}(x,y\,|z) \tag{5.8}$$

and are evaluated by using the previously obtained set of lateral wavefunctions. The third term in Eq. (5.5) causes the mixing of lateral modes and is non-zero unless the system is uniform in the z-direction. The first derivative term of $\chi_\gamma(z)$ in Eq. (5.5) can be eliminated by applying the unitary transformation:

$$\chi_\gamma(z) = \sum_{\gamma'} M_{\gamma,\gamma'}(z)\ f_{\gamma'}(z) \tag{5.9}$$

where a unitary matrix $M_{\gamma\gamma'}(z)$ is defined as follows:

$$M_{\gamma,\gamma'}(z) = \exp\left(-\int^{z} C^{(0,1)}_{\gamma,\gamma'}(z')dz'\right) \tag{5.10}$$

The matrix $M_{\gamma\gamma'}(z)$ is calculated by using a second order expansion approximation [27] which guarantees unitarity of the matrix. Substituting Eqs. (5.9) and (5.10) into Eq. (5.5), the transformation leads to the following equation:

$$\frac{d^2}{dz^2} f_\gamma(z) = -\sum_{\gamma'} \omega_{\gamma,\gamma'}(z)\ f_{\gamma'}(z) \tag{5.11}$$

where a matrix $\omega_{\gamma\gamma'}(z)$ is written as

$$\omega_{\gamma,\gamma'}(z) = \sum_{\gamma''}\sum_{\gamma'''} \left(M^{-1}\right)_{\gamma,\gamma''}(z)\ W_{\gamma'',\gamma'''}(z)\ M_{\gamma''',\gamma'}(z) \tag{5.12}$$

$$W_{\gamma,\gamma'}(z) = k^2{}_\gamma(z)\delta_{\gamma,\gamma'} - \left\{C^{(0,1)}(z)\right\}^2_{\gamma,\gamma'} - C^{(1,1)}_{\gamma,\gamma'}(z) - \frac{2m^*}{\hbar^2}\, V^{IM}_{\gamma,\gamma'}(z) \tag{5.13}$$

$$C^{(1,1)}_{\gamma,\gamma'}(z) = \int dx \int dy\ \frac{\partial}{\partial z}\varphi_{\gamma}(x,y\,|z)\frac{\partial}{\partial z}\varphi_{\gamma'}(x,y\,|z) \tag{5.14}$$

$$V^{IM}_{\gamma,\gamma'}(z) = \int dx \int dy\ \varphi^*_{\gamma}(x,y\,|z)\ V_{IM}(x,y,z)\ \varphi_{\gamma'}(x,y\,|z) \tag{5.15}$$

and the expression $\left\{C^{(0,1)}(z)\right\}^2_{\gamma,\gamma'}$ in Eq. (13) means the (γ, γ')-element of the multiplied matrix $C^{(0,1)}(z)\cdot C^{(0,1)}(z)$.

A set of renormalized complex wavenumbers $K_{\gamma'}(z)$, which includes the lateral mode mixing, is obtained by solving an eigenvalue equation:

$$\sum_{\gamma''} W_{\gamma,\gamma''}(z)\, V_{\gamma'',\gamma'}(z) = \left\{K_{\gamma'}(z)\right\}^2 V_{\gamma,\gamma'}(z) \qquad (5.16)$$

where $V_{\gamma\gamma'}(z)$ is a unitary matrix which diagonalizes the matrix $W_{\gamma\gamma'}(z)$. Then the z-component of the wavefunction can be expressed as a superposition of plane waves:

$$\chi_{\gamma}(z) = \sum_{\gamma'} \sum_{\gamma''} M_{\gamma,\gamma'}(z)\, V_{\gamma',\gamma''}(z)\left\{A_{\gamma''}(z)\exp(iK_{\gamma''}(z)\, z) + B_{\gamma''}(z)\exp(-\, iK_{\gamma''}(z)\, z)\right\} \qquad (5.17)$$

where $A_{\gamma}(z)$ and $B_{\gamma}(z)$ are coefficients of forward and backward plane waves in the γ-th lateral mode with the complex wavenumber $K_{\gamma}(z)$. Equation (16) is discretized on the finite-difference z-mesh points. Assuming these coefficients to be constant between two adjacent z-mesh points, the three-dimensional wavefunction $\Psi(x,y,z)$ can be finally written as

$$\Psi^{(i)}(x,y,z) \cong \sum_{\gamma} \sum_{\gamma'} \sum_{\gamma''} \varphi_{\gamma}(x,y\,|z) M^{(i)}_{\gamma,\gamma'}\, V^{(i)}_{\gamma',\gamma''}\left\{A^{(i)}_{\gamma''}\exp(iK^{(i)}_{\gamma''}\, z) + B^{(i)}_{\gamma''}\exp(-\, iK^{(i)}_{\gamma''}\, z)\right\} \qquad (5.18)$$

where the index (i) denotes a small region between adjacent z-mesh points z_i and z_{i+1}.

From the continuity of electron probability flux of electrons through the system, the following conditions on the total wavefunctions hold at the z-mesh point z_{i+1} for given x and y:

$$\Psi^{(i)}(x,y,z_{i+1}) = \Psi^{(i+1)}(x,y,z_{i+1}) \qquad (5.19)$$

$$\frac{1}{m^*}\frac{\partial}{\partial z}\Psi^{(i)}(x,y,z)\bigg|_{z = z_{i+1}} = \frac{1}{m^*}\frac{\partial}{\partial z}\Psi^{(i+1)}(x,y,z)\bigg|_{z = z_{i+1}} \qquad (5.20)$$

The coefficients at the adjacent z-mesh points are then related as follows:

$$\begin{pmatrix} A^{i+1}_{\gamma} \\ B^{i+1}_{\gamma} \end{pmatrix} = \sum_{\gamma'} T^{(i)}(\gamma,\gamma') \begin{pmatrix} A^{i}_{\gamma'} \\ B^{i}_{\gamma'} \end{pmatrix} \qquad (5.21)$$

A matrix $T^{(i)}(\gamma, \gamma')$ can be expressed as

$$T^{(i)}(\gamma,\gamma') = \begin{pmatrix} \alpha^{(i)}_{+}(\gamma,\gamma')\exp\left\{ i\left(K^{(i)}_{\gamma'} - K^{(i+1)}_{\gamma}\right) z_{i+1}\right\} & \alpha^{(i)}_{-}(\gamma,\gamma')\exp\left\{- i\left(K^{(i)}_{\gamma'} + K^{(i+1)}_{\gamma}\right) z_{i+1}\right\} \\ \alpha^{(i)}_{-}(\gamma,\gamma')\exp\left\{ i\left(K^{(i)}_{\gamma'} + K^{(i+1)}_{\gamma}\right) z_{i+1}\right\} & \alpha^{(i)}_{+}(\gamma,\gamma')\exp\left\{- i\left(K^{(i)}_{\gamma'} - K^{(i+1)}_{\gamma}\right) z_{i+1}\right\} \end{pmatrix}$$

$$\cdot\, X^{(i)}_{\gamma,\gamma'} \qquad (5.22)$$

where matrices $\alpha^{(i)}_{\pm}(\gamma, \gamma')$ and $X^{(i)}_{\gamma,\gamma'}$ are given by the following expressions:

$$\alpha_{\pm}^{(i)}(\gamma,\gamma') = \frac{1}{2}\left(1 \pm \frac{m_{i+1}^{*}}{m_i^{*}} \frac{K_{\gamma'}^{(i)}}{K_{\gamma}^{(i+1)}}\right) \tag{5.23}$$

$$X_{\gamma,\gamma'}^{(i)} = \sum_{\gamma_1} \sum_{\gamma_2} \sum_{\gamma_3} V_{\gamma_1,\gamma}^{(i+1)} M_{\gamma_2,\gamma_1}^{(i+1)} M_{\gamma_2,\gamma_3}^{(i)} V_{\gamma_3,\gamma'}^{(i)} \tag{5.24}$$

Hence the coefficients at the cathode (A_{γ}^{L}, B_{γ}^{L}) and anode (A_{γ}^{R}, B_{γ}^{R}) edges of the device are related by using a multi-mode transfer matrix $T(\gamma, \gamma')$:

$$\begin{pmatrix} A_{\gamma}^{L} \\ B_{\gamma}^{L} \end{pmatrix} = \sum_{\gamma'} T(\gamma,\gamma') \begin{pmatrix} A_{\gamma'}^{R} \\ B_{\gamma'}^{R} \end{pmatrix} \tag{5.25}$$

$$T = T^{(N)}T^{(N-1)}T^{(N-2)}\ldots T^{(2)}T^{(1)} \tag{5.26}$$

It should be noted that the transfer matrix contains both propagating and evanescent modes depending on the total energy and lateral mode eigenenergies. Nakazato et al. [27] calculated a reduced transfer matrix from the above full transfer matrix to separate the propagating modes from the evanescent ones. In the present calculations, however, there is always a difference in the number of the propagating modes at the cathode and anode edges under a non-zero external bias, and the resulting reduced transfer matrix is no longer regular. Thus in the following calculations the full transfer matrix is adopted rather than the reduced transfer matrix. A relevant multi-mode scattering matrix $S(\gamma, \gamma')$ which is defined as

$$\begin{pmatrix} B_{\gamma}^{L} \\ A_{\gamma}^{R} \end{pmatrix} = \sum_{\gamma'} S(\gamma,\gamma') \begin{pmatrix} A_{\gamma'}^{L} \\ B_{\gamma'}^{R} \end{pmatrix} \tag{5.27}$$

is calculated from the transfer matrix. The multi-mode transmission probability $t_{L,R}(E;\, \gamma\, \gamma')$ and the total transmission rate $T(E)$, i.e. conductance at zero temperature, are then obtained from the S-matrix as follows:

$$t_R(E;\, \gamma\, \gamma') = |S_{12}(\gamma,\gamma')|^2 \tag{5.28}$$

$$t_L(E;\, \gamma\, \gamma') = |S_{21}(\gamma,\gamma')|^2 \tag{5.29}$$

$$T(E) = \sum_{\gamma} \sum_{\gamma'} t_R(E;\, \gamma\, \gamma')\theta(E - \varepsilon_{\gamma}^{L})\theta(E - \varepsilon_{\gamma'}^{R}) = \sum_{\gamma} \sum_{\gamma'} t_L(E;\, \gamma\, \gamma')\theta(E - \varepsilon_{\gamma}^{L})\theta(E - \varepsilon_{\gamma'}^{R}) \tag{5.30}$$

where $\theta(E)$ is the step-function. A complete set of the three-dimensional wavefunctions $\Psi(x,y,z)$ can be obtained by using the following scattering boundary conditions:

$$(A^L_\gamma, B^R_\gamma) = (\delta_{\gamma,\gamma_0}, 0) \quad (\gamma = 1,2,3,\cdots\cdots \quad) \tag{5.31}$$

for an incident electron-wave with a lateral mode γ_0 originating at the cathode edge of the system, and

$$(A^L_\gamma, B^R_\gamma) = (0, \delta_{\gamma,\gamma_0}) \quad (\gamma = 1,2,3,\cdots\cdots \quad) \tag{5.32}$$

when it originates at the anode edge. In Eqs. (5.30) and (5.31) δ_{γ,γ_0} is the delta function. If the system has a real bound state which may be caused by an attractive scatterer such as an InGaAs quantum well or a deep donor trap level, a bound state problem has to be solved as well as the above scattering state problem to obtain a complete set of wavefunctions. Finally, total tunnelling current I_{tunnel} is calculated assuming the global coherent tunnelling of electron waves throughout the device as follows:

$$I_{tunnel} = \frac{e}{\pi\hbar}\int_{eV}^{\infty} T(E)\,\{f_L(E) - f_R(E)\}\,dE \tag{5.33}$$

where $f_L(E)$ and $f_R(E)$ are Fermi distribution functions in the cathode and anode regions respectively.

5.2.2 Lateral mode conserving and non-conserving resonant tunnelling

In this section the three-dimensional scattering theory described in the previous section is applied to the 0D-RTD structure shown in Fig. 5.4, and multi-mode quantum transport is analyzed numerically. The hour-glass shaped confinement potential due to surface Fermi-level pinning is calculated in advance using a classical device simulation with Spicer's surface defect model (see Tab. 2.2). This potential is then used to solve the three-dimensional Schrödinger equation. We focus on the effect of lateral mode mixing which is caused by elastic scattering due to the hour-glass shaped confinement potential on the multi-mode transmission properties and current-voltage characteristics of the device. The S-matrix is calculated to analyze momentum non-conservation tunnelling which can be observed in the off-diagonal components of the transmission probability. Furthermore a total tunnelling current through the device is calculated and compared with results for a device with uniform lateral confinement in order to investigate the mechanism of the fine structure in the current-voltage characteristics.

In the present work we adopt a laterally confined AlGaAs/InGaAs/AlGaAs double barrier resonant tunnelling structure. The assumed layer structure consists of a undoped $In_{0.08}Ga_{0.92}As$ quantum well of 5 nm in thickness, two undoped $Al_{0.25}Ga_{0.75}As$ barriers of 4 nm in thickness, two undoped GaAs spacer layers of 6 nm in thickness, and n^+-type GaAs cathode and anode layers with donor concentration of 1.0×10^{18} cm^{-3}. The conduction band discontinuities in the GaAs / $Al_{0.25}Ga_{0.75}As$ and GaAs / $In_{0.08}Ga_{0.92}As$ heterostructures are assumed to be 187.0 and -37.2 meV respectively. The electron effective mass in the GaAs, $Al_{0.25}Ga_{0.75}As$, and $In_{0.08}Ga_{0.92}$ layers are assumed to be 0.067, 0.088, and 0.064 m_0 respectively. Lateral dimensions of the device are set to be 80 nm in both x and y dimensions.

The first part of the numerical simulation is to obtain a realistic lateral confinement potential distribution created by carrier trap levels on the lateral surface. The exact lateral confinement potential should be determined through a fully self-consistent calculation of the three-dimensional Schrödinger equation. However, this would require an enormous amount of computational time which is beyond our present requirements. The self-consistent calculations are left for a future analysis of Coulomb blockade tunnelling where the self-consistent field produced by a single electron is dominant. In the present work the confinement potential is calculated by using a classical device simulation [28] in which surface carrier traps are taken into consideration by using Spicer's unified defect model [29]: a deep donor level at 0.925 eV measured from the conduction band edge and a deep acceptor level at 0.75 eV from the valence band edge are assumed for the GaAs lateral surface. As long as the size of the lateral confinement is much larger than the width of the quantum well, the calculated potential distribution should be a fairly good approximation for the exact potential distribution determined by the self-consistent calculation. Figure 5.4 shows the calculated potential distribution where the sheet concentration of the surface deep level is assumed to be 5.0×10^{12} cm^{-2}, which is a plausible value large enough to pin the Fermi-level on the surface. It can be seen that the hour-glass shaped confinement potential results from the different surface depletion widths in the intrinsic and contact regions.

The second part of the simulation is to calculate the lateral eigenenergies and two-dimensional eigenstates at each z-point by using the hour-glass confinement potential. Equation (5.4) is discretized by using a three-dimensional finite-difference mesh lattice, shown in Fig. 5.6, which has a uniform mesh spacing in the x and y dimensions and a non-uniform spacing in the z dimension.

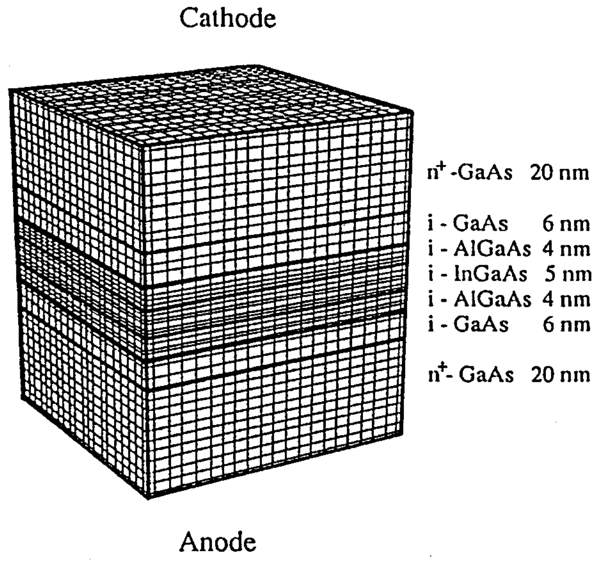

Figure 5.6 *Three-dimensional finite difference mesh lattice used for numerical calculations. The mesh spacing has been chosen to be small for the double barrier structure.*

Eigenenergies of the resultant finite-difference equation are obtained up to a given value of total energy by using the bisection method following Householder's tridiagonalization. The corresponding eigenvectors are then calculated by the inverse iteration method. To speed up finding the eigenvectors, the set of eigenstates obtained at the previous z-mesh point is used as an initial guess for the eigenstates at the next z-mesh point. For numerical calculations a cut-off value is introduced for the maximum eigenenergy although all of lateral modes would be necessary to make a complete set. The number of wavefunctions required for realistic calculations depends on the system under consideration. In general at least all of the lateral eigenstates with eigenenergies below the Fermi energy should be taken into account. In the present calculations, for instance, there are four lateral eigenstates below the Fermi level and thirteen lateral modes are calculated for all z-mesh points.

By making use of the lateral eigenstates, the mixing coefficients, $C^{(0,1)}_{\gamma,\gamma'}$ and $C^{(0,2)}_{\gamma,\gamma'}$, and the unitary transformation matrix, $M_{\gamma\gamma'}(z)$, can be evaluated from Eqs. (5.7), (5.8), and (5.10). The eigenvalue equation (5.16) is then solved to get the renormalized wavenumbers, $K_\gamma(z)$, and the unitary matrix, $V_{\gamma\gamma'}(z)$. As the matrix $W_{\gamma\gamma'}(z)$ is real and symmetric, all of the eigenvalues and eigenvectors can be obtained by using the QL method. Finally, by using the lateral eigenstates at the cathode and anode edges, the multi-mode transfer matrix and the resultant scattering matrix are calculated from Eqs. (5.21) - (5.27).

The multi-mode transmission probability calculated for the 0D-RTD structure is shown in Fig. 5.7. Figure 5.7 (a) shows the total energy dependence of transmission probability for the diagonal tunnelling from the γth-incident-mode to the γth-transmission-mode, $|S_{12}(\gamma, \gamma)|^2$ and Fig. 5.7 (b) that for the off-diagonal tunnelling from the 1st-incident-mode to γth-transmission-mode, $|S_{12}(1, \gamma)|^2$.

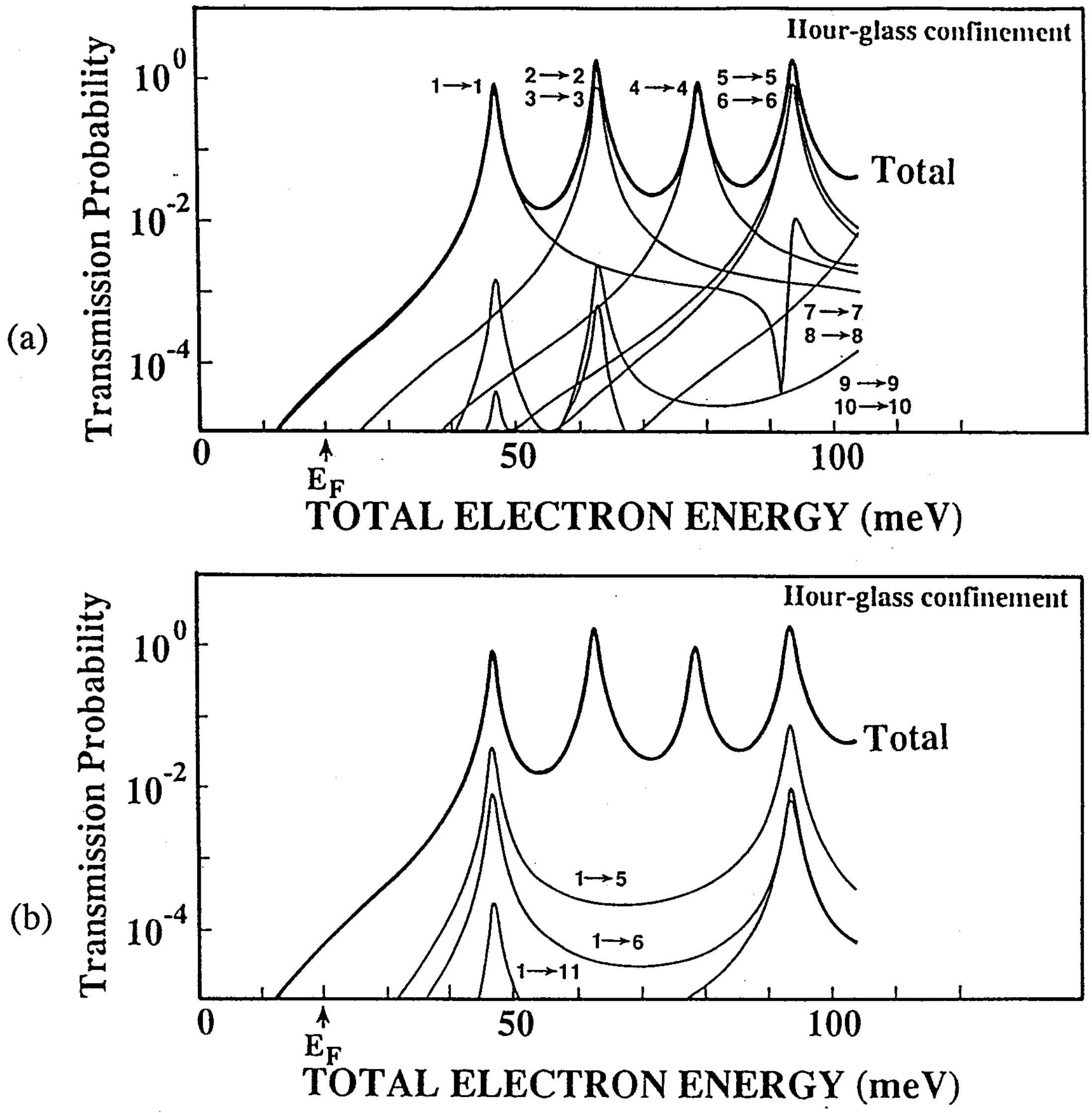

Figure 5.7 Multi-mode transmission probability calculated for the 0D-RTD with the hour-glass lateral confinement: (a) total energy dependence of transmission probability for the diagonal tunnelling from the γ-th-incident mode to γ-th-transmission mode, $|S_{12}(\gamma, \gamma)|^2$, and (b) that for the off-diagonal tunnelling from the 1st-incident-mode to γ-th-transmission mode, $|S_{12}(1, \gamma)|^2$. The S-matrix elements are drawn for γ's up to 11. A thick solid line represents total transmission probability T(E) defined by Eq. (5.30).

The S-matrix elements are drawn for values of γ's up to 11. In addition, the transmission probability calculated for a device with completely uniform confinement is shown in Fig. 5.8. Before proceeding the detailed discussion of these results, it is worth commenting on this structure. The uniform lateral confinement used for the calculation in Fig. 5.8 could be realized by doping the resonant tunnelling structure uniformly as well as the contact regions. However, resonant tunnelling is hardly observed in such doped structures because resonant electron-waves suffer from frequent impurity scattering in the quantum well. Thus the results in Fig. 5.8 are based on an unrealistic assumption that electron-waves travel ballistically even in a doped tunnelling structure and are given simply for comparison with the results for the hour-glass confinement. In Fig. 5.8 the S-matrix has no off-diagonal elements since there is no lateral wavefunction mismatch anywhere in the system. This is called independent channel tunnelling, as the lateral modes are not mixed. The total transmission rate is then just a superposition of the transmission probabilities through these independent channels shown as a thick solid line in Fig. 5.8.

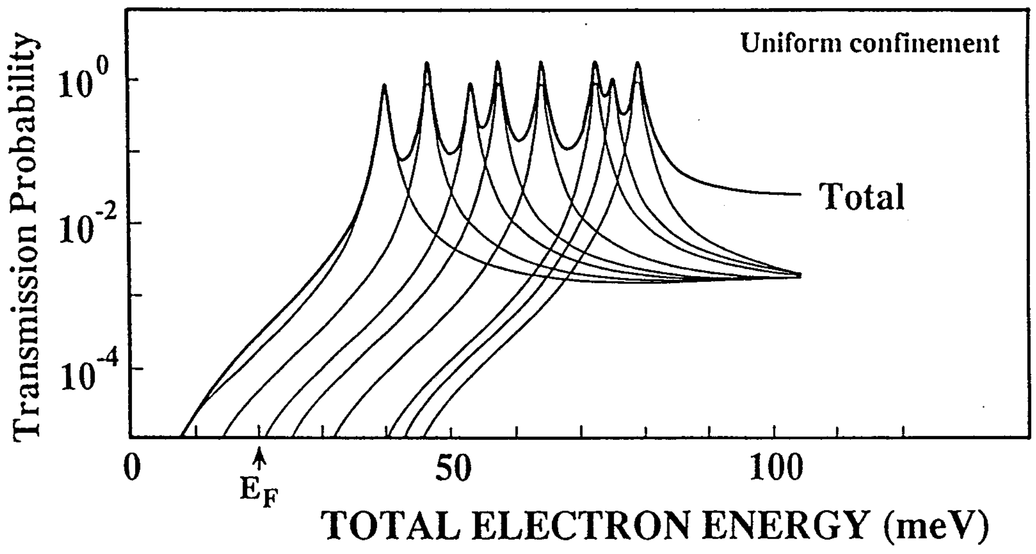

Figure 5.8 Multi-mode transmission probability $|S_{12}(\gamma, \gamma)|^2$ *calculated for the 0D-RTD with the uniform lateral confinement. The off-diagonal elements are now zero.*

Electronic states corresponding to the first three transmission probability peaks in Fig. 5.8 are shown in Figs. 5.9 (a) - (d). These figures show visualized three-dimensional existent probability of electrons, $|\psi_E(x, y, z)|^2$, in the device: (a) $|\psi_E(x, y, z)|^2$ obtained for the 1st mode incident wave from the cathode at the first peak energy, (b) for the 2nd mode incident wave from the cathode at the second peak energy, (c) for the 3rd mode incident wave from the cathode at the second peak energy, and (d) for the 4th mode incident wave from the cathode at the third peak energy. It should be noted that the wavefunctions for these states are virtually localized in the quantum box and clearly reflect eigenstates of the quantum box itself. This fact means that the lateral mode index γ is a good quantum number throughout the device.

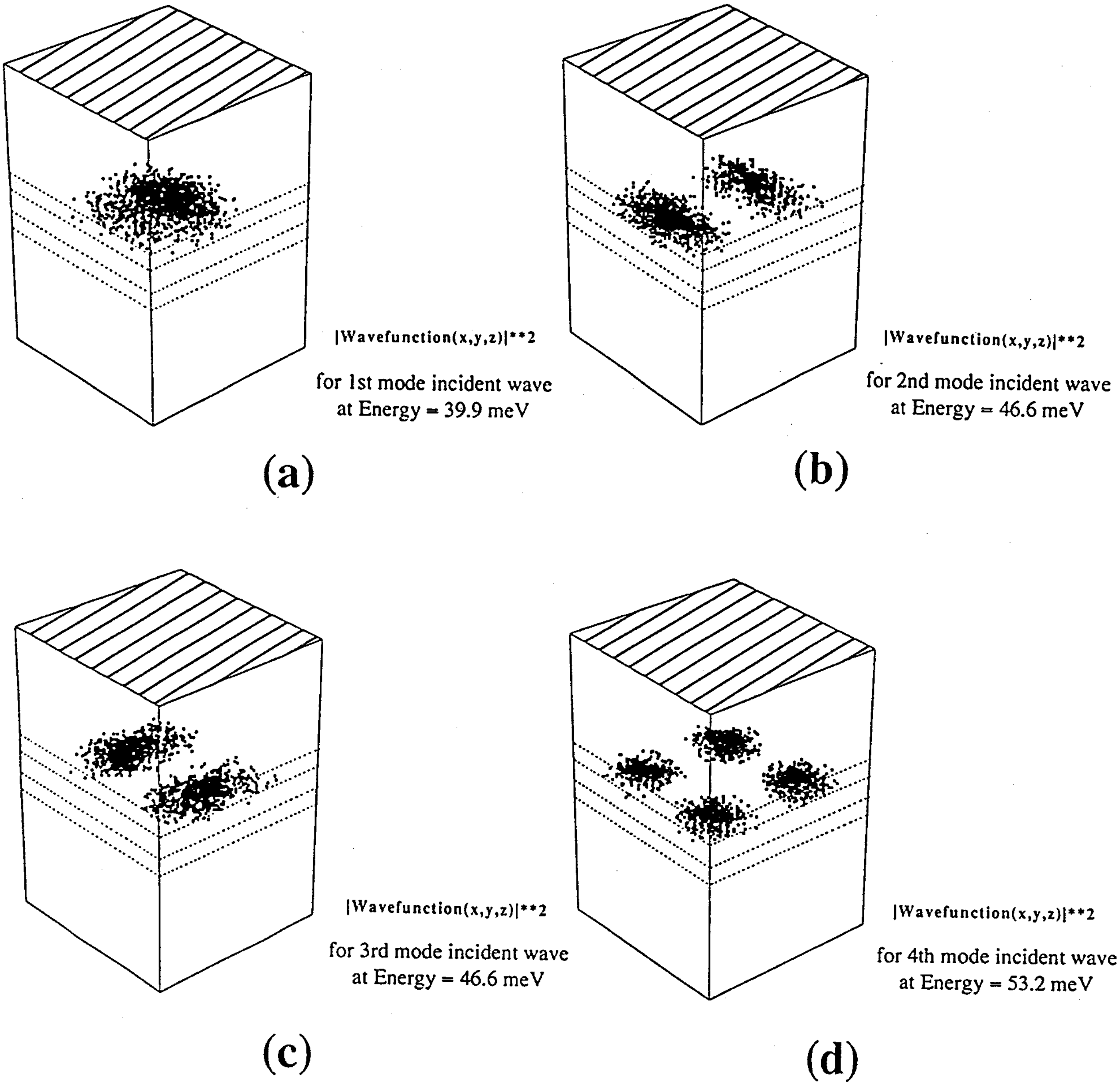

Figure 5.9 *Visualised three-dimensional existence probability of electrons, $|\psi_E(x, y, z)|^2$, at the lowest three transmission peaks in Fig. 5.8: (a) for the 1st incident mode at the first peak energy, (b) for the 2nd incident mode at the second peak energy, (c) for the third incident mode at the second peak energy, and (d) for the 4th-incident mode at the third peak energy. It should be noted that the second peak in Fig. 5.8 is caused by both tunnelling processes 2 $\rightarrow$ 2 and 3 $\rightarrow$ 3. It can be seen that the electron distribution clearly reflects the lateral eigenstates in the quantum box.*

On the other hand the following two major differences can be seen in the tunnelling properties of the hour-glass confinement shown in Fig. 5.7. First, the energy intervals between transmission probability peaks become larger than those in Fig. 5.8 leading to a large peak-to-valley ratio of transmission probability. Second, the elastic scattering due to the the hour-glass confinement potential mixes the lateral modes and opens new off-diagonal tunnelling channels. In Fig. 5.7 (b) two peaks can be found in the off-diagonal elements of the S-matrix which represent lateral-mode non-conserving resonant tunnelling. It should be noted that off-diagonal tunnelling with the 1st incident mode is observed only for the 5th, 6th, and 11th transmission modes. This is purely because of a selection rule for parity of lateral wavefunctions. Because the elastic scattering due to the hour-glass confinement potential does not break symmetry under mirror reflection in x and y dimensions, a lateral mode couples only with other modes having the same parity. The lowest wavefunction has even parities in both x and y dimensions, and can therefore couple only with upper modes described above. Additional structures are also observed in the diagonal elements in Fig. 5.7 (a). For example, an asymmetric resonant structure can be seen at a total energy of 91.7 meV. It should be noted that the off-diagonal tunnelling probability is quite large for the process, 1 → 5, at this energy.

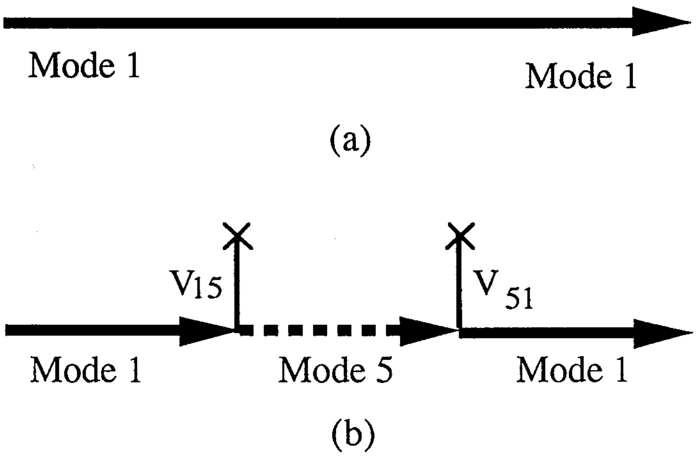

Figure 5.10 Diagramatic representation of two processes involved in the diagonal tunnelling, 1 → 1, at Fano resonance: (a) zero order tunnelling and (b) second order tunnelling. V_{51} and V_{15} denote the elastic scattering between 1st and 5th lateral modes due to an hour-glass confinement potential.

In these circumstances the ratio of the second order diagonal tunnelling is enhanced in which two elastic scattering events are involved between the 1st and 5th lateral modes: this is shown diagrammatically in Fig. 5.10 (b). This process is now at resonance and interferes with the major diagonal tunnelling process, shown in Fig. 5.10 (a), which is at off-resonance. The interaction between these two tunnelling processes results in the Fano-resonance type lineshape in the transmission probability [30]. The three-dimensional existent probability of electrons, $|\psi_E(x, y, z)|^2$, at the energy of 91.7 meV is shown in Fig. 5.11. It should be noted that the electron existent probability in the quantum box reflects features of the 5th-mode rather than 1st-mode despite the 1st mode nature of the incoming wave. This signifies that a large part of the incoming wave is converted to the 5th-mode in the quantum box by suffering from lateral mode non-conserving perturbation due to the change in the lateral confinement. In these circumstances the lateral mode index γ is no longer a good quantum number for the system.

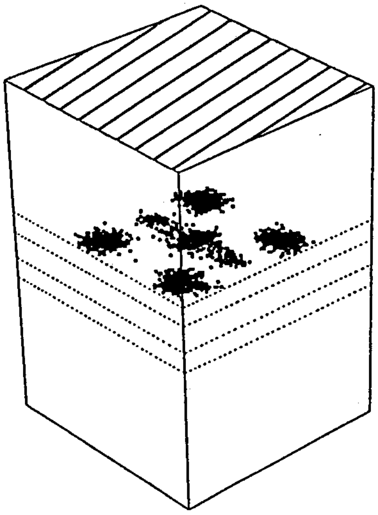

|Wavefunction(x,y,z)|**2

for 1st mode incident wave
at Energy = 91.7 meV

Figure 5.11 *Visualised three-dimensional existent probability of electrons,$|\psi_E(x, y, z)|^2$, for the first incident mode at an energy of 91.7 meV which corresponds to the dip of the Fano-resonance in Fig. 5.7. It should be noted that the electron existent probability in the quantum box reflects feature of the 5th-mode rather than 1st-mode despite the first mode nature of the incoming wave.*

The applied voltage dependence of the total tunnelling current is calculated by assuming ballistic transport throughout the device (Eq. (5.33)). Figure 5.12 (a) shows the I-V characteristics of the device with the hour-glass lateral confinement calculated at a temperature of 77 K. Under an applied bias a piecewise linear model has been adopted for the external potential $V_{EX}(z)$ in Eq. (5.2), which was introduced in Sec. 3.3.2 for large-area RTDs: uniform external electric field is assumed in the intrinsic regions of the device.

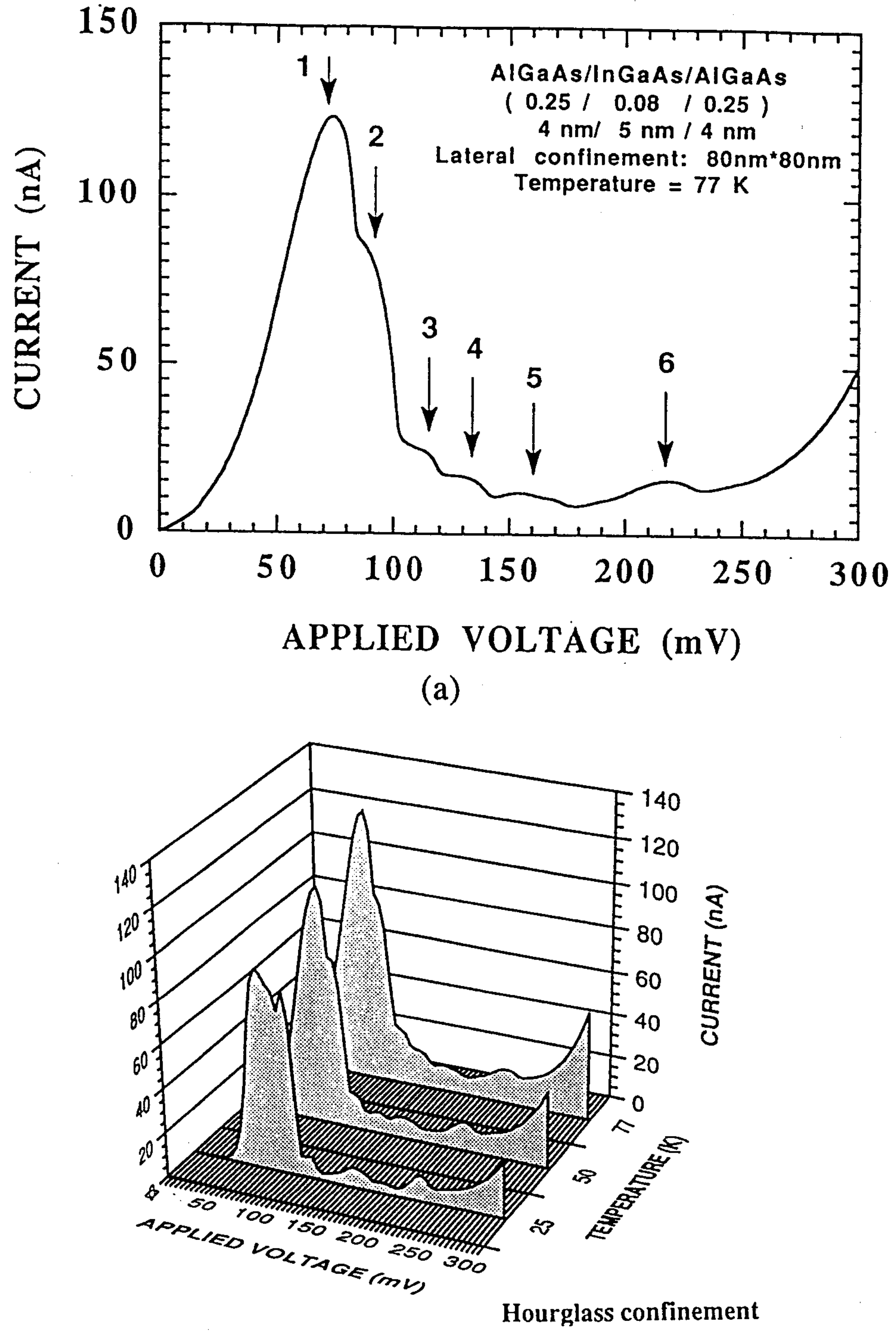

(a)

(b)

Figure 5.12 (a) Applied voltage dependence of total tunnelling current calculated by using Eq. (5.33) at a temperature of 77K: Observed satellite current peaks and shoulders are indicated by arrows. (b) I-V characteristics calculated at lower temperatures.

Several satellite current peaks and shoulders are observed superposed on the conventional negative conductance characteristics of 2D-RTDs. Figure 5.12 (b) shows the I-V characteristics calculated at lower temperatures. The fine structure in the I-V characteristics can be seen more clearly at a lower temperature.

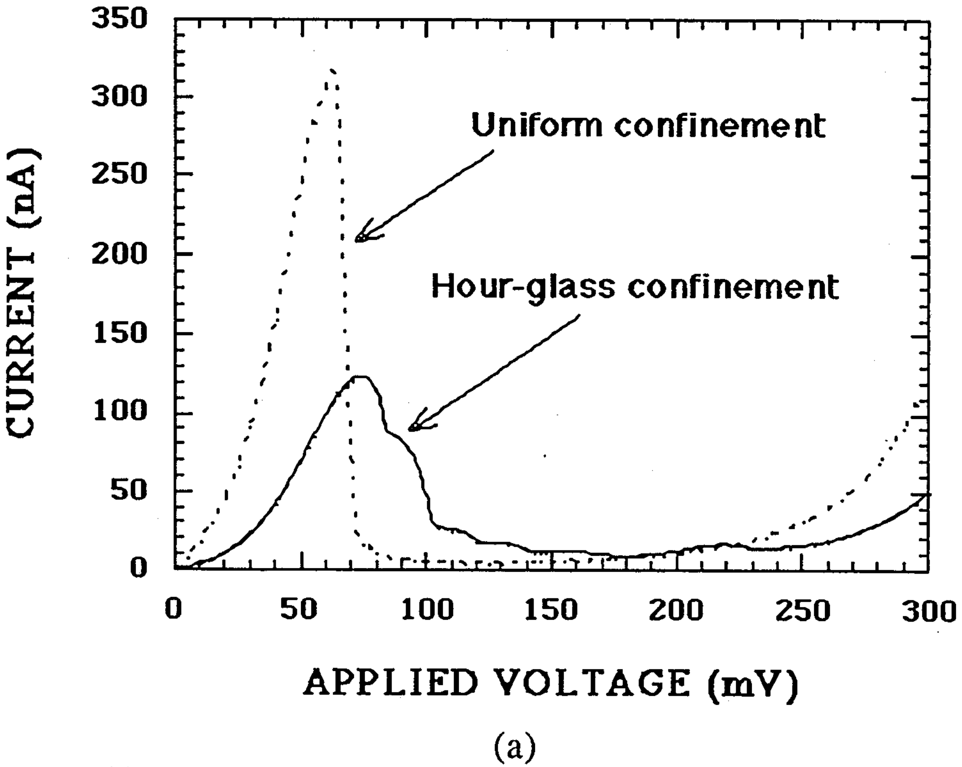

(a)

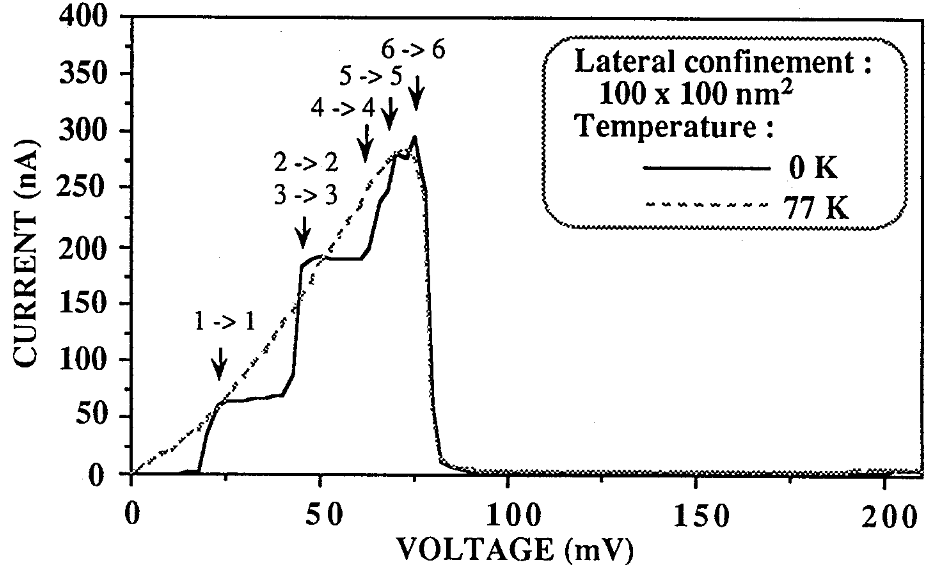

(b)

*Figure 5.13 (a) Comparison of current-voltage characteristics calculated at 77K for the hourglass confinement (solid line) with those for the uniform confinement (broken line). (b) The I-V characteristics calculated at T = 0K for the uniform lateral confinement of 100 nm * 100 nm.*

Also the current-voltage characteristics are compared with those of the device with the uniform confinement (broken line) in Fig. 5.13. It should be noted that, at a temperature of 77K, only one major current peak is found without any fine structure in the case of the uniform confinement as the peak-to-valley ratio of the transmission probability shown in Fig. 5.8 is not large enough to separate the contribution from each mode at this temperature. At lower temperatures peaks and shoulders are clearly seen which exactly correspond to transmission peaks as indicated in Fig. 5.13(b).

In the case of the hour-glass confinement, on the other hand, the mechanism of the fine structure seen in Fig. 5.12 is found more complicated as is explained below. The total energy dependence of the transmission probability calculated at the first four peak (shoulder) voltages are shown in Figs. 5.14 (a) - (h): the diagonal elements, $|S_{12}(\gamma, \gamma)|^2$, calculated at the first, second, third, and fourth peak voltages in Figs. 5.14 (a), (c), (e), and (g) and the off-diagonal elements, $|S_{12}(1, \gamma)|^2$, in Figs. 5.14 (b), (d), (f), and (h). Total transmission rate is shown by using thick solid lines as in Figs. 5.7 and 5.10. The current peak (shoulder) appears when the new transmission peak (indicated by an arrow) plunges into the Fermi sea. It can be seen that all of the four peaks are caused mainly by the diagonal tunnelling (Figs. 5.14 (a), (c), (e), and (g)) since the off-diagonal tunnelling shown in Figs. 5.14 (b), (d), (e), and (h) contributes much less to the total transmission probability. Thus these four peaks mainly result from the lateral-mode conserving resonant tunnelling: 1 → 1 tunnelling for the first main peak, 2 → 2 and 3 → 3 for the second, 4 → 4 for the third, and 5 → 5 and 6 → 6 for the fourth. As shown in Fig. 5.12 (b) the fourth peak becomes smaller with decreasing temperature since it is caused by the tunnelling of electrons which are thermally excited to the 5th and 6th modes located above the quasi-Fermi level in the cathode region. Obviously other higher diagonal channels such as the 7 → 7, 8 → 8, etc. play a negligibly small role since very few electrons occupy the higher eigenstates in the cathode region.

Let us now turn to the two small current peaks at higher applied voltages in Fig. 5.12. The total energy dependence of the transmission probability calculated at the two peak voltages are shown in Figs. 5.15 (a) - (d). Figs. 5.15 (a) and (b) show the diagonal, $|S_{12}(\gamma, \gamma)|^2$, and off-diagonal, $|S_{12}(1, \gamma)|^2$, at the fifth peak voltage, and Figs. 5.15 (c) and (d) the diagonal, $|S_{12}(\gamma, \gamma)|^2$, and the off-diagonal, $|S_{12}(2, \gamma)|^2$, at the sixth peak voltage.

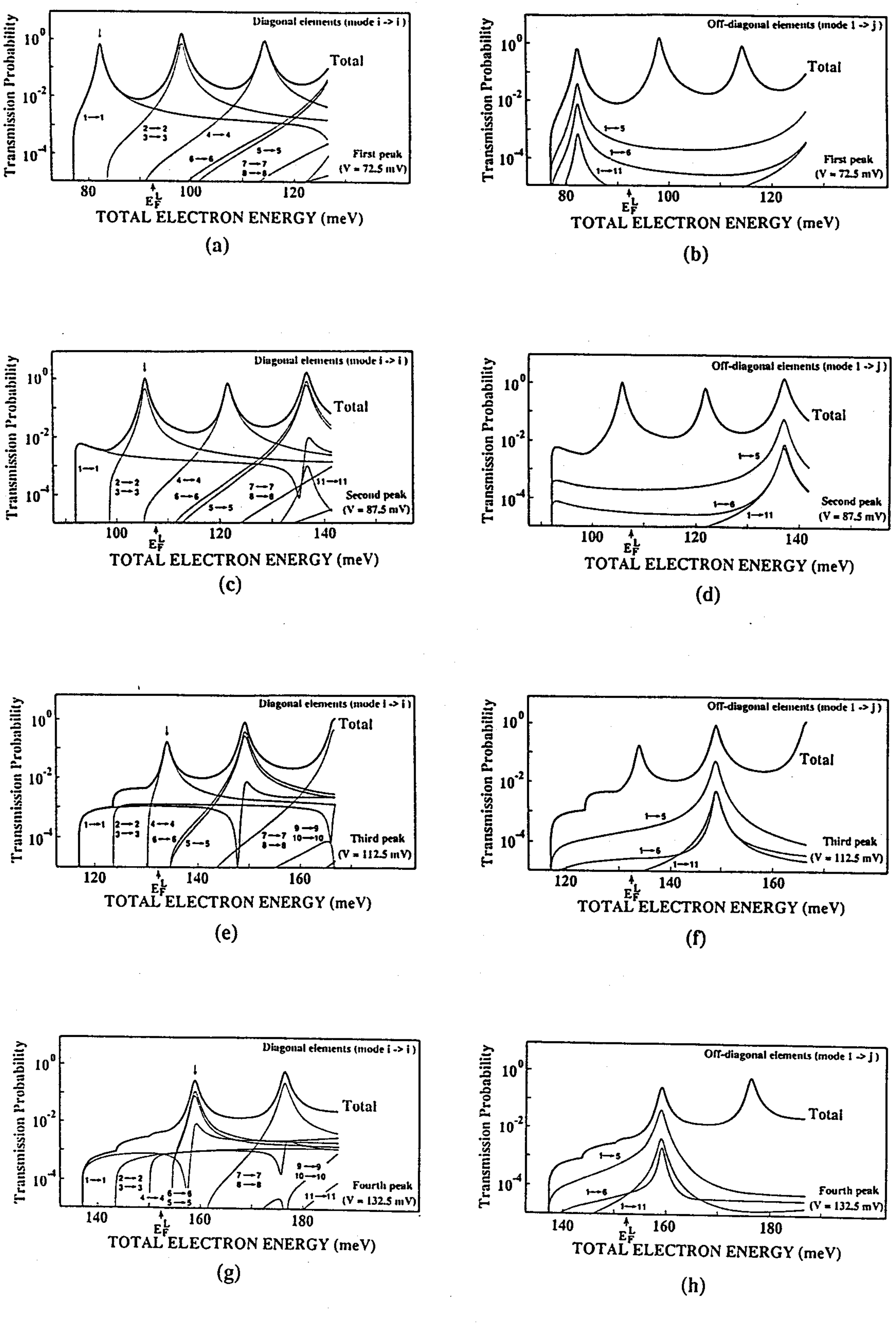

Figure 5.14 Total energy dependence of the transmission probability calculated at the first four peak (shoulder) voltages indicated by arrows with numbers 1, 2, 3, and 4 in Fig. 5.12: (a), (c), (e), and (g) show the diagonal elements, $|S_{12}(\gamma, \gamma)|^2$ *, and (b), (d), (f), and (h) the off-diagonal elements,* $|S_{12}(1, \gamma)|^2$*. Total transmission rate is shown by using thick solid lines as in Figs. 5.7 and 5.8.*

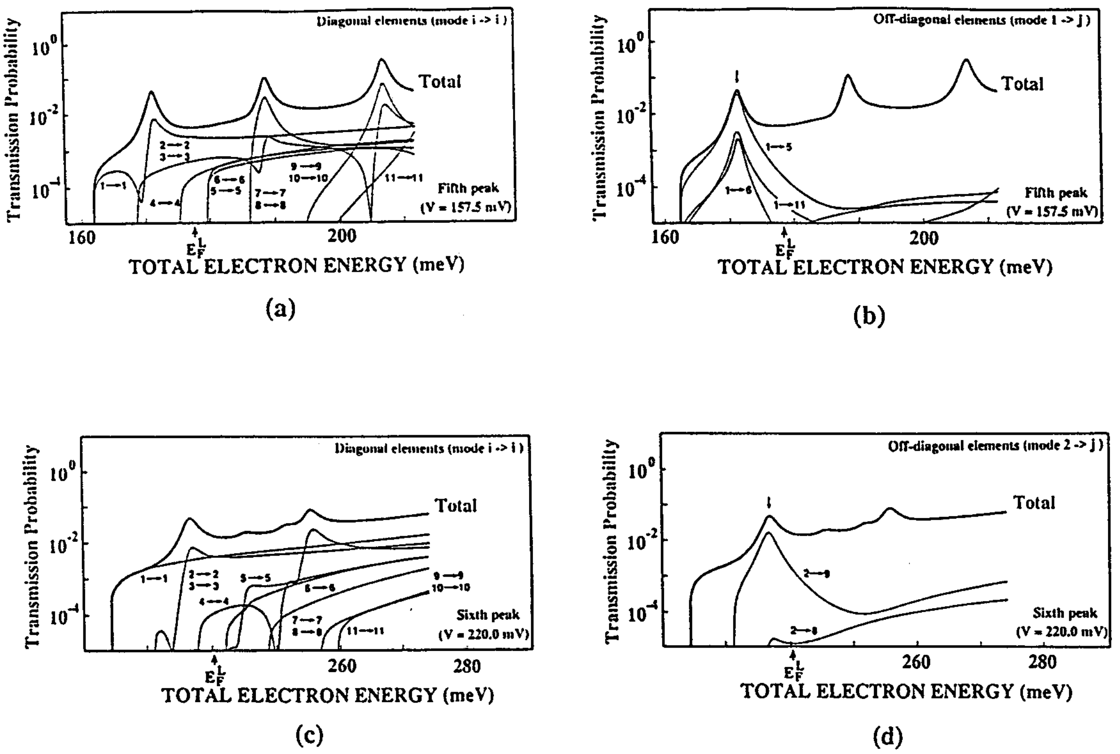

Figure 5.15 Total energy dependence of the transmission probability calculated at the last two peak voltages indicated by arrows with numbers 5 and 6 in Fig. 5.12.: (a) and (c) show the diagonal elements,$|S_{12}(\gamma, \gamma)|^2$*, (b) the off-diagonal,*$|S_{12}(1, \gamma)|^2$*, and (d) the off-diagonal,* $|S_{12}(2, \gamma)|^2$.

Small transmission peaks located under the Fermi energy are again found which lead to the fifth and sixth current peaks. These transmission peaks are, however, attributed not to the diagonal tunnelling but to the off-diagonal tunnelling: the lateral-mode non-conserving resonant tunnelling 1 → 5 for the fifth peak shown in Fig. 5.15 (b) and 2 → 9 for the sixth peak in shown Fig. 5.15 (d). It should be mentioned that, for the sixth current peak, the 3 → 10 tunnelling channel is simultaneously opened with the 2 → 9 channel. As described above, the fourth current peak is mainly due to the 5 → 5 and 6 → 6 diagonal tunnelling, along with a small contribution from the 1 → 5 off-diagonal tunnelling. Even after the diagonal tunnelling channels close, at a voltage such that the fifth and sixth lateral eigenstates in the quantum well simultaneously line up with the fifth and sixth lateral eigenstates in the cathode region, the off-diagonal channel 1 → 5 is still open resulting in another current peak. Thus the fifth 1 → 5 peak can be thought of as a satellite peak of the main fourth 5 → 5 peak. However, in the case of the sixth 2 → 9 peak the diagonal 9 → 9 channel cannot give rise to a main peak because the 9th eigenstate in the cathode region is essentially unoccupied, and the 2 → 9 channel gives rise to a new main peak.

As shown here the number of extra current peaks (shoulders) observed in the I-V characteristics directly measures the number of the resonant tunnelling channels in which the lateral mode is not conserved. Also it is possible to estimate the magnitude of the lateral mode mixing by analyzing the extra peak current.

5.3 Gated resonant tunnelling structures -squeezable quantum dots-

As found in the previous section the hourglass shaped confinement potential in a simply etched structure results in the lateral mode mixing and makes the characteristics of the device difficult to understand. Ideal lateral confinement that we want to have is the one which is virtually flat around the tunnelling barriers (see Fig. 5.16) and does not cause the complicated mode mixing. As shown in Sec. 5.2.2 the independent mode tunnelling would be achieved if the pseudo-uniform confinement were realised. In addition, the size of the confinement is desired to be controllable for systematic investigations of three-dimensional confinement.

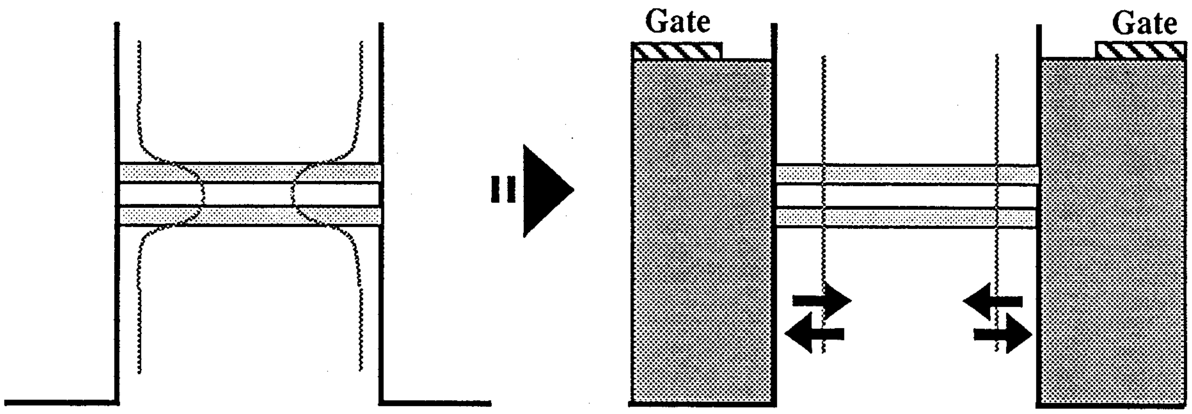

Figure 5.16 Ideal pseudo-uniform confinement potential controlled by gate electrodes.

For this purpose a new variable area resonant tunnelling diode (VARTD) [31] has been fabricated by Chris Goodings of Microelectronics Research Centre, University of Cambridge, in collaboration with the author by using Samples 2 and 3. Specifications of the tunnelling barrier structures in Samples 2 and 3 can be found in Fig. 4.2. Cross sectional and perspective views of the VARTD are shown in Fig. 5. 17 (a) and (b), respectively.

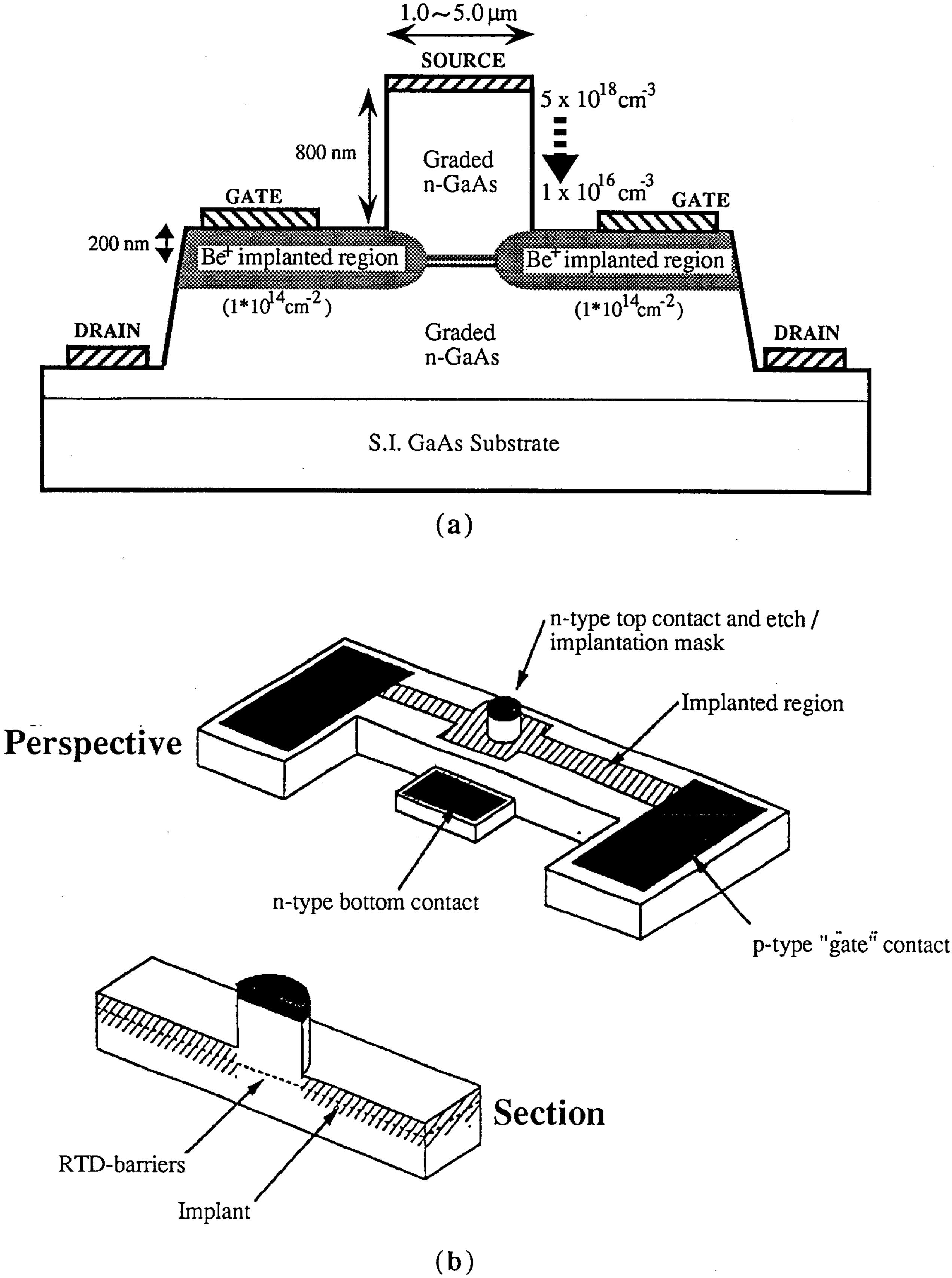

Figure 5.17 Schematic cross sectional (a) and perspective (b) views of a new gated VARTD.

In the VARTD lateral confinement arises from a reverse biased p-n junction which is formed by using beryllium focused ion beam implantation (at 60 keV with dose of 1×10^{14} cm^{-2}) after an anisotropic etch of depth 800 nm above the barriers. In both Samples 2 and 3 a graded doping profile is adopted in which the concentration of Si is reduced from 5×10^{18} cm^{-3} adjacent to the contact to 1×10^{16} cm^{-3} near the barriers in order to achieve a large variation in depletion width. Thickness of a layer remained above the barriers is adjusted to be about 200 nm so that the concentration peak of the implanted Be$^+$ can be aligned to the quantum well resulting in a symmetric confinement potential. The size of the top contact pad is varied from 5 μm down to 1 μm in diameter.

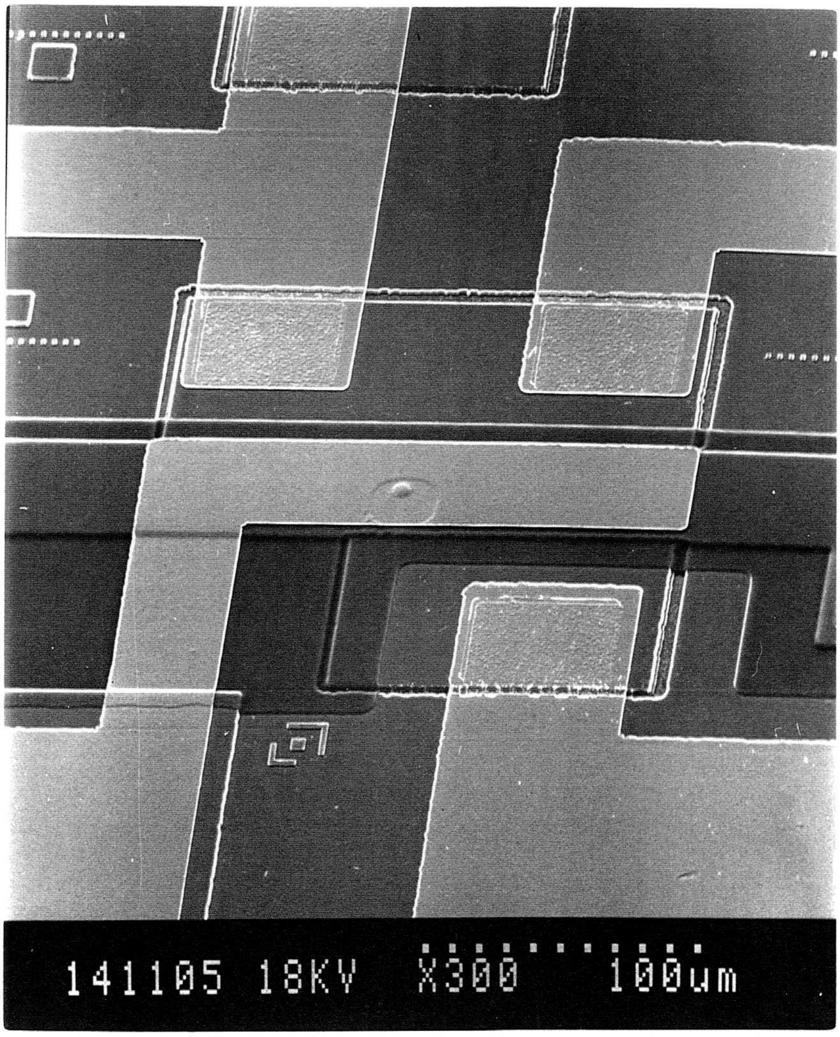

Figure 5.18 A perspective view of a completed device. A small dot seen at centre of the photograph is a device area.

A perspective view of a completed device is also shown in Fig. 5.18 in which two sets of the VARTDs are framed. In this picture the VARTD has been already planarized by using a thin dielectric layer and then an interconnect to the top contact has been deposited.

The potential and current distributions are calculated for a VARTD with a large-area contact pad by using the same classical hydrodynamic device simulation HIHEART introduced in Chapter 2 to see the effects of the graded doping on the shape of the lateral confinement. Figures 5.19 (a) - (c) show (a) potential distribution, (b) current distribution, (c) lateral confinement potential wells calculated for a 2 μm VARTD at a gate voltage of -2.0 V and an emitter-collector voltage of 1.0 V. In Figs. 5.19 (a) and (b) lateral confinement turns out to be virtually flat around the barriers as required. This results from the alignment of a concentration peak of implanted ions to the double barrier structure and enables us to reduce cumbersome effects of the asymmetric confinement potential on the characteristics which have been reported in the resonant tunnelling device with a surface Schottky gate [33]-[35].

We see from (c) that, as expected for a device of this size, the width of the lateral confinement potential well is far from the region in which the lateral quantization would appear and a smaller-area VARTD is necessary to observe the lateral confinement effects. In the next section, however, we first analyze VARTDs with 2 μm and 3 μm top contact pads which are supposed to be in an intermediate regime between conventional 2D-RTDs with complete lateral translational invariance and three-dimensionally confined 0D-RTDs. We show the squeezing effects of applied gate bias on the current-voltage characteristics. In Sec. 5.3.2, secondly, the results on three-dimensional confinement effects obtained from smaller VARTDs are presented.

5.3.1 Variable area resonant tunnelling devices

First let's see the characteristics for the large-area VARTDs. Devices with various size top contact pads (from 2 μm to 5 μm in diameter) have been fabricated by using Sample 2. Typical I-V characteristics for a 3 μm diameter VARTD at 4.2K are shown in forward and reverse bias directions in Fig. 5.20. With increasing negative gate bias the peak current can be altered by a factor of approximately 2. The range of the negative gate bias is limited by reverse breakdown of the P-N junction which occurs at about -7 V. So a pinch-off regime where the effects of lateral quantization are expected to be observable can not be seen in this 3 μm device.

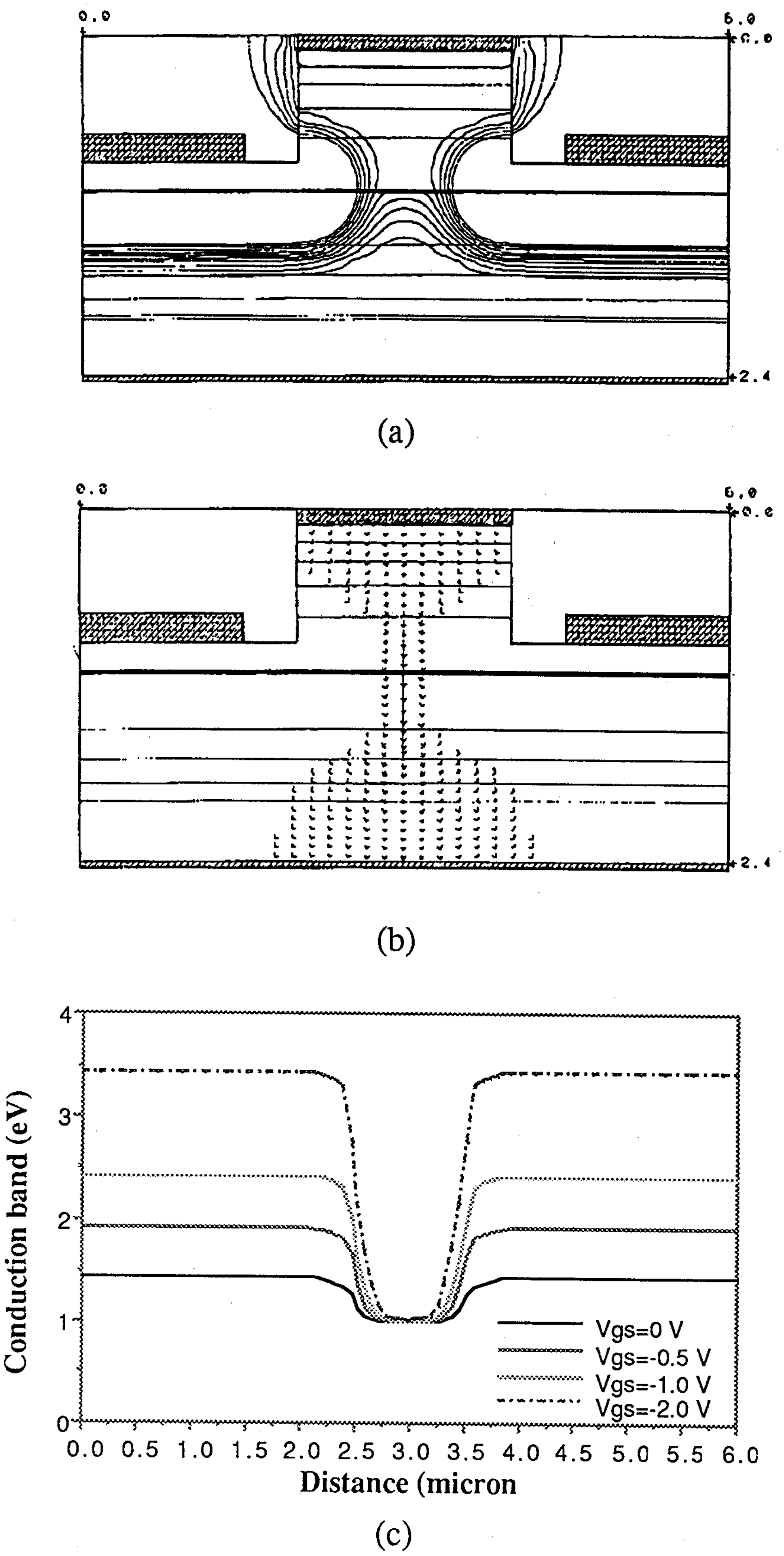

Figure 5.19 Two-dimensional potential (a) and current (b) distributions at a gate bias of -2.0 V and an emitter-collector voltage of 1.0 V, and lateral confinement potential profile for various values of gate bias calculated for a 2 μm device by using HIHEART (see Chap. 2).

It should be noted that a small shift is seen in the resonant voltage for the 3 μm device (Fig. 5.20), and it is pronounced more for a 2 μm device (see Fig. 5.21). For larger devices than 3 μm this shift is not noticeable and becomes greater as the device size is further reduced as shown in the next section.

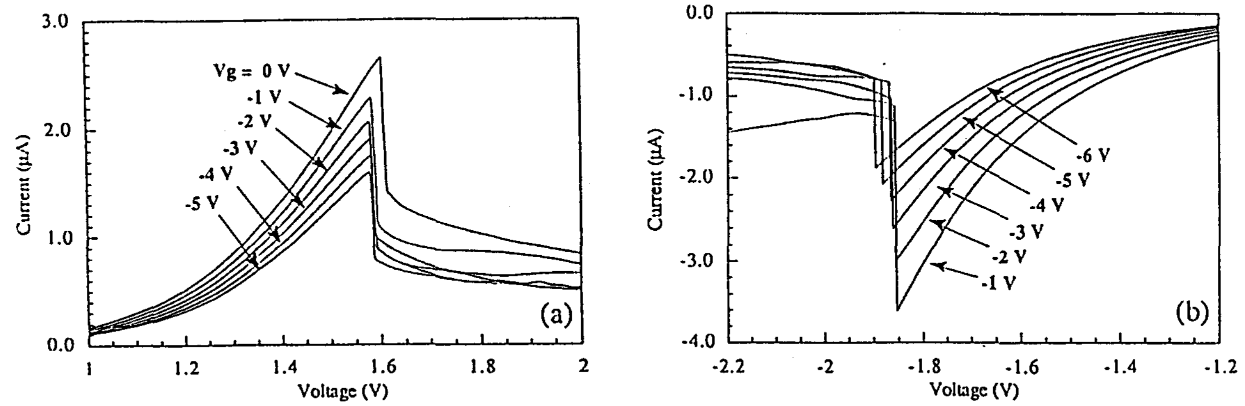

(a) (b)

Figure 5.20 *Characteristics of a 3 μm diameter device at 4.2K in (a) forward bias and (b) reverse bias. The gate bias is referred to the potential of the bottom contact. Gate leakage currents of order 100 pA were measured for this device. Data taken by C. Goodings, Microelectronics research centre, University of Cambridge, in collaboration with the author.*

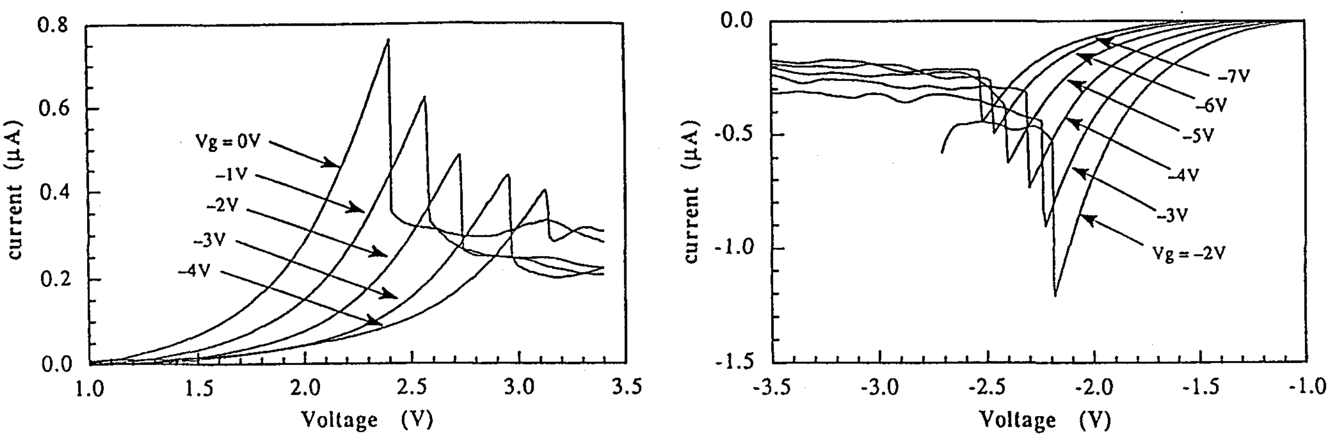

(a) (b)

Figure 5. 21 *Characteristics for a 2 μm device at 4.2K (a) in forward bias and (b) reverse bias. Data taken by C. Goodings, Microelectronics research centre, University of Cambridge, in collaboration with the author.*

The shift of the resonant voltage towards a larger bias regime observed for the 3 μm device indicates that the gate depletion regions induced by the reverse biased PN junction begins to affect the potential energy of the channel though it is still small, and the system is under transition from two-dimensional to zero-dimensional. This becomes clearer by plotting the resonant voltage as a function of the applied voltage relative to the turn-on voltage of the PN-juction which is discussed in the next chapter.

The symmetry of the lateral confinement potential around the barriers which is expected for the VARTD becomes evident through the observed P/V current ratios. In the case of the surface gated VARTDs referred above it has been found by Beton et al. [38] that the P/V ratio in one bias remained roughly constant while in the other bias the ratio diminished rapidly with applied gate voltage. This has been attributed to a gate-voltage dependent asymmetry in the lateral confinement potential, resulting from the gate electrode located on the surface . In the present case, however, the P/V ratio shows similar characteristics in both the forward and reverse directions as seen in Fig. 5.20. With increasing negative gate bias, a gradual decrease is found in the P/V current ratio which could be caused by the gate-bias induced asymmetry of the confinement potential discussed below, The amount of degradation is, however, similar for both the positive and negative gate voltages. This indicates that the implanted gate is itself roughly symmetrical.

From the data shown in Fig. 5.20 an effective device diameter can be estimated as a function of gate bias, and some information can be derived on the amount of the depletion occuring at the resonant tunnelling barriers. We introduce the effective device diameter, $(D - x)$, defined by the following expression:

$$I = I_0 \pi (D - x)^2 / 4 \tag{5.34}$$

where I_0 is the peak current density. The effective device diameter obtained for both 3 μm and 2 μm diameter devices are shown in Fig. 5. 22 as a function of gate voltage.

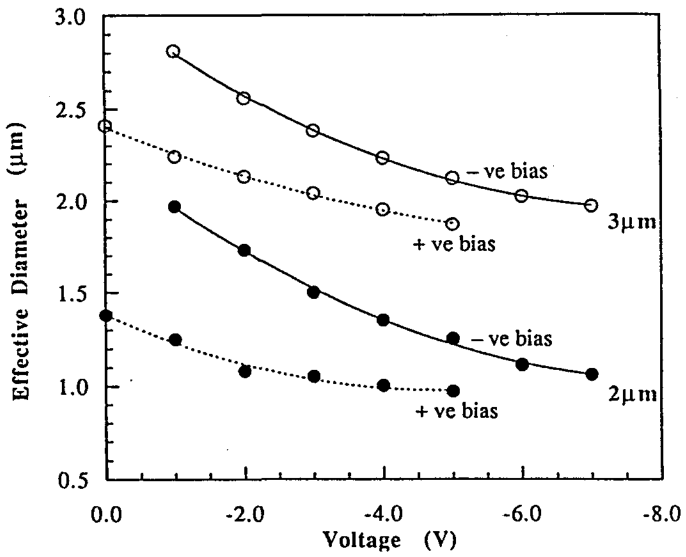

Figure 5.22 Effective electrical device diameter for 2 μm and 3 μm diameter top pads in forward and reverse bias at 4.2K. Data taken by C. Goodings, Microelectronics research centre, University of Cambridge, in collaboration with the author.

It should be noted that a difference in the depletion is seen for the diodes in positive and negative bias directions. This asymmetry in the I-V characteristics arises not from the asymmetry in the implanted region but from the geometry of the fabricated device and the configuration of electrodes: the potential distribution inside the present device is not symmetric for two ways of applying bias. The amount of squeezing depends on the voltage difference between the gate and the channel (the n-type region between the gate). For the present material there is a large voltage drop across the barriers at resonance which significantly affects this. For the measurement configuration used, the potential difference between the gate and the lower part of the channel remains constant in both forward and reverse bias, whereas the potential difference between the gate and the upper part of the channel alters by approximately twice the resonance voltage, with the greatest squeezing occurring in forward bias. For the 3 μm device here this is about 3.4 V. Assuming that the implant is symmetrical we would therefore expect that the effective device diameter for the 3 μm diode in forward and reverse bias would be identical but displaced by a gate voltage of about 3.4 V. The results in Fig. 5. 21(a) are indeed consistent with this.

5.3.2 Three-dimensional confinement effects on tunnelling characteristics

Now let's consider smaller devices in which we would expect to see three-dimensional quantization effects on the characteristics. VARTDs with top pads of 1.4, 1.2, and 1.0 μm have been fabricated by using the same material. Among these devices the smallest 1.0 μm one has been found to be completely pinched off even at zero gate bias. This is contrasted with the results obtained by using the surface-gated VARTDs which has an open channel even for sizes as large as 0.4 μm. This fact implies that the implanted gate structure can achieve a wider depletion region, which enables us to observe an important regime by using relatively large devices. Therefore VARTDs with sizes between 1.0 and 2.0 μm are supposed to be appropriate for the present purpose. Figure 5.23 shows the characteristics of a 1.4 μm device at various gate bias: this device is pinched off with a gate bias of about -3.5 V.

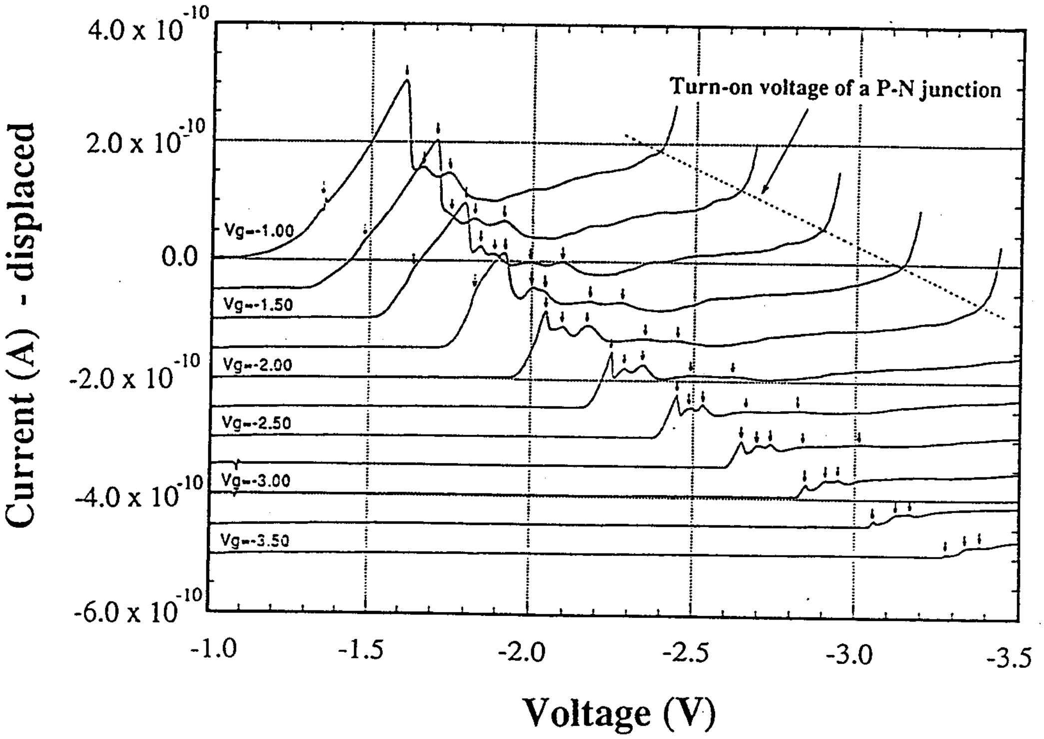

Figure 5.23 Characteristics of a 1.4 μm diameter device at 4.2K in reverse bias. The main resonance peak is seen to sharpen and extra structure occurs in the valley current. Data taken by C. Goodings, Microelectronics research centre, University of Cambridge, in collaboration with the author.

The I-V curves are with a constant displacement along the current axis for clarity. Only the reverse-bias characteristics are shown since in the positive bias the channel is pinched-off even at zero gate bias probably due to the asymmetry of squeezing discussed in the previous section.

This device, in contrast to the larger devices, is found to have the I-V characteristics rich in structure: six small current peaks can be seen in total and their positions strongly depend on the gate bias. Also an increase in the resonance voltage with increasing gate bias is much larger than that for 3 μm device. The I-V curves are given in an extended voltage region, and so a steep increase in the current is seen at a larger voltage than the peak voltage which results from the turn-on of the gate-to-emitter PN-junction. The shift of the current threshold for the turn-on of the PN-junction is found almost exactly the same as the increase in the applied gate bias as expected. The resonant peak voltage increases more slowly than the turn-on voltage for smaller gate bias, but starts to follow it as the gate bias is increased.

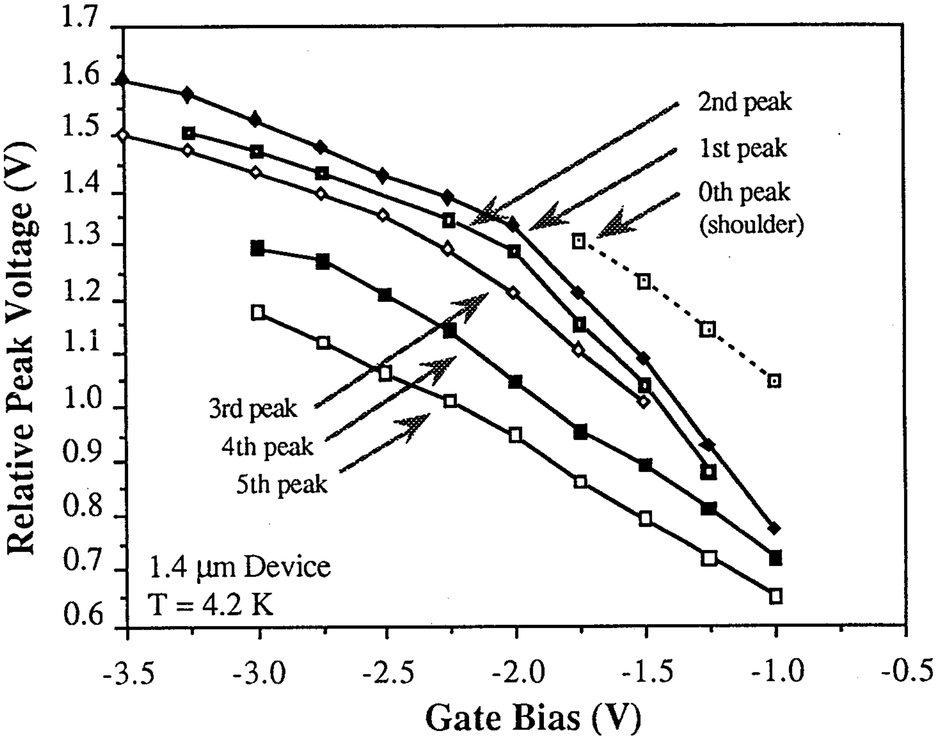

Figure 5.24 The voltage positions of fine structure relative to the PN junction turn-on threshold. The points connected by a dashed line correspond to a shoulder seen on the main resonance in Fig. 5.23.

The situation becomes much clearer by calibrating the observed fine structure relative to the turn-on voltages. Due to the unknown amount of depletion region on the collector side of the barriers, the absolute voltages of the observed peaks are not meaningful. However, the PN threshold relates the emitter voltage to the gate voltage so as to be used as a reference point.

Figure 5.24 shows the gate voltage dependence of all the six peak voltages. Except the first current shoulder indicated by a broken line the graph appears to show some sort of splitting of levels up to a gate voltage of about -2.0 V followed by a common shift in the relative peak positions. This shoulder is reminiscent of the characteristics produced by the 3D-emitter states discussed in Sec. 4.1. As mentioned there, the low-doped emitter region gives rise to a triangle potential well next to the emitter barrier and an electrostatic bump forms slightly further away. The main tunnelling occurs from the localised 2D states in the emitter well, but the small contribution from non-localised 3D-states results in broadening of the resonance and in even a separated resonance peak of it's own under the right conditions. If this is the case here, increasingly negative gate bias will act to raise the electrostatic bump still further, thereby reducing the contribution to the non-localised states and sharpening the resonance.

Lateral confinement potential profiles calculated for the 1.4 μm device by using the classical simulation HIHEART are shown in Fig. 5.25.

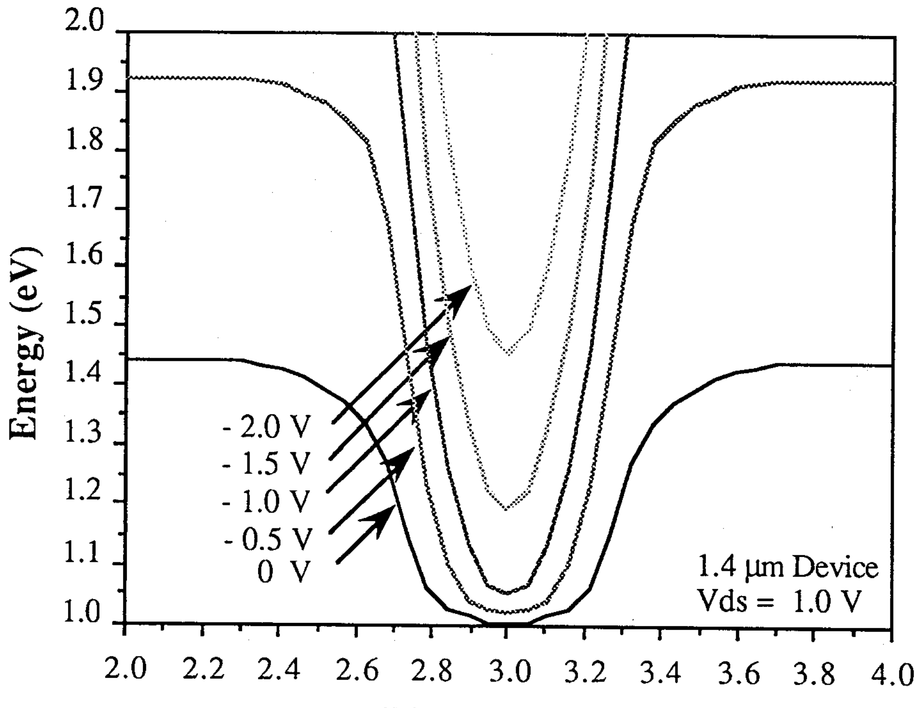

Figure 5.25 Lateral confinement potential profile calculated for the 1.4 μm device at various negative gate bias by using HIHEART (see Chap. 2).

As the gate bias is increased the lateral confinement well becomes progressively narrower until about -2.0V, where a minimum size is reached. Beyond this bias voltage the effect is simply to shift the whole well upwards in energy without altering its shape. Such a result appears consistent with the observations of a splitting of levels followed by a uniform shift. Therefore energy level splitting between quantized levels are no longer increased after this squeezing limit. The energy level splitting evaluated at Vg = -1.5 V is about 5.5 meV which is sufficiently large to be resolved at 4.2K. Using the energy level associated with the large-area RTD resonance to calibrate the measured voltages to the energies in the well, this predicts a measured splitting of about 150 mV, which is again consistent with Fig. 5.24.

Similar results have been observed for the 1.2 μm device which are shown in Figs. 5.26 (a) and (b). In Fig. 5.26, all the curves become flatter for higher gate voltages since the system exceeds the squeezing limit at a lower value than that for the 1.4 μm device. These results are consistent with the above discussion on the fine structure and may indicate that the fine structure obtained here is attributable to the three-dimensional quantization.

5.3.3 Tunnelling through a single impurity state

Fabricated VARTDs in general exhibit another interesting feature at their current threshold. Figure 5.27 shows the I-V characteristics of the 2 μm device around the threshold in forward bias (see the difference in the scale for the longitudinal axis from that in Fig. 5.21). This shows a series of plateau-like structures at threshold. Similar structures are seen for devices with different sizes: I-V curves of the 4 μm device are shown in Fig. 5.27 for both bias directions: (b) in forward and (c) reverse bias. It should be noted that the structure seen is different in forward and reverse bias directions. The gate bias dependences of these characteristics look different: for the 2 μm device the position of these is dependent on gate voltage, while for the larger devices this is not the case. This gate bias dependence seen for the 2 μm device, however, is supposed to be caused by the same mechanism of the peak voltage shift explained in the previous section. Thus the present fine structure is expected to have very small gate bias dependence in general.

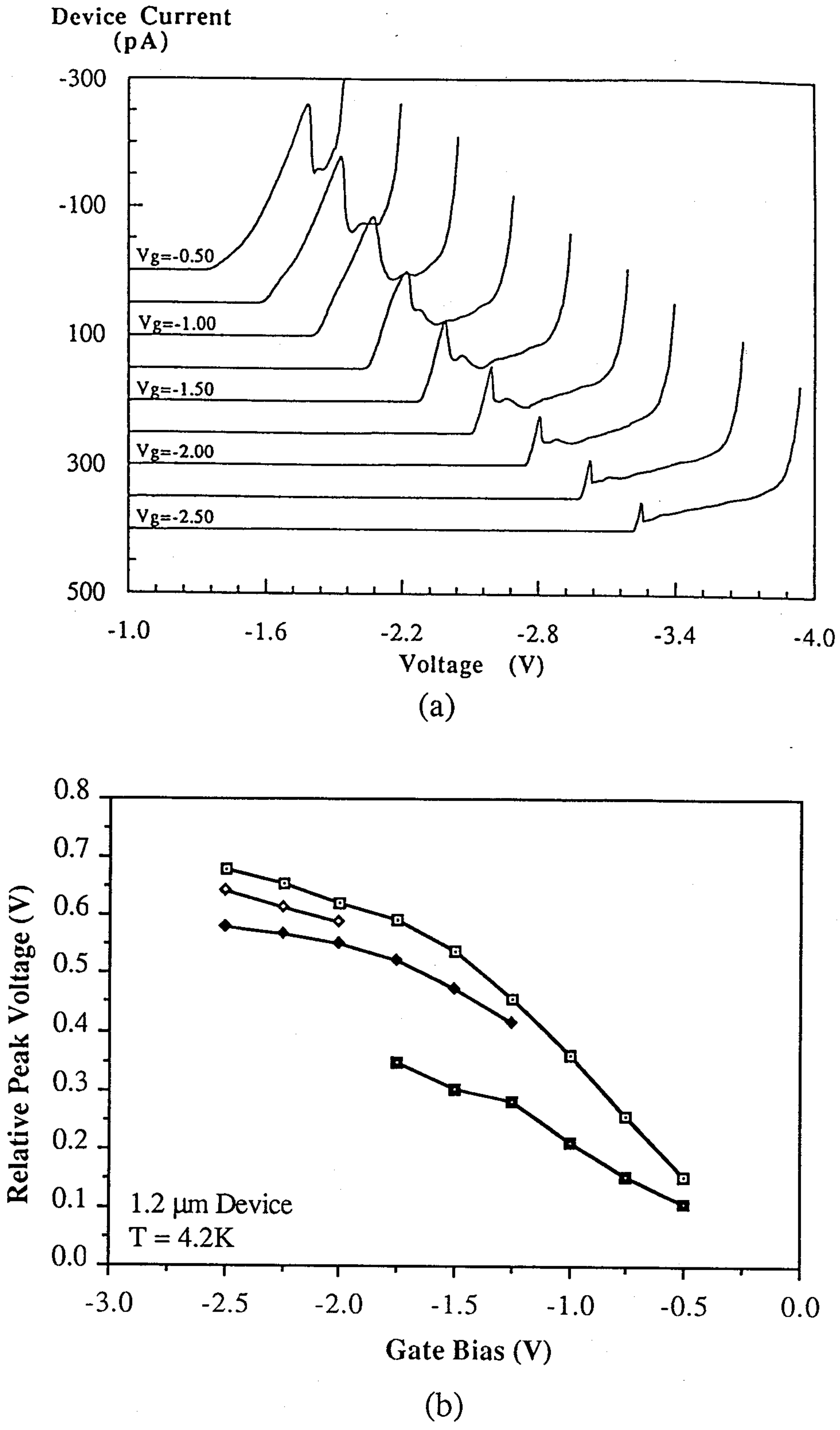

Figure 5.26 (a) Characteristics of a 1.2 μm diameter device at 4.2K in reverse bias. The main resonance peak seen sharpen and extra structure occurs in the valley current. (b) plots the voltage positions relative to the PN junction turn-on threshold. Data taken by C. Goodings, Microelectronics research centre, University of Cambridge, in collaboration with the author.

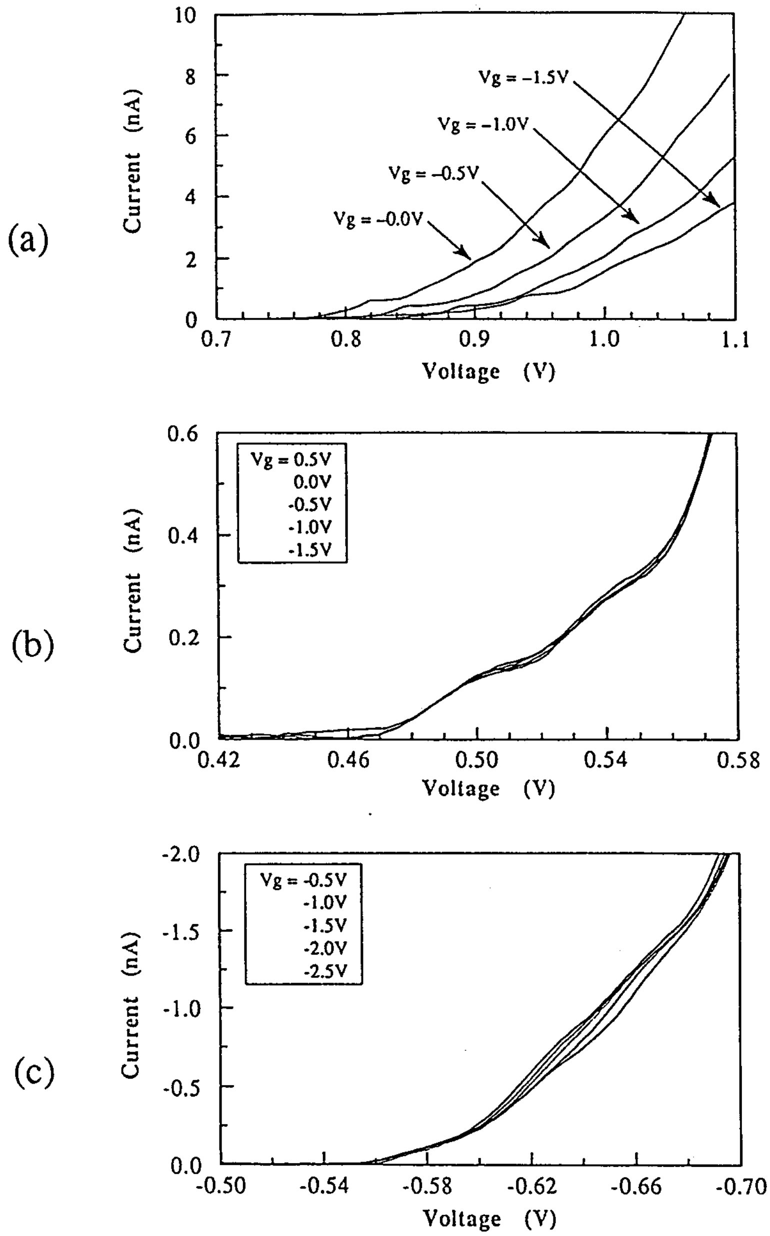

Figure 5.27 *Fine structure observed near threshold for VARTDs at 4.2K. (a) for a 2 μm diameter device in forward bias. (b) for 4 μm device in forward bias, and (c) for the same 4 μm diameter device in reverse bias. Data taken by C. Goodings, Microelectronics research centre, University of Cambridge, in collaboration with the author.*

Very similar results have been reported by Dellow et al. [33]-[35] for their surface-gated VARTDs. They pointed out that a possibility for the origin of the structure is tunnelling through impurity states in the active region of the device (see Fig. 5.28). An ionised donor in the quantum well will give a localised potential well and associated bound states through which electron tunnelling can occur for biases below the threshold voltage. The binding energy of such states depends on the position of the donors in the well with a maximum for donors in the centre of the well. Using modelled results by Greene and Bajaj [36],[37] we can estimate this maximum binding energy to be about 14 meV for the system, indicating that these effects are much greater than the thermal broadening at 4.2K. For relatively large-area devices such numerous donors randomly distributed in the well wash out any fine structure so that just a collisional broadening of the resonant state is remained as discussed in Sec. 3.4. However, for small devices with a single or few donors only, fine structure will be expected to appear around threshold as electrons tunnel through the local quasi-bound state associated with the ionised donors.

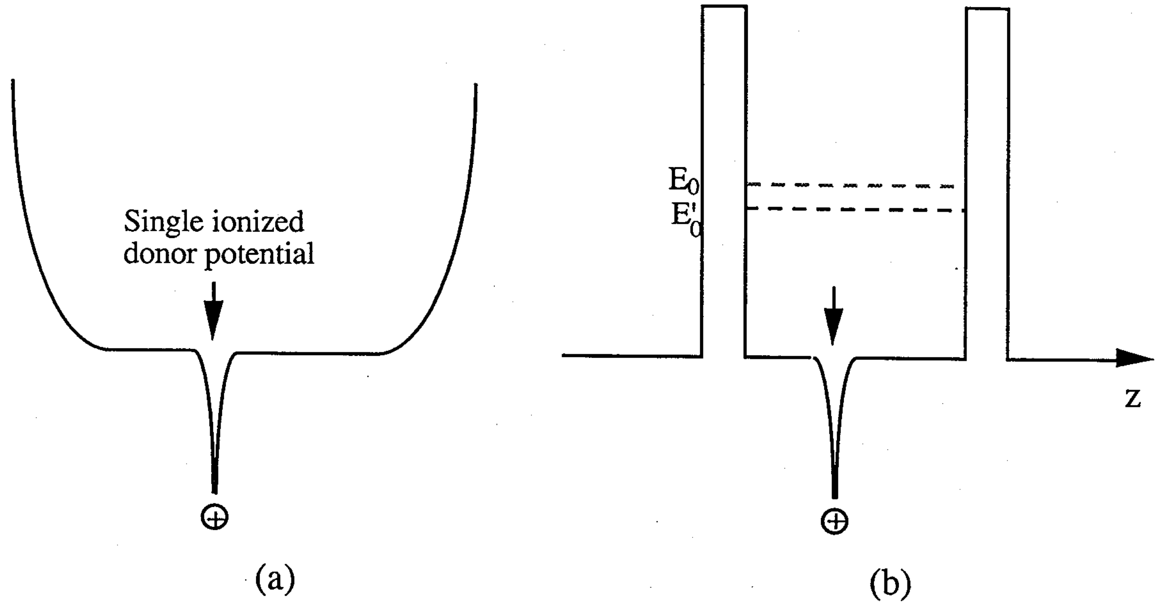

Figure 5.28 Schematic energy band-diagram of the device in which a single ionized donor is placed: (a) in lateral and (b) in vertical directions.

The total number of donor states expected in the quantum well can be estimated from the background doping density and the active device volume (Tab. 5.1). Taking a background doping of 10^{14} cm^{-3} this gives an estimate of 1 to 5 donor sites in the three device sizes considered here, which is consistent with the single- or few-electron tunnelling picture. The observed asymmetry of the forward and reverse characteristics is also consistent with this picture as a single impurity is placed in a completely random way in the well. Unless the impurity is located at the centre of the active area, some asymmetry is always expected for the characteristics.

Let's consider an extreme case in which only one electron can contribute at a time to the conduction. Tunnelling current associated with a single electron tunnelling through a single ionised donor state is roughly estimated by the following expression:

$$I = e/\tau_{esc} \tag{5.35}$$

which corresponds to Eq. (4.18) for large-area devices. By assuming this model and using the observed current of the first plateau the values of τ_{esc} are obtained for three VARTDs which are listed in Table 5.1.

Device diameter	First plateau current (pA)	Tunnelling excape time (ps)
2.0	500	320
3.0	250	640
4.0	150	1500

Table 5.1 *A list of the first plateau currents and associated lifetimes derived by using Eq. (5.35) assuming that only single electron tunnelling is involved.*

The value of τ_{esc} obtained for large-area devices by using Eq. (4.18) and σ_w estimated from the magnetotransport measurement (see Sec. 4.3.2) is about 500 psec. The above calculated values of τ_{esc} by assuming the single electron tunnelling model (Eq. (5.35)) are fairly close to this value derived for the large-area devices. This fact may indicate that the observed plateaus are attributable to single electron tunnelling through few ionised donor states. The tunnelling escape time varies with device size as seen in Tab. 5.1, but this could be accounted for the difference in the effective electric field across the double barrier structure.

Detailed analysis of the single impurity related tunnelling requires the three-dimensional S-matrix simulation introduced in Sec. 5.2. Attractive potential due to an ionized single donor, $V_{IM}(x,y,z)$, is simply modelled by using three-dimensional delta function:

$$V_{IM}(\vec{r}) = -V_0\,\delta(\vec{r} - \vec{r}_0) \tag{5.36}$$

which is introduced into Eq. (5.2). Scattering matrix elements (Eq. (5.15)) are calculated by using the lateral wavefunctions which are obtained from two-dimensional Schrödinger equation (Eq. (5.4)). Uniform lateral confinement has been adopted for the present analysis taking into account that the virtually flat confinement is achieved in the developed gated RTD. Present analysis has been performed for the $Al_{0.3}Ga_{0.7}As$(4 nm)/GaAs(5 nm)/$Al_{0.3}Ga_{0.7}As$(4 nm) double barrier RTDs with a relatively large area (150 nm * 150 nm) in which contributions from different lateral modes are hardly separable, and so the I-V characteristics show only a single current peak even at zero temperature if no ionized impurity is introduced.

Current-voltage characteristics for the RTD in which a single ionized donor is located at centre of the structure is shown in Fig. 5.29. Beside a main current peak seen at about 120 V, an additional small peak is found near current threshold.

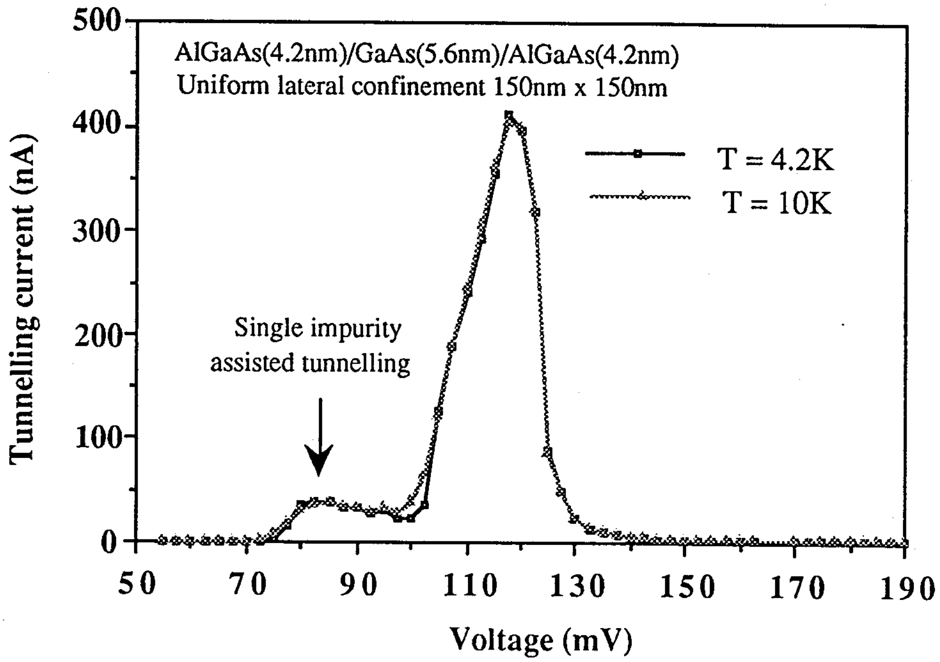

Figure 5.29 Current-voltage characteristics of a large area RTD with an single ionized donor placed at centre of the resonant tunnelling structure calculated at 4.2K (solid line) and 10K (dotted line).

Multi-mode transmission probability through the RTD in which a single ionized donor is located at the centre of the structure is shown in Figs. 5.30(a) - (c). Figure 5.30(a) shows characteristics calculated at threshold (V = 55 mV). A single transmission peak is found at lower energy isolated from a series of other peaks which are well overlapped leading to a broad transmission band. This transmission peak is found to give rise to a small current peak as shown in Fig. 5.30(b). Three-dimensional existence probability calculated for the 1st mode incident wave at an energy of 80.5 meV under an applied bias of 55 mV is shown in Fig. 5.31: It can be clearly seen that the electron wave is now localized around the single ionized donor despite a widely spread nature of the incident wave at the emitter edge. After this single peak goes down below the conduction band edge in the emitter, a group of other transmission peaks falls down to the Fermi sea leading to a main current peak (Fig. 5.30(c)). These preliminary results demonstrate that a single ionized donor placed in a quantum well indeed gives rise to a small but observable current peak near the threshold of the main current peak.

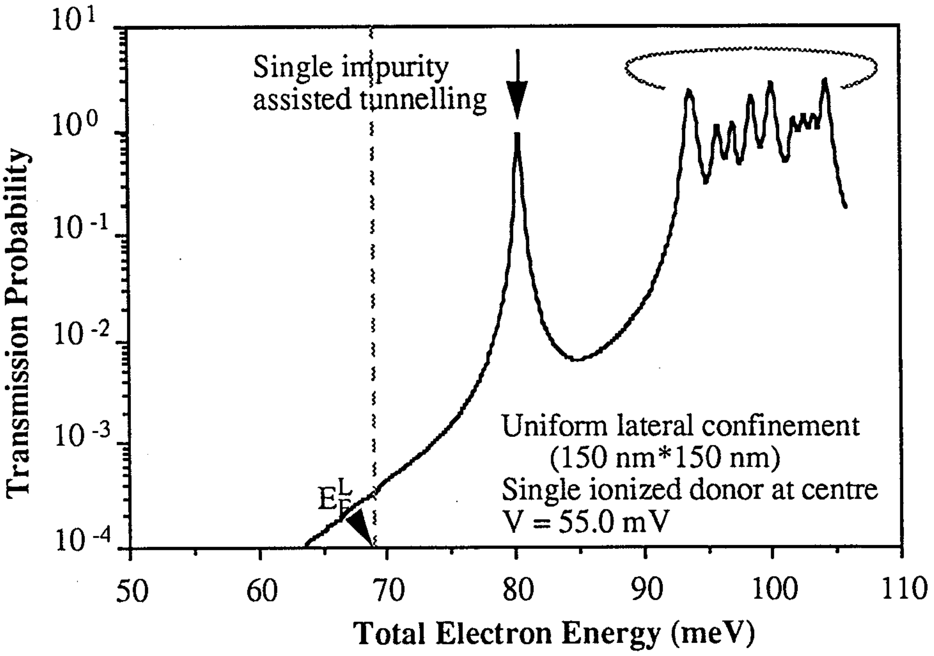

(a)

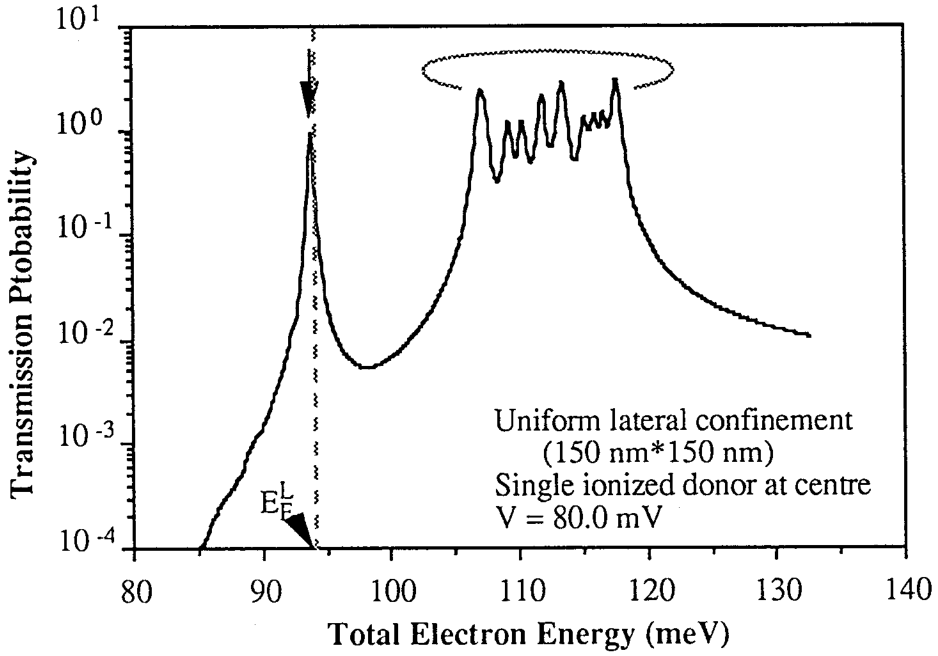

(b)

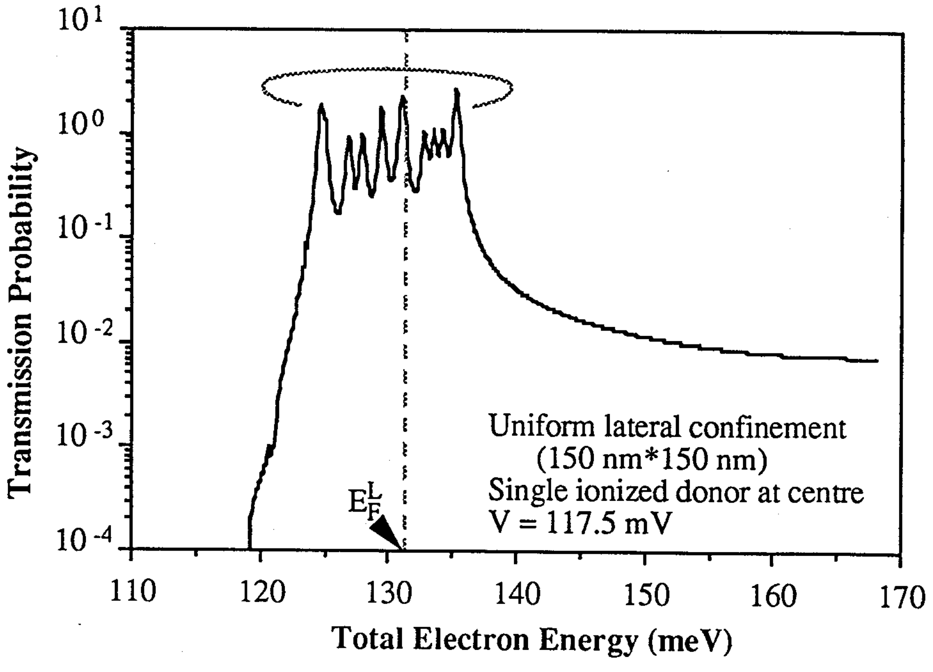

(c)

Figure 5.30 Transmission probability through a large area RTD with an single ionized donor placed at centre of the resonant tunnelling structure calculated at three different bias: (a) at current threshold, (b) at subcurrent peak, and (c) at main current peak. An arrow indicates that transmission peak caused single ionized donor potential.

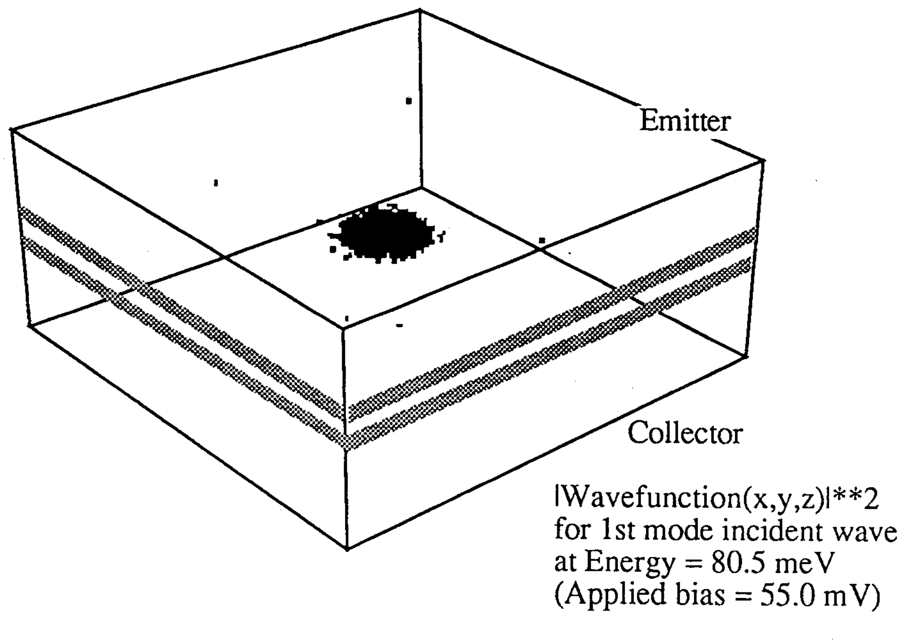

Figure 5.31 Visualized existent probability of electrons calculated for the 1st mode incident wave with an energy of 80.5 meV (at a single impurity related resonance). An ionized donor places at centre of the structure

In summary of this chapter multi-mode resonant tunnelling through a laterally-confined double barrier nanostructure has been investigated. A three-dimensional S-matrix theory has been introduced to analyze the effect of lateral mode mixing, caused by elastic scattering due to an hour-glass shaped confinement potential, on the transmission properties. The calculated S-matrix shows new transmission peaks in the off-diagonal components which measure the lateral mode non-conserving process as well as the related Fano-resonance type structures in the diagonal components. This transmission properties lead to a fine structure in the I-V characteristics in which satellite peaks in the high voltage regime result from the lateral mode non-conserving tunnelling.

To achieve uniform and controllable confinement a gated resonant tunnelling device has been fabricated by adopting graded doping profile and beryllium ion implantation. A large area device with a 3 mm top contact shows single peak NDR and, by applying negative gate bias, the peak current is altered by a factor of 2. The characteristics for a smaller 1.4 mm device show five small peaks in a pinch-off regime. Voltage intervals between these peaks first increase with increasing gate bias and then remain almost constant. This result indicates that the fine structure may attributable to three-dimensional quantization. Also different fine structure near the current threshold seen in relatively larger devices has been investigated and found likely to result from a few ionized donor impurities unintentionally located in a quantum well.

5.4 References V

[1] M. A. Reed, J. N. Randall, R. J. Aggarwal, R. J. Matyi, T. M. Moore, and A. E. Westel, "Observation of discrete electronic states in a zero-dimensional semiconductor nanostructure", Phys. Rev. Lett. **60**, 535, 1988.

[2] M. A. Reed, J. N. Randall, and J. H. Luscombe, "Non-equilibrium quantum dots: transport", Nanotechnology **1**, 63, 1990.

[3] S. Tarucha, Y. Hirayama, T. Saku, and T. Kimura, "Resonant tunneling through one- and zero-dimensional states constricted by $Al_xGa_{1-x}As/GaAs/Al_xGa_{1-x}As$ heterojunctions and high-resistance regions induced by focused Ga ion-beam implantation", Phys. Rev. **B41**, 5459, 1990.

[4] Bo Su, V. J. Goldman, M. Santos, and Shayegan, "Resonant tunneling in submicron double-barrier heterostructures", Appl. Phys. Lett. **58**, 747, 1991.

[5] S. Tarucha and Y. Hirayama, "Magnetotunneling in a coupled two-dimensional-one-dimensional electron system", Phys. Rev. **B43**, 9373, 1991.

[6] M. W. Dellow, P. H. Benton, M. Henini, P. C. Main, L. Eaves, S. P. Beaumont, and C. D. W. Wilkinson, "Gated resonant tunnelling devices", Electronics Lett. **27**, 134, 1991.

[7] P. Gueret, N. Blanc, R. German, and H. Rothuizen, "Confinement and single-electron tunneling in Schottky-gated, laterally squeezed double-barrier quantum-well heterostructure", Phys. Rev. Lett. **68**, 1896, 1992.

[8] S. Tarucha, Y Tokura, and Y. Hirayama, "Resonant tunneling of three-dimensional electrons into degenerate zero-dimensional levels", Phys. Rev. **B44**, 13815, 1991.

[9] A. Groshev, "Single electron trapping in ultrasmall double barrier semiconductor structures", 20th international conference on the physics of semiconductors, Thessaloniki, World Scientific, 1238, 1990.

[10] A Groshev, T. Ivanov, and V. Valtchinov, "Charging effects of a single quantum level in a box", Phys. Rev. Lett. **66**, 1082, 1991.

[11] M. P. Stopa, "Charging energy and collective response of a quantum dot resonant tunneling device", Surface Science **263**, 433, 1991.

[12] S. Y. Chou, E. Wolak, and J. S. Harris, Jr., "Resonant tunneling of electrons of one or two degrees of freedom", Appl. Phys. Lett. **52**, 657, 1988.

[13] G. W. Bryant, "Resonant tunneling in zero-dimensional nanostructures", Phys. Rev. **B39**, 3145, 1989.

[14] G. W. Bryant, "Understanding quantum-box resonant-tunneling spectroscopy: Fine structure at Fermi-level crossings", Phys. Rev. **B44**, 3782, 1991.

[15] G. W. Bryant, "Nonadiabatic transport through quantum dots", Phys. Rev. **B44**, 12837, 1991.

[16] M. Luban, J. H. Luscombe, M. A. Reed, and D. L. Pursey, "Anharmonic oscillator model of a quantum dot nanostructure", Appl. Phys. Lett. **54**, 1997, 1989.

[17] J R Barker, 'Theory of quantum transport in lateral nanostructures', Nanostructure physics and fabrication, Proceedings of the International Symposium, Texas, Academic Press, 253, 1989.

[18] F. Sols, M. Macucci, U. Ravaioli, and K. Hess, "Theory of a quantum modulated transistor", J. Appl. Phys. **66**, 3892, 1989

[19] J. A. Brum, "Superlattice effects in quantum dots", 20th international conference on the physics of semiconductors - volume 3, Thessaloniki, World Scientific, 511, 1990.

[20] S. E. Ulloa, E. Castano, and G. Kirczenow, "Ballistic transport in a novel one-dimensional superlattice", Phys. Rev. **B41**, 12350, 1990.

[21] Z. L. Ji and K. F. Berggren, "Numerical study of ballistic conductance in parallel configuration", Semicond. Sci. Technol. **6**, 63, 1991.

[22] A. Weisshaar, J. Lary, S. M. Goodnick, and V. K. Tripathi, "Negative differential resistance in a resonant quantum wire structure", IEEE Electron Device Lett. **EDL-12**, 2, 1991.

[23] A. Kumar and P. H. Bagwell, "Resonant tunneling in a quasi-one-dimensional wire: Influence of evanescent modes", Phys. Rev. **B43**, 9012, 1991.

[24] F. M. de Aguiar and D. A. Wharam, "Transport through one-dimensional channels", Phys. Rev. **B43**, 9984, 1991.

[25] A. Kumar, S. E. Laux, and F. Stern, "Electron states in a GaAs quantum dot in a magnetic field", Phys. Rev. **B42**, 5166, 1990.

[26] A. Kumar, "Self-Consistent Calculations on Confined Electrons in Three-Dimensional Geometries", Surface Science **263**, 335, 1992.

[27] K Nakasoto and R. J. Blaikie, "The effect of mode coupling on ballistic electron transport in quantum wires", J. Phys: Condens. Matter **3**, 5729, 1991.

[28] H. Mizuta, K. Yamaguchi, M. Yamane, T. Tanoue, and S. Takahashi, "Two-dimensional numerical simulation of Fermi-level pinning phenomena due to DX centers in AlGaAs/GaAs HEMTs", IEEE Trans. Electron. Device **ED-36**, 2307, 1989.

[29] W. E. Spicer, P. W. Chye, P. R. Skeath, C. Y. Su, and I. Lindau, "New and unified model for Schottky barrier and III-V insulator interface states formation", J. Vac. Sci. Technol., **16**, 1422, 1979.

[30] U. Fano, "Effects of configuration interaction on intensities and phase shifts", Phys. Rev. **124**, 1866, 1961.

[31] C. J. Goodings, J. R. A. Cleaver, and H. Ahmed, "Variable-area resonant tunnelling diode using implanted gates", Electron. Lett. **28**, 1535, 1992.

[32] H. Mizuta, C. J. Goodings, M. Wagner, and S. Ho, "Three-dimensional numerical analysis of multi-mode quantum transport in zero-dimensional resonant tunnelling diodes", J. Phys.: Condens. Matter **4**, 8783, 1992.

[33] M. W. Dellow, C. J. G. M. Langerak, P. H. Beton, T. J. Foster, P. C. Main, L. Eaves, M. Henini, S. P. Beaumont and C. D. W. Wilkinson, "Zero dimensional resonant tunneling through single donor states", Superlattices and Microstructures **11**, 149, 1992.

[34] M. W. Dellow, C. J. G. M. Langerak, P. H. Beton, T. J. Foster, P. C. Main, L. Eaves, M. Henini, S. P. Beaumont and C. D. W. Wilkinson, "Single electron tunnelling through a donor state in a gated resonant tunnelling device", Surface Science **263**, 438, 1992.

[35] M. W. Dellow, P. H. Beton, C. J. G. M. Langerak, T. J. Foster, P. C. Main, L. Eaves, M. Henini, S. P. Beaumont and C. D. W. Wilkinson, "Resonant tunneling through the bound states of a single donor atom in a quantum well", Phys. Rev. Lett. **68**, 1754, 1992.

[36] R. L. Greene and K. K. Bajaj, "Effect of magnetic field on the energy levels of a hydrogenic impurity center in GaAs/$Ga_{1-x}Al_xAs$ quantum-well structures", Phys. Rev. **B31**, 913, 1985.

[37] R. L. Greene and K. K. Bajaj, "Far-infrared absorption profiles for shallow donors in GaAs-$Al_xGa_{1-x}As$ quantum-well structures", Phys. Rev. **B34**, 951, 1986.

[38] P. H. Beton et al., "Edge effects in a gated submicron resonant tunneling diode", Appl. Phys. Lett. **60**, 2508, 1992.

CHAPTER 6

SUMMARY

Electron transport in nanometer-scale compound semiconductor devices has been theoretically studied. Four different transport regimes have been described and investigated in detail: classical drift-diffusion transport, coherent quantum transport, dissipative quantum transport, and zero-dimensional quantum transport. These transport phenomena may be classified based on a typical dimension of structures under consideration. Heterojunction devices with sizes of deep submicrometers which are currently under development have been first dealt with in Chapter 2 by using the classical drift-diffusion modelling. The SRH modelling of carrier emission-absorption processes via deep trap states which are inevitable in compound semiconductor devices has been successfully incorporated into DD-trasnport modelling of heterojunction devices. Two major deep-level-related phenomena which are dominant in heterojunction devices with sizes of deep submicrons have been analyzed by using the present modelling: The Fermi-level pinning effects of DX centres in AlGaAs/GaAs HEMTs and the surface-state-induced Fermi-level pinning and carrier recombination effects on the characteristics of AlGaAs/GaAs HEMTs and HBTs. It has been revealed that the Fermi-level pinning in general degrades transconductance of the HEMTs as has been seen for DX centres in the N-AlGaAs supply layer and the surface states. Also the deep level induced carrier recombination processes have been found to influence current gain of HBTs greatly.

Chapter 3 has described a coherent quantum transport of electrons in resonant tunnelling heterojunction devices. The global coherent tunnelling model has been adopted which is based on Tsu-Esaki formula with the transfer matrix calculations and takes account of Hartree's self-consistent field. By using this modelling multiple-well resonant tunnelling diodes have been numerically studied, and possibility of their applications to multiple-valued logic has been discussed: The new AlGaAs/GaAs triple well structure and the InGaAs/InAlAs double well structures are found suitable for triple value logic applications. Finally the effects of collisional broadening on the coherent tunnelling calculations has been discussed by using a phenomelogical Breit-Wigner modelling. Fairly good agreements have been found for the current peak widths and P/V current ratios within reasonable values of phase-coherence breaking time estimated for LO-phonon scattering.

Chapter 4 has been dedicated to analysis of dissipative resonant tunnelling and resultant non-equilibrium distribution in RTDs which are theoretically studied by using the statistical density matrix and the Wigner distribution function. Time-dependent one-dimensional Liouville-von Neumann transport equation for statistical density matrix has been introduced to investigate femtosecond electron dynamics and quantum correlations in the device and to discuss the P/V ratio degradation due to dissipation process. Dynamical space-charge build-up has been demonstrated in the quantum well resulting in the intrinsic current bistability in the negative differential conductance regime of RTDs. Further investigations of the space-charge build up has been studied by using magneto-transport measurement. Reasonable values of the concentration of electrons accumulated in the pseudo-triangle well and quantum well have been obtained. It has become evident that electrons tunnelling into the quantum well are partly thermalized by phase-breaking scattering processes leading to the P/V current ratios of RTDs.

Finally Chapter 5 has been intended to study the zero-dimensional quantum transport through three-dimensionally confined nanostructures which is topical and controversial at present. A three-dimensional S-matrix theory has been introduced to analyze the effect of lateral mode mixing, caused by elastic scattering due to an hour-glass shaped confinement potential, on the transmission properties. The calculated S-matrix shows new transmission peaks in the off-diagonal components which measure the lateral mode non-conserving process as well as the related Fano-resonance type structures in the diagonal components. This transmission properties lead to a fine structure in the I-V characteristics in which satellite peaks in the high voltage regime result from the lateral mode non-conserving tunnelling. Based on these results a new gated resonant tunnelling device has been proposed and fabricated by adopting graded doping profile and beryllium ion implantation to achieve uniform and controllable confinement. Fine current peaks have been successfully observed in a pinch-off regime of relatively small devices. Voltage intervals between these peaks were found to increase with increasing gate bias and then remain almost constant. These results are supposed to indicate that the fine structure is attributable to three-dimensional quantization. Another different fine structure seen near the current threshold has been investigated by using the S-matrix simulation in which a single impurity scattering is included and found to result from a few ionized donor impurities unintentionally located in a quantum well.

Acknowledgements

First of all the author would like to express a great debt of gratitude to Prof. C. Hamaguchi, Prof. K. Yoshino, Prof. K. Oura, Prof. H. Nishihara, and Prof. S. Kodama for their intensive thesis examination and their great deal of valuable advice and discussion on the whole contents of the present thesis.

The author would like to thank his collaborators, Dr K. Yamaguchi, Mr K. Ka and Dr M. Wagner of Central Research Laboratory, Hitachi, Ltd. for their valuable discussions on transport theory and numerical simulations throughout the present work. Also the author would like to gratefully acknowledge the substantial contribution of his collaborators in the experimental part: Dr C. Goodings of Microelectronics Research Centre, University of Cambridge for his collaboration on the work in Chapters 4 & 5, and Dr T. Tanoue, Mr C. Kusano, Mr T. Tanimoto and Dr M. Yamane* of Central Research Laboratory (* Present address: Semiconductor Design & Development Centre), Hitachi Ltd for their collaborations on the works in Chapters 2 and 3. The author is indebted to Dr D. Williams, Dr. J. Allam, Dr. J. White, Dr. R. Blaikie and Dr. T. Thornton of Hitachi Cambridge Laboratory, Hitachi Europe Ltd., and Dr J. R. A. Cleaver of Microelectronics Research Centre, University of Cambridge for their helpful discussions. Finally the author would like to express his special acknowledgements to Dr K. Yamaguchi and Dr S. Takahashi* of Central Research Laboratory, Hitachi, Ltd. (*present address: Hitachi Cable Ltd.), Dr M. Nakamura*[1], Dr H. Matsumura*[2], Dr T. Masuhara*[3] and Dr K. Miyauchi, successive managers of Advanced Devices Research Department (formerly, 1st Dept.), Central Research Laboratory, Hitachi, Ltd. (*[1]: present manager of Central Research Laboratory, Hitachi, Ltd., *[2] present address: Production Engineering Research Laboratory, Hitachi, Ltd., *[3] present address: Semiconductor & Integrated Circuits Division, Hitachi, Ltd.), as well as to Dr K. Nakazato, manager of Hitachi Cambridge Laboratory, Hitachi Europe Ltd., Dr Y. Murayama of Advanced

Research Laboratory, Hitachi, Ltd., and Prof. H. Ahmed of Microelectronics Research Centre, University of Cambridge for their continuous support and encouragement during this work.

Publications

1. H. Mizuta, K. Yamaguchi, and S. Takahashi, "Surface Potential Effect on Gate-Drain Avalanche Breakdown in GaAs MESFET's", IEEE Trans. on Electron Devices, **ED-34**, 2027, 1987.
2. T. Tanoue, H. Mizuta, and S. Takahashi, "A Triple-well resonant tunneling diode for multiple-valued logic application", IEEE Electon Device Lett., **EDL-9**, 365, 1988.
3. H. Mizuta, T. Tanoue, and S. Takahashi, "A new triple-well resonant tunneling diode with controllable double-negative resistance", IEEE Trans. on Electron Devices, **ED-35**, 1951, 1988.
4. K. Hiruma, M. Mori, E. Yanakura, H. Mizuta, and S. Takahashi, "Improved performance of submicrometer-gate GaAs MESFET's with an $Al_{0.3}Ga_{0.7}As$ buffer layer grown by metal organic vapor phase epitaxy", IEEE Trans. on Electron Devices, **ED-36**, 314, 1989.
5. H. Mizuta, T. Tanoue, and S. Takahashi, "Theoretical analysis of peak-to-valley ratio degradation caused by scattering processes in multi-barrier resonant tunneling diodes", Proceedings of IEEE/Cornell Conf. on Advanced Concepts in High Speed Semiconductor Devices and Circuits, Ithaca, NY, 274, 1989.
6. H. Mizuta, K. Yamaguchi, M. Yamane, T. Tanoue, and S. Takahashi, "Two-dimensional numerical simulation of Fermi-level pinning phenomena due to DX centers in AlGaAs/GaAs HEMT's", IEEE Trans. on Electron Devices, **ED-36**, 2307, 1989.
7. P. D. Rabinzohn, T. Usagawa, H. Mizuta, and K. Yamaguchi, "The new two-dimensional electron gas base HBT (2DEG-HBT): Two-dimensional numerical simulation", IEEE Trans. on Electron Devices, **ED-38**, 222, 1991.
8. H. Mizuta and C J. Goodings, "Transient quantum transport simulation based on the statistical density matrix", J. Phys.: Condens. Matter **3**, 3739, 1991.
9. H. Mizuta, C. J. Goodings, M. Wagner, and S. Ho, "Three-dimensional numerical simulation of multi-mode quantum transport in zero-dimensional resonant tunneling diodes", J. Phys.: Condens. Matter **4**, 8783, 1992.
10. C. Kusano, H. Mizuta, K. Mochizuki, H. Mizuta and K. Yamaguchi, "Simulation of the effect of emitter doping on the delay time in AlGaAs/GaAs heterojunction bipolar transistors", Jpn. J. Appl. Phys. **31**, L1651, 1992.
11. M. Wagner and H. Mizuta, "Multistable charge build-up and a new switching principle in coherent-electron tunneling devices", Jpn. J Appl. Phys, **32**, **L520**, 1993.
12. I. Ohbu, M. Takahama and H. Mizuta, "Time dependence of the surface Fermi level of GaAs in atomosphere", submitted to Appl. Phys. Lett.
13. M. Wagner and H. Mizuta, "Coherent-electron intrinxic multistability in a double-barrier tunnelling diode", submitted to Appl. Phys. Lett.

Presentations (International)

1. E. Yanokura, H. Mizuta, M. Mori, and S. Takahashi, "GaAs MESFET's fabricated by new self-alignment technology", 19th Conference on Solid State Devices and Materials, Tokyo, 1987.

2. C. Kusano, T. Tanoue, H. Mizuta, and S. Takahashi, "Multiple-valued logic applications of a triple-well resonant tunneling diode", Device Research Conference, 1988.

3. T. Tanoue, H. Mizuta, and S. Takahashi, "Double negative resistance properties of a triple-well resonant tunneling diode", Advanced Heterostructure Device, Hawaii, 1988.

4. C. Kusano, H. Mizuta, and K. Yamaguchi, "The influence of DX centers in heavily doped emitter of AlGaAs/GaAs heterojunction bipolar transistors", APS Meeting, 1989.

5. H. Mizuta, T. Tanoue, and S. Takahashi, "Theoretical analysis of peak-to-valley ratio degradation caused by scattering processes in multi-barrier resonant tunneling diodes", IEEE/Cornell Conf. on Advanced Concepts in High Speed Semiconductor Devices and Circuits, Ithaca, NY, 274, 1989.

6. T. Usagawa, P. D. Rabinzohn, H. Mizuta, K. Hiruma, M. Kawata, and K. Yamaguchi, "Comprehensive analysis of bifunctional 2DEG-HBTs", 22nd Conference on Solid State Devices and Materials, Sendai, 1990.

7. T. Tanoue, H, Mizuta, and T. Tanoue, "Multiple-well RTD with InGaAs strained quantum wells", Advanced Heterostructure Device, Hawaii, 1990.

8. C. J. Goodings, H. Mizuta, Y. Ochiai, J. R. A. Cleaver, and H. Ahmed, "Fabrication of lateral superlattices on GaAs/AlGaAs heterostructures by gas-assisted focused ion beam etching", Symbosium on Nanostructures: Fabrication and physics, 1990 Fall Meeting of MRS, Boston, 1990.

9. H. Mizuta and C. J. Goodings, "Density matrix calculations of femtosecond electron dynamics in resonant tunnelling diodes", 11th general conference of the condensed matter division of EPS, Exeter, 1991.

10. H. Mizuta and C. J. Goodings, "Transient quantum transport simuation based on the statistical dinsity matrix", IOP semiconductor group meeting, Sheffield, 1991.

11. S. Ho, H. Mizuta, and K. Yamaguchi, "Effects of reservoirs on tunneling and interference in mesoscopic systems", Condensed Matter and Material Physics Conference 1991 (CMMP'91), Birmingham, 1991.

12. S. Ho, H. Mizuta, and K. Yamaguchi, "Degradation in transconductance of GaAs MESFETs in high frequency domain", Condensed Matter and Material Physics Conference 1991 (CMMP'91), Birmingham, 1991.

13. H. Mizuta, M. Wagner, S. Ho, and K. Yamaguchi, "Three-dimensioal numerical simulation of multi-mode quantum transport in zero-dimensioanl resonant tunnelling diodes", 1st International Workshop on Quantum Functional Devices, Nasu Heights, 1992.

14. M. Wagner and H. Mizuta, "Effect of LO-phonon scattering on electrical bistability in resonant tunneling diodes", 1st International Workshop on Quantum Functional Devices, Nasu Heights, 1992.

15. Y. Yazawa, H. Mizuta, S. Fukatsu, A. C. Gossard and Y. Shiraki, "Optical properties of electric field controlled lateral superlattices", 2nd International Symposium on "New Phenomena in Mesoscopic Structures, Kauai, Hawaii, 1992.

16. H. Mizuta, C Goodings, M Wagner and S. Ho, "Quantum transport in laterally confined resonant tunnelling structures", Condensed Matter and Material Physics Conference 1992 (CMMP'92), Sheffield, 1992.

17. S. Ho, M. Oohira, O. Kagaya, A. Moriyoshi, H. Mizuta, and K. Yamaguchi, "Dynamic simulation of multiple trapping processes and anomalous frequency dependence in GaAs MESFETs", Int. Workshop on VLSI Process and Device Modeling (1993 VPAD), Nara, 1993.

18. S. Ho, A. Moriyoshi, I. Ohbu, O. Kagaya, H. Mizuta, and K. Yamaguchi, "Theoretical analysis of transconductance enhancement due to electron concentration dependent screening in heavily doped systems", Int. Workshop on VLSI Process and Device Modeling (1993 VPAD), Nara, 1993.

19. C Goodings, H. Mizuta, J. R. A. Cleaver and H. Ahmed, "Electron confinement in variable-area resonant tunnelling diodes using in-plane implanted gates", to be presented at EP2DS-10, Newport, Rhode Island, Jun 1993.

Presentations (Domestic)

1. 水田、山口、高橋、"GaAs MESFETゲート／ドレイン間なだれ降伏の理論解析",
電子通信学会電子デバイス研究会 86年4月

2. 水田、山口、矢ノ倉、森、高橋、"GaAs MESFETの表面電位効果",
第47回応用物理学会学術講演会 86年9月

3. 矢ノ倉、森、水田、高橋、"ナノメータオフセットゲート構造GaAs MESFET",
電子通信学会 87年3月

4. 水田、山口、高橋、"Analysis of surface potential effect in GaAsMESFETs", '87
VLSI Process/Device Modeling Workshop 87年7月

5. 森、矢ノ倉、水田、高橋、"Ka帯オフセットゲート高出力GaAs MESFET",
電子情報通信学会 87年11月

6. 水田、田上、高橋、"GaAs/AlGaAs共鳴トンネリング三値論理素子",
第35回応用物理学会関係連合講演会 88年3月

7. 矢ノ倉、森、水田、高橋、"0.1μm GaAs MESFET",
第35回応用物理学会関係連合講演会 88年3月

8. 森、矢ノ倉、水田、高橋、"30GHz帯高出力GaAs MESFET",
電子情報通信学会 88年3月

9. 水田、田上、草野、高橋、"3重量子井戸構造を有する共鳴トンネルダイオード
の理論解析", 電子情報通信学会電子デバイス研究会 88年3月

10. 山口、水田、高橋、"化合物半導体汎用デバイスシミュレータ",
電子情報通信学会 88年9月

11. 水田、田上、高橋、"3重量子井戸構造RTDのセルフコンシステント解析",
第49回応用物理学会学術講演会 88年9月

12. 田上、水田、高橋、"InGaAs/InAlAs三重障壁RTDの試作と解析",
第49回応用物理学会学術講演会 88年9月

13. 宇佐川、P. Rabinzohn、水田、山口、"2DEG-HBTの二次元数値シミュレーション
-バイポーラ特性-", 電子情報通信学会電子デバイス研究会 89年2月

14. 水田、山口、山根、田上、高橋、"AlGaAs/GaAs HEMTにおけるDXセンターのフ
ェルミレベルピンニング効果", 第36回応用物理学会関係連合講演会 89年4月

15. 宇佐川、P. Rabinzohn、水田、山口、"2DEG-HBTの二次元数値シミュレーション", 第36回応用物理学会関係連合講演会 89年4月

16. 草野、水田、山口、"AlGaAs/GaAs HBTにおける高濃度エミッタ効果", 第36回応用物理学会関係連合講演会 89年4月

17. 田上、水田、高橋、"InGaAs/InAlAs三重障壁RTDのセルフコンシステント解析", 第50回応用物理学会学術講演会 89年9月

18. 宇佐川、水田、山口、"2DEG-HBTのBi-Function特性", 第50回応用物理学会学術講演会 89年9月

19. 何、水田、田上、山口、"Wigner形式による共鳴トンネリングダイオードの解析(I)", 第50回応用物理学会学術講演会 89年9月

20. 谷本、田上、水田、高橋、"第一井戸にInGaAsを用いた三重障壁RTDの試作と解析", 第37回応用物理学会関係連合講演会 90年3月

21. 何、水田、田上、山口、"Wigner形式による共鳴トンネリングダイオードの解析(II)", 第37回応用物理学会関係連合講演会 90年3月

22. 谷本、田上、水田、高橋、"InGaAsひずみ量子井戸を用いた3重障壁RTD", 電子情報通信学会電子デバイス研究会 90年4月

23. 山口、何、水田、"微細構造化合物半導体デバイスシミュレーション", 電子情報通信学会 91年9月

24. 何、水田、大平、森吉、山口、"GaAs MESFETの電気特性における周波数依存性(1): 電流増幅率の低減機構", 第39回応用物理学会関係連合講演会 92年3月

25. 大平、何、森吉、水田、山口、"GaAs MESFETの電気特性における周波数依存性(2): 出力抵抗の低減機構", 第39回応用物理学会関係連合講演会 92年3月

26. 森吉、何、水田、山口、"二次元数値シミュレーションによるDoped-channel FETの容量解析", 電子情報通信学会秋季大会 92年9月

27. 何、加賀谷、大平、森吉、水田、山口、"マルチ準位の介在したGaAs MESFETの周波数分散機構の解明", 第40回応用物理学会関係連合講演会 93年3月

28. 何、大部、森吉、水田、山口、"スクリーン移動度モデルの提案による高ドープ系の輸送機構解明(I)相互コンダクタンスのエンハンス効果", 第40回応用物理学会関係連合講演会 93年3月

29. 森吉、何、加賀谷、大倉、水田、山口、"スクリーン移動度モデルの提案による高ドープ系の輸送機構解明(II)電気特性におけるエンハンス効果の実証", 第40回応用物理学会関係連合講演会 93年3月